ABSTRACT

Title of Document: NUCLEATE POOL BOILING CHARACTERISTICS FROM A HORIZONTAL MICROHEATER ARRAY

Christopher Henry, Ph.D., 2005

Directed By: Associate Professor, Jungho Kim, Department of Mechanical Engineering

Pool boiling heat transfer measurements from different heater sizes and shapes were obtained in low-g (0.01 g) and high-g (1.7 g) aboard the NASA operated KC-135 aircraft. Boiling on 4 square heater arrays of different size (0.65 mm^2, 2.62 mm^2, 7.29 mm^2, 49 mm^2) was investigated. The heater arrays consist of 96 independent square heaters that were maintained at an isothermal boundary condition using control circuitry. A fractional factorial experimental method was designed to investigate the effects of bulk liquid subcooling, wall superheat, gravitational level, heater size and aspect ratio, and dissolved gas concentration on pool boiling behavior.

In high-g, pool boiling behavior was found to be consistent with classical models for nucleate pool boiling in 1-g. For heater sizes larger than the isolated bubble departure diameter predicted from the Fritz correlation, the transport process was dominated by the ebullition cycle and the primary mechanisms for heat transfer were transient conduction and microconvection to the rewetting liquid in addition to latent heat transfer. For heater sizes smaller than this value, the boiling process is dominated by surface tension effects

which can cause the formation of a single primary bubble that does not depart the heater surface and a strong reduction in heat transfer.

In low-g, pool boiling performance is always dominated by surface tension effects and two mechanisms were identified to dominate heat and mass transport: 1) satellite bubble coalescence with the primary bubble which tends to occur at lower wall superheats and 2) thermocapillary convection at higher wall superheats and higher bulk subcoolings. Satellite bubble coalescence was identified to be the CHF mechanism under certain conditions. Thermocapillary convection caused a dramatic enhancement in heat transfer at higher subcoolings and is modeled analytically. Lastly, lower dissolved gas concentrations were found to enhance the heat transfer in low-g. At higher dissolved gas concentrations, bubbles grow larger and dryout a larger portion of the heater surface.

NUCLEATE POOL BOILING CHARACTERISTICS FROM A HORIZONTAL MICROHEATER ARRAY

By

Christopher Douglas Henry

Thesis or Dissertation submitted to the Faculty of the Graduate School of the
University of Maryland, College Park, in partial fulfillment
of the requirements for the degree of
Doctor of Philosophy
2005

Advisory Committee:
Associate Professor Jungho Kim, Chair
Professor Marino Di Marzo
Professor James Duncan
Associate Professor Greg Jackson
Associate Professor Gary Pertmer

Dedication

Dedicated to my grandfather

Dr. Victor Charles Dawson

Urbanus et Instructus

Acknowledgements

I am forever grateful to my parents, Richard and Joan Henry, for their unfading support and encouragement throughout my academic career. Their strength, hard work, determination, courage, and love is a constant reminder of the triumph of the human spirit and is a testament to their character and integrity. They have provided me with tremendous opportunity without which this work would not have been possible.

This effort is built on the solid foundation created by previous researchers including John Benton, Toby Rule, and Dr. Kim. I would like to sincerely thank my advisor, Dr. Jungho Kim, for his insight into the physical process, and guidance. His constant motivation enabled me to see this effort through to fruition. The personal and professional growth that I experienced while working for him were the result of opportunity and scholarly discourse and I am grateful for his generosity.

I would like to thank my colleagues, Johnathan Coursey, Fatih Demiray, Dr. Sakamoto, and all of my peers in the Phase Change Heat Transfer Lab for their friendship and encouragement. The countless inquiries and arguments in which we engaged were enlightening and invaluable to the progress and quality of this endeavor.

This project was supported by the Office of Biological and Physical Research at NASA Headquarters. I would like to personally thank John McQuillen, Jerry Myers, John Yaniec, and the entire team at the microgravity office for their assistance and guidance during flight weeks aboard the KC-135.

Table of Contents

LIST OF TABLES

Table of Figures

Nomenclature

A_i	area of individual heater element [m^2]
A_h	total heater area [m^2]
α_i	temperature coefficient of resistance (TCOR) for i^{th} heater [Ω/Ω°C]
α_t	theoretical TCOR for heater element
α	thermal diffusivity [m^2s]
A_v	cross-sectional area of vapor stems [m^2]
A_w	area of heated surface [m^2]
Bo	Bond number
Bo_B	Bond number (with bubble diameter as length scale)
c	concentration
c_p	specific heat of liquid [J/kgK]
C_{sf}	Rohsenhow constant
D_d	bubble departure diameter [m]
f	bubble departure frequency [Hz]
$\dot{f}$	Mean area fraction
f_{obj}	possible objective function
f_i	objective function
g	gravitational constant [m/s^2]
γ	1.4 for air
h	heat transfer coefficient [W/m^2K]
h_b	bulk heat transfer coefficient [W/m^2K]
h_{fg}	heat of vaporization [J/kg]
H_n	Distance between nozzle and heater [mm]
k	thermal conductivity [W/mK]
k_v	vapor thermal conductivity [W/mK]
L_b	capillary length [m]
λ_c	critical wavelength [m]
λ_d	most dangerous wavelength [m]
L_h	heater length [m]

M	molecular weight [kg/mol]
M_a	Mach number
m	$0.12 - 0.2 \log_{10} R_p$
n	number of powered heaters
μ	dynamic viscosity of liquid [Ns/m^2]
μ_v	dynamic viscosity of vapor [Ns/m^2]
Ma	Marangoni number
Nu	Nusselt number
P	pressure [N/m^2]
P_c	critical pressure [N/m^2]
Pr	Prandtl number
P_r	reduced pressure
$q_{CHF, sub}$	critical heat flux, subcooled bulk conditions [W/m^2]
$q_{CHF, sat}$	critical heat flux, saturated bulk conditions [W/m^2]
q''	heat flux [W/m^2]
q''_b	boiling heat flux [W/m^2]
q''_{nc}	natural convection heat flux [W/cm^2]
$q_{raw,i}$	heat flux from heater element I [W/cm^2]
$q_{sc,i}$	substrate conduction from heater element i [W/cm^2]
$q_{sc,vert,i}$	y-direction vertical substrate conduction from heater element i [W/cm^2]
$q_{sc,lat,i}$	x-direction substrate conduction from heater element i [W/cm^2]
q_{vap}	heat flux from heater to vapor FC-72 [W/cm^2]
q_i	boiling heat transfer from heater element I [W/cm^2]
$q_{total}(t)$	spatially averaged heat flux [W/cm^2]
$q_{w,i}$	heat transfer from heater i [W]
$\overline{q}_{total}$	time and spatially averaged heat flux [W/cm^2]
ρ_l	liquid density [kg/m^3]
Ra_L	Rayleigh number
Re	Reynolds number

R_c	conduction resistance [m^2K/W]
R_{conv}	convection resistance [m^2K/W]
R_h	heater resistance [Ω]
R_{DP}	digital potentiometer resistance [Ω]
$R_{1\text{-}5}$	feedback circuit resistors [Ω]
R_p	rms roughness of surface [m]
R_{ref}	reference heater res. at T_{ref} [Ω]
ρ_e	nozzle exit density [kg/m^3]
ρ_v	vapor density [kg/m^3]
s	1.7 for most liquids [1.0 for water]
σ	surface tension [N/m]
Δt	0.004 [s]
T	temperature [C]
T_e	nozzle exit temperature [C]
T_t	total heat transfer averaging time [s]
T_{bulk}	bulk liquid temperature [C]
T_h	heater temperature [C]
θ	contact angle [radians]
T_{ref}	reference temperature [C]
ΔT_{sub}	bulk liquid subcooling = $T_{sat} - T_{bulk}$ [C]
ΔT_{sat}	wall superheat = $T_w - T_{bulk}$ [C]
T_{sat}	saturated temperature [C]
T_w	wall temperature [C]
U_{Ai}	area uncertainty [cm]
u_{Vi}	voltage uncertainty [volts]
$u_{qraw,i}$	uncertainty in raw heat flux [W/cm^2]
u_{Ri}	resistance uncertainty [Ω]
V_i	i^{th} heater voltage [volts]
v_e	Nozzle exit velocity [m/s]

v_n	normal velocity [m/s]
v_t	Tangential velocity [m/s]
ν	kinematic viscosity [m^2/s]
x	quality
φ	electrical potential [V]

Chapter 1: State of the Art in Pool Boiling

1.1 INTRODUCTION / MOTIVATION

Studies pertaining to the influence of gravity on boiling processes have been stimulated by two motivations. Firstly, higher accuracy predictive modeling is desired for the design of robust, efficient, economical, and reliable space applications that utilize the efficiency of latent heat transport. This type of modeling requires a firm understanding of boiling mechanisms in a host of operational environments. Secondly, a comprehensive physical understanding of the complicated boiling mechanisms is sought.

An important industrial application of heat transfer science and engineering in recent years has been electronics thermal control. The relentless emphasis on miniaturization is the primary driving force behind systems with dramatically higher spatial densities. Power dissipating devices, such as computer processors, are being designed to achieve higher computing performance while dissipating larger amounts of power per unit area, Fig. 1.1. These trends pose significant challenges for future thermal design that are not easily solved using contemporary thermal solutions. Boiling heat transfer has gained considerable attention over the years due to the relatively large heat fluxes that can be achieved at relatively small temperature differences, Fig 1.2. Two-phase cooling systems have the ability to provide efficient, application specific, temperature control, and these benefits have led to research efforts aimed at quantifying boiling efficiency at the small scale and in variable gravitational environments. One of the goals of research in this area is to determine the feasibility of applying boiling technology in a space environment. Such efforts will provide a predictive design aid to

scientists and engineers tasked with the design, analysis, fabrication, and testing of space based hardware that utilize two-phase transport.

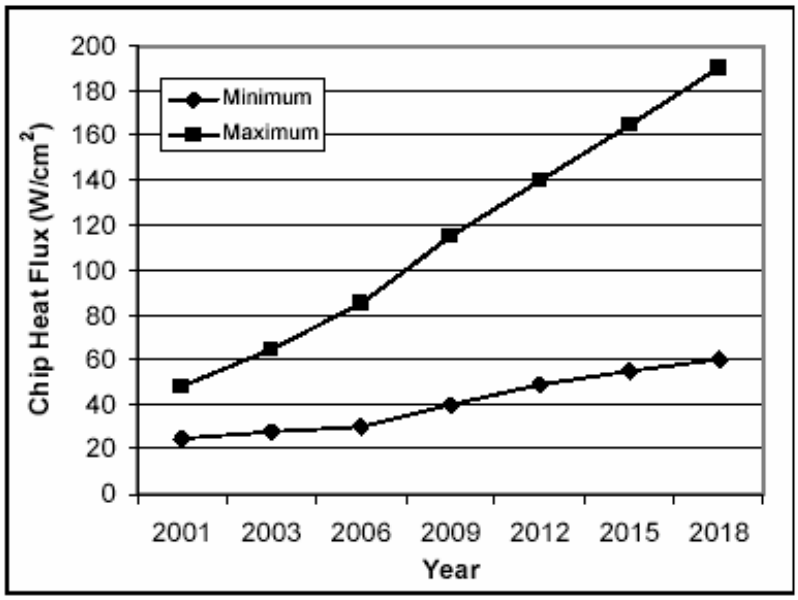

Figure 1.1: Projected microchip cooling requirements (iNEMI Technology Roadmaps, Dec 2004).

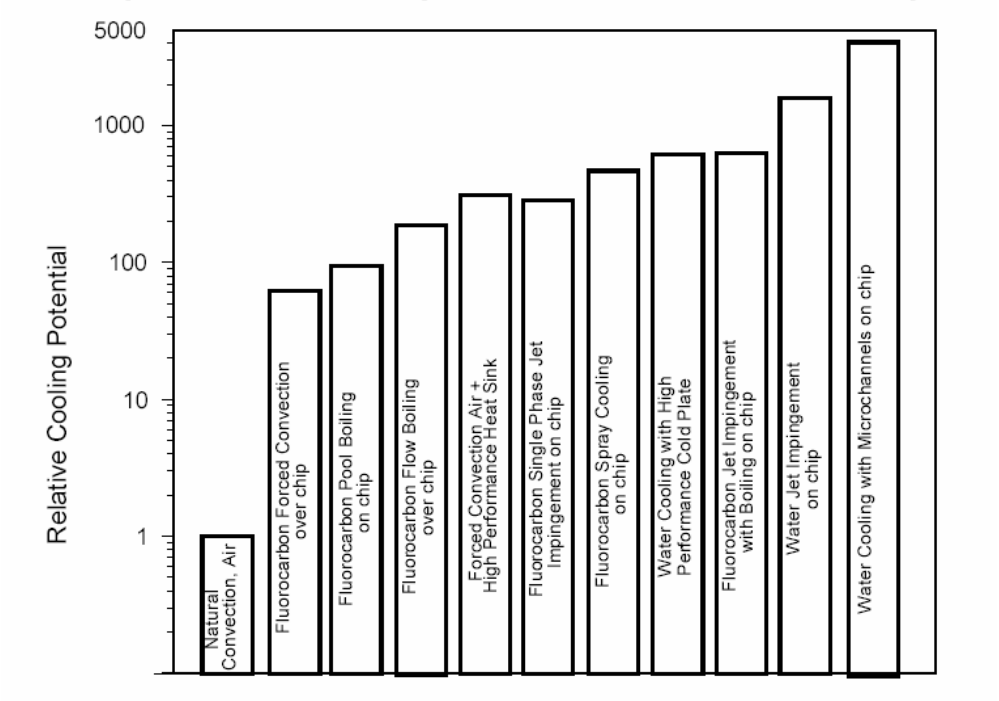

Figure 1.2: Cooling potential for various processes (iNEMI Technology Roadmaps, Dec 2004).

The second motivation for work in this area is centered on the desire to understand natural physical processes in space. Many natural two phase processes occur in space systems such as liquid droplet formation in humid environments and vapor generation during distillation and purification. These processes and others require a basic understanding of two-phase transport processes in order to affect reliable and robust operation. For such processes, the design and research objectives are to understand and predict the behavior of the system as opposed to maximizing the efficiency of the transport process as in electronics thermal control. Other multiphase applications where a basic understanding of the physical process is desired are: cryogenic fuel storage and transportation, wastewater recovery, distillation systems, air revitalization, water purification, and material processing.

The third motivation for such work focuses on the space environment itself which creates an intriguing setting whereby complex processes on earth can be studied in a more simplistic manner. The pool boiling process is an excellent example of this in which the complex interaction between various boiling mechanisms can be de-coupled and studied at a fundamental level. The various mechanisms referred to and their relative effect on the pool boiling process will be discussed in detail throughout this thesis.

Lastly, the human desire to understand their physical environment cannot be overlooked as a primary motivation for research in a general sense. Such work is an intellectually stimulating endeavor providing its own benefits to those who enjoy studying fascinating complex problems. Scientific idealism rooted in inquisitive minds has led to a greater understanding of our relationship with our environment, technological innovation, and provides tremendous insight into our prospects for the future.

A logical place to begin the discussion of boiling heat transfer in space is to briefly review the extensive data that has been collected regarding the phenomenon in higher gravitational environments. Under such conditions, the pool boiling process is fairly well understood and the available data provides an excellent introduction into the complexities of a low-gravity boiling environment. Along with introducing the relevant background information, this chapter provides the context in which to begin analysis of the microgravity boiling environment.

1.2 CLASSICAL BOILING LITERATURE REVIEW

Boiling in space is poorly understood. The costs associated with experimentation, challenges of creating a suitable space environment, and logistical issues associated with space transportation have hindered progress to date. The lack of progress requires one to look elsewhere to gain insight into the particular process under investigation. In the case of pool boiling, extensive knowledge exists regarding the 1-g condition. A review of the state of the art in 1-g pool boiling therefore provides a number of benefits to the researcher including; a foundation with which to begin further analysis, insight into some of the physical mechanisms of the process, and a plethora of models with which to begin an investigation and comparison.

1.2.1 Terrestrial Boiling

The pool boiling process is an extremely complicated one that extends into many disciplines. The physical manifestations of the boiling process can be observed daily from boiling of water for cooking applications to natural processes such as hot spring evaporation. It involves the physics of heterogeneous bubble nucleation, the chemistry of

two-phase and triple phase interfaces, the thermodynamics of local heat transport, and the hydrodynamics of two-phase flow. Boiling heat transfer has traditionally been thought of as a combination of free convection, vapor liquid exchange, microconvection, transient conduction, and latent heat transport. Vapor bubble dynamics associated with nucleation, bubble growth, departure, collapse, and subsequent rewetting of the heater surface characterize the classical ebullition cycle which constitutes the primary mechanisms of heat transfer from a superheated wall during nucleate pool boiling in earth gravity.

Some of the early work mentioned above has laid the foundation for the classical boiling curve and its constituent boiling regimes, Fig 1.3. At low superheats, natural convection dominates the transport process (a-b, Fig 1.3). As the wall superheat is increased, the process progresses through the isolated bubble regime and regime of vapor

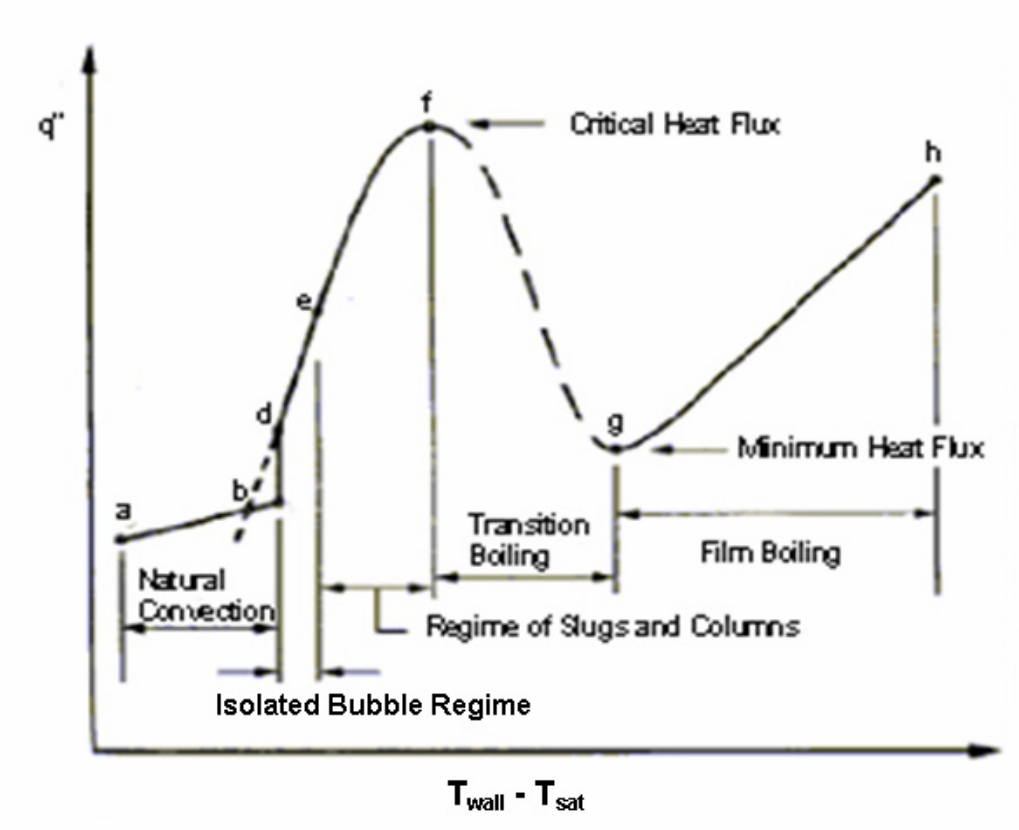

Figure 1.3: Classical nucleate pool boiling curve.

slugs and columns (d-f, Fig 1.3). Eventually critical heat flux (CHF) is reached and the measured heat flux begins to decrease as transition boiling occurs (f-g, Fig 1.3). Eventually, the boiling process is completed dominated by film boiling (g-h, Fig 1.3).

Early studies in the field focused on the qualitative aspects of the nucleate pool boiling process. Photographic results identified the four heat transfer regimes mentioned above which were characterized based on the mode of vapor generation. Consider first a heated flat surface. As the surface temperature increases, vapor structures progress through a sequence of discrete bubbles, vapor columns, vapor mushrooms, and vapor patches, Fig. 1.4 (Gaertner, 1965). The individual vapor structures and their various combinations determine the mechanism of transport. Many researchers have studied these mechanisms in isolation and collectively. A large portion of their results are from heater sizes much larger than the capillary length scale (Eq. 1.1). The capillary length, L_b, as shown for various fluids in Table 1, is derived from a balance between surface tension and buoyant forces acting on a vapor bubble. This length scale is relatively small

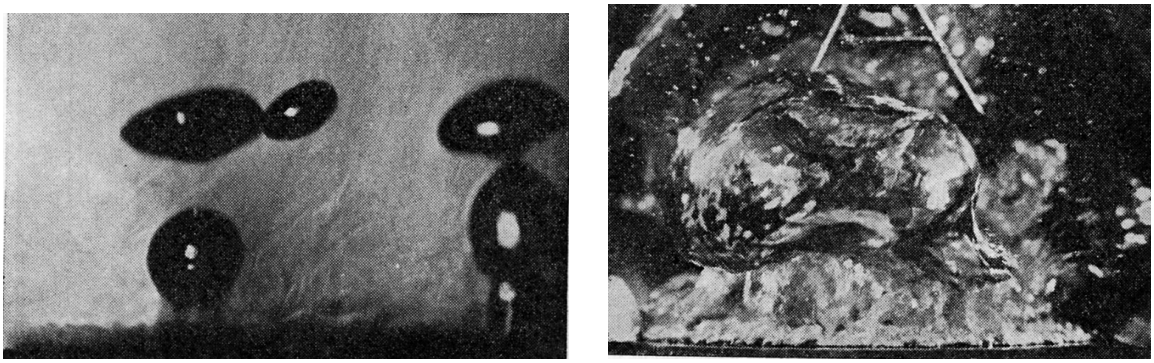

Figure 1.4: Discrete bubble region (left), vapor mushroom (right), (Courtesy of Gaertner, 1965).

$$L_b = \sqrt{\frac{\sigma}{g(\rho_l - \rho_v)}} \tag{1.1}$$

and many of the traditional sensors have been unable to accurately resolve heat transfer data at the capillary length scale or smaller. In space, as the g-level goes to zero, the capillary length scale goes toward infinity which indicates that all finite sized heaters appear small compared to this length in space. Boiling from heaters much smaller than the capillary length scale is less well known and is a large motivation for low-gravity pool boiling research.

	Capillary Length, L_b (mm)		
Fluid	Low-g (0.01g)	1-g	high-g (1.7g)
FC-87	7.48	0.75	0.57
FC-72	7.81	0.78	0.60
R113	12.00	1.20	0.92
R22	12.08	1.21	0.93
Water	27.13	2.71	2.08

Table 1.1: Capillary length of different fluids (NIST, 2003; 3M).

1.2.1.1 Nucleate Boiling Regime. Consider the nucleate pool boiling curve in greater detail, Fig 1.3. At low wall superheats natural convection is the dominant transport mechanism. Natural convection is characterized by single-phase buoyancy effects with no active nucleation sites on the heated surface. Increasing the wall superheat eventually causes boiling incipience to occur with a resulting increase in heat transfer (labeled d in Fig. 1.3). Many researchers have aimed to model the transport process in the nucleate boiling regime using single bubble models. Latent heat transport as well as microconvection is thought to contribute to a relatively high heat transfer between the heater and working fluid. Some researchers have proposed that latent heat transfer due to evaporation of a liquid microlayer near the three-phase contact line is the dominant energy removal mechanism (Straub et al. 1997, Moore and Mesler 1961, Fig 1.5). In contrast, experiments conducted by Gunther and Kreith showed that the majority of heat

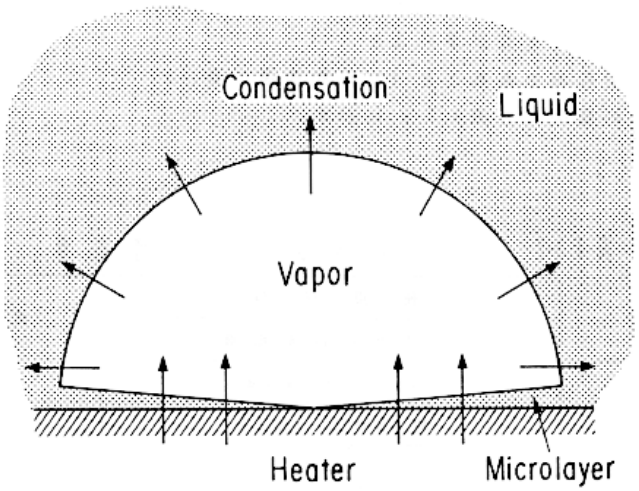

Figure 1.5: Microlayer formation beneath bubble (Courtesy of Van Carey, 1992).

transfer during subcooled nucleate pool boiling could be attributed to microconvection during liquid rewetting of the heated surface (Gunther and Kreith, 1956). Yaddanapuddi and Kim later confirmed these experimental findings while studying nucleate boiling under saturated bulk conditions (Yaddanapuddi and Kim, 2001). Their results showed that during one ebullition cycle, the majority of heat transfer occurred after the bubble departed through transient conduction and microconvection to the rewetting liquid. Additional studies by Zhang et. al. measured a very small amount of heat transfer through the microlayer during the isolated bubble regime lending further support to the microconvection theory (Zhang et. al. 2000). Considerable debate still exists regarding the primary mechanism for heat transfer during isolated bubble growth and departure and is the primary motivation for current work in the area.

The various isolated bubble models mentioned above provide some insight into the parameters which tend to enhance the heat transfer during isolated bubble growth and departure. Microconvection theory predicts an increase in time averaged heat transfer from the heated surface if the bubble departure frequency increases. Methods aimed at

increasing the bubble departure frequency, such as electrohydrodynamic (EHD) pool boiling, have clearly shown an increase in the attainable heat flux (DiMarco & Grassi, 1992). This technique involves applying an electric field body force which can produce forces that induce localized fluid motions enhancing the two-phase transport process in thermal systems. The EHD mechanisms include a Coulomb force, dielectrophoretic force, and electrostriction force. Baboi et al., while studying boiling from a platinum wire, observed an increase in nucleate boiling heat transfer and CHF in the presence of a strong electric field force collinear with buoyancy (Baboi et al. 1968). They attributed the large increase in heat transfer primarily to an increase in bubble departure frequency. In addition, bubble growth times were diminished and departure diameter was reduced in the presence of an electric field. Such work characterizes the importance of two critical physical parameters of the ebullition cycle on heat transfer: the frequency of bubble departure or surface rewetting, f, and the bubble departure diameter, D_d.

The bubble departure diameter depends directly on the forces acting on the bubble during dynamic vapor bubble growth while attached to the heater surface. Many forces have been shown to influence departure dynamics including: surface tension ($F_{\tau,s}$), buoyancy (F_B), inertia of induced liquid motion (F_{LM}), Marangoni or thermocapillary forces ($F_{\tau,v}$), and vapor bubble coalescence ($F_{C,E}$), Fig. 1.6. The magnitude and influence of these forces have in turn been shown to be a function of many system parameters including: bulk liquid subcooling (ΔT_{sub}), gravity (g), wall superheat (ΔT_{sat}), the thermophysical properties of the fluid, heater geometry, surface characteristics, and pressure.

The frequency of bubble departure depends on the time needed for the bubble to

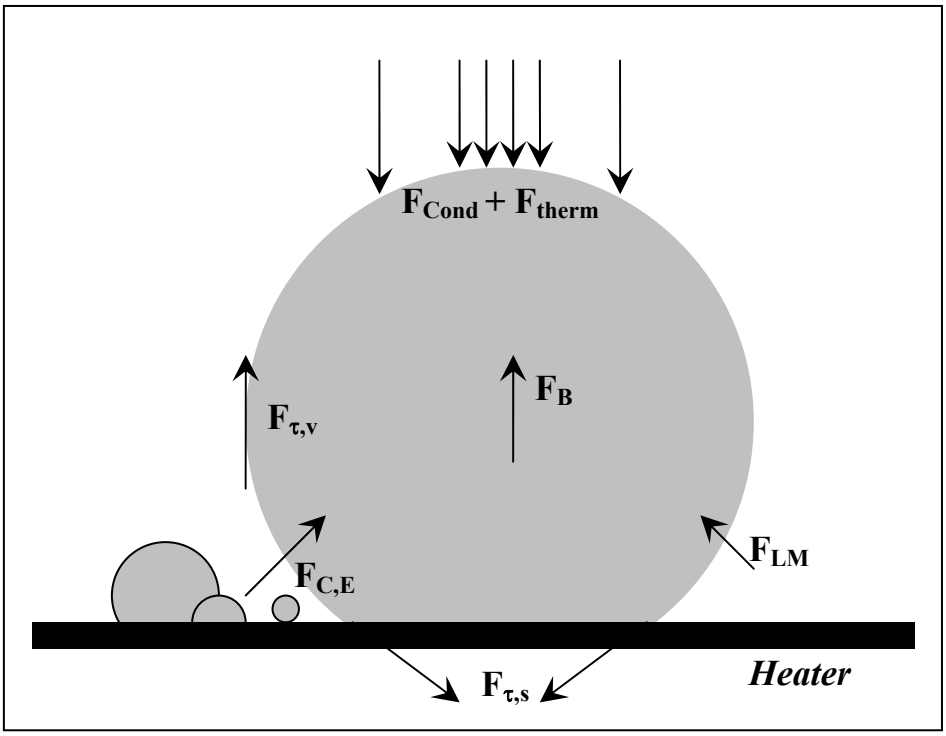

Figure 1.6: Forces acting on a bubble.

grow to the departure size (growth time) and the amount of time it takes after a bubble departs for nucleation to occur (waiting time). The departure frequency in the isolated bubble regime tends to increase with wall superheat due to the increased rate of vapor generation producing a smaller growth time. In addition, higher wall superheats tend to reduce the waiting time by decreasing the time needed for the rewetting liquid to reach the superheat limit required for nucleation. It is clear from the research cited previously that bubble departure is critical to the enhancement of heat and mass transport during the pool boiling process. Very little work has been conducted on systems where bubble departure is less frequent or non-existent.

As the wall superheat is increased beyond the isolated bubble regime, bubble coalescence becomes a dominant physical occurrence characterized by the formation of vapor columns and slugs. In this regime, metrics such as bubble departure frequency and

departure diameter tend to be much less useful due to turbulent vapor and liquid interaction where isolated bubbles are no longer present. For large heaters, vapor is generated at a high rate and at multiple locations enabling lateral and vertical bubble coalescence to occur. This causes vapor columns to form due to Taylor instability and the spacing between columns has been shown to be related to the capillary length scale, Fig. 1.7.

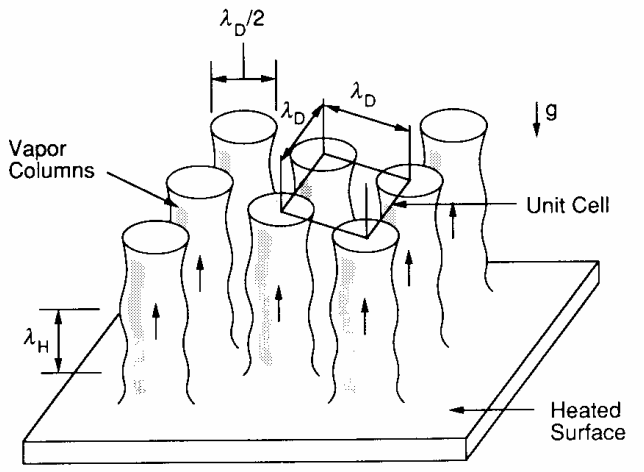

Figure 1.7: Vapor columns formation and the Taylor wavelength, λ_d (Courtesy of Van Carey, 1992).

Many analytical models have been developed that predict nucleate boiling behavior throughout the isolated bubble regime and into the regime of vapor slugs and columns in earth gravity from horizontal heaters significantly larger than L_b. An early model developed by Fritz (1935), based on a quasistatic analytical force balance between surface tension and buoyancy, assumes the non-dimensional Bond number to be the governing parameter for bubble departure diameter, Eq. 1.2. This equation predicts

$$Bo_B^{1/2} = 0.0208\,\theta = \sqrt{\frac{g(\rho_l - \rho_v)D_d^2}{\sigma}} \tag{1.2}$$

departure occurs at a constant Bond number for a given fluid/surface combination. A major deficiency in this model is that it only accounts for the effects of wall superheat and bulk subcooling through their influence on the contact angle, θ. Later correlations [Eq. 1.3 (Rohsenhow, 1962), Eq. 1.4 (Cooper, 1984), and Eq. 1.5 (Stephan and Abdelsalam, 1980)] provide an estimate of nucleate boiling heat transfer

$$\frac{q''}{(T_w - T_{sat})^3} C_{sf}^3 = \frac{\mu c_p^3}{h_{fg}^2 \, \mathrm{Pr}^{3s}} \sqrt{\frac{g(\rho_l - \rho_v)}{\sigma}} \tag{1.3}$$

$$h = 55(q'')^{0.67} M^{-0.5} P_r^m (-\log_{10} P_r)^{-0.55} \tag{1.4}$$

$$Nu = 207 X_1^{0.745} X_5^{0.581} X_6^{0.533}, \quad X_1 = \frac{q''}{kT_w}, \quad X_5 = \frac{\rho_v}{\rho_l}, \quad X_6 = \mathrm{Pr} \tag{1.5}$$

from relatively large heaters in earth gravity. The Rohsenow model is based on microconvection theory in which the heat transfer is attributed to local agitation due to liquid flowing behind the wake of departing bubbles. The equation is a modification of a single-phase forced convection correlation using the appropriate length (bubble departure diameter) and velocity scales. The correlation developed by Stephan and Abdelsalam is a curve fit of available data and its accuracy varies widely depending on the operating conditions.

1.2.1.2 Critical Heat Flux. If the wall superheat is further increased along the nucleate pool boiling curve, Fig. 1.3, CHF will eventually occur. CHF is the maximum heat flux that can be achieved without a significant rise in the heater wall temperature. CHF is

perhaps the most critical design parameter for two-phase cooling systems and accurate modeling of this phenomenon is paramount to predicting the operating range and reliability of cooling systems.

Many mechanisms have been proposed to explain the behavior of CHF in earth gravity. In one mechanism, a Helmholtz instability results from vapor columns that break down to form local dry patches on the heater. The breakdown results from severe vapor drag on rewetting liquid that is flowing in the opposite direction and causes a liquid flow crisis to the heater surface. The Helmholtz wavelength is shown in Fig. 1.7 as λ_h. Zuber's CHF model for an infinite horizontal surface assumes that vapor columns formed by the coalescence of bubbles become Helmholtz unstable, blocking the supply of liquid to the surface (Zuber, 1959). These vapor columns are spaced λ_D apart (Eq. 1.6), Fig 1.7. In this equation, the critical wavelength, $\lambda_{c,}$ is the wavelength below which a vapor layer

$$\lambda_D = 2\pi\sqrt{3}\left[\frac{\sigma}{g(\rho_l - \rho_v)}\right]^{1/2} = 2\pi\sqrt{3}LBo^{-1/2} = \sqrt{3}\lambda_c \qquad (1.6)$$

can be stable underneath a liquid layer. Only perturbations with a wavelength greater than λ_c will grow and cause interfacial instabilities. The critical wavelength for a number of fluids is provided in Table 1.2. The Zuber model predicts a maximum heat transfer of the form given by Eq. 1.7. It is important to note that the gravitational dependence on

	Critical Wavelength λ_c(mm)		
Fluid	Low-g (0.01g)	1-g	high-g (1.7g)
FC-87	47.02	4.70	3.61
FC-72	49.08	4.91	3.76
R113	75.40	7.54	5.78
R22	75.92	7.59	5.82
Water	170.48	17.05	13.08

Table 1.2: Critical wavelength for different fluids.

$$q''_{\max} = 0.149\rho_v h_{fg}\left[\frac{\sigma(\rho_l-\rho_v)g}{\rho_v^2}\right]^{1/4} \tag{1.7}$$

CHF predicted by Zuber's model, indicates that CHF in a zero-g environment would be zero. This prediction differs greatly from experimental findings in low-gravity which will be presented in the next section. Furthermore, the critical wavelength increases dramatically in low-g environments making it difficult to observe Taylor instabilities in low-g.

Another popular model assumes CHF is governed by a hydrodynamic instability where large vapor bubbles hovering slightly above a surface are fed by smaller vapor columns (Haramura and Katto, 1983), Fig 1.8. This model postulates that CHF occurs if the hovering time exceeds the time necessary to evaporate the liquid film between the hovering bubble and the heater causing the heater to dry out. This model assumes the Bond number to be the governing parameter controlling the development of CHF in earth gravity and for horizontal flat plates is predicted by Eq. 1.8.

$$\left(\frac{q_{CHF}}{\rho_v h_{fg}}\right)\Bigg/\left[\frac{\sigma g(\rho_l-\rho_v)}{\rho_v^2}\right]^{1/4} = \left(\frac{\pi^4}{2^{11}\cdot 3^2}\right)^{1/16}\left(\frac{A_v}{A_w}\right)^{5/8}\left(1-\frac{A_v}{A_w}\right)^{5/16}\left[\left(\frac{\rho_l}{\rho_v}+1\right)\Bigg/\left(\frac{11\rho_l}{16\rho_v}+1\right)^{3/5}\right]^{5/16} \tag{1.8}$$

Increasing the wall superheat beyond CHF causes a decrease in boiling performance. In the transition boiling regime (f-g, Fig 1.3), the boiling process is increasingly dominated by dryout of the heater surface. Eventually, a local minimum in heat transfer occurs when vapor completely covers the heater surface, commonly referred to as the Liedenfrost point. Physically, this is the beginning of film boiling where a stable vapor film forms between the heater surface and the surrounding bulk liquid. The major transport mechanism in this regime is conduction and radiation exchange through

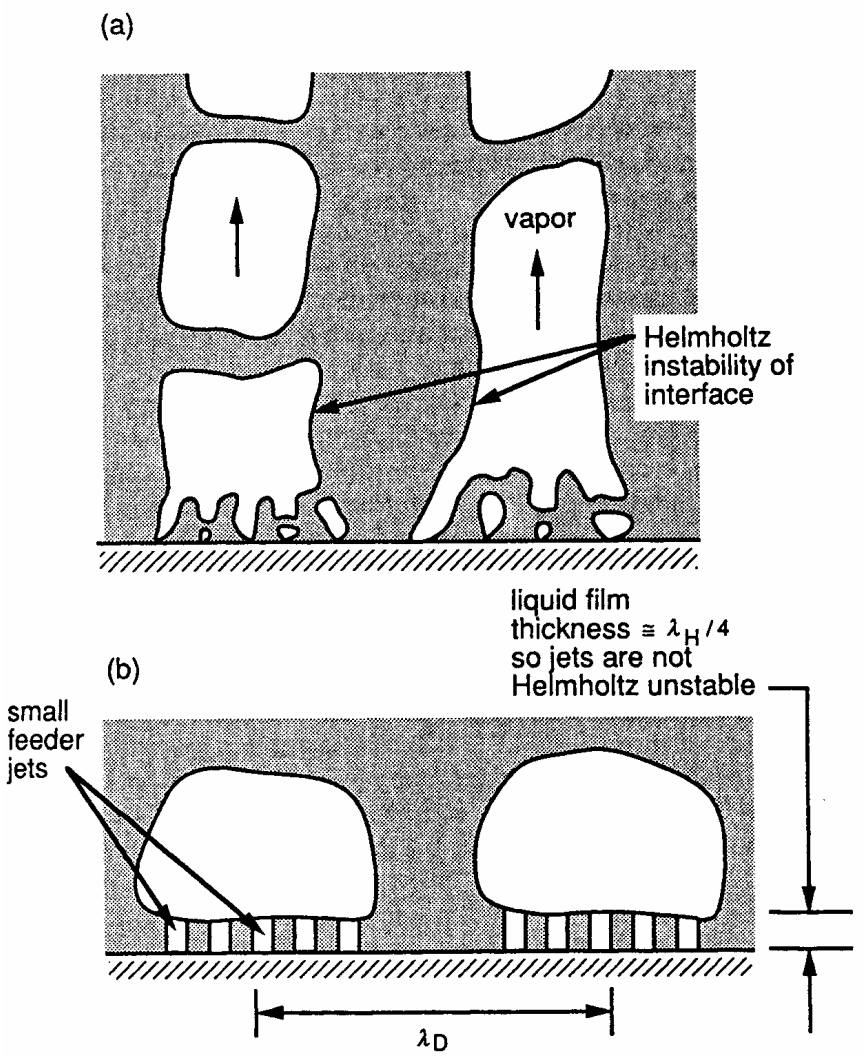

Figure 1.8: Helmholtz instability mechanisms (Courtesy of Van Carey, 1992).

the vapor film. The transport characteristics of this regime are quite poor and therefore operating conditions that create film boiling in two-phase cooling systems are largely avoided by the practicing design engineer.

1.2.2 Terrestrial Pool Boiling Enhancement

At first glance, the microconvection models provide some insight into the parameters which affect the heat transfer performance during the pool boiling process. In addition to electrohydrodynamic and acoustic field bubble removal which focus on

altering the bubble departure frequency and departure diameter, other system operating parameters have been shown to dramatically influence heat transfer performance during pool boiling in earth gravity. A commonly applied method for increasing heat transfer performance is to cool the bulk liquid below the saturation temperature under the system operating conditions, commonly referred to as subcooling the fluid.

The effect of bulk liquid subcooling on nucleate pool boiling heat transfer has been of particular interest to some researchers over the years due to the enhancement in heat transfer that can be achieved by the additional sensible energy storage mode. An increase in subcooling is thought to provide higher heat transfer rates during the initial rewetting process in which the cool liquid contacts the heated surface and the mechanism for heat transfer is conduction and micro-convection. Subcooling has been experimentally shown to influence bubble geometry as reported by Gunter and Kreith who observed a decrease in bubble size with an increase in bulk subcooling. In addition departing bubbles rapidly collapsed in the presence of higher subcooling (Gunter and Kreith, 1949).

At first glance one might expect to measure an enhancement in heat transfer under highly subcooled conditions in the nucleate boiling regime. Smaller, rapidly collapsing bubbles provide less resistance for rewetting liquid and may increase the bubble density on the heated surface. Despite such enhancement effects, experimental investigations have shown subcooling to have no effect on heat transfer during nucleate boiling in earth gravity (Forster and Grief, 1959). Such measurements may be explained by the effect of subcooling on bubble departure frequency. As condensation is increased from the top surface of growing bubbles that are attached to the heated surface, the bubbles tend to

grow much more slowly, increasing the bubble growth time and reducing the liquid rewetting frequency. In addition, higher bulk subcoolings may tend to reduce the active site density on the heated surface. In total, subcooling effects on bubble departure frequency, bubble size, liquid rewetting temperature, and active site population density act to mitigate heat transfer differences compared to near saturated bulk conditions in the nucleate pool boiling regime.

Although negligible subcooling effects have been measured during nucleate pool boiling, it appears to significantly increase CHF. From a hydrodynamic perspective, an increase in subcooling acts to condense the vapor generated at the heated surface providing less resistance for bulk liquid to rewet the surface, delaying the onset of CHF to higher wall superheats. Kutateladze postulated that CHF in subcooled boiling should increase above similar saturated conditions by the amount of energy required to bring the subcooled liquid to a saturated state, Eq. 1.10 (Kutateladze, 1962). Ivey and Morris (1962) suggested C_o=0.1 and n=0.75 based on available data.

$$\frac{q_{CHF,sub}}{q_{CHF,sat}} = 1 + C_0 \left(\frac{\rho_l}{\rho_v} \right)^n \frac{c_p \left(T_{sat} - T_{bulk} \right)}{h_{fg}} \tag{1.10}$$

1.2.3 High-g Boiling

Boiling mechanisms at higher gravity levels are not thought to differ significantly from earth gravity. The dominant effect of higher gravity levels on boiling is the increase in buoyancy driven flows such as bubble motion and natural convection. Most natural convection correlations predict heat transfer of the form given by Eq. 1.11, with C and n being empirical constants (Incropera and Dewit, 2002). Studying natural convection

using a centrifuge at up to 1200g, Eschweiler and Benton provide a representative natural convection heat transfer correlation given by Eq. 1.12 (Eschweiler and Benton, 1967).

$$\overline{Nu_L} = CRa_L^n \qquad Ra_L = Gr_L \,\mathrm{Pr} = \frac{g\beta(T_s - T_\infty)L^3}{\nu\alpha} \tag{1.11}$$

$$\overline{Nu_L} = 0.15 Ra_L^{0.363} \qquad 2\times10^7 \le Ra_L \le 8\times10^{10} \tag{1.12}$$

As mentioned previously, boiling is dramatically affected by the bulk liquid conditions of the system. The increase in natural convection at higher gravity levels can dramatically influence the bulk liquid characteristics and thus the boiling dynamics.

An increase in natural convection can delay boiling incipience or suppress boiling completely depending on the level of liquid subcooling, the gravity level, and wall superheat (Koerner, 1970). Studies performed by Beckman and Merte focused on the influence of acceleration on pool boiling of water up to 100g. They found an increase in acceleration caused a decrease in the number of active nucleation sites on the heated surface. This was attributed to a thinning of the superheated boundary layer near the surface as buoyancy driven flows increased (Beckman and Merte, 1965).

Some pool boiling studies performed on horizontal heaters in high-g show similar trends to those mentioned above. Using a centrifuge, Ulucakli and Merte studied boiling from a horizontal heater. At 10g, they observed low heat flux boiling to be independent of subcooling for subcooling levels up 50°C. Such observations agree with the 1-g results previously mentioned. A further increase in bulk subcooling at this g-level suppressed boiling activity, and heat transfer was dominated by natural convection. At high heat flux, an increase in subcooling resulted in an increase in the wall superheat (at 50°C subcooling, a 35% increase in wall superheat was measured), holding all other

variables constant. At 100g, little effect of subcooling on wall superheat for subcooling up to 30°C was observed and boiling was completely suppressed as the subcooling was increased further (Ulucakli and Merte, 1990). In addition, bubble departure frequency increased while the bubble growth rate was found to be essentially constant and independent of acceleration. This indicates that the bubble departure diameter was reduced at higher gravity levels and is consistent with the Fritz model.

Ulucakli and Merte used the Mikic and Rosenhow Model (Mikic and Rosenhow, 1968) as the basis for explaining why, under certain conditions, a decrease in heat transfer at higher subcoolings and heat flux are observed compared to near saturated conditions. This model assumes the net heat transfer from a surface can be approximated by the sum of the boiling and natural convection components Eq. 1.13. In this equation, f represents the mean area fraction of the heater surface not experiencing boiling. Based

$$q'' = q''_b + f\, q''_{nc} \tag{1.13}$$

on this model, Ulucakli and Merte stated that the degradation of heat transfer at higher heat flux with increased subcooling resulted from a reduction in the superheated boundary layer thickness. This caused the suppression of some active nucleation sites and increased the non-boiling natural convection component to overall heat transfer. The natural convection contribution to the total heat flux began to outweigh that associated with the active nucleation sites as the subcooling was increased further, and eventually complete suppression of all boiling on the surface occurred (Ulucakli and Merte, 1990). Such experimental results clearly contradict what is predicted by Kutateladze and others and emphasizes the need for additional gravity dependent parameters in such correlations.

The contradictory results summarized here suggest that relatively little is known on the coupling between g-level and bulk subcooling. Current models do not accurately account for this effect and further research is needed in order to clarify the conditions where gravity and subcooling combine to increase or decrease the level of heat transfer.

1.2.4 Summary of Classical Boiling

In summary, nucleate boiling at scales larger than the capillary length under terrestrial gravitational conditions are dominated by gravity effects such as buoyancy. Buoyancy driven convection is the fundamental transport mechanism at the macroscale and affects bubble departure characteristics and the complex interaction between vapor and liquid flows. Heat transfer enhancement occurs in the nucleate pool boiling regime if the bubble departure frequency is increased, bubble departure diameter decreases, active nucleation site density increases, or any combination of these. In high-gravity, the effects of liquid subcooling are still unclear and this has hindered the development of analytical and numerical models in this area. Many models estimate performance based on various physical mechanisms such as surface tension and buoyancy.

Much less experimental work has been devoted to studying the phenomena at significantly smaller scales and at lower gravity levels where buoyancy effects are less significant, and where the heater size is much smaller than the capillary length. Microgravity environments provide an intriguing setting to study smaller scale boiling activity due to the large increase in the capillary length with decreasing g-level. Microgravity environments may also provide a more desirable setting to study heat transfer mechanisms such as microlayer evaporation.

In conclusion, the models presented above tend to predict a very small heat transfer in low-g. The heat and mass transport process is expected to be much less efficient as buoyancy driven flows become less significant. The following section addresses this issue.

1.3 MICROGRAVITY BOILING

Although buoyancy driven flows have been shown to dominate the transport process at higher gravity levels, relatively little is known of the boiling phenomenon in the microgravity environment. The principle reason for this can be related to the difficulty in creating a quality microgravity environment for long periods of time and the relatively high costs involved in space studies.

The microgravity environment provides a setting in which some of the complex mechanisms previously mentioned are decoupled, simplifying the physical process. As a result, microgravity environments provide an ideal setting to study reduced gravity effects as well as gather information about significant earth gravity mechanisms that are typically masked by natural convection.

A strong reduction in buoyancy driven flow is thought to dramatically affect the thermal boundary region near the heated surface. In the case of a small heater submerged in a large pool of liquid without the presence of bubbles, the thermal boundary layer can be modeled assuming semi-infinite solid conduction. In contrast, in earth gravity, the boundary layer is much thinner due to rising and falling convection cells near the surface. As a result, in low–g under constant heat flux conditions, the temperature of the heated surface tends to rise more quickly and reach a higher temperature at steady-state. Energy transport within the fluid is dominated by diffusion transport and the thermal boundary

region is much larger than under comparable earth gravity conditions where advection tends to dominate the process, Fig. 1.9. Such characteristics may explain why boiling incipience tends to occur at lower wall superheats and lower heat fluxes in low-g. The thermal boundary layer is much larger and therefore nucleating bubbles have more energy within the superheated region to sustain growth.

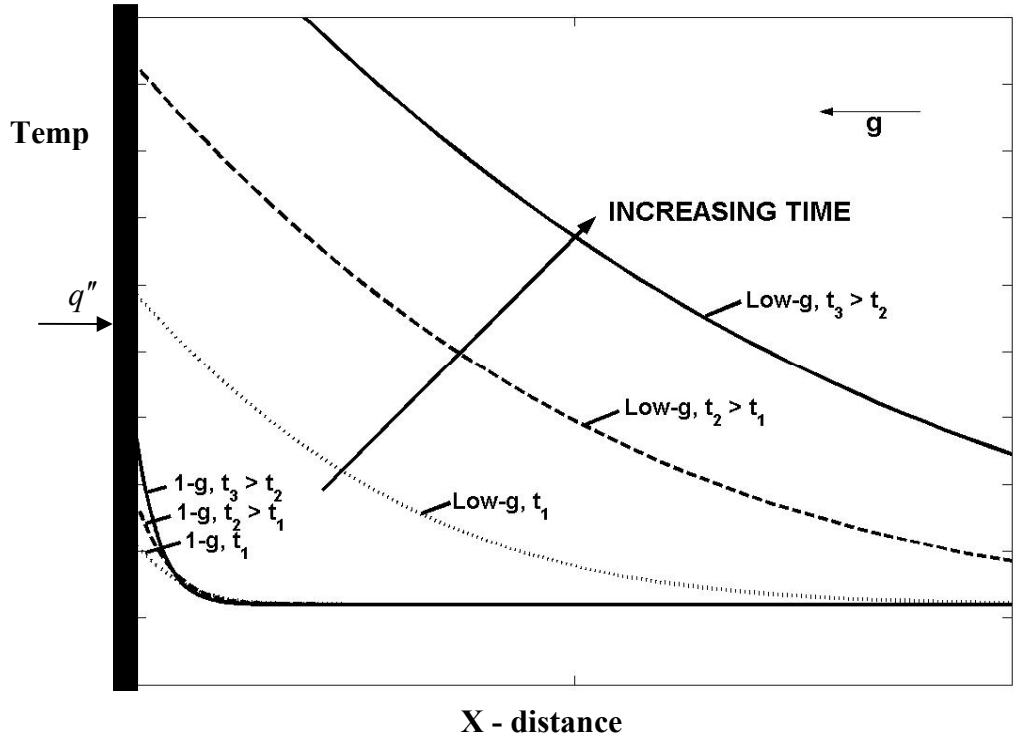

Figure 1.9: Single phase thermal boundary layer development at various times.

As mentioned previously, extensive research has been conducted on heaters larger than the capillary length while less is known of boiling on the smaller scale and at lower gravity levels. Under low-g and microgravity conditions, the capillary length becomes quite large, raising questions about its scaling effectiveness. Analyzing the boiling mechanisms at the small scale in earth gravity, Bakru and Lienhard studied boiling from small wires. Boiling curves presented in their work deviate significantly from classical

boiling behavior in that no transitional boiling regime from nucleate boiling to film boiling was observed, and the formation of "patchy" boiling partially covered the wire. The Liendenfrost point and CHF were not observed in their study, leading to the conclusion that such regimes vanish for heater sizes smaller than $L_h/L_b < 0.01$. They concluded that classical pool boiling behavior is observed if the heater length is of the order $L_h/L_b > 0.15$ (Bakru and Lienhard, 1972).

Keshok and Siegel were one of the first researchers to study boiling from flat heaters. They observed that a reduction in gravity resulted in a decrease in buoyancy and inertial forces acting on vapor bubbles caused them to grow larger and stay on the surface longer (Keshok and Siegel, 1964). Drop tower tests performed by Susumu showed that boiling in low-g can produce large primary bubbles that are surrounded by smaller satellite bubbles. Susumu measured small changes in heat flux compared to normal gravity conditions and observed occasional bubble departure which was attributed to induced inertial effects within the liquid resulting from explosive bubble growth during nucleation (Susumu, 1969).

DiMarco and Grassi performed additional studies of boiling on thin wires in low-g where no remarkable effect of gravity on heat transfer was found. Although the boiling heat transfer coefficient was largely unaffected by gravity, bubble dynamics were strongly affected. The bubbles in low-g grew much larger than in earth gravity and occasionally departed the wire, Fig. 1.10. The departure mechanisms in low-g were thought to be bubble coalescence and induced liquid motion from rapidly growing bubbles. Such results indicate the inability of the Bond number to scale both effects of heater size and gravity level on boiling heat transfer (DiMarco and Grassi, 1999).

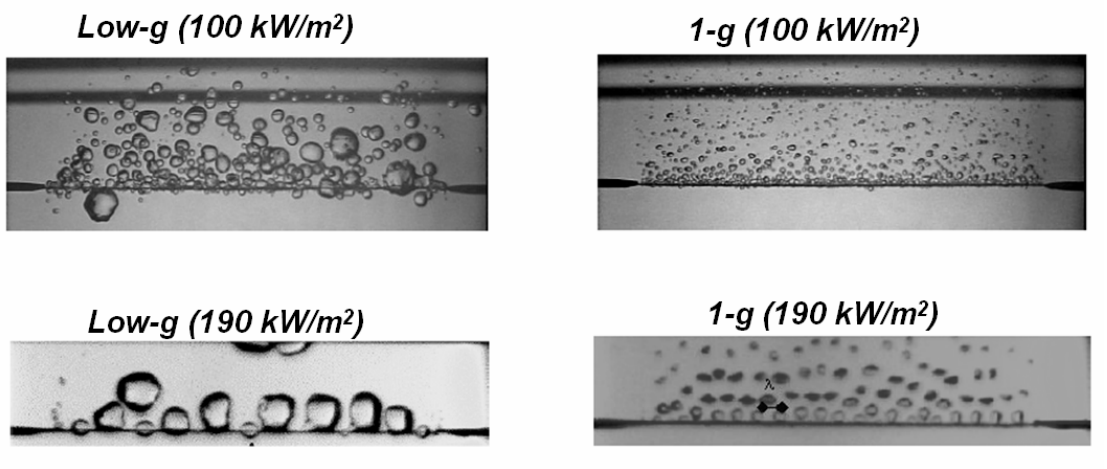

Figure 1.10: Pool boiling from wires (Courtesy of DiMarco and Grassi, 1999).

Additional studies performed by Steinbichler et al. on boiling from a small hemispherical heater and wire under microgravity conditions demonstrate that the overall heat transfer coefficient under microgravity conditions is very similar to normal gravity. They measured a slight enhancement in the heat transfer at saturated and slightly subcooled conditions. This was attributed to bubble departure caused by bubble coalescence and induced liquid motion around the vapor bubble (Steinbichler et al. 1998). All of these results indicate that the nucleate boiling correlations mentioned previously (Eq. 1.2-1.8) do not accurately account for the gravitational dependence on boiling in low-g.

For flat horizontal heaters, the observations indicate the formation of a primary bubble that causes significant dryout over the heater surface. At low heat flux, some researchers have measured a higher heat transfer compared to similar 1-g conditions (Merte et al., 1998), Fig. 1.11. Under such conditions, bubble departure can be non-existent and bubble dynamics associated with the classical ebullition cycle no longer occur.

Under highly subcooled conditions in low-g, it has been shown that for heater sizes where the primary bubble does not cause total dryout, bubble coalescence on the peripheral regions of the heater array causes similar heat transfer performance to classical

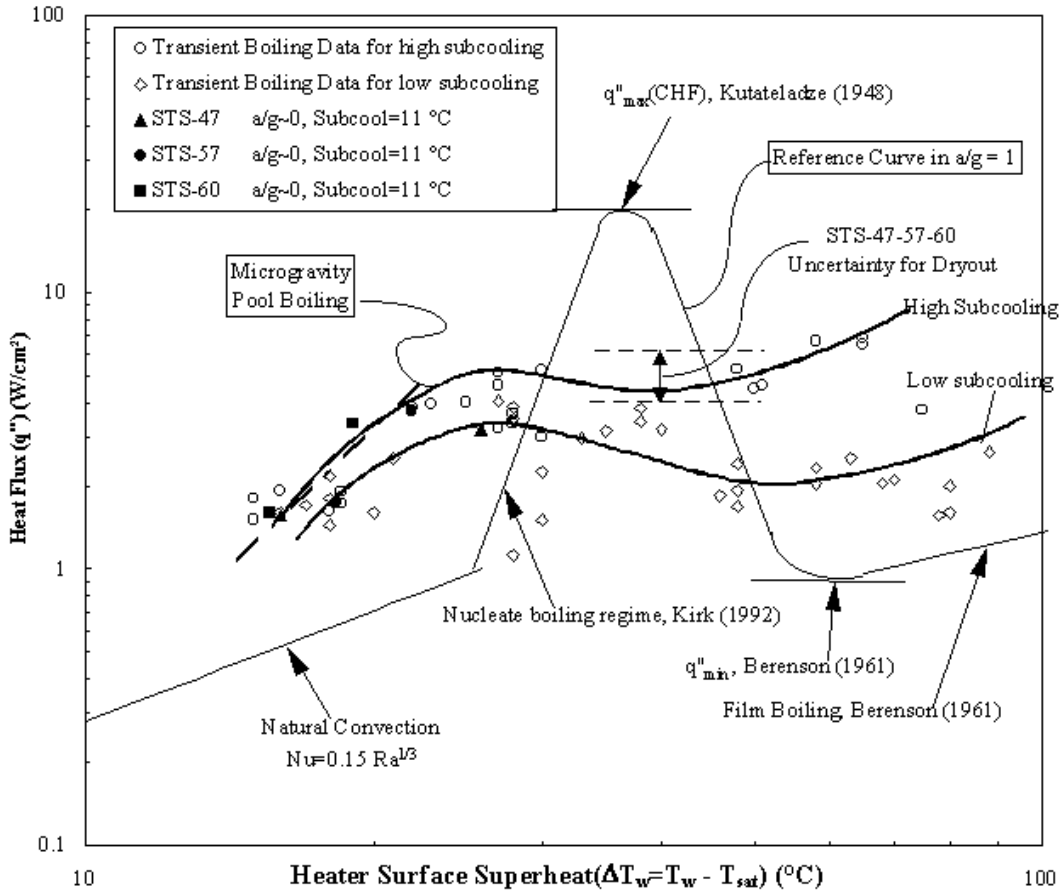

Figure 1.11: Comparison between low-g boiling and 1-g boiling predictions (Courtesy of Herman Merte).

1-g nucleate boiling (Kim et al. 2002).

Parametric studies dealing with the effects of fluid type on boiling in low-g have been performed by a few researchers. Preliminary research has identified a significant impact on heat transfer in low-g for various fluids. Oka et al. found CHF in low-g from a flat horizontal heater in n-pentane and CFC-113 are lowered by 40 percent when compared to earth gravity. At smaller heat flux, only a slight change was measured, which agrees with previously mentioned measurements. Studies using water as the working fluid showed a significantly higher deterioration (> 50%) in CHF at low-g. The differences in performance can be attributed to the thermophysical properties of the fluids

and in wetting characteristics on the heater surface. For organic fluids, a smaller contact angle was measured and hemispherical bubbles shapes were observed while for water the contact angle is much larger causing the bubbles to be nearly spherical on the surface in low-g causing dryout to occur more rapidly (Oka et al., 1995).

Studies on boiling in low-g indicate a strong gravitational dependence on CHF. For example, Kim et al. (2002) observed bubble coalescence to be the primary mechanism for CHF, which differs from the hydrodynamic instability model proposed by Zuber, Fig. 1.12. CHF in low-g was measured to be significantly smaller and occurred at

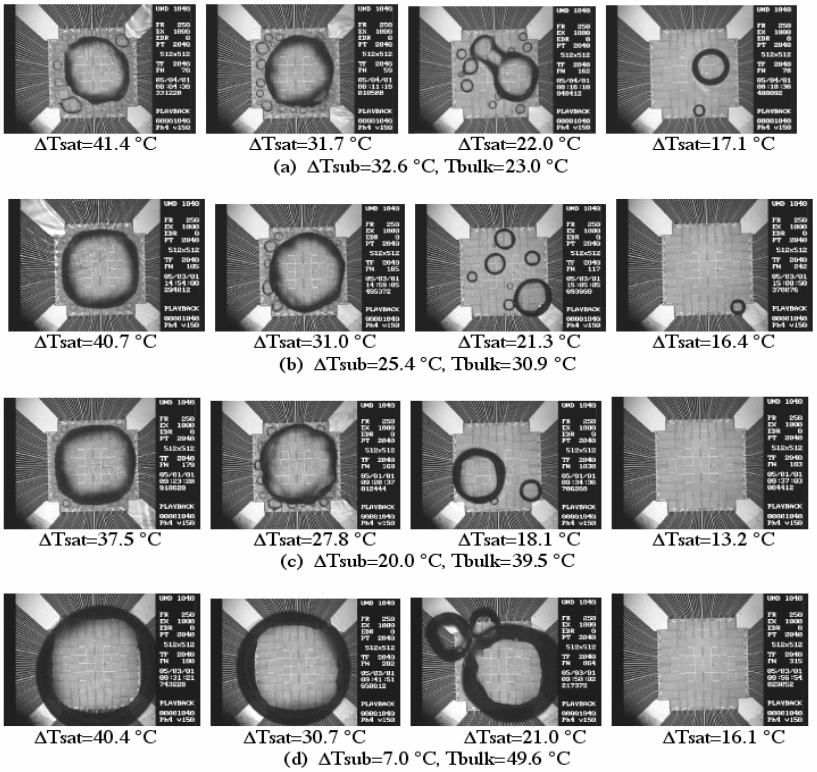

Figure 1.12: Pictures of the Boiling Process in Low Gravity at Various Superheats and Subcoolings (Courtesy of J. Kim).

lower wall superheats compared to higher gravity boiling. They measured a gravitational dependence on CHF shown in Fig. 1.13. This gravitational trend further emphasizes deficiencies in Kutateladze's CHF model (Eq. 1.10).

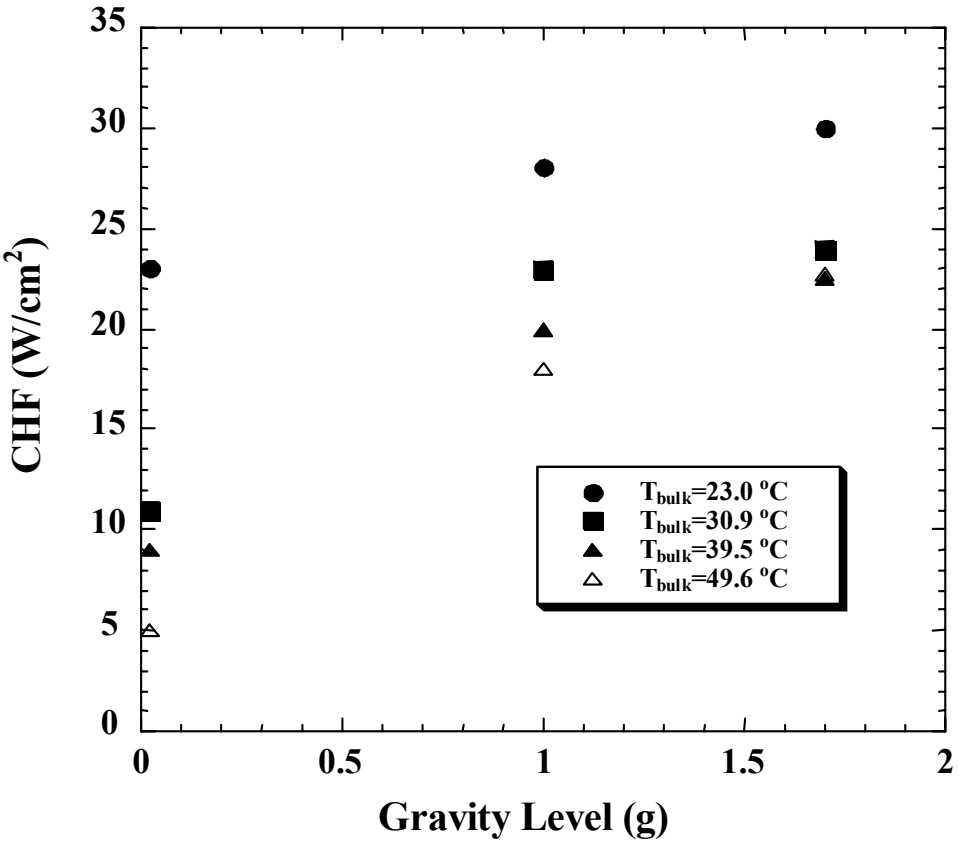

Figure 1.13: Gravitational dependence on CHF (Courtesy of J. Kim).

In contrast to horizontal heater studies in low-g, Shatto and Peterson studied the mechanisms for CHF from cylindrical heater cartridges and found that the previously mentioned Taylor-Helmholtz instability governs the critical heat flux mechanism in low-g for this geometry (Shatto and Peterson, 1999). Clearly, additional research is needed in order to clarify the mechanisms responsible for CHF in low-g on different heater geometries in addition to identifying the gravitational dependence on this critical value. Earth gravity CHF mechanisms, such as Taylor and Helmholtz instabilities do not accurately predict performance in low-g as measured by most researchers.

1.3.1 Thermocapillary Convection

The absence of gravity increases the contribution of other mechanisms normally masked by natural convection and buoyancy, such as Marangoni or thermocapillary convection. Thermocapillary flow results from surface tension gradients along a two-phase interface which can form due to temperature gradients, material composition, and electrical potentials (Ostrach, 1982), Eq. 1.14. In equation 1.14, t is the tangential coordinate direction along the bubble interface.

$$\frac{d\sigma}{dt} = \frac{\partial\sigma}{\partial T}\frac{\partial T}{\partial t} + \frac{\partial\sigma}{\partial c}\frac{\partial c}{\partial t} + \frac{\partial\sigma}{\partial \varphi}\frac{\partial \varphi}{\partial t} \tag{1.14}$$

Thermocapillary effects were first observed by Trefethen and McGrew where it was shown that flow around vapor and air bubbles can be very similar. They predicted that thermocapillary flow is the primary mechanism for boiling in low-g supplanting ebullition cycle heat transfer mechanisms, although it should be noted that they were unable to validate this claim (Trefethen, 1961; McGrew, 1966).

Raake and Siekmann studied temperature and velocity fields near an air bubble in silicon oil in the presence of a uniform temperature gradient and observed strong surface tension driven flows. They measured convective velocities near the surface of a bubble on the order of 10^{-3} m/s which provided an additional force preventing departure in low-g. This additional force increased the departure size and decreased the bubble departure frequency (Raake and Siekmann, 1989). Numerical studies performed by Kao and Kenning (1972) on gas bubbles showed that the magnitude of thermocapillary liquid flow is determined primarily by the Marangoni number (Ma, Eq. 1.15), the Prandtl number (Pr), and the Biot number (Bi). They also found that the flow is very sensitive to surface active contaminants, a small amount of which can entirely suppress the thermocapillary

motion. In addition, most of the driving surface tension gradient develops close to the liquid-vapor-solid interface and this driving gradient moves closer to the heater surface for higher Marangoni numbers (Kao and Kenning, 1972).

$$Ma = \left|\frac{\partial \sigma}{\partial T}\right| \cdot \left|\frac{\partial T}{\partial t}\right| \frac{L^2}{a_1 \eta_1} \tag{1.15}$$

Wang et al, used high-speed photography and laser PIV techniques to investigate liquid jets emanating from boiling on ultrathin wires during subcooled boiling in 1-g. Bubbles diameters were typically 0.03 mm and affected liquid velocities above the bubble ranging from 15mm/s to 140 mm/s. Their results indicate that near the bubble, superheated liquid near the nucleation site is drawn toward the bubble and then expelled along its cap, Fig. 1.14. These experimental results agreed very well with 3-D numerical simulations which predicted velocities between 20-40 mm/s above the bubble.

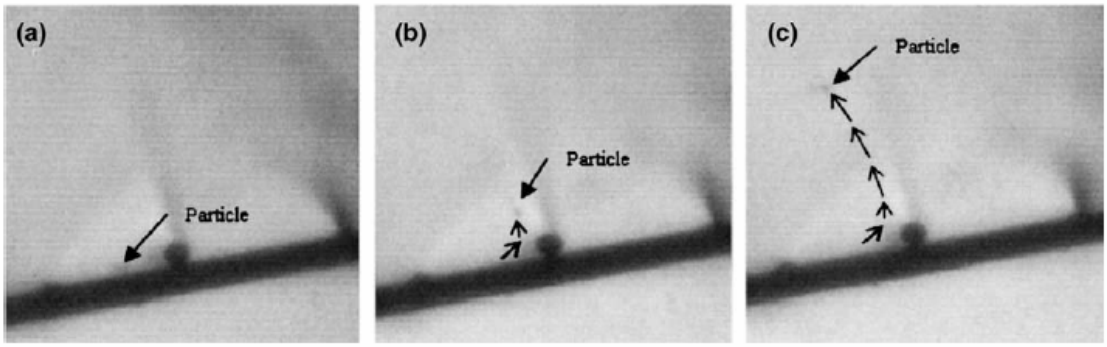

Figure 1.14: Suspended particle tracing during Marangoni convection, heat flux 6.0×10^5 W/m^2, 379 K, bulk temp 325K (Courtesy of Wang et al, 2005).

Most of the above mentioned studies (except Wang et al.) were performed in a binary system with either gas bubbles injected into the chamber or large amounts of dissolved gases already present. For a gas bubble on a vapor surface, it is clear that temperature gradients can exist along the liquid-gas interface due to the lack of latent heat transport across the interface. For pure fluids however, much debate has centered on the

ability of the bubble's liquid-vapor interface to maintain a temperature gradient during phase transition. Recent studies in low-gravity show the formation of strong thermocapillary convection under highly subcooled conditions around a vapor bubble in systems with very low to minimal gas concentrations (nominally pure systems). As first suggested by Straub, thermocapillary flows can form in such systems in the following manner. In subcooled boiling, the top of a growing bubble may extend out of the superheated boundary layer and start to condense. With evaporation occurring near the three-phase contact line, impurities such as dissolved gas in the liquid are liberated and carried along with vapor to the top of the bubble. The vapor subsequently condenses while the noncondensable gases accumulate along the interface. Under steady-state conditions, the presence of the noncondensables reduces the vapor pressure locally along the interface and therefore the saturation temperature is decreased locally. A negative temperature gradient along the bubble interface forms which induces a thermocapillary motion directed from the base of the bubble to its top. A diagram of some of the key transport mechanisms of this theory is presented in Fig. 1.15. A force balance along the interface yields the boundary equations (Eq. 1.16-1.17). Under near saturated boiling conditions, this theory predicts an absence of thermocapillary motion due to a nominally constant temperature interface (Straub, 2000).

Marek and Straub found the bubble growth time to have a major effect on the accumulation of noncondensable gases. Under saturated conditions, the bubble grows so fast (microseconds) that no accumulation of gas inside the bubble can occur. In contrast, under subcooled conditions where the growth time can be on the order of milliseconds, significant gas accumulation occurs. In addition, Straub measured strong thermocapillary

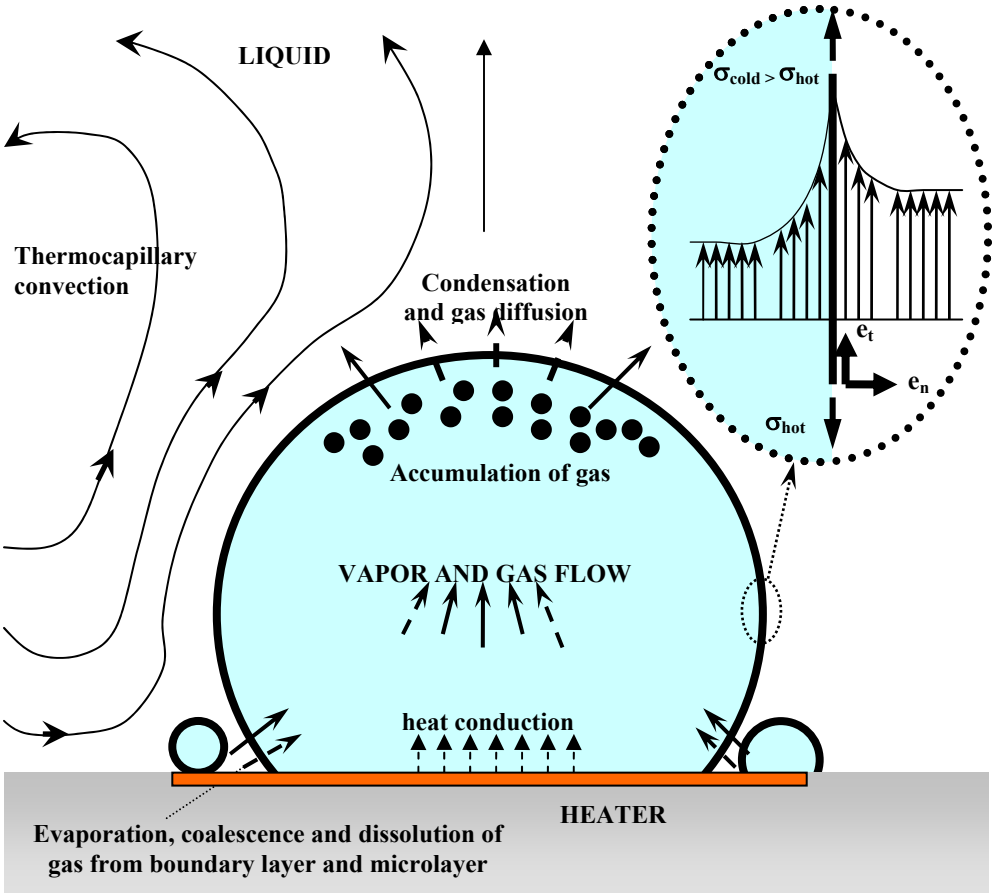

Figure 1.15: Thermocapillary flow transport mechanisms.

$$\mu_B\left(\frac{\partial(v_t)_B}{\partial n}+\frac{\partial(v_n)_B}{\partial n}\right)-\mu_A\left(\frac{\partial(v_t)_A}{\partial n}+\frac{\partial(v_n)_A}{\partial n}\right)=\frac{d\sigma}{dt}=\mu_B\frac{\partial(v_t)_B}{\partial n}-\mu_A\frac{\partial(v_t)_A}{\partial n} \tag{1.16}$$

$$P_B-P_A+\sigma\left(\frac{1}{R_B}+\frac{1}{R_A}\right)=2\left(\mu_B\frac{\partial(v_n)_B}{\partial n}-\mu_A\frac{\partial(v_n)_A}{\partial n}\right)=0 \tag{1.17}$$

flow in systems with extremely low gas concentrations (Marek and Straub, 2001).

The strength of thermocapillary convection has been observed to alter the wall heat transfer by changing the size of the bubble and allowing additional liquid to wet the surface in low-gravity. Part of this thesis documents the important role this phenomenon plays in limiting the extent to which the heater temperature can rise in the post-CHF

regime. The complex nature of thermocapillary flows involving vapor/gas flow through the bubble, a dynamic phase boundary, accumulation of non-condensable gases, the dissolution of the gas in the liquid, and diffusion of gas through the liquid vapor interface poses a tremendous challenge.

1.3.2 Summary

Although no analytical models have been developed that accurately predict boiling behavior in microgravity, many of the research efforts to date share common observations including:

1) The formation of a primary bubble in low-g and coalescence with smaller bubbles seems to dominate the boiling heat transfer process. At low heat flux, boiling performance can exceed comparable 1-g boiling.
2) Different heater geometries appear to affect bubble departure in low-g.
3) The influence of thermocapillary motion increases significantly in low-g in the absence of natural convection. Further research is necessary in order to quantify this effect. Current theories such as those developed by Marek and Straub need to be investigated further.
4) Low-g environments appear to cause boiling incipience to occur at lower wall superheats, which is attributed to a thicker superheated liquid region in the absence of natural convection.
5) The use of the Bond number as a single scaling parameter is in serious doubt and additional non-dimensional numbers are needed to predict boiling behavior across different gravity levels.

Although CHF has been researched extensively in earth gravity, strong disagreements still exist over conditions just before CHF, the trigger mechanisms responsible for initiating CHF, and the combined influence of system parameters on CHF. In low-g a fundamental identification and understanding of the relevant mechanisms is desired. The ability to both greatly increase and predict the magnitude of CHF is of importance to high heat transfer applications in space. A summary of the relevant low-gravity work to date is presented in Table 1.3.

Summary of Low-Gravity Boiling Research					
REFERENCE	**DATE**	**ENV**	**FLUID**	**HEATER**	**SUMMARY**
R. Siegel and Keshock	1961-1967	DT	water	flat smooth nickel surface 22 mm dia. nichrome ribbon 3.2 x 22.2 mm	large bubbles with coalescence
Straub et al.	1986 - 2001	OF DT PF	R12 R11 R123 R113	Wire, 0.2 / 0.5 mm Pipe, 8mm o.d. Flat plate 40 x 20 mm (gold coated) Hemispherical heater 0.26 mm diameter Circular heaters, 1 / 1.5 / 3 mm dia.	enhancement at low heat flux, unaffected by subcooling
Merte et al	1992 - 2002	DT	liquid nitrogen	Flat heater, SiO_2, 19 x 38 mm^2 22 mm dia. copper sphere	Thermocapillary convection impells large bubble toward heater, 30% enhancement at lower heat flux
Di Marco and Grassi	1999 - 2002	PF SR	R113 FC72	Wire, 0.2 mm diameter	no, appreciable effect on heat transfer coefficientCHF reduced by 50%
Abe and Oka	1992-1999	PF DT	n-pentane CFC12-CFC112 water CFC113 CFC11	glass heater, flat ITO coating 30 x 30 mm^2 artificial cavities	reduced CHF, observed microlayer, marangoni effect observed
Ohta et al.	1996-2002	PF SR	water ethanol	transparent surface, flat ITO, 50 mm dia. Dh = 50 mm	enhancement at low heat flux, unaffected by subcooling
Dhir et al	1999-2002	PF	water	Flat heater, strain gage heater, 45 mm dia.	bubble departure observed from micromachined nucleation sites
Kim et al	2000 - 2004	SR PF	FC72	Microheater array 2.7 x 2.7 mm^2	increasing subcooling increase CHF, satellite bubble heat transfer independent of subcooling and gravity level
LEGEND: DT - Drop Tower, OF - Orbital Flight, PF - Parabolic Flight, SR - Sounding Rocket					

Table 1.3: Summary of Low-g Experimental Work

1.4 PROBLEM STATEMENT / RESEARCH OBJECTIVE

Considerable resources have been expended in recent years toward the study of phase change phenomena in low-g environments. Particular attention has been given to the pool boiling process which is relatively well characterized under terrestrial conditions. Despite such efforts, relatively little is known about the mechanisms responsible for energy, momentum, and mass transfer during the boiling process in low-g environments, placing considerable constraints on the nature and type of designs that can be incorporated into space based hardware. If the boiling process can be quantified and modeled accurately, significant advances in the design and manufacture of space based hardware can be made.

This thesis summarizes a mechanistic approach developed to identify measure, characterize, and model the fundamental heat and mass transfer mechanisms associated with the boiling process in space. Experimental, analytical and numerical techniques are employed to provide further insight into the phenomenon.

This study aims to further the state of the art in low-g pool boiling by providing accurate and reliable information for future scientists and engineers. In addition to being a validation of previous work, the research objectives of this study include:

1. Obtain spatially resolved heat flux information
    a. Develop optimized sensor for local temperature and heat flux measurement
    b. Obtain boiling data from small scale heaters (< capillary length scale)
2. Characterize boiling in the absence of ebullition cycle behavior
    a. Determine applicability of 1-g models

        i. Recommend revisions to current models

3. Identify scaling parameters
4. Identify boiling enhancement parameters
5. Validate / identify the mechanisms responsible for boiling
    a. Model analytically and numerically
6. Develop / recommend new mechanistic approaches where applicable

Chapter 2: Experimental Method

2.1 INTRODUCTION

The experimental methodology was focused on measuring and characterizing the primary mechanisms important to the pool boiling process in low-g. The mechanisms identified through literature surveys and experimentation mentioned in the previous chapter includes: bubble coalescence, thermocapillary convection, and interfacial molecular kinetics. System parameters, such as bulk subcooling, wall heat flux and wall superheat, appear to affect these mechanisms in a systematic manner. The experimental research objective aims to identify, quantify, characterize, and model the relationships between system operating factors and boiling mechanisms as summarized in Fig 2.1.

A brief study of the primary physical mechanisms identified above reveals a great deal about where to begin an experimental investigation. The initial research effort was aimed at identifying, measuring, and characterizing important factors that are thought to influence the primary mechanisms and the phenomenon as a whole. Such factors include; heat flux, wall superheat, bulk subcooling, pressure, and others. Experimental factors were identified that would most dramatically influence coalescence and thermocapillary convection in low-g. After identifying the global system factor space, a parametric experimental investigation was performed for a selected subset of the factor space. In some cases, the results provided the impetus for modification of the experimental test apparatus allowing additional factors to be measured. The results were also used to characterize the physical mechanisms and the relationship between factors

and mechanisms, and develop quantitative models to be presented in the following chapters.

This chapter provides a summary of the design of the experiments. It is organized to provide a discussion of the experimental design logic, a description of the various systems factors identified and parametrically investigated, and also to provide a rationale for design and fabrication of the experimental apparatus used. The quantity and quality of the experimental data to be presented in the next chapter is largely dependent on the quality of the experimental design methodology presented below.

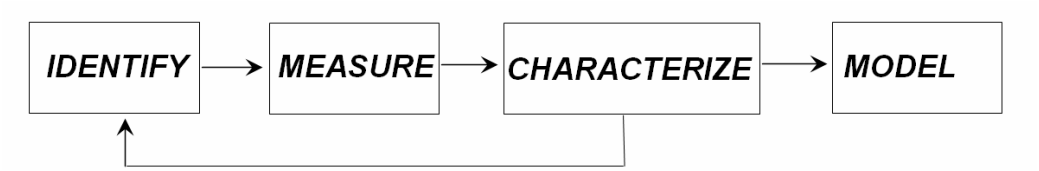

Figure 2.1: Block diagram of research process.

2.2 EXPERIMENTAL METHODOLOGY

The experimental methodology followed a fractional factorial approach which provides a number of advantages over a total factorial plan. The primary advantage of this method rests in the ability to selectively study interaction effects between factors as opposed to a complete factorial plan which looks at interaction effects over the entire factor space. A complete factorial design usually involves extensive experimentation which correlates to long periods of time and large data sets that can be difficult to obtain if significant constraints associated with cost and availability exist.

The experimental approach first aimed to identify and quantify two types of factors; control factors and noise factors (non-controllable factors). Control factors are variables that can be controlled in both the experiment and the physical process. Control

factors include; wall superheat, bulk subcooling, g-level, fluid type, heater size, and heater aspect ratio. The wall superheat is a critical parameter to study in any pool boiling experiment due to its influence on heterogeneous bubble nucleation, vapor formation, thermal boundary layer thickness, and liquid –vapor hydrodynamics as summarized in the previous chapter. Bulk liquid subcooling plays a very strong role in the boiling dynamics primarily through its influence on the thermal boundary layer and vapor liquid hydrodynamics. The capillary length scale has been proposed as a governing length scale for nucleate pool boiling performance and therefore an effort was made to study various heater sizes and heater aspect ratios that were on the order of and significantly smaller than this length. The primary objective of this effort, quantifying the pool boiling phenomenon in low-gravity environments, necessarily identifies g-level as a parametric variable. A complete list of the control factors studied in this experiment is shown in Table 2.1.

Experimental factors investigated
Factor
Wall Temperature / Wall Superheat
Bulk Temperature / Bulk Subcooling
Gravity Level
Heater Size
Heater Aspect Ratio
Fluid Type

Table 2.1: Experimental factors

The design factors were chosen based on their suggested effects on the pool boiling process as identified from the literature review. Factor operating ranges were determined from an iterative design process that looked at experimental design capability, NASA safety requirements, previous experimental ranges mentioned in the literature review, and preliminary experimental results mentioned in the next chapter. For

example, the heater array control circuitry used in this study was designed for a maximum operating temperature which was later found to be too low to provide information about important trends in the low-g boiling curve. As a result, redesign of the control circuits for the heater array focused on increasing the temperature range to a desirable limit that provided the maximum amount of information possible while ensuring safe and reliable operation of the heater. Similar design scenarios were often encountered throughout the duration of this effort.

Noise factors are predominately control factor uncertainties. Noise factors naturally arise in any experiment. The primary noise factor in this experiment is the g-level uncertainty referred to as g-jitter. Other noise factors include nucleation site location and bubble motion. An effort is made throughout this thesis to quantify and explain the effect of noise factors on both the control factors and the phenomena being investigated.

2.3 PARAMETRICALLY INVESTIGATED FACTORS

2.3.1 Gravitational Environment

Gravitational effects on the pool boiling process are the primary motivation for this study. Over the years, microgravity environments have been difficult to create due to the technological, environmental, and economic challenges encountered. Such an environment presents unique design, safety, and economic requirements that are not trivial. Traditionally, drop towers, parabolic flight, sounding rocket flight, orbital flight, and space station operation have been thought of as "microgravity" platforms although in almost all cases, 10^{-6} g levels are not attained. Throughout this thesis the term

"microgravity" and "low gravity" will be used interchangeably referring to a gravitational environment (10^{-2} g) produced in parabolic flight.

As mentioned above, different means of achieving microgravity conditions exist and the various platforms provide different levels of quality and duration of microgravity periods. Drop towers provide microgravity conditions without having to travel into space. A drop tower is typically a vertical shaft which provides microgravity conditions during the free fall of the experimental package for a duration that depends on the length of the tower. Two drop towers currently exist in the US and are operated by NASA in Cleveland, Ohio. The major disadvantages of drop towers are the short duration of microgravity conditions and in some cases the cost. Parabolic flight can circumvent one of these disadvantages by providing microgravity conditions for up to 25 sec at comparable costs. The major advantages of parabolic flight include the frequency of experimentation, and the ability to modify the experimental package preflight, in-flight, and post flight. The primary disadvantage is that the quality of microgravity achieved is low, 10^{-2} g, and the duration is limited compared to other techniques such as orbital flight.

Sounding rockets have the ability to reach 400 km during parabolic flight and can achieve good microgravity levels ($10^{-5} – 10^{-6}$ g) for 5 to 6 minutes. Disadvantages include the need for recovery and high cost. Recoverable satellites provide an on-orbit laboratory for conducting research in microgravity typically 500 km above earth in low earth orbit. The space shuttle is a typical recoverable spacecraft that orbits the earth at 300 km and can provide microgravity conditions for up to two weeks. Last, the international space station provides a nearly indefinite microgravity condition to

researchers. This facility offers microgravity levels of 10^{-6} g for months or years and can include isolation techniques for reducing the g-level even further (Thomas et al, 2000). Unfortunately, the latter microgravity platforms mentioned above are very expensive. A summary of the various microgravity platforms and their respective quality and duration can be seen in Table 2.2.

Microgravity Platform	Duration	Gravity level
Drop tower/shafts	*2-9 sec*	*10^{-2}—10^{-5}g*
Parabolic flights (aircraft)	*25 sec*	*10^{-2}—10^{-3}g*
Balloon-drop	*60 sec*	*10^{-2}—10^{-3}g*
Sounding rocket	*6 min*	*10^{-3}—10^{-4}g*
Space shuttle	*> 9-11 days*	*10^{-3}—10^{-5}g*
Space station/recoverable satellite	*> months*	*10^{-5}—10^{-6}g*

Table 2.2: Microgravity platform characteristics (Thomas et al, 2000).

Selection of the appropriate microgravity platform for this particular study was motivated by cost, microgravity duration, ability to continually modify the test apparatus, and logistics. The NASA operated KC-135 provided a relatively low cost and long duration microgravity environment and allowed continual test modification during flight operations. All experimental data to be presented were taken aboard the NASA operated KC-135 in parabolic flight. Data presented in this paper was taken over a 6 week period totaling 24 flights. During portions of the parabolic flight, low-g (0.01g) and high-g (1.7g) levels are produced. A typical flight consisted of 40 parabolic maneuvers. Each parabolic maneuver consisted of a high-g pull-up (1.7g), a low-g period of about 25 s, followed by a high-g pullout (1.6g-1.7g), Fig. 2.2. Data acquisition for a particular wall temperature was initiated during the transition from high-g to low-g, Fig 2.3. Data were obtained for 90 s throughout the entire low-g period and into the high-g pullout and pull-up.

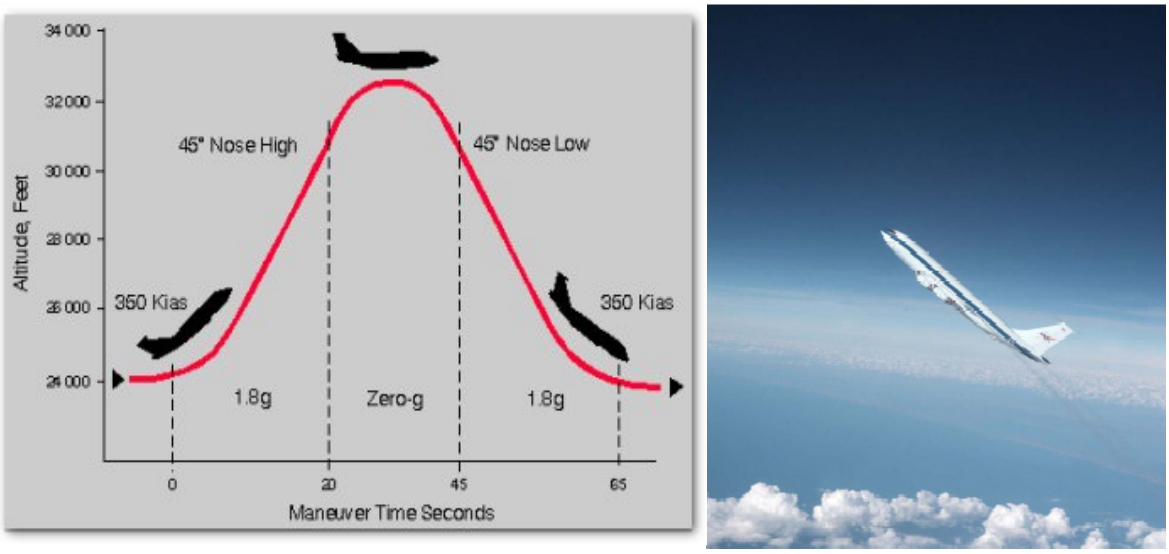

Figure 2.2: KC-135 flight profile (left); KC-135 in flight (right) (Courtesy of NASA).

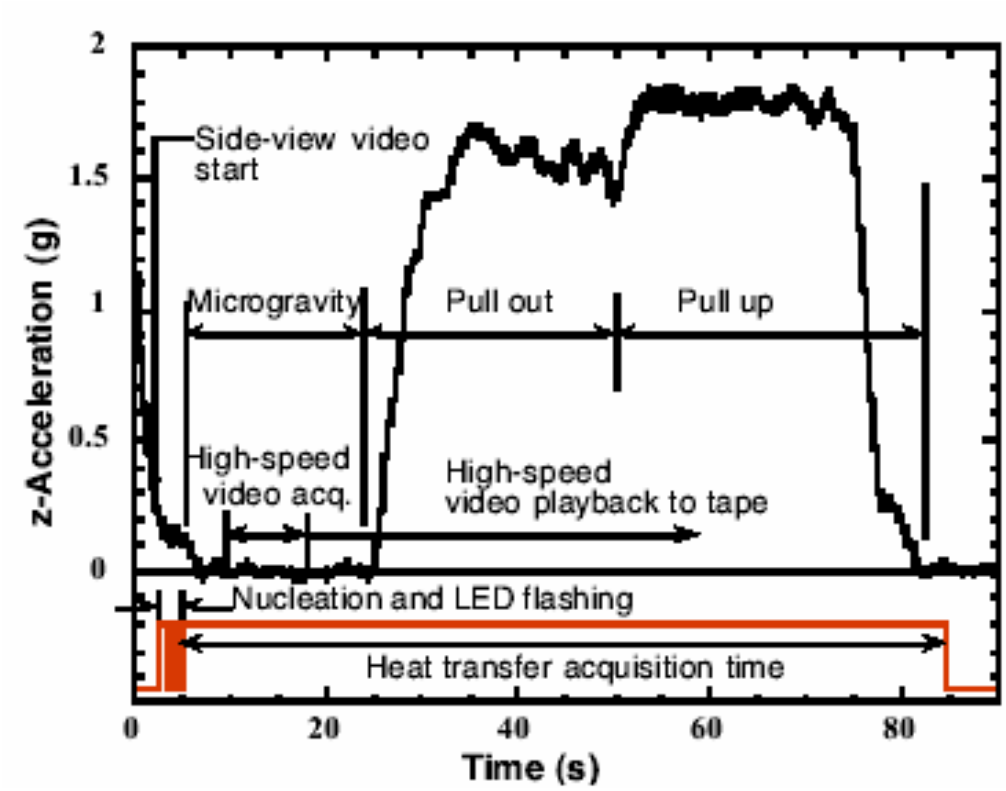

Figure 2.3: Gravitational profile for a typical parabola (Courtesy of J. Kim).

Experimentation aboard the KC-135 requires comprehensive design, analysis and testing of each experimental subsystem and the overall system. Some of the design

considerations encountered include: physical constraints such as size, weight, structural considerations, power requirements, physiological issues, in-flight spatial constraints, setup, and logistical design & management. A comprehensive description of the experimental design challenges and an in-depth analysis of the experimental system is included in Appendix A (TEDP). Logistical challenges included: apparatus testing and preparation, transport to and from NASA facilities, loading onto the KC-135, and pre-flight testing and qualification. Experimentation during parabolic flight is not a trivial endeavor, requiring diligence and attention to detail surpassing the norm, Fig. 2.4. Physiological challenges encountered during flight included disorientation, nausea, lightheadedness, fatigue.

Figure 2.4: Pictures of the Test Environment

The g-level was a parametrically investigated parameter having a maximum and minimum value of 0.01g and 1.7g respectively. The majority of experimental data obtained during flight was taken at these gravity levels. A few data points were obtained at lunar, 0.17g, and earth gravity, 1g. A summary of the g-level range studied and the percentage of experiments conducted at each level is shown in table 2.3.

Parameter: Gravity-Level		
g-level	**% exp**	**Uncertainty**
0.01g	47	10^{-2}g
0.3g	1	10^{-2}g
1g	5	10^{-2}g
1.7g	47	10^{-2}g

Table 2.3: Gravity level parameter range

2.3.2 Fluid

Pool boiling is strongly dependent on the type of fluid undergoing phase transition. Organic and inorganic fluids differ in both heat transfer performance and hydrodynamic manifestations at similar operating conditions. The primary considerations in selecting a suitable working fluid for this experiment were the thermophysical properties and electrical properties of the fluid.

As mentioned in the introduction, direct immersion electronic cooling applications require the use of an electrically inert working fluid. The heater array used to initiate and sustain boiling activity in this experiment also required an electrically inert fluid. The maximum heater array temperature studied was 100° C and in order to study an adequately large wall superheat range, the fluid boiling point need to be between 40° C and 70° C. Last, the fluid needed to be non-toxic and non-flammable and satisfy stringent safety requirements set forth by NASA for operation aboard the KC-135.

A class of fluids which satisfied all of these conditions was the 3M fluorinert electronic liquids. These fluids are part of a family of fully-fluorinated compounds known as perfluorocarbons. Such liquids have been used as heat transfer media for direct immersion cooling, automated testing, reflow soldering, etching, CVD, and more. In addition, these fluids were selected due to their good material compatibility, low toxicity, nonflammability, and documented working history.

The working fluid, FC-72 (C_6F_{14}), was chosen from this class of fluids primarily based on the boiling point of the fluid at room pressure. FC-72 is a clear, colorless, odorless, highly wetting, dielectric fluid manufactured by 3M. Its dielectric properties and relatively low boiling point (T_{sat} = 56 °C, at 0.1 MPa) make it a desirable fluid for thermal management solutions in the electronics industry. Of particular interest is the fluid's relatively high density, low viscosity, and low surface tension, Table 2.4.

FC-72 Properties, P = 1 atm, saturated fluid properties	
Boiling Point (K)	329.15
ρ_l (kg/m^3)	1614
ρ_v (kg/m^3)	14.8
μ (kg/ms)	6.40e-04
C_p (J/kgK)	1097
h_{fg} (J/kg)	83536
k_l (W/mK)	0.0522
σ (N/m)	0.008
β (1/K)	0.0094
MW (kg/kmole)	338
Dielectric constant	1.75
T_{crit} (K)	451.15
solubility of water (ppm)	10
solubility of air (ml/100ml)	48

Table 2.4: FC-72 saturated fluid properties.

Current theories on the origin of thermocapillary convection indicate that surface active contaminants may play a significant role in the interfacial kinetics at the two-phase interface. As a result, significant effort was made to accurately quantify the purity of the fluid. For FC-72, two impurities are typically present: dissolved gases and the fluid isomers.

2.3.2.1 Dissolved Gas Measurement. A thorough distillation process was followed to remove less volatile contaminates in the fluid. Unfortunately this process did very little to reduce the isomer concentration within in the fluid. After distillation, the fluid was degassed by periodically reducing the pressure inside the boiling chamber down to the vapor pressure of FC-72 at room temperature. The air concentration in the liquid was reduced to less than 3 ppm by repeatedly pulling a vacuum on the vapor/air mixture above the liquid. For a given partial pressure of gas (P_g) above the liquid, the dissolved gas concentration C_g (moles gas/mole liquid) in the liquid phase is given by Henry's law $C_g=H(T)\ P_g$ where H(T) is Henry's constant. For air in FC-72, H has been measured to be $5.4x10^{-8}$ mole/mole-Pa between 31 °C<T<60 °C. P_g can be determined from a measurement of the total pressure (P_T) and temperature (T_{sat}) of the gas above the liquid after it has come to equilibrium in a sealed container from $P_g=P_T-P_{sat}(T_{sat})$ where P_{sat} is the saturation pressure of the liquid at the measured temperature T_{sat}.

Consider now the case where liquid and air are sealed in a container of volume V, and that the volume of liquid containing dissolved air is V_l and the volume of vapor/air is V_g. We wish to determine the number of times V_g must be removed to reduce C_g below a specified value. The initial partial pressure of air above the liquid is assumed to be $P_{a,i}$.

The initial concentration of gas in the liquid is then $C_{a,i}=H(T)P_{a,i}$. The mass of air in the liquid ($M_{a,l}$) can be shown to be:

$$M_{a,l} = H(T)P_{a,i}\rho_l V_l \frac{MW_a}{MW_l} \tag{2.1}$$

where MW_l and MW_a are the molecular weights of the liquid and air, respectively. If the vapor and air above the liquid are removed using a vacuum pump (we will assume the liquid volume does not change) and the chamber allowed to equilibrate, the air contained in the liquid must come out of solution to fill this volume. The total mass of air in the container is the sum of the air within and above the liquid:

$$H(T)P_{a,i}\rho_l V_l \frac{MW_a}{MW_l} = \frac{P_{a,i+1}}{R_a T} V_g + H(T)P_{a,i+1}\rho_l V_l \frac{MW_a}{MW_l} \tag{2.2}$$

where $P_{a,i+1}$ is the partial pressure of air above the liquid after the vacuum has been applied. Rearranging equation 2.2 yields

$$\frac{P_{a,i+1}}{P_{a,i}} = \frac{H(T)\rho_l V_l \dfrac{MW_a}{MW_l}}{\dfrac{V_g}{R_a T} + H(T)\rho_l V_l \dfrac{MW_a}{MW_l}} = \frac{1}{1+Z} \tag{2.3}$$

where

$$Z = \frac{1}{R_a T H(T)\rho_l} \frac{V_g}{V_l} \frac{MW_l}{MW_a} \tag{2.4}$$

Equations 2.3 and 2.4 give the reduction in partial pressure of air above liquid due to the removal of the air and vapor above the liquid.

As an example, assume we wish to reduce the air concentration to below 3 ppm for liquid and air at 25°C (this corresponds to a partial pressure of air of 55 Pa), and we have a container half filled with liquid ($V_g=V_l$). Using the properties of FC-72 we find

Z=1.57, so the partial pressure of air is reduced to 39% of its previous value every time a vacuum is applied. If the initial total pressure is 101 kPa, then the vapor pressure is 36.6 kPa, and the partial pressure of air above the liquid is 64.7 kPa, resulting in an initial air concentration in the liquid of 3500 ppm. If we wish to reduce this to below 3 ppm, we find that a vacuum must be applied a minimum of eight times, Fig. 2.5.

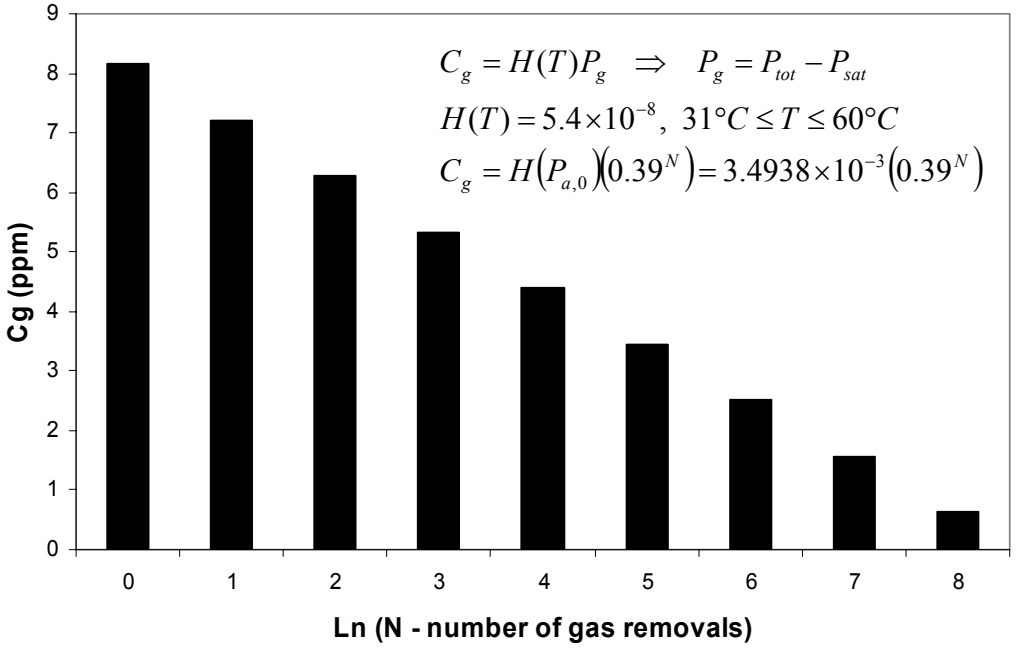

Figure 2.5: Theoretically predicted gas concentration during degassing procedure.

High performance vacuum pumps are not needed to thoroughly degas the fluid because the pressure in the chamber is never below the vapor pressure of the liquid. During the degassing procedure, the pressure was measured using a high-accuracy pressure transducer (PTG PX01C1-015A5T 15 PSIA, 0.01% FS). The accuracy of this transducer is about 10 Pa, well below the partial pressure of air at 3 ppm concentration. Accurate temperature measurements are also required. Near room temperature, the vapor pressure of FC-72 changes by 3280 Pa/°C, so a 3 ppm error (55 Pa error) can result from a temperature change of 0.016 °C. The temperature was measured with a high precision

RTD (Techne, Inc. model WSP350 PRT with TECAL Accutemp RTD indicator, ±0.001 °C). Both of the instruments were chosen such that the dissolved gas content could be determined to levels well below 3 ppm.

In practice, the chamber pressure and temperature were measured just before degassing, and the pressure measurements were corrected to obtain what the total pressure would be at a reference temperature of 25°C. A vacuum pump was then connected to the chamber and the pressure above the liquid was lowered long enough to boil the liquid for a few seconds, ensuring that all of the vapor/air was removed. The pressure was observed to quickly stabilize to levels below what would be expected at C_g=3 ppm after a few rounds, Fig. 2.6. Once the liquid was degassed, the pressure around the bellows was brought up to 101 kPa—since there was no pressure differential across the seals in the boiling chamber, gas infiltration back into the liquid was minimized.

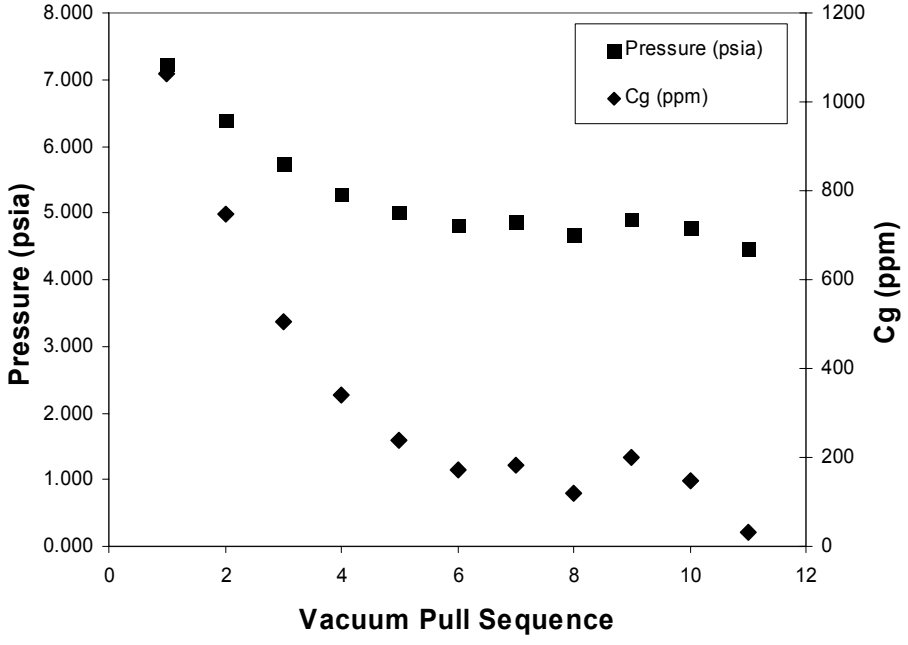

Figure 2.6: Chamber pressure and gas concentration during degassing procedure.

Gas concentrations smaller than $2x10^{-3}$ have been shown to have little to no influence on the boiling behavior in earth gravity (You, 1995). However even the presence of small amounts of dissolved gas mat cause the formation of Marangoni convection around vapor bubbles in subcooled, low-g environments (Straub, 2000). Strong Marangoni convection was observed in the present study under high subcoolings and therefore the effect of small gas concentrations is currently unknown.

2.3.2.2 Isomer Concentrations. The second fluid purity consideration analyzed was the effect of different isomer concentrations. FC-72 was analyzed using mass spectrometry and gas chromatography by researchers from Rutgers University (Hartman, 2004). The results of this analysis indicate that FC-72 is made up of various isomers of the chain C_6F_{14}. The 6 highest concentration isomers in the FC-72 sample do not have similar boiling points at 1 atm and theoretically could introduce a temperature gradient along a two-phase interface if accumulation along the interface occurs, Table 2.5. An effort was made to study as pure a fluid as possible due to this effect. A purer form of FC-72 (99% n-perflurohexane) was obtained, and the experimental results were compared to those obtained using FC-72 (73% pure).

Substance	M.W.	GC Area %	BP (^oC)	
n-perfluorohexane	338	73.2	56	C6F14
perfluoro-2-methylpentane	338	17.892	57.66	C6F14
perfluoro-3-methylpentane	338	5.954	58.37	C6F14
perfluoro-2,3-dimethylbutane + perfluoro-2,2-dimethylbutane	338	1.723		
perfluorocyclohexane	300	1.105	50.61	
perfluoromethylcyclopentane	300	0.126	48	C6F12

Table 2.5: Mass spectrometry results for FC-72 (Hartman, 2004).

A decision was made early in the experimental design process to study the effect of various factors at single pressure of 1 atm. This decision was based on NASA design constraints and the extensive pressure vessel certification process. Significantly higher pressures would require more robust seals for the boiling chamber as well as redundant containment vessels. It was concluded that in order to study the effect of pressure on boiling activity, much larger pressures than what is allowed aboard the KC-135 would have been desired. In addition, pressure effects on nucleate pool boiling are thought to be similar (at relatively low pressure, 1-10 atm) to bulk subcooling effects which are studied extensively in this work. In summary, the fluid purity level was parametrically investigated by varying the dissolved gas level and isomer content of the fluid, Table 2.6.

Parameter: Fluid	
Fluid Description	**Description**
FC-72 degassed w/isomers	3M commercially available FC-72, < 3 ppm gas concentration, isomer concentration (Table 2.5)
FC-72 w/gas & isomers	3M commercially available FC-72, < 3 ppm gas concentration, isomer concentration (Table 2.5)
n-perfluorohexane (pure)	3M, < 3 ppm gas concentration, 99% pure

Table 2.6: Parametrically investigated fluids.

2.3.3 Wall Temperature / Heat Flux Measurement

The wall superheat is perhaps the most critical parameter study in any pool boiling experiment. Accurate measurement of the wall superheat requires an accurate measure of both the temperature of the heater and pressure near the heater surface. As mentioned previously, all experiments were run at nominally 1 atm and therefore heater wall temperature was the dominant factor affecting the wall superheat. The heater temperature was controlled using a microheater array as opposed to constant heat flux techniques. This method allows the entire boiling curve to be quantified in a single incremental temperature run. The complex shape of the nucleate pool boiling curve also requires that the wall superheat be measured with sufficient resolution to provide information about higher frequency effects.

2.3.3.1 Microheater Array. Local heat flux measurement and temperature control were performed using an array of platinum resistance heater elements deposited on a quartz wafer in a serpentine pattern. Each of these heater elements in the array was 0.27 mm x 0.27 mm in size, had a nominal resistance of 1000 Ω, and a nominal temperature coefficient of resistance of 0.002 $°C^{-1}$. The *reference* heater array consisted of ninety-six individual heaters arranged in a square array approximately 2.7 mm on a side, Fig. 2.7.

The quartz heater array is mounted in a PGA socket using an epoxy adhesive and electrical connections were made using a gold wire bonding method. This package was then connected to a PCB board for interface with feedback electronics and data acquisition, Fig. 2.8. Contact resistance due to the bonding method had a negligible nominally 700 Ω. The quartz substrate has a thermal conductivity of 1.5 W/mK which limits the amount of substrate conduction. A silicon dioxide passivation layer deposited

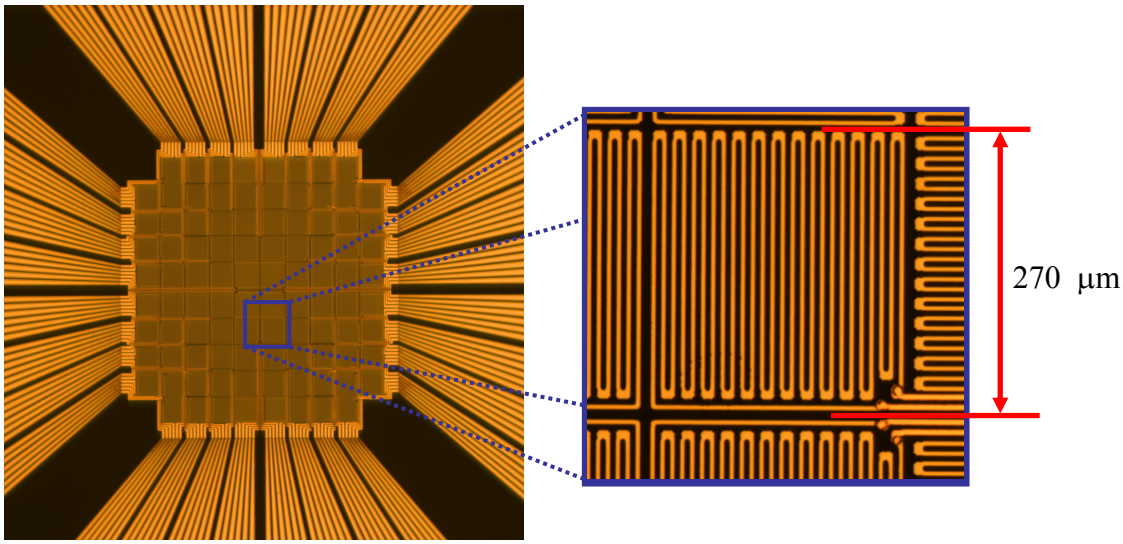

Figure 2.7: Representative platinum resistance heater array, each heater element = 0.27 mm x 0.27 mm (Courtesy of J. Kim).

above the etched platinum was used to provide a uniform surface free energy over the heater. The reader is referred to Rule and Kim (1999) and Rule (1997) for additional details. Fig. 2.9 is a cross-sectional diagram of an individual heater.

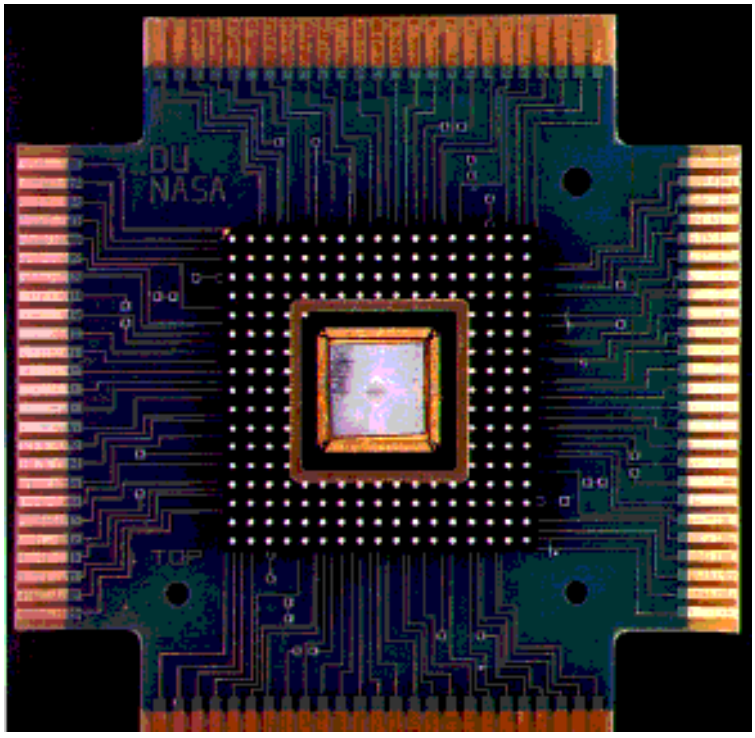

Figure 2.8: Heater array connected to PCB board (Courtesy of J. Kim).

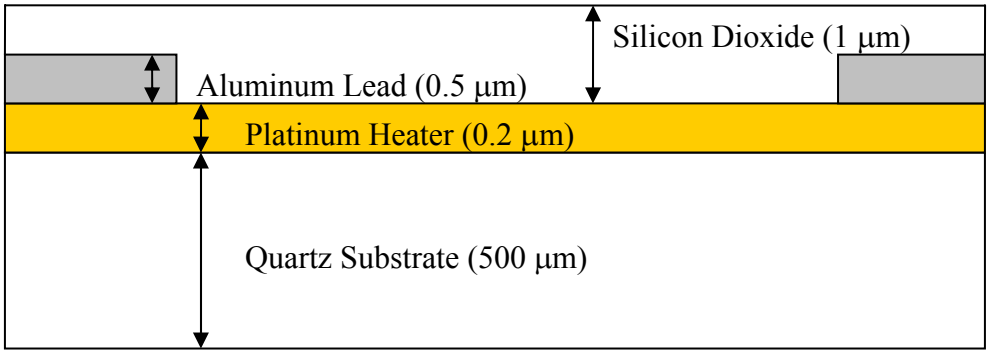

Figure 2.9: Cross-sectional view of heater array (drawing not to scale).

2.3.3.1 Feedback Control Circuit. The temperature of each heater in the array was kept constant by a bank of 96 feedback control circuits similar to those used in hot wire anemometry, Fig. 2.10. The control circuit operates in the following manner: The chopper op amp is used to sense an imbalance in the wheatstone bridge, represented by R_1, R_3, R_4, R_5, R_h, and R_{DP}. If an imbalance exists, the op-amp outputs a proportional voltage to the gate of the transistor allowing additional current to flow from the 24 volt source through the bridge. This current causes an increase in the temperature of the heater (joule heating) with a corresponding increase in resistance. The resistance of the heater will continue to rise until a new equilibrium state is reached corresponding to a balance in the wheatstone bridge. The wheatstone bridge balance can be adjusted by changing the digital potentiometer setting. This change causes current to flow through the heater array heating it up until the bridge is once again balanced. The circuit is designed so that very little power is dissipated across the right side of the bridge (R_3, R_4, R_5 are very large). R_1, R_2, R_3, R_4, and R_5 are high tolerance metal film resistors and change very little with temperature. This entire process occurs very quickly, in approximately 66μs, much faster than the dynamic behavior of the boiling process.

During data acquisition, the time-varying voltage across the heater resistance, V_o in Fig. 2.10, is measured and used along with the heater resistance at the given temperature to determine the total power dissipated by the heater to maintain it at constant temperature.

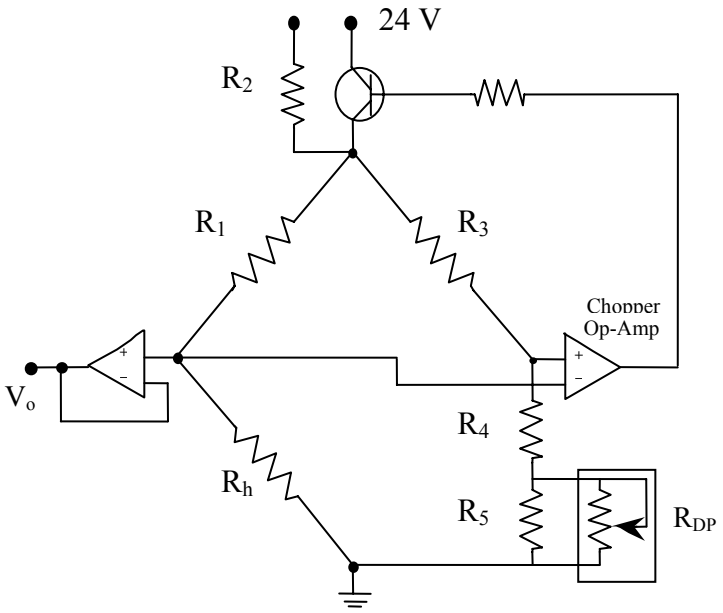

Figure 2.10: Feedback control circuit (Courtesy of J. Kim).

The feedback control circuits were individually optimized to extend the operational temperature range of each heater while simultaneously optimizing the heater temperature resolution. An optimization model was developed based on the physical response of the feedback circuit. The goals of the analysis included the desire to maintain the highest fidelity in measurement and to operate the heater array with the maximum number of operational heaters as possible. The microheater array operates most effectively when there is a minimum temperature difference between adjacent heaters allowing all heaters to turn on. A small temperature difference reduces lateral substrate conduction between heaters providing a better estimate of the heat transfer due to boiling. Lateral substrate conduction can also cause adjacent heaters to "turn off" during the

boiling process resulting in a non-uniform isothermal boundary condition and making it difficult to infer information about the boiling process.

As mentioned above, under certain conditions conduction between heaters becomes significant. Such conditions occur when there is very small heat transfer above and below the heater array. Consider first a single heater in the array that is surrounded by other heaters that are 0.4 K higher in temperature (this value hypothetically represents the temperature resolution of a given heater), Fig. 2.11. Under such conditions, heat will

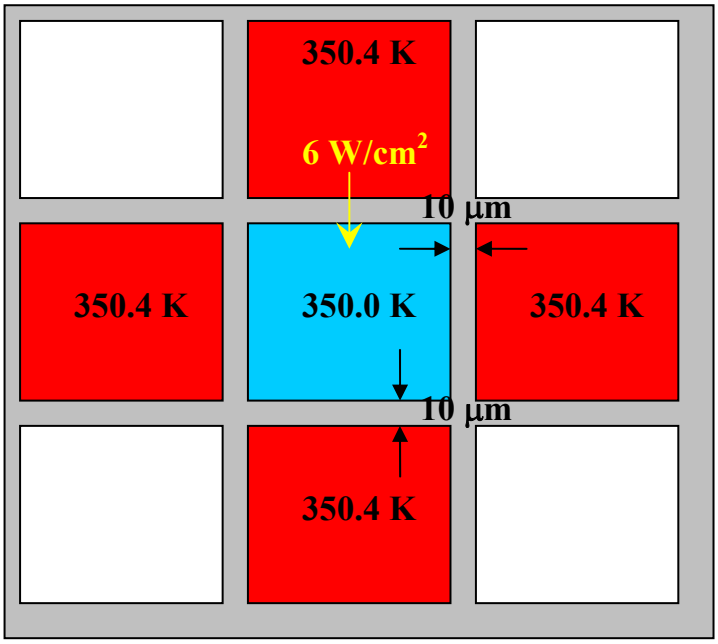

Figure 2.11: Model of lateral conduction between heaters.

be conducted from adjacent heaters toward the center at a rate of 6 W/cm^2. The total heat energy transferred in this case is approximately 300 μW. In order for this heater to operate correctly, there must be a net energy removal from the heater so that power can be supplied to the heater and measured. For this to occur, boundary conditions above and directly below the heater must be such that they remove heat at a rate greater than 300 μW. At the bottom of the heater, a large thermal resistance due to conduction through

the quartz substrate and convection to air exists creating a nearly adiabatic boundary under most operational conditions. The area for heat transfer to occur above the heater is 7.29×10^{-8} (for a 2.7 x 2.7 mm^2 array). Assuming a temperature difference between the heater and surrounding medium of 60 K, the heat transfer coefficient would have to exceed 70 W/m^2K in order to remove the 300 μW of energy being transferred from adjacent heaters. For such a circumstance, the heater will turn off if the overall heat transfer coefficient above the heater is less than 70 W/m^2K. Many natural convection processes at the small scale can affect heat transfer rates close to this value and therefore in order to ensure effective heater operation under such conditions it would be desireable to reduce the required *h* so that an additional range of boundary conditions can be investigated. The goal of the optimization analysis was to try and reduce the temperature difference between heaters by 50% which would result in a 50% reduction in the required heat transfer coefficient above the heater extending the range of conditions the array can be used to study.

The optimization analysis modeled the control circuit analytically using electrical circuit theory. A schematic of the feedback control circuit was shown in Fig. 2.10. The circuit is characterized by three main electronic components: resistors, an operational amplifier, and a transistor. Resistors, represented by R_1, R_3, R_4, R_5, R_h, and the digital potentiometer (R_{DP}), define a wheatstone bridge that characterizes the performance of the control circuit as mentioned previously. R_1, R_3, R_4, R_5, are metal film resistors with a manufacturer specified tolerance of 1% and are rated at 0.6 Watts. High tolerance metal film resistors are used in this application for their relative insensitivity to temperature, high power dissipation, and commercial availability. These resistors, in addition to R_{DP},

form the set of design variables which are optimized in the analysis. R_{DP} is a dual digital potentiometer consisting of two digitally controlled potentiometers manufactured by Dallas Semiconductor. It consists of 512 resistive sections providing a resistance range of 0 – 20 kΩ. R_h represents the resistance of a specific heater element. As mentioned previously, each heater element can be modeled as an equivalent temperature dependent resistance (R_h has a temperature coefficient of resistance 1000 times larger that the metal film resistors described above). The circuit regulating op-amp, labeled "Chopper Op-Amp" in Fig 2.10, is a high-voltage, high-performance operational amplifier. An additional op-amp is used to measure the voltage, V_o, across the heater element but does not directly influence the performance of the control circuit. The transistor shown in Fig. 2.10 is a high current, low voltage, NPN switching transistor that is used to provide power to the heater elements. It is important to note that the analysis presented subsequently applies to a single heater and its respective feedback control circuit. An analysis similar to that shown below can be performed for each heater in the array to obtain an optimized heater array.

A single objective optimization formulation (Eq. 2.5 – 2.11) was developed alongside a number of linear and nonlinear constraints. This set of mathematical equations defined the optimization model that was solved using a number of methods in Matlab. A parametric investigation was performed on a number of design parameters providing additional information about the optimized solution. An in-depth description of the optimization model and its solution is provided in Appendix B. In summary, the design variables are defined as $\mathbf{R_1, R_3, R_4, R_5, R_{DP}}$ (see Fig. 2.10). The goal was to optimize these variables for maximum temperature resolution of a given heater in the

array subject to physical constraints. All design variables are approximated as continuous variables.

Single-Objective Optimization Formulation:

Objective Function:

$$\Delta T_h = \frac{39 R_1 R_5^2}{\alpha_h R_{ref} R_3 \left(R_5 + R_{DP}\right)^2} \tag{2.5}$$

Subject to:

$$g_1: \quad \frac{\left(R_1 R_4 \big/ R_3 R_{ref} - 1\right)}{\alpha_h} + T_{ref} - T_{low} \le 0 \tag{2.6}$$

$$g_2: \quad C_{\min} - \frac{R_3 + R_4}{R_1 + R_{ref}} \le 0 \tag{2.7}$$

$$g_3: \quad \frac{24}{\left(1 + \frac{R_4}{R_3} + \frac{R_5 R_{DP}}{R_5 R_3 + R_{DP} R_3}\right)} - V_{drop} \le 0 \tag{2.8}$$

$$g_4: \quad T_{high} - \frac{R_1 R_4}{\alpha_h R_3 R_{ref}} - \frac{20000 R_1 R_5}{\alpha_h R_5 R_3 R_{ref} + 20000 \alpha_h R_3 R_{ref}} + \frac{1}{\alpha_h} - T_{ref} \le 0 \tag{2.9}$$

$$\begin{aligned} g_5 - g_{11}: \quad & R_{ref} D_{\min} \le R_1 \le R_{1Ubnd}, \quad 0 \le R_3 \le R_{3Ubnd}, \\ & 0 \le R_4 \le R_{4Ubnd}, \quad 0 \le R_5 \le \infty, \\ & 0 \le R_{DP} \le 20000 \end{aligned} \tag{2.10}$$

$$h_1: \quad -\frac{R_1 R_4}{\alpha_h R_3 R_{ref}} - \frac{R_{DP} R_1 R_5}{\alpha_h R_5 R_3 R_{ref} + R_{DP} \alpha_h R_3 R_{ref}} + \frac{1}{\alpha_h} - T_{ref} + T_{opt} = 0 \tag{2.11}$$

One drawback to solving the optimization model is the time necessary to analyze and determine the optimized resistor values for all 96 circuits. Therefore an effort was made to use as many of the same resistors as possible. This saved a tremendous amount of time and money as resistors could be ordered in bulk. As a result, R_1 was the only resistor that was optimized for the individual circuits. R_3, R_4, and R_5 were chosen based on the analysis described above and the availability of in-house components. The final resistor values for each feedback circuit can be found in Appendix C (Table C.1). The heater numbering scheme is presented in Figure C.1.

The optimized heater array resulted in a 50% increase in temperature resolution over the older design at higher operating temperatures, 100-120°C. The optimized design has the same temperature resolution at low operating temperatures, 70°C, Fig 2.12. The final worst case operational specifications of a heater in the entire array are a temperature

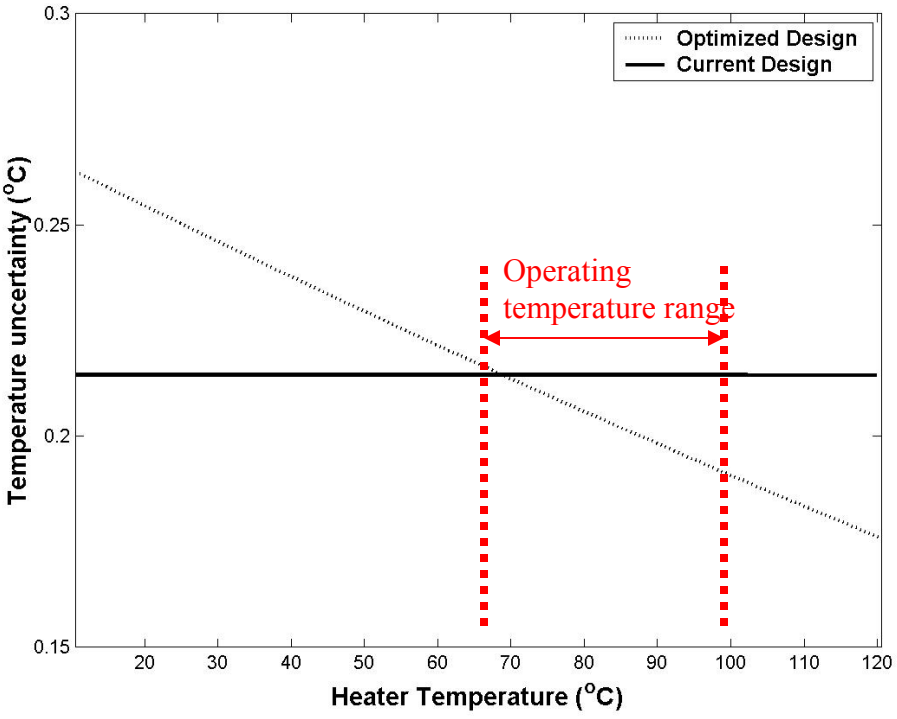

Figure 2.12: Comparison between optimized heater temperature resolution and older heater temperature resolution (current design).

range of 15°C -120°C with a temperature resolution of ~ 0.21°C. Results of the optimization analysis also identified a unique relationship between the temperature range and temperature resolution as shown in Fig. 2.13. This figure indicates that a higher desirable temperature range creates a larger temperature uncertainty between heaters and very low temperature uncertainties can be created at higher operating temperatures for a given temperature range.

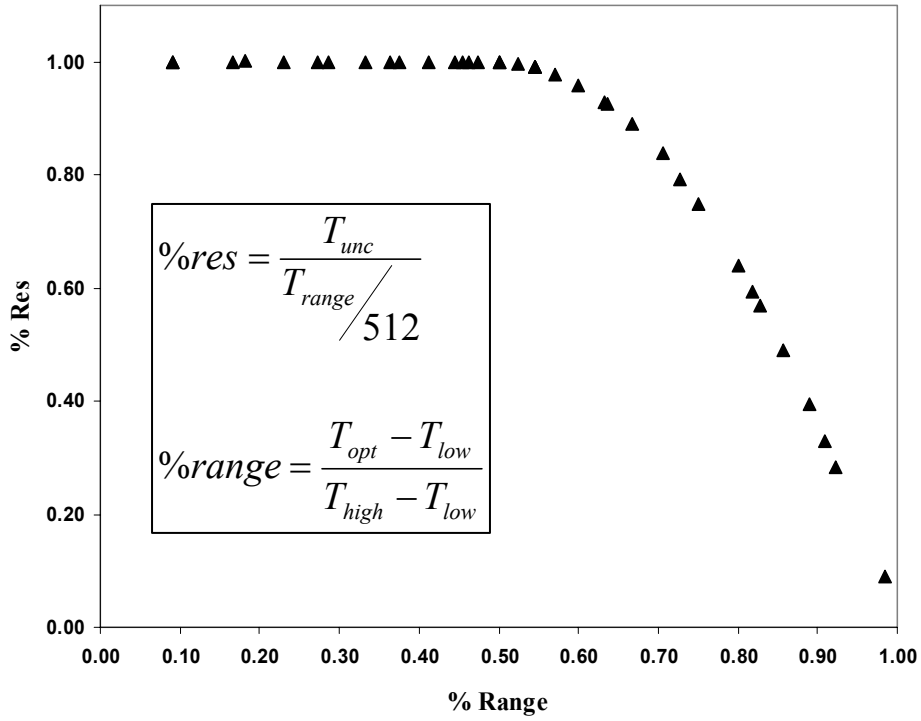

Figure 2.13: Non-dimensional optimization results.

2.3.3.2 Heater Calibration. The heater array was calibrated using a constant temperature oven. PID temperature controllers, two thermocouples, and two thin film heaters were used to maintain a constant temperature environment inside the oven. The heater was allowed to equilibrate within the oven for two hours before the calibration program was

run. The temperature of the heater array was measured using a NIST calibrated thermocouple which was attached using Kapton high-temperature tape close to the heater surface. Pictures of this setup are shown in Fig. 2.14.

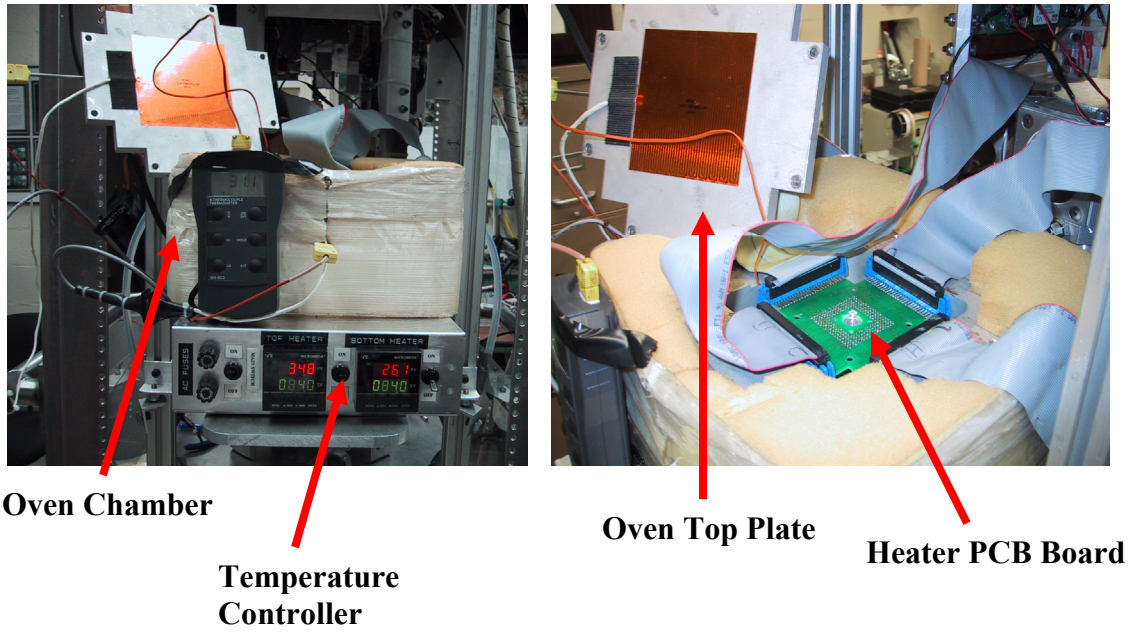

Figure 2.14: Calibration chamber (left), top view of PCB board inside oven (right).

At thermal equilibrium inside the oven, the calibration program determines the digital potentiometer resistance setting which balances the wheatstone bridge (Fig. 2.10). These settings, called DQ values, are written to a text file and stored on a flash disk for future use. This process was repeated for 5°C temperature increments ranging from 65°C to105°C. The actual measured DQ values (DQ_{meas}), which are the values of the potentiometer wiper positions which corresponds to a resistance (R_{DP} = 39*DQ Ω), agree very well with the predicted values (DQ_{pred}) Fig. 2.15. Errors in the theoretical model are due to uncertainties in feedback circuit resistance measurements and uncertainties in the temperature reading of the heater elements.

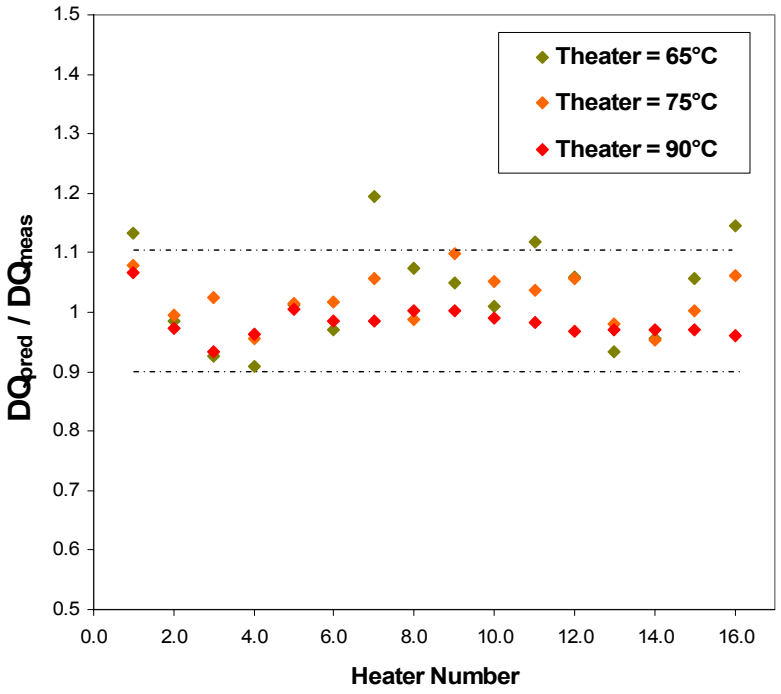

Figure 2.15: Comparison between measured and predicted DQ values for a representative heater data set.

The temperature range investigated was chosen based on safety requirements, heater reliability, and wall superheat resolution and range, Table 2.7. Based on previous studies (Merte 1994 , Dimarco & Grassi 1999), it appears that 5°C temperature increments provides a sufficient boiling curve resolution to measure higher-frequency effects in low-g. Wall temperatures below 70°C were unable to sustain boiling activity on the heated surface and were therefore of little interest. The maximum wall temperature studied, 100°C, corresponds to a safe and reliable operational temperature limit of the heater array and is usually beyond the temperature at which CHF occurs. At higher heater temperatures, thermal expansion of the wire bonding metal and the encapsulation epoxy can create strong stresses within the device, causing individual wire bonds to detach from the bonding pads. In addition, higher heater temperatures can cause high stresses within the quartz wafer due to thermal expansion mismatches between the

deposited metal layers and the substrate. A more detailed analysis of the heater wall temperature uncertainty is provided in the next section. Last, during experimentation, the heater wall temperature was initially set to 100 - 120 °C for 1 second in order to initiate boiling activity. This large superheat was required due to very low dissolved gas concentrations within the boiling chamber.

Parameter: Heater Wall Temperature	
Wall Temperature (^{o}C)	Uncertainty (^{o}C)
70	0.8
75	0.8
80	0.8
85	0.8
90	0.8
95	0.8
100	0.8

Table 2.7: Heater wall temperature range parametrically investigated.

2.3.4 Heater Geometry

2.3.4.1 Heater Size. As mentioned in the literature review, heater size appears to have an effect on the boiling performance when the size of the heater is below or near the capillary length. In low-g, the capillary length for FC-72 is 7.8 mm and therefore an effort was made to study boiling from scales close to and much smaller than this length. Two heater arrays were manufactured for this purpose (7 x 7 mm^2 and 2.7 x 2.7 mm^2). Various heater sizes were investigated by selectively powering a number of heaters in the 96 heater arrays. As fewer heaters are powered, the spatial resolution of heat flux measurement deteriorates and therefore the minimum size studied was a 3 x 3 array of heaters (0.65 mm^2) and not a single heater. Four heater sizes were selected from the entire heater size domain space providing information about higher-order heater size

effects on the boiling performance. A summary of the square heater sizes is presented in Table 2.8 and Fig. 2.16.

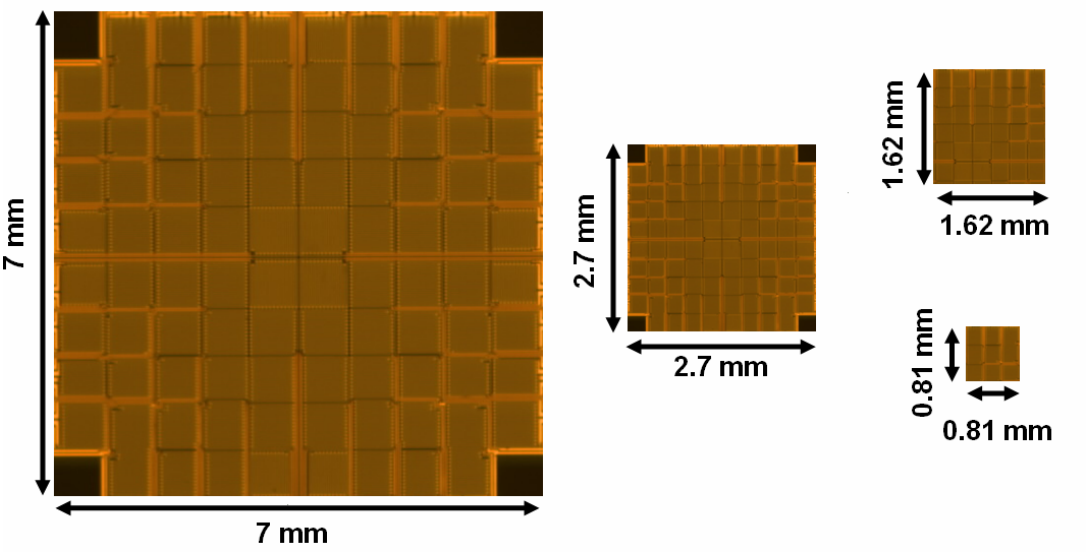

Figure 2.16: Relative heater sizes parametrically investigated.

Parameter: Square Heater Size				
Heater Array Area (mm^2)	# heaters	Description	Ind. Heater Area (mm^2)	Uncertainty (mm^2)
0.66	9	3 x 3 array	0.073	0.005
2.62	36	6 x 6 array	0.073	0.005
7.29	96	10 x 10 array	0.073	0.005
49.00	96	10 x 10 array	0.49	0.01

Table 2.8: Heater sizes parametrically investigated.

2.3.4.2 Heater Aspect Ratio. In low-g, primary bubbles that form from square heater geometries tend to be highly symmetrical which may affect thermocapillary convection. The question was raised regarding the effect of rectangular heaters shapes that potentially could create and sustain boiling from ellipsoidal bubbles. This was achieved by powering rectangular arrays of heaters with high aspect ratios. The goal of this parametric investigation was to determine the extent to which stable ellipsoidal bubbles tend to form in low-g and the effect of elongated bubble shapes on thermocapillary

convection and heat transfer. The minimum aspect ratio investigated was a square heater array. The maximum aspect ratio heater array studied was determined by two considerations: the maximum length of the array (10 heaters), and the minimum desired heat flux resolution. The latter refers to the selection of a 2 x 10 array instead of a 1 x 10 array which provides a heat flux distribution in both orthogonal coordinate directions instead of in one direction. From the 7 x 7 mm^2 heater array, five different heater aspect ratios were investigated as shown in Fig. 2.17 and are summarized in Table. 2.9.

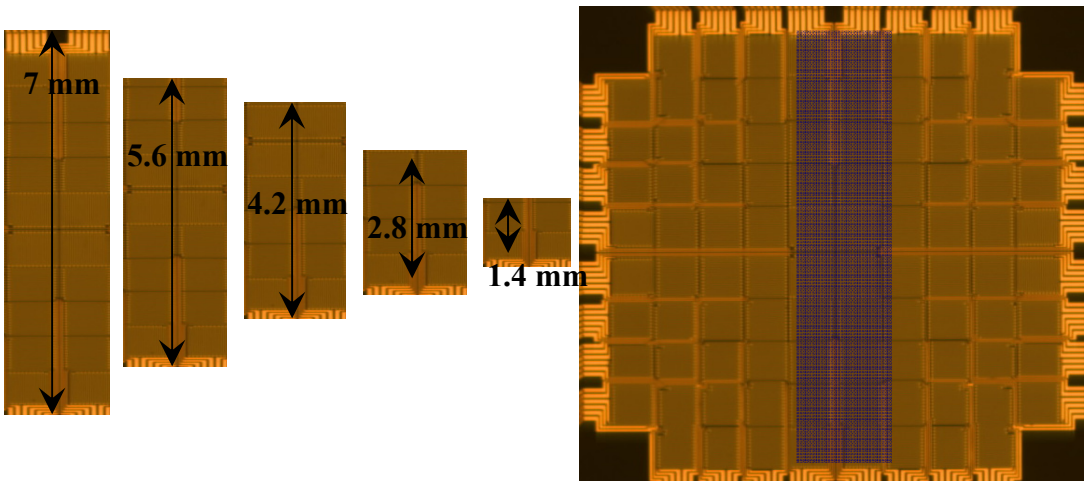

Figure 2.17: Heater aspect ratios investigated.

Parameter: Heater Aspect Ratio					
Aspect Ratio	Heater Area (mm^2)	# heaters	Description	Ind. Heater Area (mm^2)	Uncertainty (mm^2)
1:1	1.96	4	2 x 2 array	0.49	0.01
1:2	3.92	8	2 x 4 array	0.49	0.01
1:3	5.88	12	2 x 6 array	0.49	0.01
1:4	7.84	16	2 x 8 array	0.49	0.01
1:5	9.8	20	2 x 10 array	0.49	0.01

Table 2.9: Summary of heater aspect ratios investigated.

2.3.5 Bulk Liquid Subcooling

The chamber working fluid temperature was controlled using a series of Kapton heaters, thermistor, and temperature controller. The thermistor measures a point temperature 5 cm above the heater array. The temperature control unit uses a PID controller and a solid state relay to supply power to the Kapton heaters attached to the exterior of the boiling vessel to maintain the bulk temperature at or above room temperature. The minimum temperature investigated, approximately room temperature, was chosen based on the desire to avoid incorporating refrigeration systems into the test apparatus. This addition would increase the complexity of the design, introduce system integration issues, require additional safety certification by NASA, and had the potential to increase the size and weight of the system dramatically. The maximum bulk temperature studied corresponds to the saturation temperature of the fluid. Table 2.10 provides a summary of the bulk fluid conditions investigated in this study. The bulk fluid temperature was recorded twice by hand during each parabolic maneuver. The temperature control unit maintained the subcooling temperature to within 2°C of the set value over the course of a given flight.

Parameter: Bulk Fluid Temperature	
Bulk Temperature (^{o}C)	**Uncertainty (^{o}C)**
28	2
35	2
45	2
55	2

Table 2.10: Bulk fluid temperatures investigated.

2.4 DATA ACQUISITION

The analog voltage signal measured across each individual heater, shown in the feedback circuit Fig. 2.10 as V_o, is sent to a 12 bit A/D converter (AD7892) which connects through a serial interface to the computer module. A PCMCIA digital I/O card takes the 12 bit digital signal and reads it into the computer. The CPU module (IDAN-CMM686) has two serial interfaces, a parallel interface, and a keyboard connection. The transient voltage across the heater was sampled at 250 Hz by a data acquisition system with a maximum sample rate of 500 Hz. The data was written to a 250 Mbyte memory flash disk for post-processing. A pressure transducer and 3-axis accelerometer were integrated into the data acquisition system and data from these sensors were acquired at the same frequency as the heater voltage signal.

2.5 IMAGING & PIV SYSTEM

Video images of boiling in low and high-g were taken throughout the data acquisition process. Side view boiling images were originally taken with a CCD camera and later with a high-speed Phantom camera capable of taking images at a rate of 10000 fps. Bottom view images of the boiling activity were recorded by a high-speed phantom camera that was later replaced with a CCD camera. The heater array substrate is quartz which is transparent to visible light allowing images to be taken of the bubble motion on the heater surface from below. Light from within the boiling chamber traveled down through the heater and was reflected at a 90 degree angle and then sensed by a horizontally mounted bottom view camera. The images taken by the CCD cameras were recorded on a handheld mini digital video camera and later uploaded to a computer for further processing. The video images were synchronized with the heater voltage

measurement using a series of light flashes (binary coding) that differed for each data run.

Marangoni convection appears to be a dominant transport mechanism in low-g pool boiling. This mechanism is known to strongly influence the liquid flow field around stable vapor bubbles. Liquid velocity field measurements can be made during the formation and growth of the primary bubble in low gravity. Particle tracking velocimetry (PTV) as well as particle image velocimetry (PIV) techniques can be used to provide valuable flow information. Although PIV experimental measurements are not presented in this thesis, PIV and PTV capabilities were demonstrated during a concept verification experiment. In this experiment, a small concentration of glass microspheres with density similar to FC-72 were used as seeding particles in the working fluid. Individual particle movement throughout the fluid as a function of time was tracked using high-speed imaging. This technique provided a good estimate of the fluid velocity and vorticity at specific points and various times. A laser was used to illuminate a plane of boiling fluid centered directly above the heater, and the light reflected off the neutrally buoyant glass microspheres was imaged using a high-speed camera, Fig. 2.18. From successive images, representative velocity vectors were obtained at various times within the fluid. Chapter 7 outlines recommendations for future work involving PIV techniques further.

A diode type class II laser manufactured by Diode Laser Concepts is used as part of the PIV measurement system. The laser has internal electronics that provide static, surge, and reverse polarity protection. The laser operates at 5 VDC and draws a maximum total power of 1 mW. Included as part of the laser assembly is a lens that converts the laser beam into a sheet of laser light at an angle of 45°. The laser

wavelength is 635 nm. The line width is 1mm at 1 meter and the fan angle is 10°. A picture of the assembled laser mounting system is shown in figure 2.19.

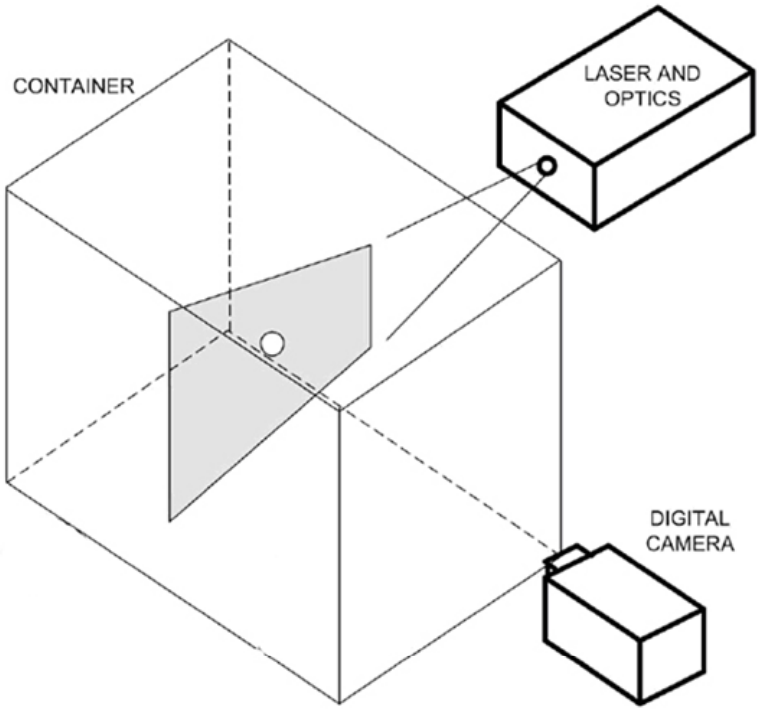

Figure 2.18: PIV conceptual drawing.

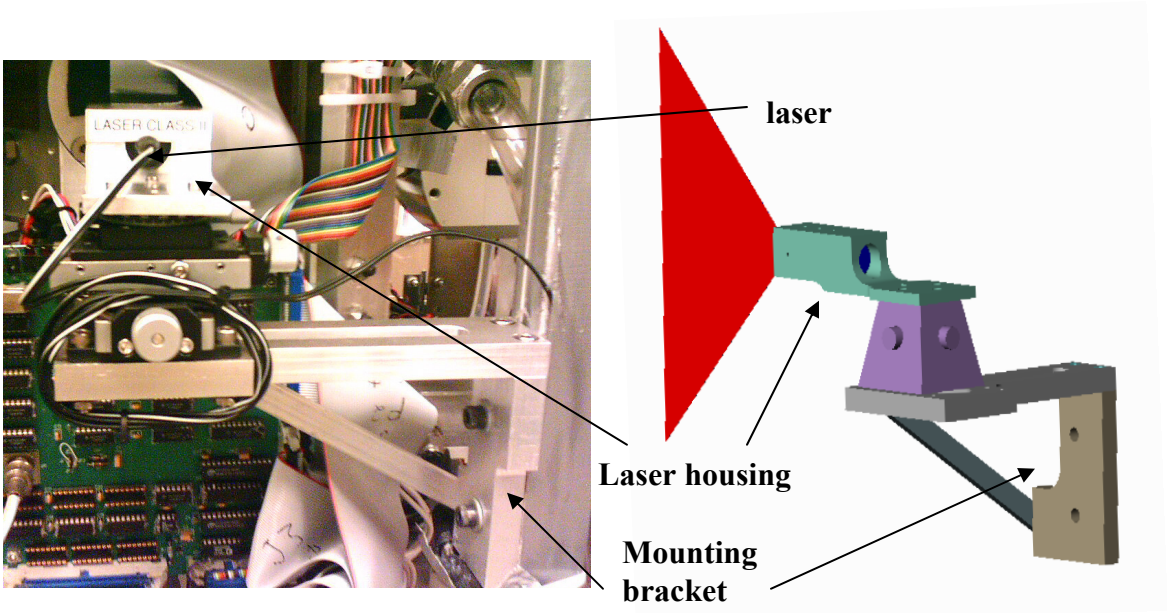

Figure 2.19: Laser mounting apparatus and CAD rendering.

2.6 SYSTEM INTEGRATION

A schematic of the boiling rig used in this study is shown in Fig. 2.20. The

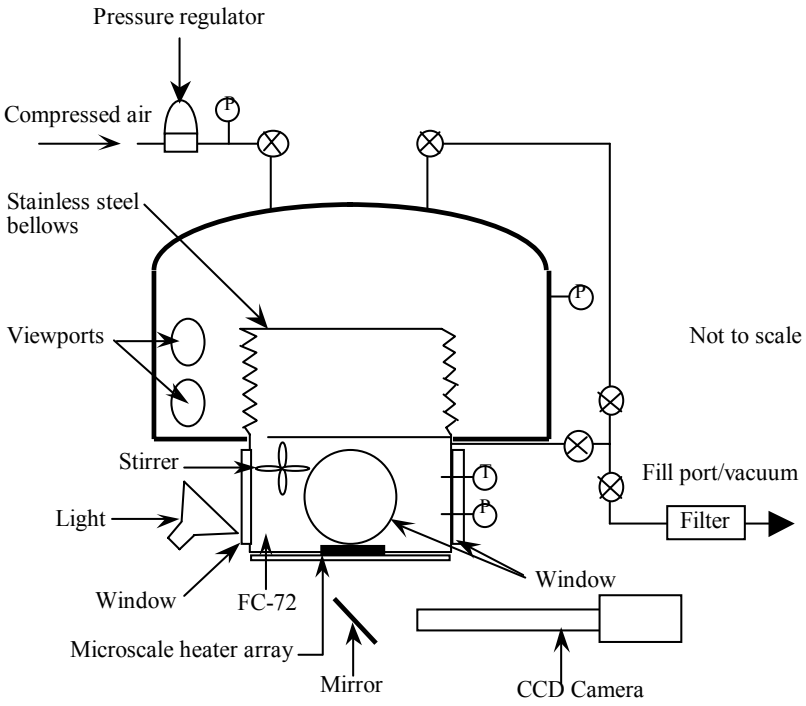

Figure 2.20: Test chamber schematic (Courtesy of J. Kim).

stainless steel bellows and the surrounding housing allowed the test section pressure to be controlled. A pressure transducer rated at 200 psia was used to measure the pressure at the heater surface. A micropump was used to break up thermal stratification within the test chamber, while a PID temperature controller, a thermistor, and thin film heaters attached to the boiling chamber were used to control the bulk fluid temperature as mentioned previously. The test chamber, Fig. 2.21, was filled with nominally 3 liters of distilled FC-72. The heater was cooled from the bottom using an air jet at ambient temperature with a flow rate of 660 cm^3/s through a 1.6 mm diameter nozzle to prevent individual heaters from shutting off at low heat transfer levels (such as occurs when a large bubble covers the heater). The heat flux associated with air jet cooling was

subtracted from the heat flux signal during data reduction to determine the actual heat transfer from the heater surface to the liquid and is discussed in greater detail in the next chapter. Side windows and the transparent nature of the heater substrate allowed for images to be taken of the boiling from the side and bottom. Two 29.97 Hz CCD cameras and mini DV camcorders were used for this purpose as described above. Acceleration data in the direction perpendicular to the floor of the aircraft was obtained using one axis of an accelerometer (Entran EGCS3) with a sensitivity of 2.5 V/g and frequency response of 0-90 Hz. The assembled test package is shown in Fig. 2.22 and 2.23.

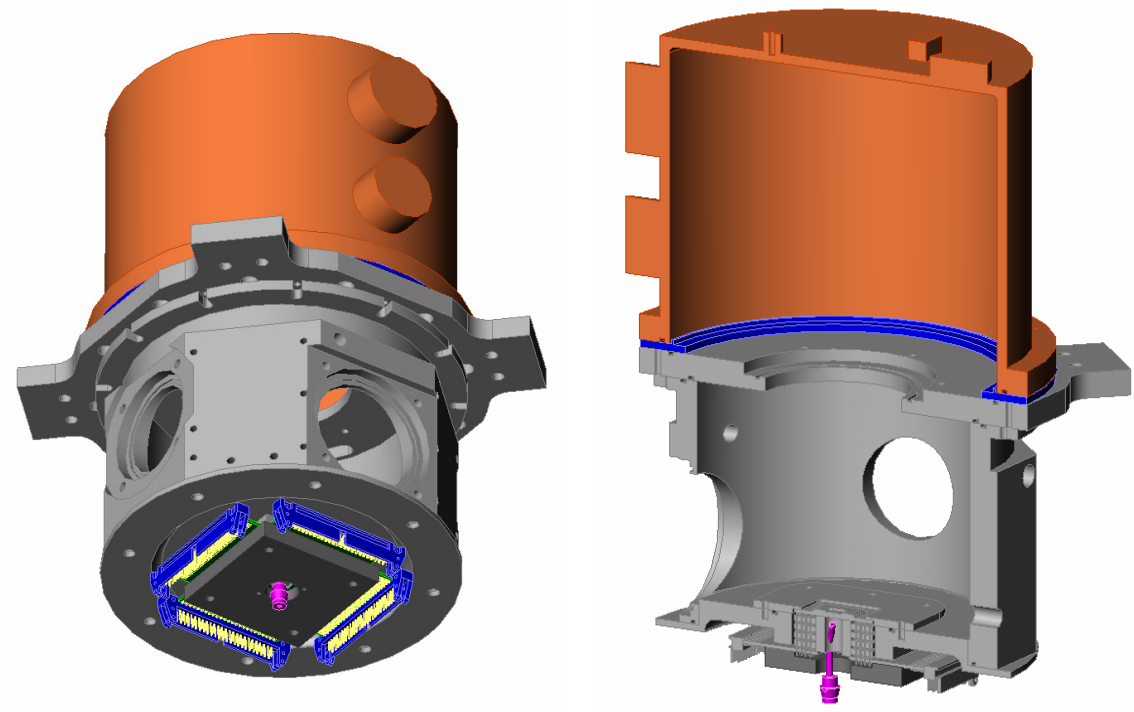

Figure 2.21: 3-D boiling chamber renderings (Courtesy of J. Benton).

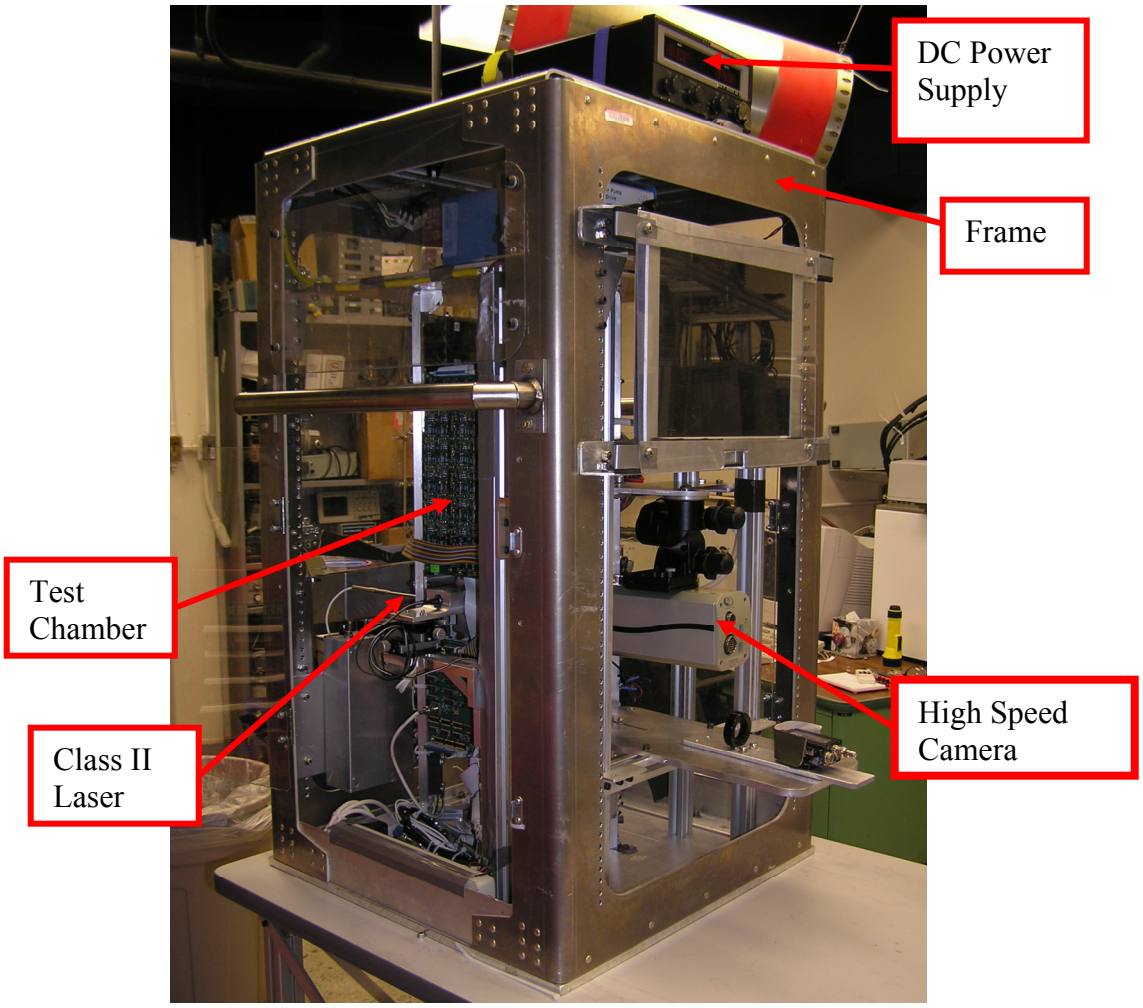

Figure 2.22: Photograph of modified test package (the VER) and its components.

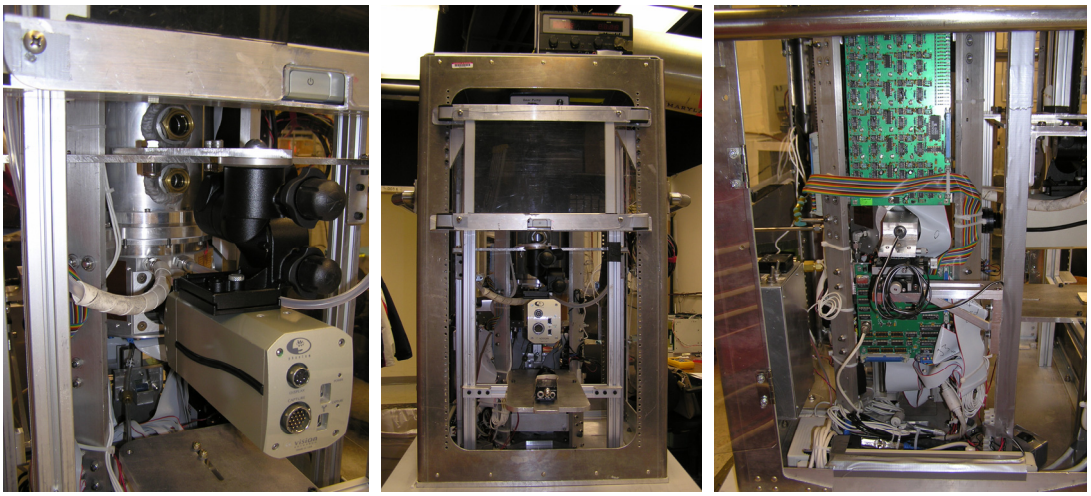

Figure 2.23: Assembled test apparatus, high speed camera mounting (left), front view (middle), side view and laser mounting (right).

2.7 EXPERIMENTAL TEST MATRIX

As mentioned earlier a fractional factorial design approach was employed taking into account experimental capabilities, design and safety requirements, and logistical challenges. The fluid charging procedure for this experiment requires multiple days to perform. Therefore only one type of fluid could be studied per flight week. The bulk fluid temperature can take up to 2 hours to stabilize after programming the temperature controller and therefore one set of data at a given bulk temperature was obtained per flight. A typical flight week consists of four flights allowing different subcoolings to be studied on successive days. A typical design matrix for a given flight is provided in Fig. 2.24. During a given flight, the g-level,

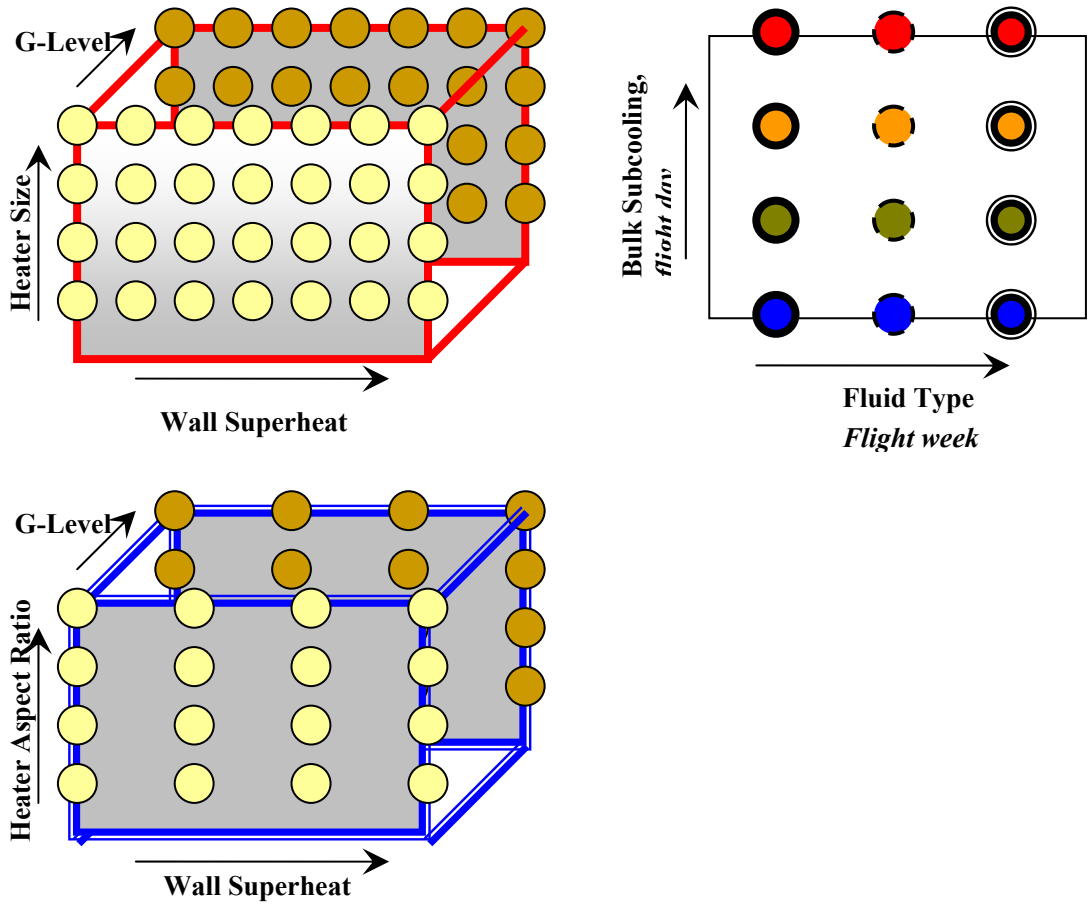

Figure 2.24: Fractional factorial experimental test matrix.

heater size, and wall superheat were parametrically varied (cubic structures in figure 2.24). In this diagram heater size and heater aspect are similar parameters. The two-dimensional figure (top right) in fig 2.24 represents a matrix of bulk subcoolings and fluid types. For each circle in this figure, there is an associated 3-D cubic structure defining the parametric factors. The color of the cubic vertices represents the subcooling and the vertices line type represents the fluid type. The order in which data were obtained on a given day at various wall superheats and heater sizes was randomized. A summary of the all of the parametric factors investigated and their respective ranges is shown in Table 2.11.

Experimental Factor Space						
T_{wall} (^oC)	T_{bulk} (^oC)	F_{body}	H_{size} (mm^2)	H_{aspect} (mm^2)	Fluid	P (kPa)
70	*55*	*0.01-g*	*0.66*	*1:1 (1.96)*	*FC-72 (no gas)*	*101*
75	*45*	*0.17-g*	*2.62*	*1:2 (3.92)*	*FC-72 (pure gas)*	
80	*35*	*1-g*	*7.29*	*1:3 (5.88)*	*FC-72 (pure no-gas)*	
85	*28*	*1.7-g*	*49.00*	*1:4 (7.8)*		
90				*1:5 (11.9*		
95						
100						
					Total Parabolas / Week	*130-160*
					Total Flight Weeks/Year	*3-6*
					Parabola/Year	*390-960*

Table 2.11: Summary of factors parametrically investigated.

2.8 EXPERIMENTAL SUMMARY

The physical problem addressed in this study is of fundamental importance to thermal/fluid management in microgravity. The goal of the experimental methodology developed is to measure and characterize the various pool boiling mechanisms in low and high gravity.

Experimentation in low-gravity environments is a non-trivial endeavor. In addition to the many design considerations and challenges mentioned herein, a risk analysis is required prior to experimentation that anticipates possible problems and either accounts for them at the design outset, or resolves the issue when it arises. In addition, the difficulty in obtaining test time aboard the KC-135 puts further emphasis on experimental functionality, efficiency, and the ability to continually modify the test matrix and experimental capabilities.

The fractional factorial experimental approach employed throughout this investigation was followed to the extent possible. At minimum, this investigation provided a much needed basis of data upon which future work can be conducted and the experiments conducted serve to characterize the potential for passive phase change systems in low-g.

Chapter 3: Data Reduction and Uncertainty Analysis

3.1 PURPOSE

The primary goal of the data reduction was to accurately quantify the amount of heat transferred from the heater surface to the boiling fluid. A number of methods are presented that were used to model, understand, and estimate this value. The methods provide a significantly more accurate representation of the heat transfer due to boiling from the microheater array than was previously available. This chapter also presents an in-depth analysis of the uncertainty in the various factors measured. Data analysis was performed using a Matlab routine. All data were stored as text files. All uncertainties stated subsequently presume a 95% confidence interval.

3.2 VOLTAGE / POWER MEASUREMENT

The transient output voltage of each heater in the array, V_i, its corresponding resistance, R_h, and area, A_i, were used to quantify the transient power flux, $q_{raw,i}$, supplied to each heater element during boiling, Eq. 3.1.

$$q_{raw,i} = V_i^2 \Big/ R_i A_i \tag{3.1}$$

Individual heater resistances were measured at selected temperatures during the calibration process using a Fluke multimeter with an error of 0.4%. A typical plot of temperature vs. resistance for seven randomly selected heaters in the 7 x 7 mm^2 heater array is shown in Fig. 3.1. These measurements were used to calculate the temperature coefficient of resistance, α_i, for each heater element. This value was used to evaluate

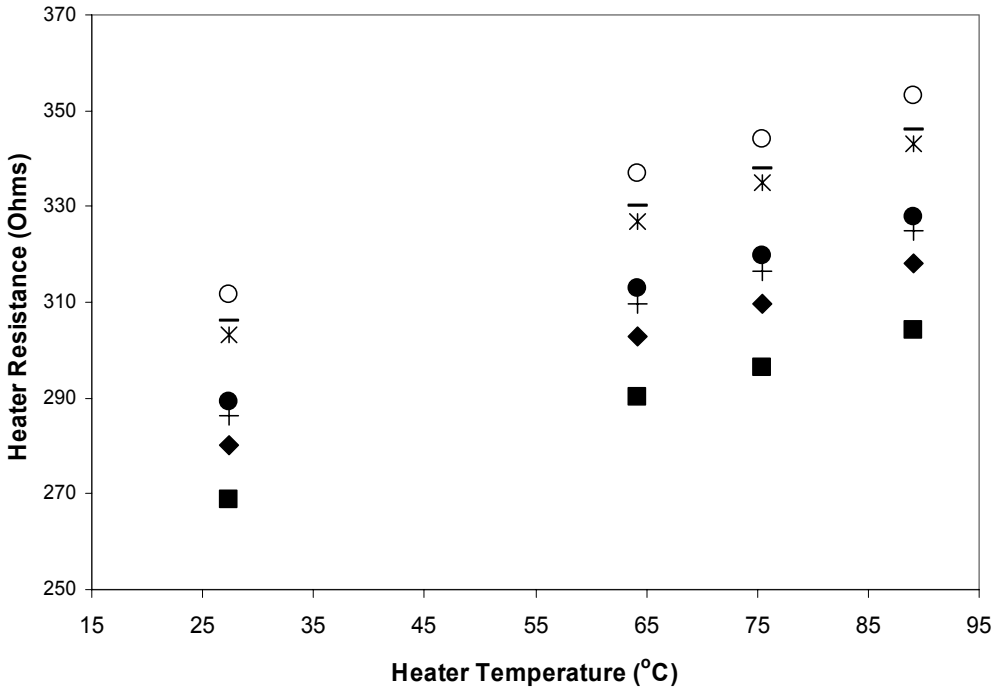

Figure 3.1: Representative heater resistance temperature dependence (7 x 7 mm^2 heater array, $\alpha = 0.003\ ^oC^{-1}$).

heaters that performed inconsistently or exhibited large performance deviations from the norm. For properly functioning heaters, the measured α_i values agree to within ± 5% of the theoretical value ($\alpha_t = 0.002\ \Omega/\Omega°C$, 2.7 x 2.7 mm^2 array), Fig. 3.2. For heater temperatures where the resistances were not measured, Eq 3.2 was used to estimate the resistance of the heater at the respective temperature.

$$R_i = R_{ref,i}\left(1 + \alpha\ dT\right) \tag{3.2}$$

In this equation, *dT*, represents the difference between the set temperature and reference temperature. The uncertainty in estimating the heater resistance from Eq. 3.2 is given by Eq. 3.3, where the temperature uncertainty, u_{dT}, temperature coefficient of resistance

uncertainty, u_α, and reference heater resistance uncertainty, u_{Rref}), are 2%, 5%, and 0.4% respectively. The total uncertainty for R_i was calculated to be 1%.

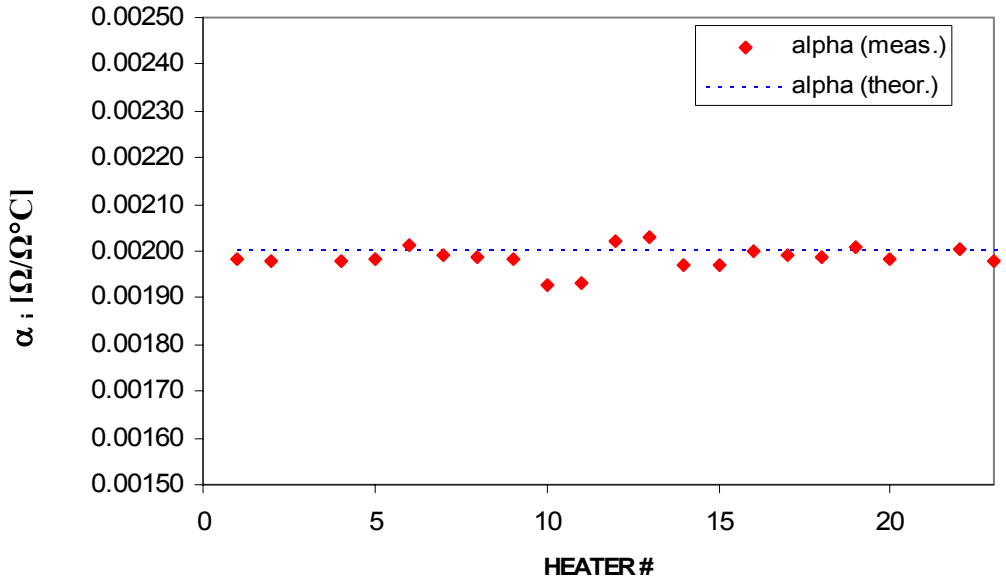

Figure 3.2: Measured α_i values for a representative set of 2.7 x 2.7 mm^2 heater array heaters (α_t = 0.002, Kim et al. 2002).

$$u_{Ri} = \sqrt{\left(\frac{\partial R_i}{\partial R_{ref,i}} u_{Rref,i}\right)^2 + \left(\frac{\partial R_i}{\partial \alpha} u_\alpha\right)^2 + \left(\frac{\partial R_i}{\partial R_{ref,i}} u_{dT}\right)^2} \tag{3.3}$$

The uncertainty associated with $q_{raw,i}$ was calculated from a propagation of uncertainty analysis using Eq. 3.4. This equation assumes a first-order Taylor

$$u_{qraw,i} = \sqrt{\left(\frac{2V_i}{R_i A_i} u_{Vi}\right)^2 + \left(-\frac{V_i^2}{R_i^2 A_i} u_{Ri}\right)^2 + \left(-\frac{V_i^2}{R_i A_i^2} u_{Ai}\right)^2} \tag{3.4}$$

expansion of the uncertainty in the independent variables in Eq. 3.1. The uncertainty in R_h, is 1% and the heater area was measured to within ± 5%. The uncertainty in the voltage measurement, which is primarily due uncertainties in the A/D converter chip (Analog Devices, AD7892), are stated as ± 0.11 %. Clearly the primary uncertainty in

$q_{raw,i}$ is due to the uncertainty in A_i and was calculated to be ± 5.1%. In contrast, the uncertainty in the total heat (W) dissipated by the i^{th} heater element, $q_{w,i}$, is much smaller (± 1%). A typical time resolved plot of $q_{raw,i}$ obtained during parabolic flight for a given heater element is shown in Fig. 3.3.

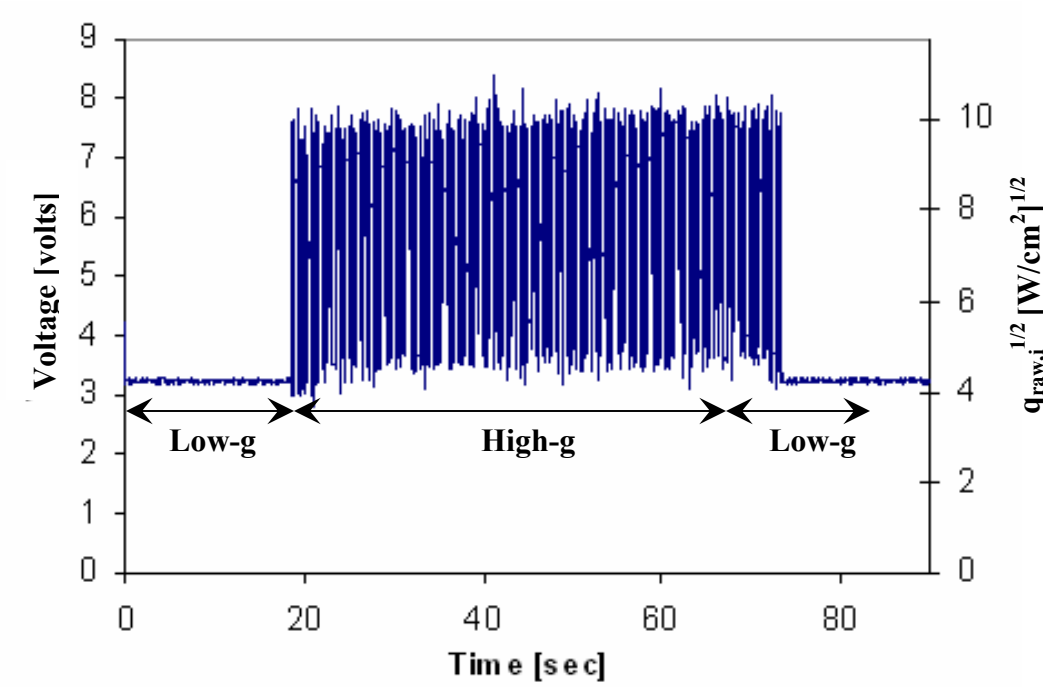

Figure 3.3: Time resolved voltage and heat flux for heater #15, ΔT_{sat} = 43°C, T_{bulk} = 28°C, 96 heater array.

3.3 SUBSTRATE CONDUCTION

3.3.1 Analytical Model

The amount of heat transferred to the boiling liquid for a given heater element, q_i, was calculated by subtracting the heat flux dissipated into the quartz substrate, $q_{sc,i}$, from $q_{raw,i}$. Substrate conduction is a complicated 3-D phenomenon that is strongly influenced by the wafer boundary conditions. A 2-D schematic of the heat transfer mechanisms around the substrate are shown in Fig. 3.4. During a given test run, the heater temperature and backside boundary conditions of the wafer remain constant resulting in

steady state substrate conduction. For heaters located in the center of the array, surrounding heaters are at approximately the same temperature and substrate conduction is predominately 1-D. A simple 1-D steady state conduction analysis was

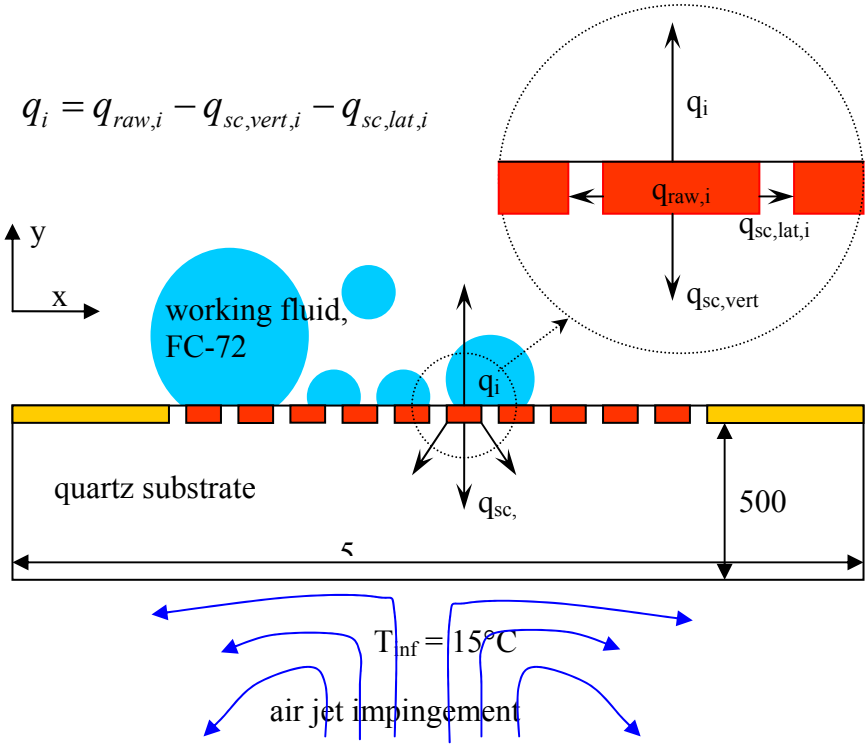

Figure 3.4: 2-D schematic of heat transfer around the 2.7 mm micro-heater array (not to scale).

used to model such heaters. In order to obtain an estimate of this value, the heat transfer coefficient on the backside of the heater due to air impingement cooling was calculated. As mentioned previously, backside cooling is provided using a circular impinging air jet produced by forcing air through a nozzle of 1.6 mm diameter (D_n) aboard the aircraft. The cooling air flow is maintained by a compressed air bottle with flow regulation typically set at 152 kPa (22 psia) for the 2.7 x 2.7 mm^2 heater array. The ambient pressure inside the aircraft averaged 83 kPa (12 psia) during the flight profile. Martin has

performed an extensive review of heat transfer coefficients for impinging air jets with single round nozzles. His results are presented in a form given by Eq. 3.5 (Martin, 1997).

$$\frac{Nu}{\Pr_{air}^{0.42}} = F(\mathrm{Re}, r/D_n)\, k\left(H_n/D_n, r/D_n\right) \tag{3.5}$$

In Eq. 3.5, Nu represents the average Nusselt number from the stagnation point to a radial distance (r). The nozzle exit was positioned approximately 10 mm (H_n) below the backside of the quartz wafer and the radial distance over which an average heat transfer coefficient was desired was 2.7 mm. Substituting these values into Eq. 3.5 yields the following (Eq. 3.6):

$$r/D_n = 1.6875 \quad H_n/D_n = 6.25 \tag{3.6}$$

For air velocities greater than Mach=0.3 ($M_a = 0.3$), compressible effects become significant and therefore the Reynolds number at the nozzle exit was calculated based on compressible flow theory. For steady-state, 1-D, adiabatic, and inviscid ideal compressible flow, an isentropic assumption can be made which reduces the energy equation to Eq. 3.7-3.8 (Liepmann and Roshko, 1957).

$$\frac{p_o}{p} = (1 + \frac{\gamma - 1}{2} M_a{}^2)^{\gamma/(\gamma-1)}. \tag{3.7}$$

$$\frac{p}{p_o} = \left(\frac{\rho_e}{\rho_o}\right)^{\gamma} = \left(\frac{T_e}{T_o}\right)^{\gamma/\gamma-1} \tag{3.8}$$

As previously mentioned, the pressure ratio, p/p_o, is equal to 0.545, and for air, $\gamma = 1.4$. Substituting these values into Eq. 3.7 yields, $M_a = 0.973$. The nozzle exit temperature and density of the airflow can be calculated from Eq. 3.8, $\rho_e = 1.21$ kg/m^3, $T_e = 15$°C. At the nozzle exit, the speed of sound is approximately 340 m/s, which gives an exit nozzle velocity of approximately 330 m/s. The corresponding volumetric flow rate at the nozzle

exit is 660 cm^3/s. Based on these exit conditions, the exit Reynolds number was calculated (Eq 3.9).

$$\mathrm{Re} = \frac{v_e D_n}{\nu} = \frac{330(1.6\times10^{-3})}{15.0\times10^{-6}} \approx 35000 \tag{3.9}$$

From the graphical results presented in (Martin, 1997, pg. 17, fig. 9), Eq. 3.5 can be represented by Eq. 3.10. All of the properties of air were taken at 15°C (ρ = 1.21 kg/m^3, ν = 15.03 *10^{-6} m^2/s, k = 0.0255 W/mK, Pr = 0.710, Incropera and Dewitt, 2002). Further manipulation results in a heat transfer coefficient at the backside of the heater equal to 2050 W/m^2K with an air temperature of 15°C. This value represents the average convection boundary condition at the backside of the wafer.

$$\frac{Nu}{\mathrm{Pr}^{0.42}} = 148 \Rightarrow h = \frac{148(.710)^{0.42}(25.5\times10^{-3})}{1.6\times10^{-3}} \approx 2050 \ W/m^2K \tag{3.10}$$

Incorporating the heat transfer coefficient obtained above into the 1-D steady state conduction model simplifies the analysis into a resistance network analogy (Fig. 3.5). The resulting temperature at the center backside of the wafer is 65°C for a heater

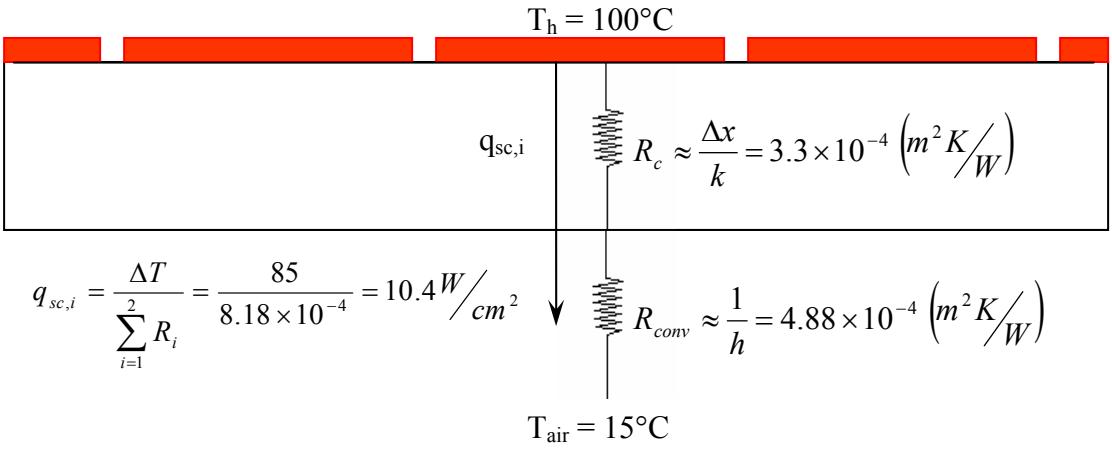

Figure 3.5: 1-D analytical conduction model for a middle heater (heater 1, Fig. 3.5).

temperature of 100°C with a corresponding substrate conduction heat flux of 10.4 W/cm^2. This substrate conduction heat flux applies to a center heater that is surrounded by many other heaters at the same temperature. This value agrees very well with experimental and numerical estimates of the substrate conduction to be presented.

3.3.2 Numerical Model

Although the substrate conduction, $q_{sc,i}$, appears to be 1-D near center heaters in the array, 2-D and 3-D effects are significant near edge and corner heaters. At edge heaters (heater 5, Fig. 3.6), $q_{sc,i}$ is clearly 2-D and at corner heaters (heater 6, 7, Fig. 3.6), 3-D effects are dominant. An effort was made to estimate substrate conduction from

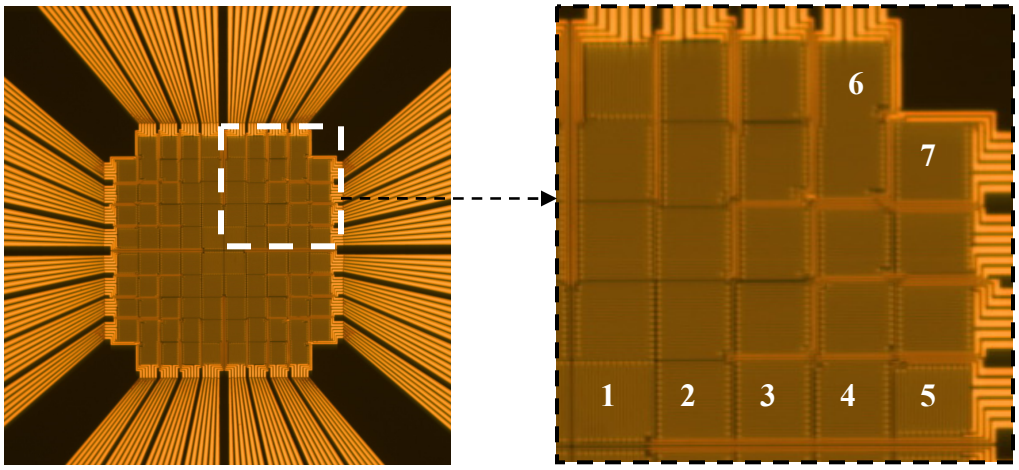

Figure 3.6: Heater numbers modeled using a numerical 3-D conduction routine.

edge and corner heaters using a numerical program developed in Matlab. Under steady state conditions, assuming no energy generation and a constant thermal conductivity, the energy equation within the substrate simplifies to Eq. 3.11. This equation was discretized using a central differencing finite element scheme. A 2-D schematic of the model

$$\frac{\partial^2 T}{\partial x^2} + \frac{\partial^2 T}{\partial y^2} + \frac{\partial^2 T}{\partial z^2} = 0 \qquad (3.11)$$

developed is shown in Fig. 3.7 (x and z coordinate planes are identical due to heater symmetry). At symmetric boundary 1, adiabatic conditions exist. At boundary 2, the

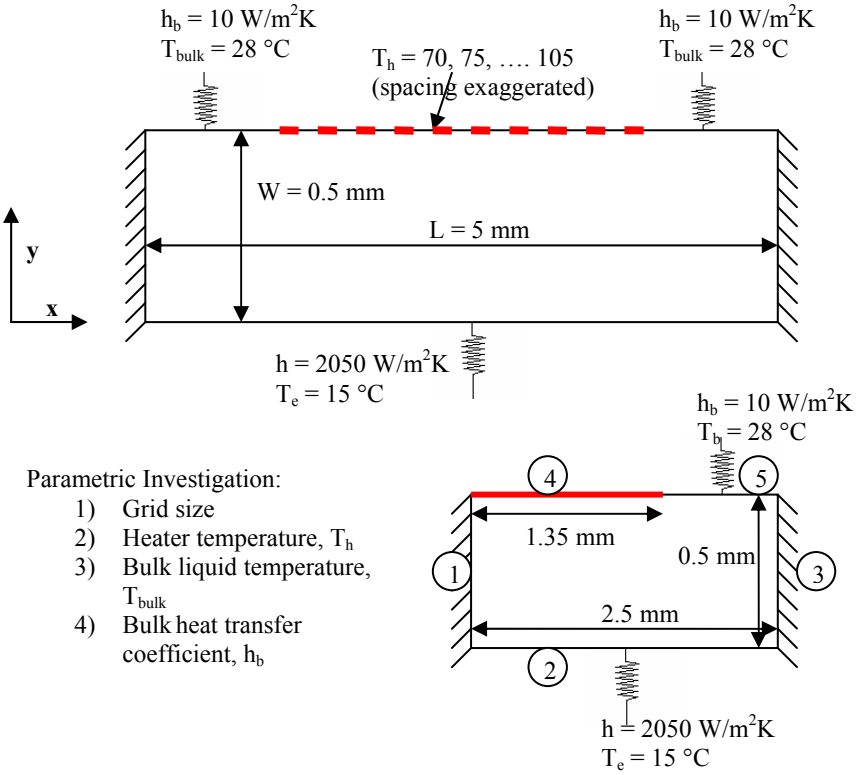

Figure 3.7: 2-D numerical model of substrate conduction (not to scale).

impinging air jet heat transfer coefficient obtained previously (h = 2050 W/m^{2}K) was used with an air temperature of 15°C. At boundary 3, the length to width ratio of the quartz substrate is sufficiently large (L/W = 10) allowing an adiabatic assumption to be made. At the top, boundary 4, the heaters were modeled as a continuous, infinitesimally thick, constant temperature boundary. Last, the top right boundary (5) condition was varied over a range of values (h_b = 10-2000 W/m^{2}K, T_{bulk} = 28°C, 55°C) due to the presence of strong thermocapillary convection which may significantly enhance the heat transfer in this region. For the results presented below, a natural convection boundary with h = 10 W/m^{2}K and T_{bulk} = 55°C was used.

The 2-D domain was discretized using a Cartesion mesh and the resulting set of linear algebraic equations obtained was solved using a Gauss-Siedel iterative scheme. Convergence was assumed to occur when an energy balance on the interior nodes (one node in from all boundaries) was < 0.001 Watts or 0.0001% of the total energy supplied by the heaters. 2-D results are shown in Fig. 3.8.

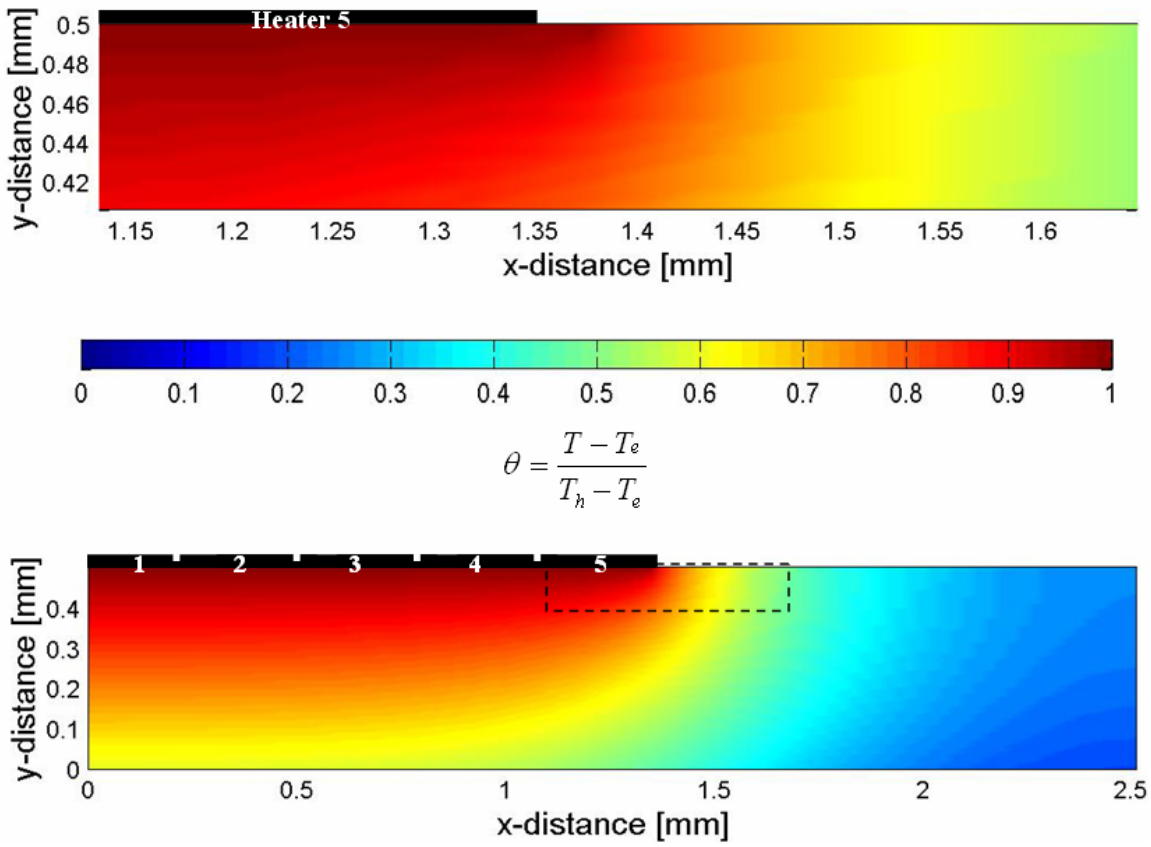

Figure 3.8: 2-D (x-y) non-dimensional temperature distribution within quartz substrate (heater numbers shown in white).

A 3-D model was also developed in a manner similar to that mentioned above. Results presented below were obtained using a 3-D mesh size of 48 x 36 x 48 nodes. A parametric numerical investigation was performed to study the effect of grid size, heater temperature, bulk fluid temperature, and bulk heat transfer coefficient on the steady state temperature profile within the quartz substrate.

Numerical results for a 96 heater array are shown below. The non-dimensional temperature distribution for h_b = 10 W/m^{2}K within the substrate is shown in Fig. 3.9. Toward the middle of the heater array, the heat flux appears to be predominately 1-D and in good agreement with the analytical results mentioned previously. For the edge heater (heater 5) 2-D conduction effects are clearly visible. The temperature contours appear to be nearly perpendicular at the top natural convection boundary indicating negligible heat

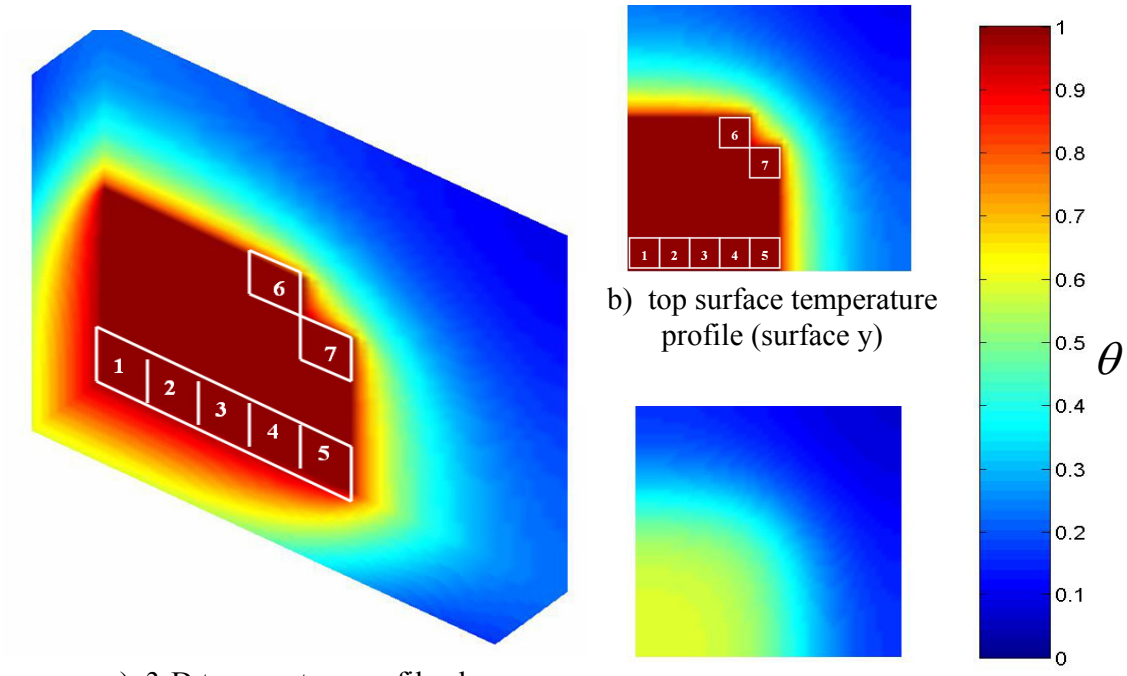

a) 3-D temperature profile along surfaces (x-y-z)

b) top surface temperature profile (surface y)

c) bottom surface temperature profile (surface -y)

Figure 3.9: 3-D non-dimensional temperature distribution within quartz substrate (h_b = 10 W/m^{2}K, T_{bulk} = 55°C, heater numbers shown in white).

transfer across this surface. Bulk liquid temperature was found to have a negligible effect on $q_{sc,i}$ over the experimental bulk temperature ranges tested (T_{bulk} = 28°C to 55 °C, h = 10 W/m^{2}K). Near the heater corners (heater 6 and 7, Fig. 3.9), the heat transfer is clearly 3-D.

A plot of the non-dimensional temperature distribution on the top and bottom of the wafer is shown in Fig. 3.10. Although a large temperature gradient exists at the corner and edge heaters in the x-direction, the heat transfer in this direction is minimal due to the small thickness of the heater elements (1μm) which results in a negligible cross-sectional area (edge heater - 270 μm^2 and corner heater - 540 μm^2).

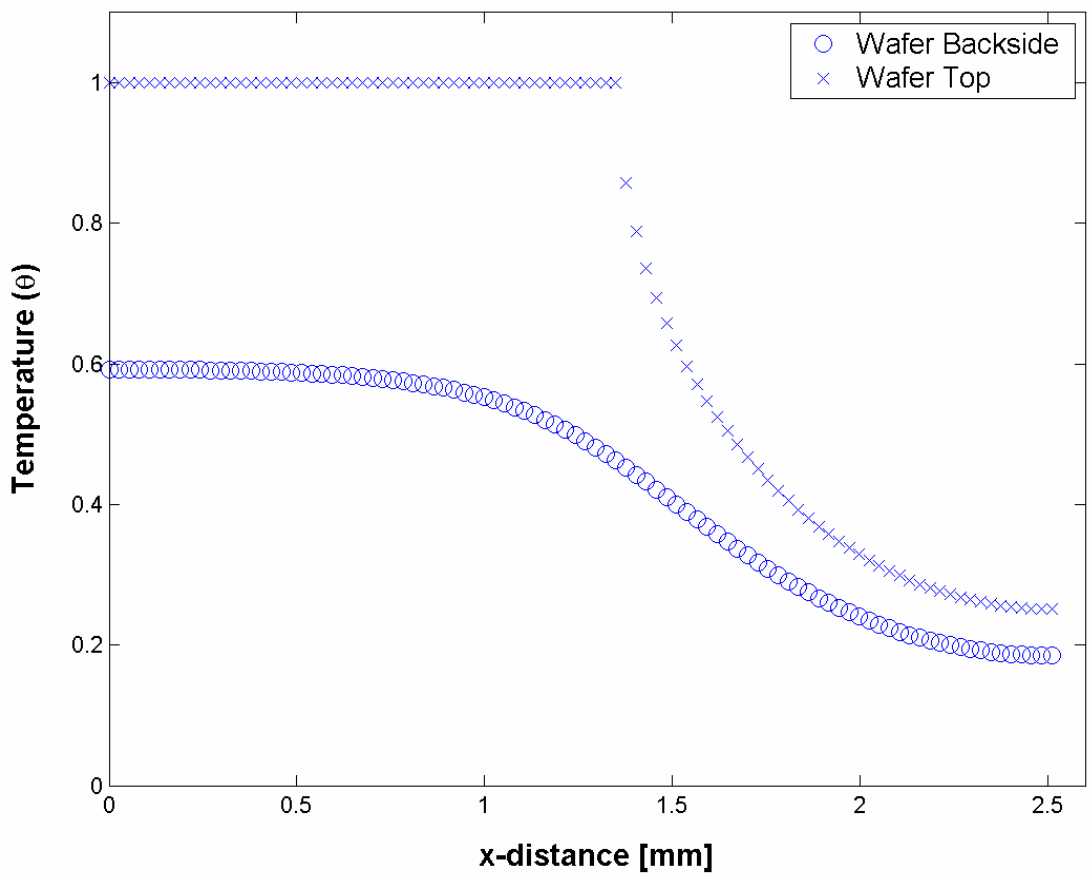

Figure 3.10: Temperature distribution on the top (y = 0) and bottom (y = 0.5 mm) of the wafer (z = 0, h_b = 10 W/m^2K, T_{bulk} = 55°C).

The continuous isothermal boundary idealized as the heater can be broken up into 24 equal size heaters of area = 0.0729 mm^2 (neglecting the distance between heaters). The heat transfer from these 24 equal area sections was summed over the area of each individual heater element and divided by 0.0729 mm^2 (the area of a 2.7 mm heater

element) to obtain an estimate of $q_{sc,i}$. The result of this calculation is shown in Fig. 3.11 for heater temperatures ranging from 65-105 °C. It should be noted that an additional line of symmetry exists running diagonal through the heater (surface y). The heat flux values were symmetric about this line (therefore $q_{sc,i}$ for heaters 6 and 7 are numerically equal). The effect of mesh size on $q_{sc,i}$ was studied using a 2-D numerical model due to greatly reduced convergence times. These results are shown in Fig. 3.12. For mesh sizes larger than approximately 1000 nodes (in 2-D), the effect on substrate conduction heat flux was negligible. For the largest mesh size studied, at convergence 99% of the energy entering the control volume from the isothermal heater surface was dissipated by the air

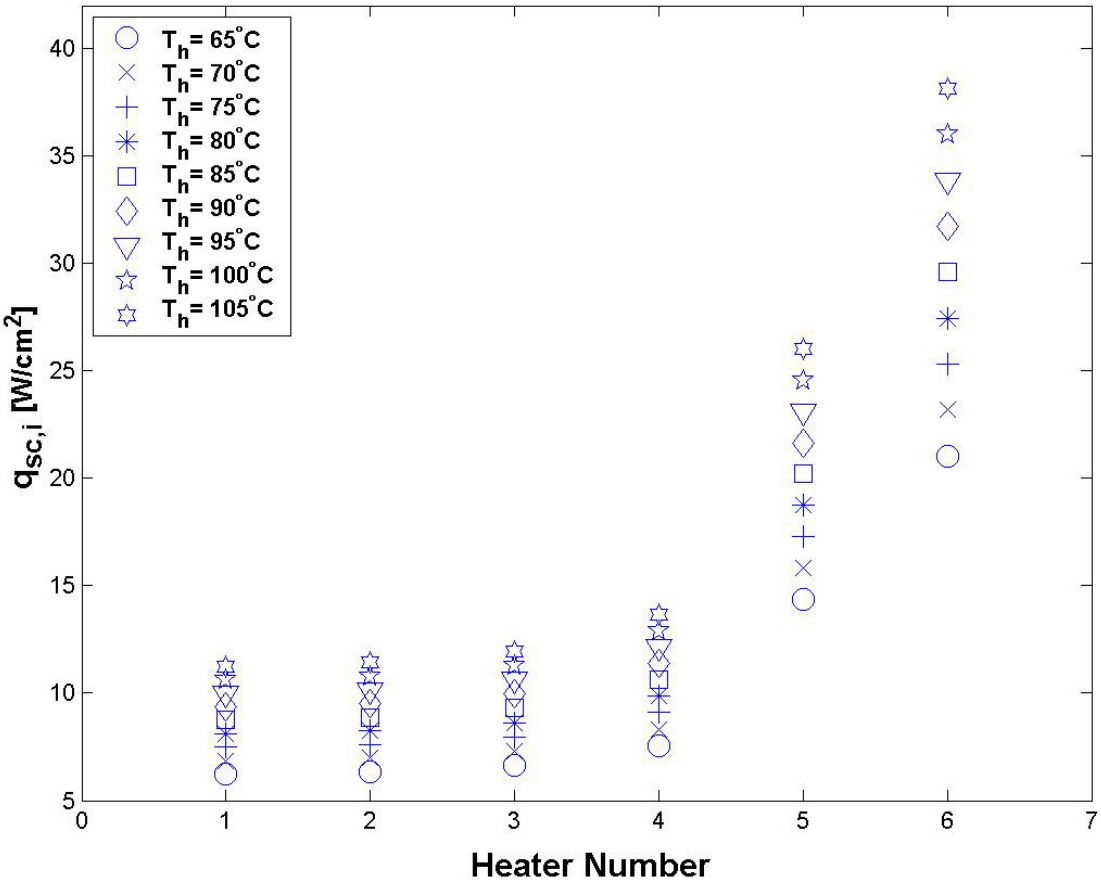

Figure 3.11: Heater temperature effects on substrate conduction (h_b = 10 W/m^{2}K, T_{bulk} = 55°C).

jet cooling on the backside of the array. A summary of the numerical results can be found in Table 3.1.

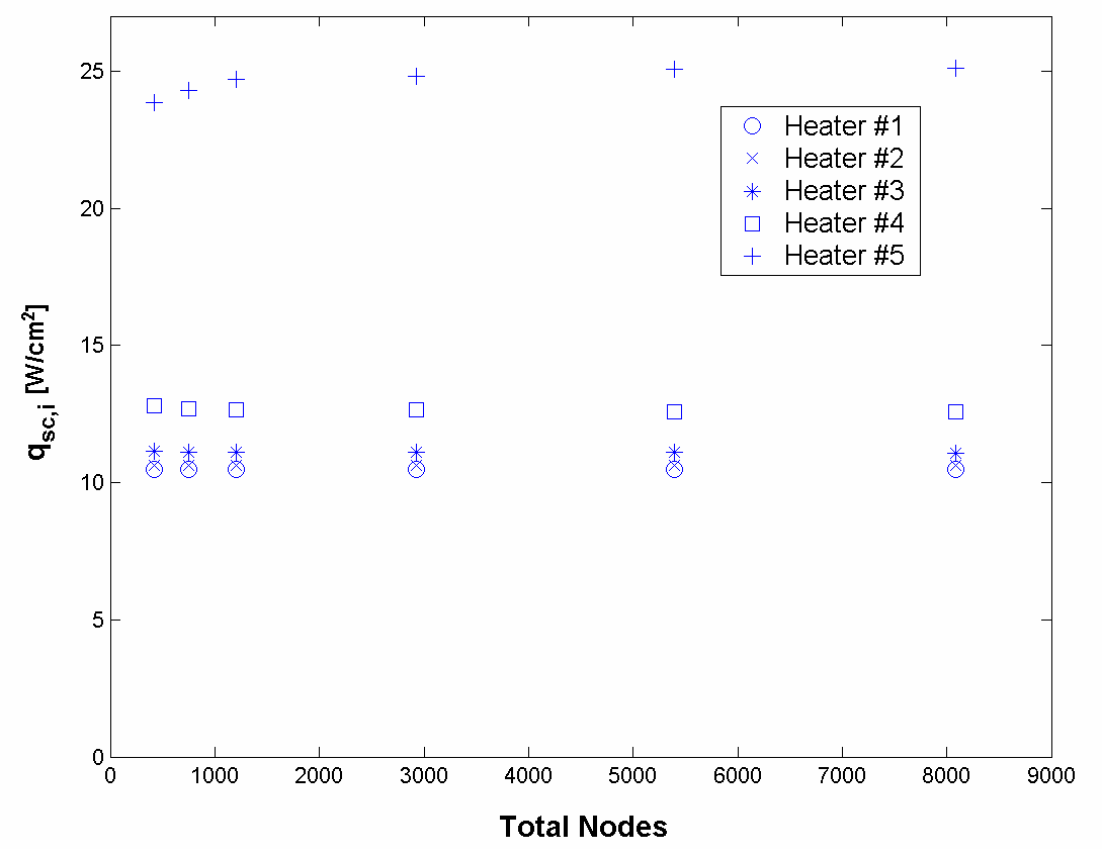

Figure 3.12: 2-D grid size effect on numerically calculated substrate conduction heat flux (h_b = 10 W/m^{2}K, T_{bulk} = 55°C).

	T_{bulk} = 28 °C, h = 10 W/m^{2}K						T_{bulk} = 55 °C, h = 10 W/m^{2}K					
T_h [°C]	**heat. 1**	**heat. 2**	**heat. 3**	**heat. 4**	**heat. 5**	**heat. 6**	**heat. 1**	**heat. 2**	**heat. 3**	**heat. 4**	**heat. 5**	**heat. 6**
65	6.16	6.25	6.53	7.43	14.57	20.93	6.16	6.25	6.53	7.43	14.53	21.04
70	6.78	6.87	7.19	8.18	16.03	23.06	6.78	6.87	7.18	8.17	15.99	23.18
75	7.39	7.50	7.84	8.92	17.49	25.19	7.39	7.50	7.84	8.91	17.45	25.32
80	8.01	8.12	8.49	9.66	18.95	27.32	8.01	8.12	8.49	9.66	18.91	27.46
85	8.62	8.75	9.15	10.41	20.41	29.44	8.62	8.75	9.14	10.40	20.37	29.59
90	9.24	9.37	9.80	11.15	21.87	31.57	9.24	9.37	9.80	11.14	21.83	31.73
95	9.86	10.00	10.45	11.89	23.32	33.70	9.86	10.00	10.45	11.89	23.29	33.87
100	10.47	10.62	11.11	12.64	24.78	35.83	10.47	10.62	11.10	12.63	24.75	36.01
105	11.09	11.25	11.76	13.38	26.24	37.95	11.09	11.25	11.76	13.37	26.20	38.14

Table 3.1: Numerical substrate conduction results, $q_{sc,i}$ (W/cm^2) (3648 nodes).

As mentioned previously, for $h_b = 10$ W/m^{2}K, T_{bulk} had a negligible effect on $q_{sc,i}$. During the boiling process in low-g, the heat transfer coefficient along this boundary (boundary 5 in Fig. 3.5) can increase at higher wall superheats and bulk subcoolings due to strong thermocapillary convection. From side view images of the boiling process taken in low-g, thermocapillary velocities on the order of 1 cm/s were estimated. This velocity is comparable to other experimental findings which recorded a thermocapillary velocity on the order of 1 mm/s (Raake and Siekmann, 1989). Based on these observations, if turbulent thermocapillary flow over boundary 5 is assumed, a well known parallel flow correlation, given by Eq. 3.12 (Incropera and Dewitt, 2002), provides an estimate of the average heat transfer coefficient over this

$$Nu_b = 0.037\,\mathrm{Re}_b^{4/5}\,\mathrm{Pr}^{1/3} \tag{3.12}$$

surface, $h_b = 60$ W/m^{2}K. In Eq.3.12, Nu_b represents an average Nusselt number over a length of approximately 2.5 mm. Based on numerical calculations for $h_b = 60$ W/m^{2}K on boundary 5, the difference in $q_{sc,i}$ (for all heaters) over a bulk temperature range of 28 – 55 °C is < 1% (see Fig. 3.13). Even if a much larger thermocapillary flow velocity is assumed, such as 10 cm/s, $h_b = 360$ W/m^{2}K and < 9% difference between $q_{sc,i}$ values result. It can therefore be concluded that under the observed experimental conditions, $q_{sc,i}$ does not vary significantly with bulk temperature, Fig. 3.13.

In high-g, strong boiling may cause a significant increase in h_b along boundary 5. During boiling, a vapor mass flux directed away from the heater surface can cause a strong radial inflow of liquid toward the heater from the surroundings. Under these turbulent conditions, h_b would take a maximum value that is well below 500 W/m^{2}K

validating the conclusions made in the previous paragraph that T_{bulk} has a negligible effect on $q_{sc,i}$ for all heaters over the experimental ranges encountered.

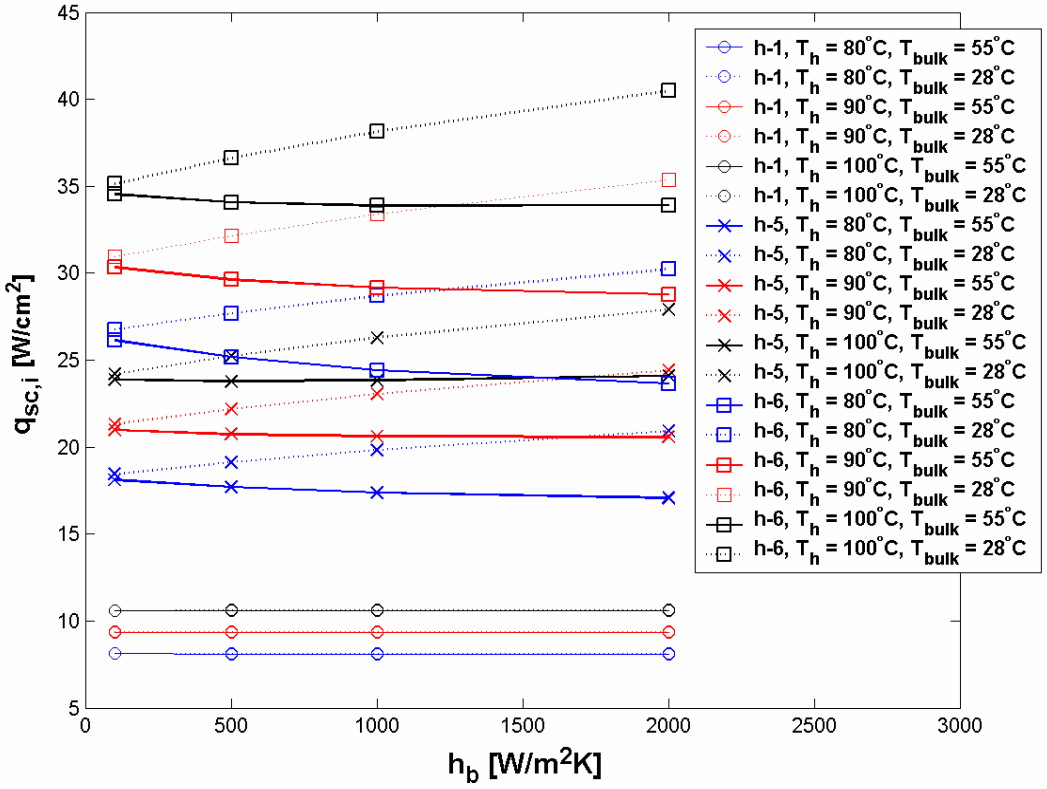

Figure 3.13: Effect of h_b and T_{bulk} on $q_{sc,i}$ for middle (h-1), edge (h-5) and corner (h-6) heaters (96 heater array, 29 x 31 x 29 grid array).

Based on the numerical results presented, the following conclusions can be made about substrate conduction:

1) For middle heaters (> 2 heaters away from boundary), $q_{sc,i}$ is 1-D and not affected by T_{bulk} with excellent agreement between analytical, numerical and experimental results (to be presented).
2) For edge and corner heaters, $q_{sc,i}$ is 2-D and 3-D respectively. When strong thermocapillary motion is present, T_{bulk} appears to have a negligible effect on $q_{sc,i}$ (< 1% over the experimental ranges studied.

3) Substrate conduction from corner and edge heaters can decrease with an increase in h_b for T_{bulk} = 55 °C. This effect is eventually offset by higher heat transfer across the top boundary surface for larger h_b values.

3.3.3 Experimental Results

Three different experimental methods for determining $q_{sc,i}$ were designed and are analyzed below. The first method, method 1, focuses on experimentally locating relatively long time periods during which vapor totally covered a heater (such as occurs when a large bubble causes dryout over a heater in low-g) element and attributing the heat flux at this time to substrate conduction. The heat transfer from the heater through the vapor is very low due to the comparatively low thermal conductivity of FC-72 vapor with quartz ($k_{FC\text{-}72} / k_q < 0.038$). Assuming a vapor thermal conductivity equal to that of the liquid, a vapor layer thickness of 0.5 mm, and a maximum temperature difference equal to the maximum wall superheat tested (47°C), a conservative estimate of q_{vap} = 0.5 W/cm^2 is obtained, Eq 3.13. This value is an order of magnitude smaller than the numerically and analytically calculated substrate conduction values. In addition, radiation heat transfer between the wall and the liquid is also negligible (0.016 W/cm^2). As a result, all heat transferred to the bulk liquid during times when dryout occurred was assumed to be negligible.

$$q'' = k_{FC-72}\frac{dT}{dx} \approx k_{FC-72}\frac{\Delta T}{\Delta x} = 0.5358\ {}^{W}\!/_{cm^2} \tag{3.13}$$

Experimentally determined $q_{sc,i}$ values using method 1 are shown in Fig. 3.14. Higher substrate conduction values are observed near the corner and edge heaters due to the increased area for 2-D and 3-D conduction effects which were confirmed

numerically. At T_{bulk} = 55°C and h_b = 10 W/m^{2}K, there is excellent agreement between numerically and experimentally determined $q_{sc,i}$ values for a 96 heater array (Fig. 3.14 - 3.15).

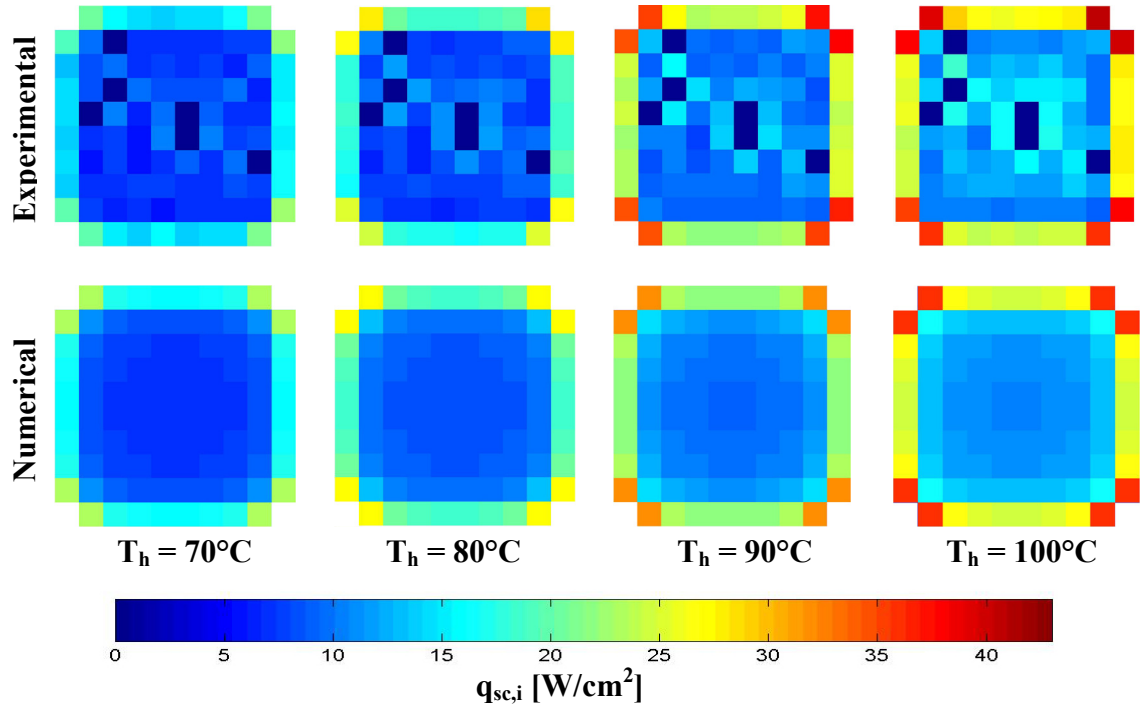

Figure 3.14: Comparison of numerical and experimental (method 1)$q_{sc,i}$ for a 96 heater array (T_{bulk} = 55°C, h_b = 10 W/m^{2}K).

At higher bulk subcoolings (T_{bulk} = 28°C, 35°C, 45°C) the experimental method for determining $q_{sc,i}$ appears to be flawed (Fig. 3.16). For middle and edge heaters at low wall superheats, T_{bulk} appears to have a negligible effect on $q_{sc,i}$ as confirmed by the numerical results mentioned previously. In contrast, at higher wall superheats a strong dependence on T_{bulk} is observed contradicting the numerical results which showed a < 9 % increase in $q_{sc,i}$ from edge heaters at higher bulk subcoolings. Such observations indicate the experimental method (method 1) for determining $q_{sc,i}$ at higher bulk subcoolings is inaccurate. The reason for this can best be explained by Fig. 3.17. At

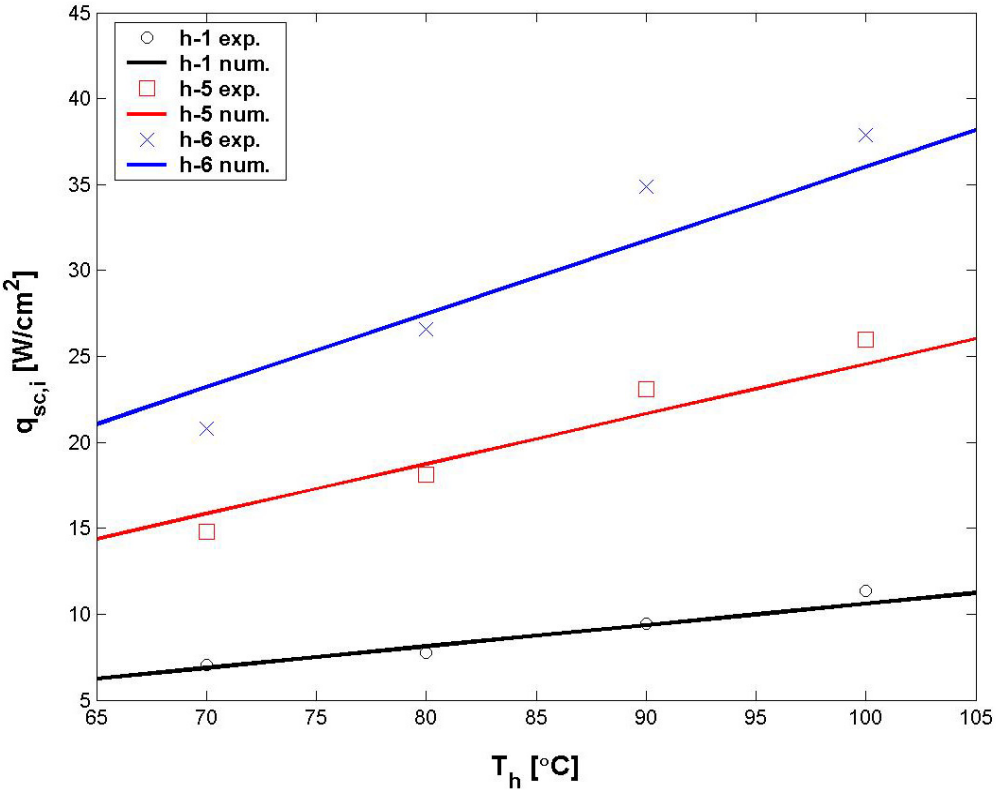

Figure 3.15: Comparison of numerical and experimental (method 1) $q_{sc,i}$ for middle (h-1), edge (h-5), and corner (h-6) heaters (T_{bulk} = 55°C, h_b = 10 W/m^{2}K).

T_{bulk} = 55°C, the primary bubble that forms in low-g causes dryout over most of the heater array. As shown in Fig. 3.17, heaters 1 and 5 are completely covered by vapor throughout the low-g boiling process and therefore the adiabatic assumption used to obtain the experimental $q_{sc,i}$ values is justified. For corner heaters (6 and 7), times do occur when the primary bubble covers most of the heater element (> 90%) and therefore the surface averaged condition for such heaters is also sufficiently adiabatic justifying method 1. For T_{bulk} = 28 °C, heater 1 is also completely covered throughout the low-g boiling process which is why there exists good agreement between experimental and numerical values (Fig. 3.15). At higher wall temperatures, 100°C, strong thermocapillary convection causes the primary bubble to shrink in size allowing bulk liquid rewetting of

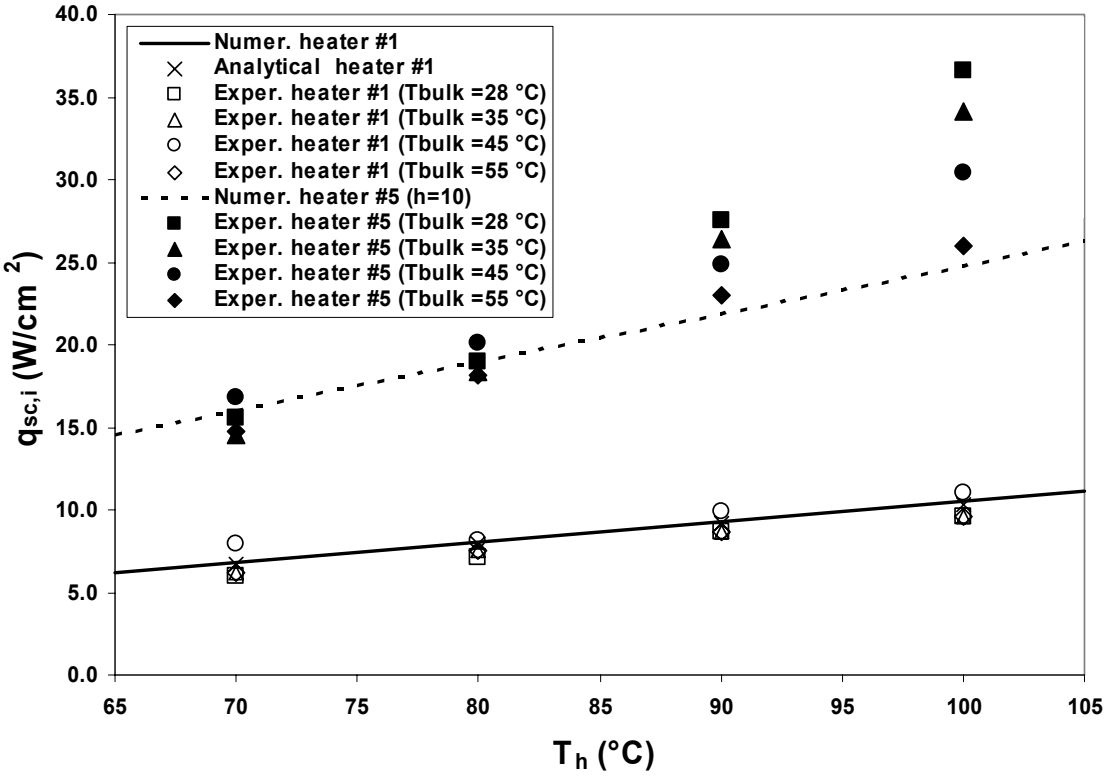

Figure 3.16: Comparison between analytical, numerical, and experimental $q_{sc,i}$ values. Emphasis should be placed on the large deviations between the experimental and numerical values for higher bulk subcoolings.

the edge and corner heaters (heaters 5, 6, 7, Fig. 3.17). The strong thermocapillary motion causes the primary bubble to remain stationary and therefore corner and edge heaters never experience adiabatic conditions above them. As a result, the heat transfer measured during such conditions for these heaters is a combination of boiling heat transfer to the liquid and substrate conduction and unfortunately the magnitude of each is unknown. This results in the large deviations observed in Fig. 3.16. At T_{bulk} = 35°C and 45°C, the primary bubble size is in between these two cases and intermediate deviations are observed.

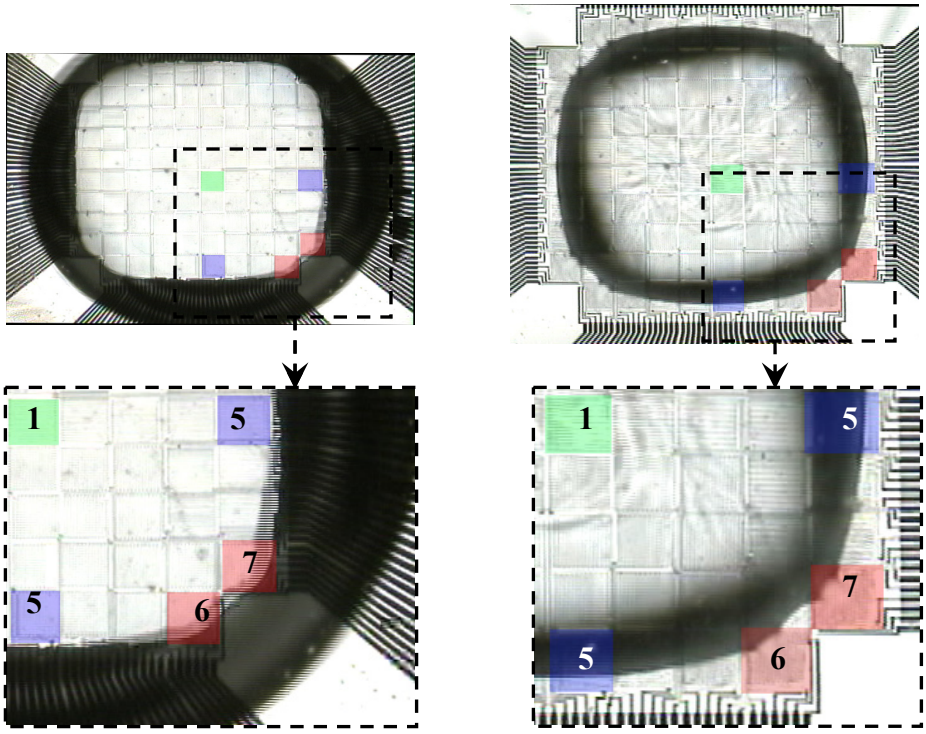

T_{bulk} = 55°C T_{bulk} = 28°C

Figure 3.17: Low-g boiling for extreme subcoolings tested (96 heater array, T_h = 100°C).

Based on these observations a modification to the experimental method for determining $q_{sc,i}$ was made. The new method, method 2 involved using the T_{bulk} = 55°C $q_{sc,i}$ values for edge and corner heaters (obtained using method 1) for all other bulk temperatures. Middle heater $q_{sc,i}$ values were calculated using method 1 for all subcoolings. This method is justified by the numerical results showing little to no effect of bulk temperature on $q_{sc,i}$. The third experimental method, method 3, incorporates a minor variation to method 2 in that all of the $q_{sc,i}$ values obtained for T_{bulk} = 55°C were used as the baselines for the other bulk subcooling cases (for all heaters including interior ones). The three different experimental methods are summarized below:

1) Method 1: $q_{sc,i}$ was calculated from the lowest heat flux measured during low-g

2) Method 2: $q_{sc,i}$ was calculated from the lowest heat flux in low-g for middle heaters and the T_{bulk} = 55°C $q_{sc,i}$ values (obtained using method 1)were used for the corner and edge heaters.
3) Method 3: $q_{sc,i}$ was calculated using T_{bulk} = 55°C (using method 1) experimental baseline for all subcoolings.

The three methods described above provide a statistical error range for the $q_{sc,i}$ measurement. Method 2 most accurately calculates the $q_{sc,i}$ experimentally and methods 1 and 3 provided an estimate of the experimental error in method 2. Method 2 provides the most accurate experimental value of substrate conduction because the air jet flow rate was set to be constant throughout a given flight week (regulator setting fixed) and therefore the backside boundary condition remained consistent across various days (subcoolings as mentioned in the experimental test matrix section). Therefore qsc,i should be subcooling independent as identified from the numerical models presented previously.

It should be noted that at very low wall temperatures (T_h = 70°C,75°C) natural convection dominates the heat transfer process and therefore no primary bubble exists allowing $q_{sc,i}$ to be measured. Under such conditions it appears that the experimental method of taking the lowest heat flux value during low-g appears to give good results that agree with correlations for the magnitude of natural convection in high-g. Such results will be presented in the next chapter.

In conclusion, estimating substrate conduction involves two methods and is based on the magnitude of the wall superheat. For low wall superheats, method 1 and method 2 provide almost identical results. For higher wall superheats (with thermocapillary

convection present) method 2 appears to be the most accurate experimental method for determining substrate conduction. A complete listing of the experimental, analytical, and numerical results can be seen in Table 3.2.

Based on the results presented above, the good agreement between analytical, numerical, and experimental data provides an estimate of the uncertainty in the experimentally measured substrate conduction values of ±10% (largest error for a given data point between experimental models). Performing another propagation of uncertainty analyses yields an uncertainty in the heat flux due to boiling of ±11%. The resulting uncertainty in q_i , the heat transfer from a heater to the bulk liquid, is due primarily to uncertainties in $q_{sc,i}$.

3.4 BOILING HEAT FLUX

Boiling heat transfer data was computed from data obtained in high-g and low-g where the heat transfer had reached steady state over an interval of 5s to 10s where the g-levels were within (± 0.05g). Low-g (0.01) time periods were determined from the accelerometer signal and confirmed by the pressure signal. Fig. 3.18 shows the typical gravitational environment with respect to time during one parabola (taken from both the pressure and accelerometer signals). Spatially averaged, time resolved heat transfer data was obtained using the following equation, (Eq. 3.14):

$$q_{total}(t) = \frac{\sum_{i=1}^{n} \left[q_{raw,i}(t) - q_{sc,i} \right] A_i}{\sum_{i=1}^{n} A_i} \tag{3.14}$$

where the subscript *i* denotes the heaters and *n* is the total number of powered heaters. A typical $q_{total}(t)$ is shown in Figure 3.19 and illustrates the variation in heat transfer during

the low-g and high-g environments. The space and time averaged heat flux were obtained using Eq. 3.15:

$$\bar{q}_{total} = \frac{\sum_{j=1}^{T} q_{total}(t)\Delta t}{T_t} \tag{3.15}$$

where Δt is the time between data points and T_t is the total time over which the average is obtained. The Matlab codes used for data reduction are given in Appendix D.

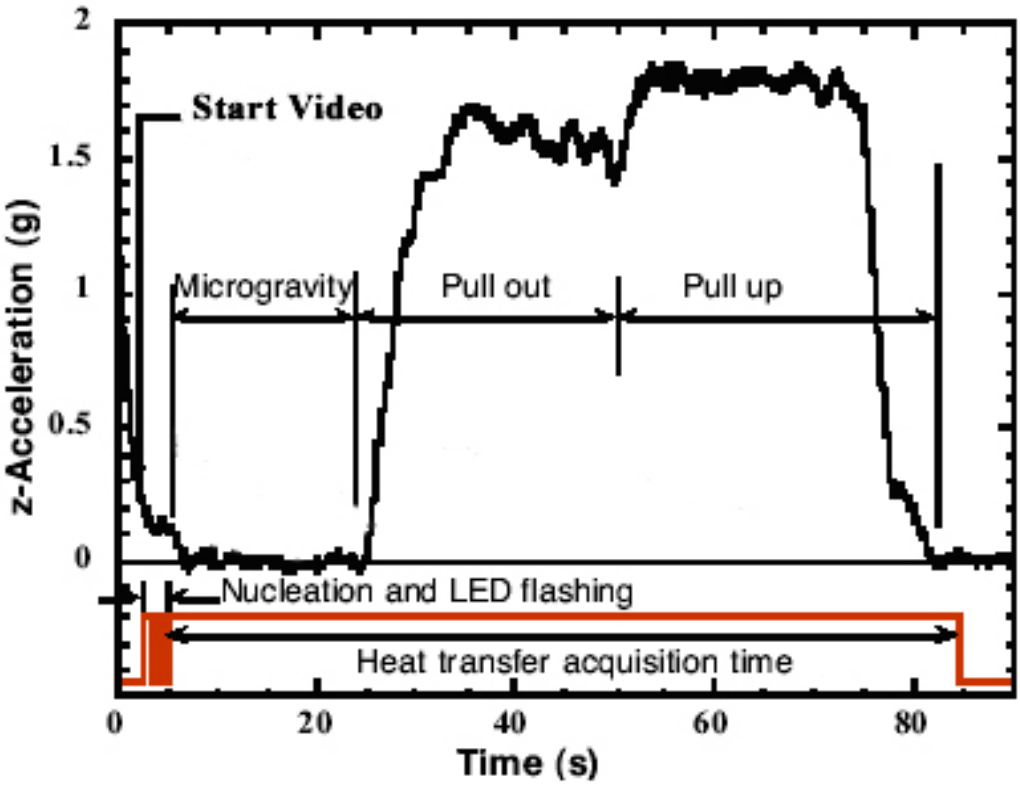

Figure 3.18: Time resolved gravitational environment for 1 parabola aboard the KC-135, (Courtesy of J. Kim).

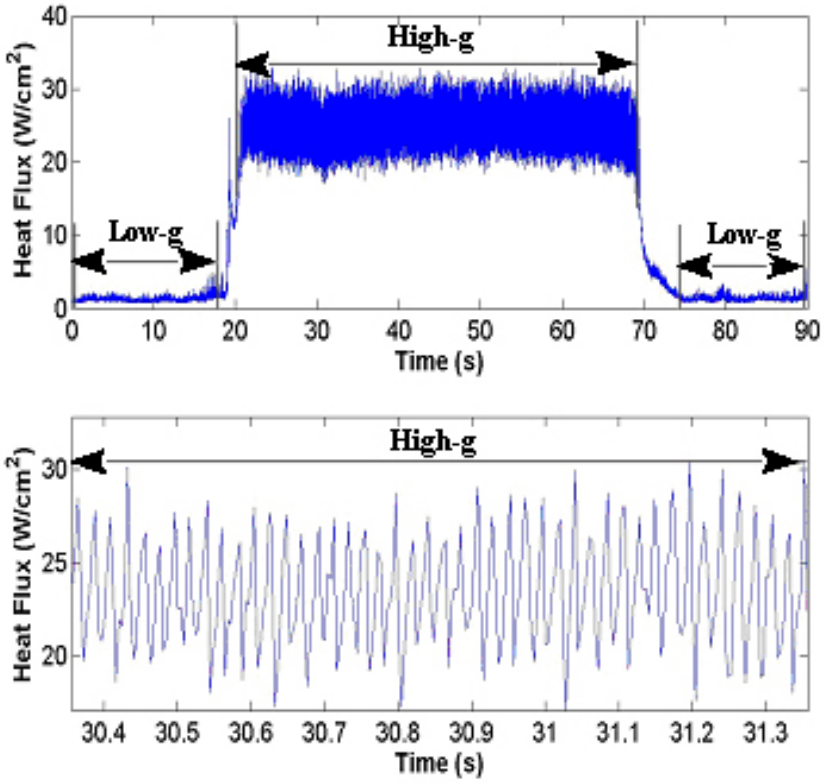

Figure 3.19: Spatially averaged, time resolved heat transfer, 96 heater array, T_{bulk} = 28°C, ΔT_{sat} = 32 °C.

3.5 ADDITIONAL PARAMETERS

Uncertainties associated with the heater wall superheat, ΔT_{sat}, are due to errors in the heater temperature resolution (2 digital potentiometer settings), calibration temperature errors, and errors in the saturation temperature of the fluid which arise from uncertainties in the pressure measurement. Considering the worst case scenario, the saturation temperature of the fluid, T_{sat}, was calculated from a measurement of the time resolved pressure at the heater surface and the saturation curve data for FC-72 (3M Product and Contact Guide, 1995). The pressure transducer was calibrated with an uncertainty of ± 0.01 atm. Incorporating this uncertainty into the saturation curve data, the resulting uncertainty in the time resolved saturation temperature is ± 0.25°C over the

ranges tested. A propagation of uncertainty analysis of the heater wall temperature yields an error due primarily to the uncertainty in the temperature resolution of the heater of ± 0.80°C. The final uncertainty in the wall superheat is ± 0.84°C.

The thermistor used to measure the fluid temperature and the RTD used to the control the chamber sidewall temperature were calibrated in a constant temperature water bath using a NIST traceable liquid-in-glass thermometer. Although the thermistor measurement represents a local temperature value, it was assumed to be a representative average temperature of the bulk fluid. The micropump adequately dissipated any thermal gradients within the fluid between runs. For a given flight, the bulk temperature reading never varied by more than 2 °C and therefore represents a good measure of the uncertainty in T_{bulk}.

The primary bubble departure frequency in high-g was determined from $q_{total}(t)$. For example, times when a peak in heat transfer occurs in Figure 3.19 (bottom) are thought to correspond to bulk liquid rewetting the heater surface. The number of heat flux peaks per unit time was taken to be the average rewetting frequency. For frequencies well below the video framing rate (29.97 Hz), the rewetting frequency as computed in this manner agreed exactly with the average primary bubble departure frequency obtained from the video. Therefore uncertainties in the frequency measurement are on the order of ± 1 %. Table 3.2 summarizes the uncertainties in the experimental variables.

Variable	Uncertainty (2s)
q_{total} [W/cm^2]	± 2 W/cm^2
$q_{w,i}$ [W]	± 0.46 %
$q_{sc,i}$ [W/cm^2]	± 1.7 W/cm^2
$q_{raw,i}$ [W/cm^2]	± 5.02 %
f [Hz]	± 1 %
T_h [^{o}C]	± 0.80 °C
T_{bulk} [^{o}C]	± 2.0 °C
T_{sat} [^{o}C]	± 0.25 °C
ΔT_{sat} [^{o}C]	± 0.84 °C
ΔT_{sub} [^{o}C]	± 2.02 °C
A_i [cm^2]	± 5.0 %
V_i [volts]	± 0.11 %
R_i [Ω]	± 0.4 %

Table 3.2: Summary of experimental uncertainties

Chapter 4: Experimental High-g Boiling Results

4.1 INTRO

The experimental results of the fractional factorial experimental investigation described in the previous chapter are presented in the chapter. Both qualitative and quantitative descriptions of the boiling behavior under the various conditions investigated are considered. A discussion of boiling in a high-g environment is first discussed and the relevant physical mechanisms and models are analyzed. This is followed by a brief description of the gravitational effects on the bubble shape and primary bubble departure frequency. Such findings provide insight into the complexities of the low-g boiling environment which constitutes the majority of the discussion mentioned thereafter. To this end, detailed experimental, analytical, and numerical results are presented and analyzed.

4.2 BOILING FROM SQUARE HEATERS

4.2.1 7 x 7 mm^2, 96 Heater Array

High-g boiling curves for a 7x7 mm^2 heater array are shown in Fig. 4.1. At low wall superheats, the heat and mass transfer process is dominated by natural convection. In this regime, the measured heat transfer is in good agreement with predictions of natural convection heat transfer from the upper surface of a horizontal heater plate, Eq 4.1 (McAdams, 1954). At higher wall superheats, the boiling dynamics are dominated by the ebullition cycle. As described in the introduction, this cycle is characterized by rapid

$$\overline{Nu}_L = 0.54 Ra_L^{1/4} \qquad \left(10^4 \le Ra_L \le 10^7\right) \tag{4.1}$$

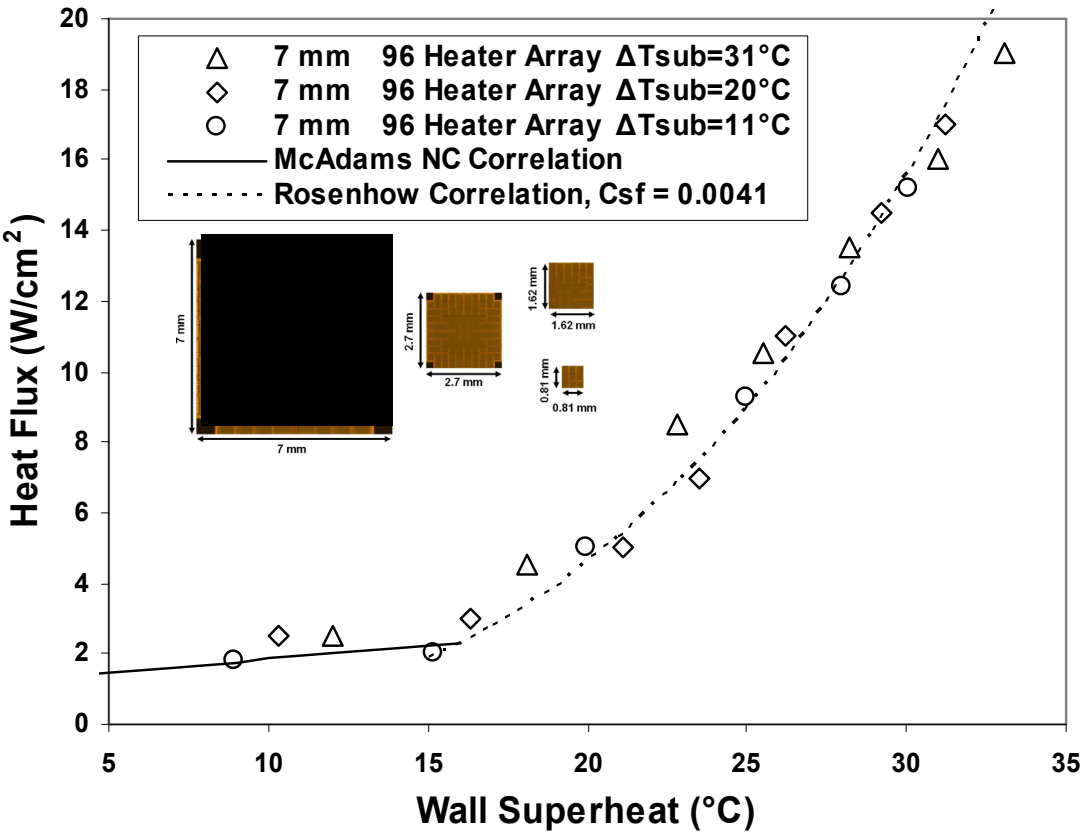

Figure 4.1: High-g boiling curves for a 7 x 7 mm^2 heater array.

bubble growth, departure, and coalescence that tend to occur in a periodic fashion. This transport process enhances the heat transfer from the surface as the phenomenon transitions from single phase natural convection to nucleate pool boiling. As expected, the onset of nucleate pool boiling is characterized by a dramatic increase in the boiling curve slope. The measured surface and time averaged nucleate boiling heat flux is in good agreement with the Rosenhow correlation, Eq. 4.2, $C_{sf} = 0.0041$ (n-perfluorohexane on quartz heater), Fig. 4.1. In Eq. 4.2, C_{sf} is a constant that is used to fit the data and varies depending on the surface/fluid combination.

$$\frac{q''}{\left(T_w - T_{sat}\right)^3} C_{sf}^3 = \frac{\mu c_p^3}{h_{fg}^2 \, \mathrm{Pr}^{3s}} \sqrt{\frac{g\left(\rho_l - \rho_v\right)}{\sigma}} \tag{4.2}$$

Bottom view images of the boiling process in high-g are shown in Fig. 4.2. As seen from these images, the *isolated* bubble departure diameter appears to be approximately the size of an individual heater, 0.7 mm, and is consistent with that observed for the smaller heaters. The *isolated* bubble departure diameter refers to the diameter of a single growing bubble (just after departure) that is not influenced by adjacent bubbles. In practice, an isolated bubble is difficult to create experimentally due to multiple active nucleation sites on the heated surface and therefore the isolated bubble departure diameter is calculated throughout this thesis using a number of models (i.e. Fritz, 1935). The characteristic length scale, assumed to be equal to the heater length, is 7 mm. This value is larger than the isolated bubble departure diameter (0.34 -0.72 mm) calculated from Eq. 4.3-4.5, and is approximately eleven times larger than the capillary length scale, Eq. 1.1.

$$Bo^{1/2} = 0.0208\theta \qquad \text{(Fritz, 1935) (4.3)}$$

$$Bo^{1/2} = \frac{1000}{P_{mmHG}} \qquad \text{(Cole and Shulman, 1966) (4.4)}$$

$$Bo^{1/2} = C(Ja)^{5/4}, \quad Ja = \frac{T_c c_p \rho_l}{\rho_v h_{fg}}, \quad Bo = \frac{g(\rho_l - \rho_v)d_d^2}{\sigma} \qquad \text{(Cole and Rosenhow, 1968) (4.5)}$$

Over the entire range of wall superheats studied, no evidence of Taylor instability was observed. This can be attributed to a number of factors. First, the highest wall superheat investigated may not have reached the required level for the formation of vapor jets that are predicted from Taylor Instability. Second, the heater length scale is sufficiently small so that if vapor jets were to form, the diameter of a single jet plus the spacing between adjacent jets would exceed the characteristic length scale of the array, as shown in Fig. 4.3. A vapor column that forms in high-g has a diameter of approximately

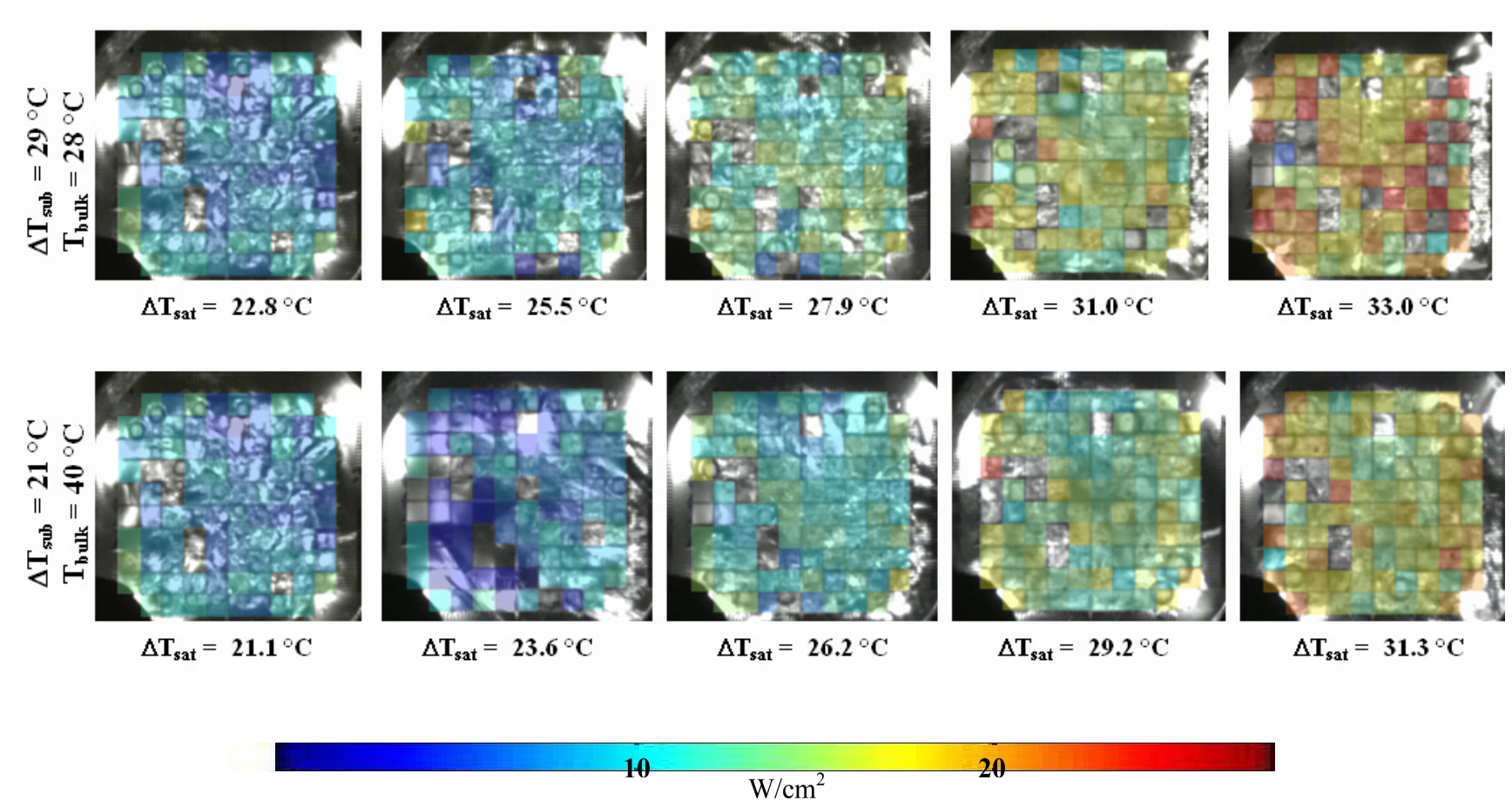

Figure 4.2: 7 x 7 mm^2 array, high-g time averaged spatially resolved heat flux (wall superheat directly below each image and each row corresponds to the bulk subcooling level defined at the far left).

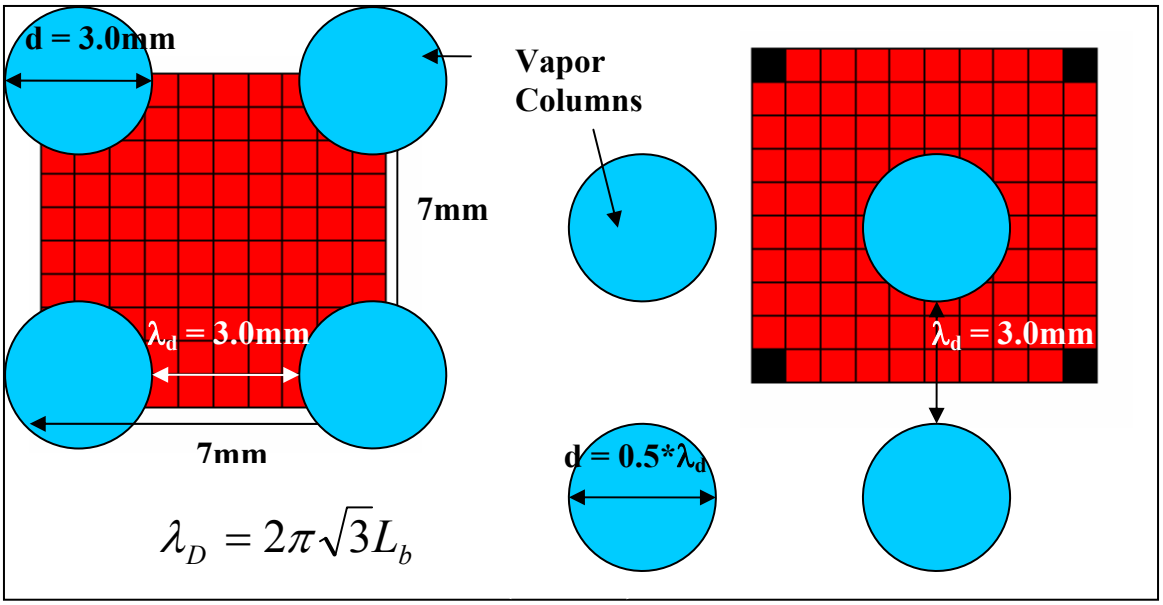

Figure 4.3: Predicted vapor column size and spacing from Taylor instability.

3.26 mm (0.5*λ_d) and a spacing between adjacent jets of 6.5 mm. This indicates that only a single vapor jet would tend to form on the heated surface at higher wall superheats as shown in Fig. 4.3. At the highest wall superheat investigated, ΔT_{sat} = 31 °C, the formation of a single primary bubble began to occur and was measured to be approximately the same size (2.8-3.5 mm) as the vapor jet diameter predicted above, Fig. 4.2. The primary bubble in high-g did not grow to cover the entire array, as was observed for the smaller heater arrays. As will be discussed later, a single primary bubble was observed above the heated surface at higher wall superheats for smaller heaters. If the heater size is smaller than a vapor column diameter predicted from Taylor instability, the boiling characteristics are qualitatively different than if the heater size is much larger than this length scale. For the cases where the heater size is smaller than the predicted vapor jet diameter (all heaters except the 7 x 7 mm^2), a single primary bubble the size of the heater is observed at high wall superheats. Lastly, a distinction should be made regarding *primary bubbles* and *individual bubbles*. Firstly, the primary bubble forms due

to bubble coalescence that results in a bubble that is much larger in size than individual bubbles. Individual bubbles tend to feed the primary bubble and are significantly smaller.

4.2.2 2.7 x 2.7 mm^2, 96 Heater Array

High-g boiling curves for a 2.7 x 2.7 mm^2 heater array are shown in Fig. 4.4. As in the larger heater case, at low wall superheats the process is dominated by natural convection and in agreement with correlation predictions. At higher wall superheats, the boiling behavior is similar to that observed during nucleate boiling at normal gravity

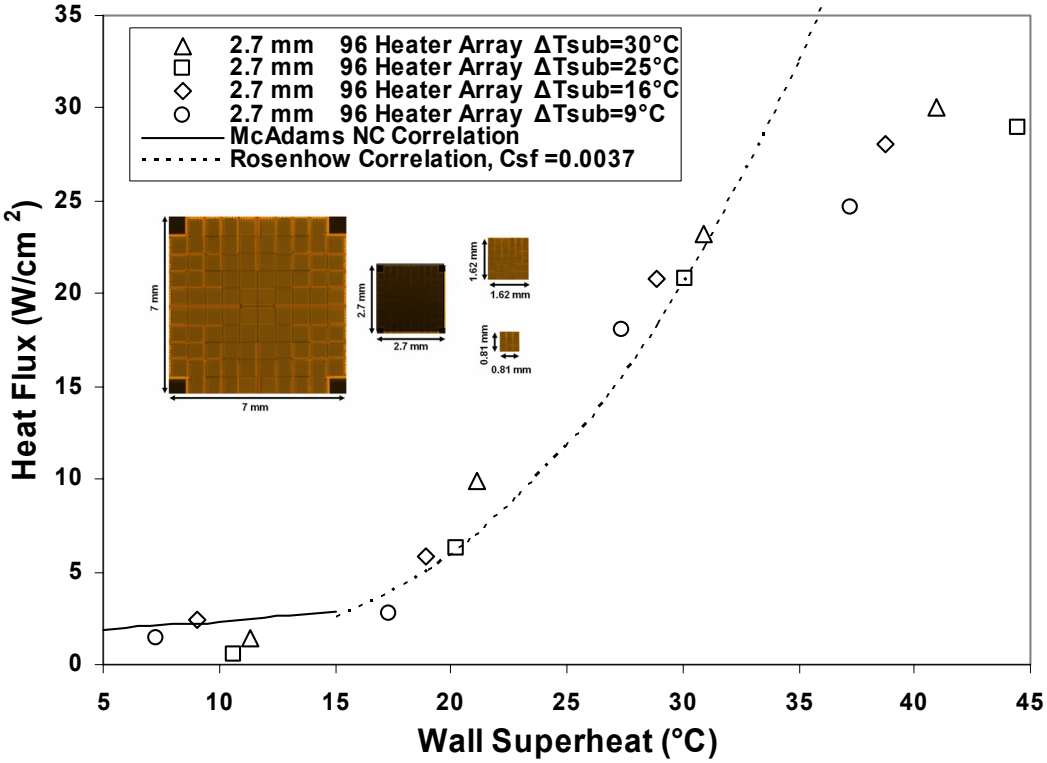

Figure 4.4: High-g boiling curves for a 2.7 x 2.7 mm^2 heater array.

levels. At low wall superheats, boiling activity on the surface is characterized by the formation of multiple bubbles on the heated surface. These bubbles had diameters ranging from 0.27 mm to 0.81 mm and were similar in size to those measured for the

larger heater. The bubbles tend to grow, depart, and merge with other bubbles on the surface and the rate of coalescence appears to increase as the wall superheat is increased. The measured heat transfer was found to be independent of bulk liquid subcooling as predicted from chapter 1. The Rosenhow correlation provides a good estimation of the data up to a wall superheat of approximately 30°C. Bottom view images of the boiling process over the whole range of superheats and subcoolings are shown in Fig. 4.5.

The Rosenhow correlation coefficient, C_{sf}, which quantifies the fluid/surface interaction effects is slightly lower ($C_{sf} = 0.0037$) than that used for the 7 x 7 mm^2 boiling curve fit ($C_{sf} = 0.0041$). There may be two explanations for this. First, in the 7 x 7 mm^2 case, the fluid was 99% n-perfluorohexane that was completely degassed. Data presented for the 2.7 x 2.7 mm^2 array, Fig 4.4, was taken with FC-72 that had a purity slightly higher than 70%. The slight difference in the purity of the fluid may result in different surface fluid interaction. Second, the heater size is slightly smaller than the predicted diameter of a vapor jet (from Taylor theory) and the qualitative differences in the boiling behavior may explain the slight quantitative differences. Taylor instability predicts the formation of a primary bubble in high-g that tends to cover the entire array at higher wall superheats. The ramifications of this are discussed below.

The formation of a single primary bubble is predicted at higher wall superheats and was experimentally validated at a wall superheat of $\Delta T_{sat} \sim 40$ °C, $\Delta T_{sub} \sim 9$°C, Fig. 4.6. The observed size of the primary bubble is in good agreement with the Taylor instability prediction of a vapor column diameter of approximately 3 mm, slightly larger than the array (Fig. 4.6a). For $\Delta T_{sub} = 31$°C and $\Delta T_{sub} = 25$°C, the primary bubble that formed at the highest wall superheat fractured into four primary bubbles (e.g., Fig. 4.7

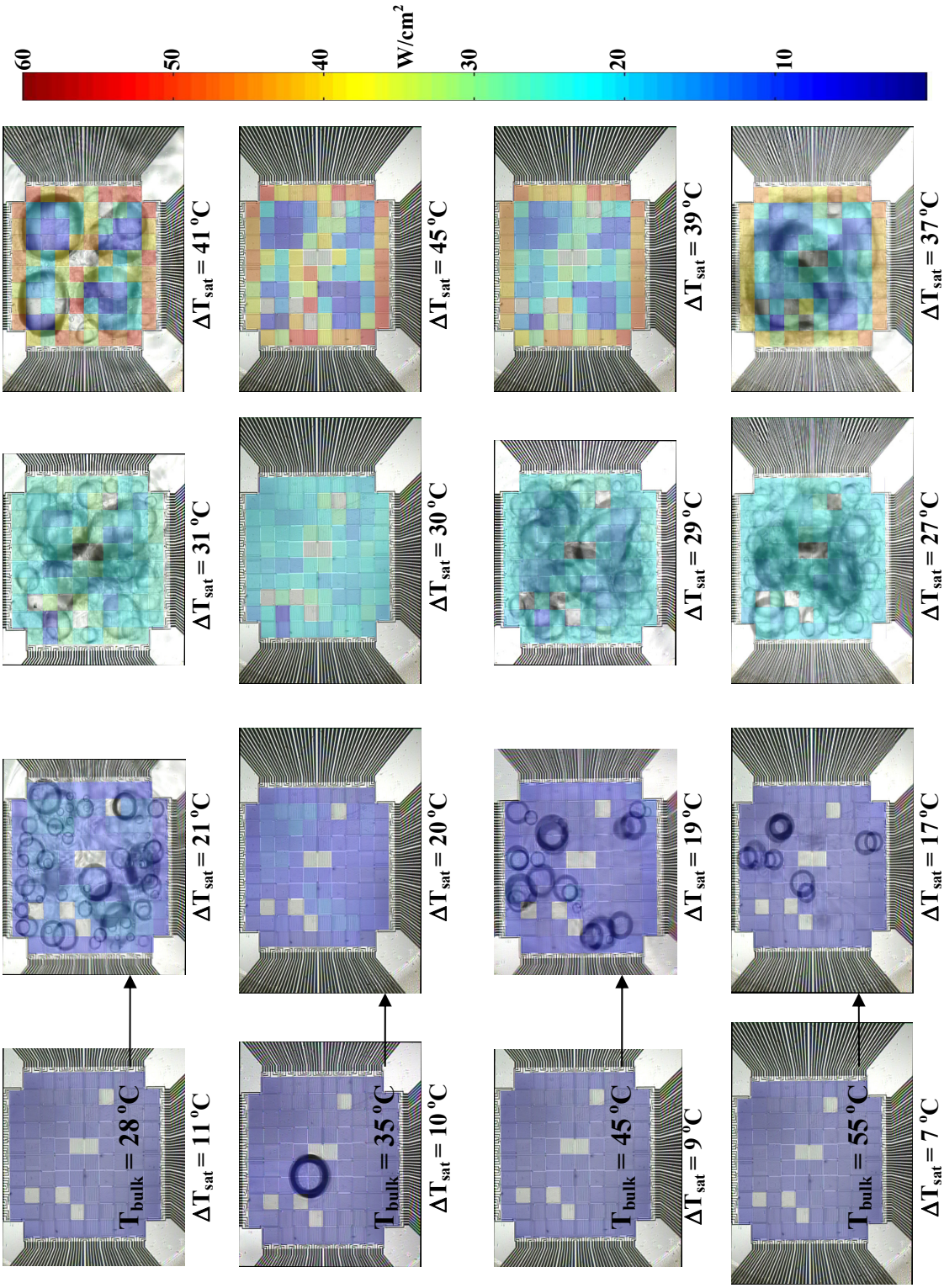

Figure 4.5: Time-averaged, spatially resolved heat flux maps of boiling process for 96 heater array in **high-g** at various ΔT_{sat} and T_{bulk}.

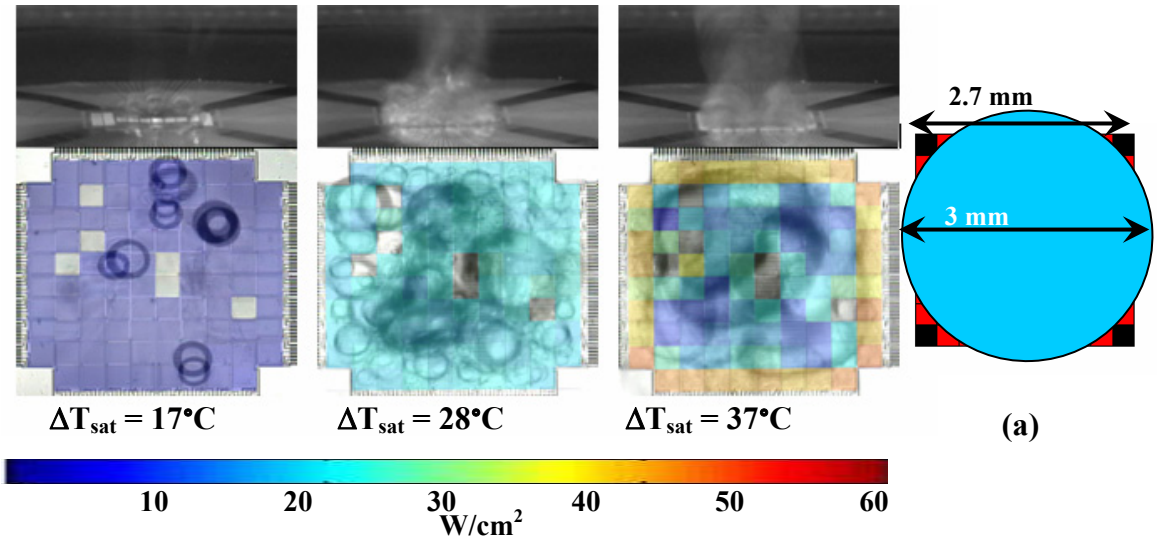

Figure 4.6: bottom and side view images of the boiling process in high-g showing vapor column formation at high wall superheats, ΔT_{sub} = 9°C.

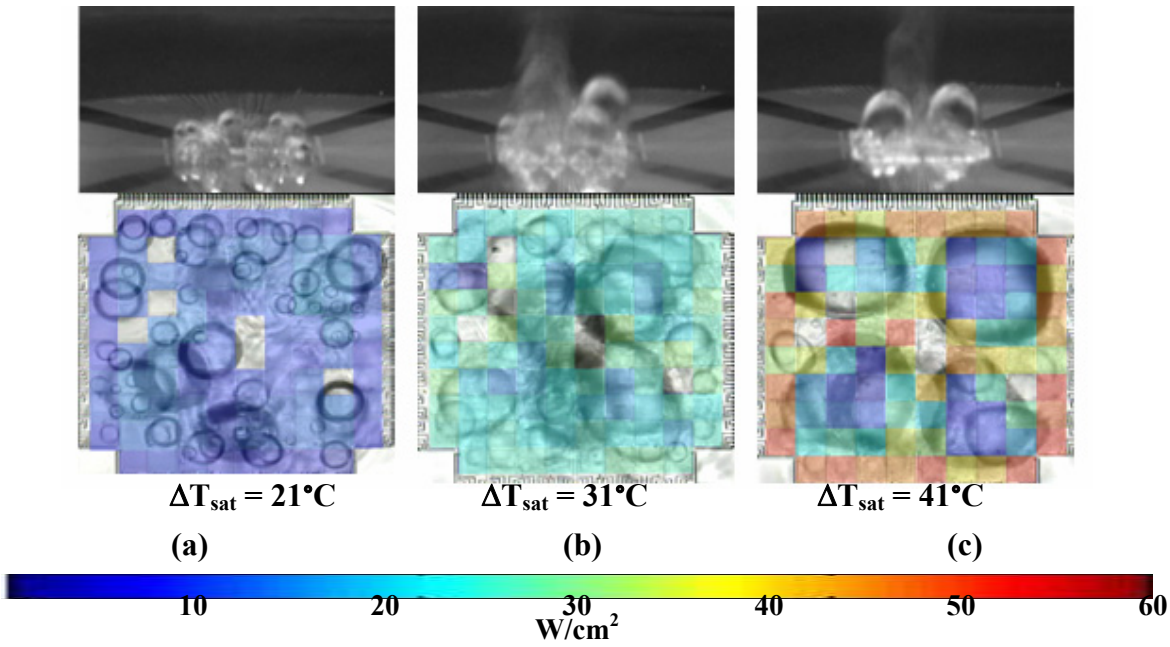

Figure 4.7: bottom and side view images of the boiling process in high-g showing the formation of 4 primary bubbles at high wall superheats, ΔT_{sub} = 31°C.

(c), ΔT_{sat}=41°C). The mechanism for fracture is unclear but may be due to the increased level of liquid subcooling which brings cooler liquid closer to the heated surface causing increased condensation from the top of the primary bubble. As the primary bubble gets

smaller, surface tension forces the bubble to fracture into four bubbles. These four bubbles occasionally coalesce and depart the heated surface forming a single vapor jet above the heater array.

At the highest wall superheats, a large time averaged heat transfer was measured from the edge heaters in the array, Fig. 4.8. The measured heat flux also deviates significantly from the Rosenhow correlation prediction. The trends in the boiling curve data as well as the time resolved boiling heat flux indicate that the boiling activity is close to CHF. It is clear from Fig. 4.8 that dryout of the center of the array occasionally occurs which lowers the time averaged heat transfer. As vapor is generated and departs from the center of the array, a strong rewetting flow from the stagnant fluid medium at the edge heaters replenishes the departing fluid. As the primary bubble departs, the resistance of liquid flow to the center of the array is larger than for the edge region due to the increased rate of vapor formation and coalescence at the center of the array.

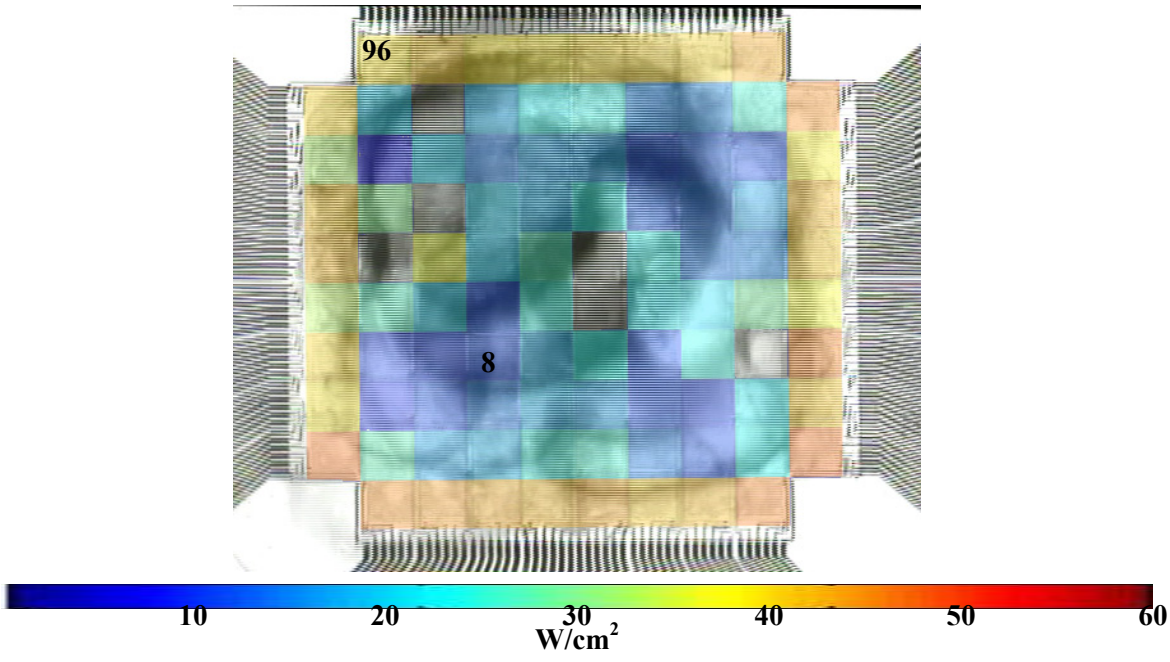

Figure 4.8: Time averaged, spatially resolved heat flux (W/cm^2) from a 2.7 x 2.7 mm^2 heater array in high-g, $\Delta T_{sat} = 37°C$, $\Delta T_{sub} = 9°C$.

The time resolved heat transfer at high wall superheats from an edge heater (Fig. 4.8, heater #96) and center heater (Fig. 4.8, heater #8) is shown in Fig. 4.9. For the interior heater, #8, complete dryout of the heater occurs periodically as indicated by the heat flux curve going to zero. For the corner heater, #96, smaller oscillations about the mean heat transfer were measured and the heat flux was always above 10 W/cm^2 indicating that dryout did not occur. This signal also contains higher frequency signals, indicating faster vapor bubble growth and departure in this region.

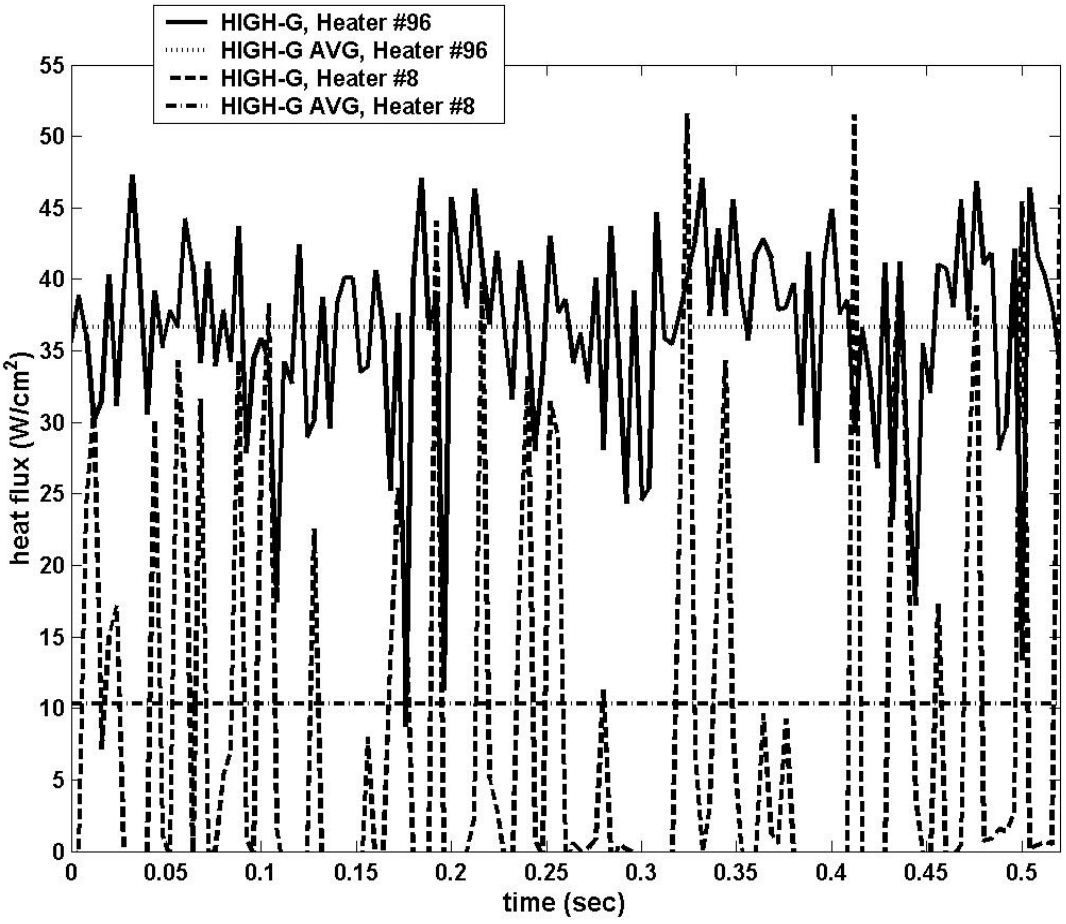

Figure 4.9: Time resolved heat transfer from two heaters in the 2.7 x 2.7 mm^2 heater array in high-g, ΔT_{sat} = 37°C, ΔT_{sub} = 9°C.

Such trends provide information regarding the mechanisms for CHF. Firstly, at low wall superheats, the time averaged heat transfer from the array is evenly distributed

across the heater area, Fig. 4.10. As the wall superheat is increased, dryout of the interior portions of the heater occur due to the increased rate of vapor generation, and as the wall superheat is increased even further, most of the measured heat flux occurs around a small area along the edge of the heater where rewetting liquid has less resistance to flow.

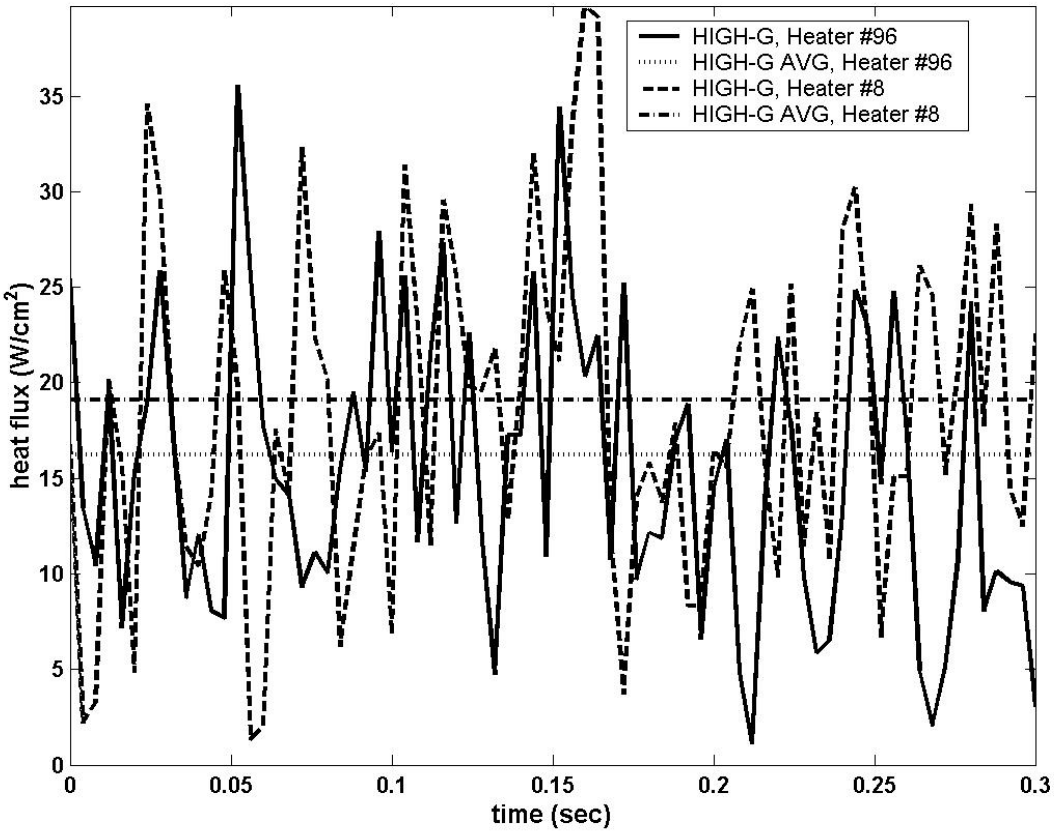

Figure 4.10: Time resolved heat transfer from two heaters in the 2.7 x 2.7 mm^2 heater array in high-g, $\Delta T_{sat} = 27°C$, $\Delta T_{sub} = 9°C$.

The Rosenhow model is not expected to predict the decrease in slope of the boiling curve at higher wall superheats near CHF. More importantly, very little predictive modeling is available from literature regarding CHF for heater sizes smaller than the Taylor wavelength. The Zuber CHF model predicts a CHF value of 16 W/cm^2 which is approximately 50% lower than the measured maximum heat flux, but the Zuber model is based on mechanisms that are proposed for large heaters. Additional

correlations used to predict CHF for finite-sized surfaces have been written in a form given by Eq. 4.6. For an infinite, heated flat plate, the predicted CHF is 18.2 W/cm^2 ($L/L_b > 30$), (Leinhard and Dhir, 1973) which is again significantly smaller than the measured value. This indicates that current CHF models do not account for the boiling performance seen from heaters with $L/L_b < 5$.

$$\frac{q''_{\max}}{q''_{\max,Z}} = f\left(\frac{L}{L_b}\right)$$

$$L_b = \sqrt{\frac{\sigma}{g(\rho_l - \rho_v)}} \qquad (4.6\text{-}4.8)$$

$$q''_{\max,Z} = 0.131\rho_v h_{fg}\left[\frac{\sigma(\rho_l - \rho_v)g}{\rho_v^2}\right]^{1/4}$$

The time and surface averaged heat transfer appears to be larger for the 2.7 x 2.7 mm^2 array than for the 7 x 7 mm^2 array across the entire range of wall superheats. This again may be due to the differences in the purity of the fluid and/or the fact that the heater size is smaller than the Taylor wavelength which can cause edge heat transfer to increase dramatically.

The formation of a single vapor column and single primary bubble was observed at higher wall superheats for the 2.7 x 2.7 mm^2 array. The time averaged edge heat transfer was measured to be dramatically higher from the heater edge (250%) indicating occasional dryout of the center of the array at higher wall superheats. The mechanism for dryout and CHF is clear from Fig. 4.11. As the wall superheat increases, vigorous boiling from the center of the array occasionally creates vapor at a rate greater than can

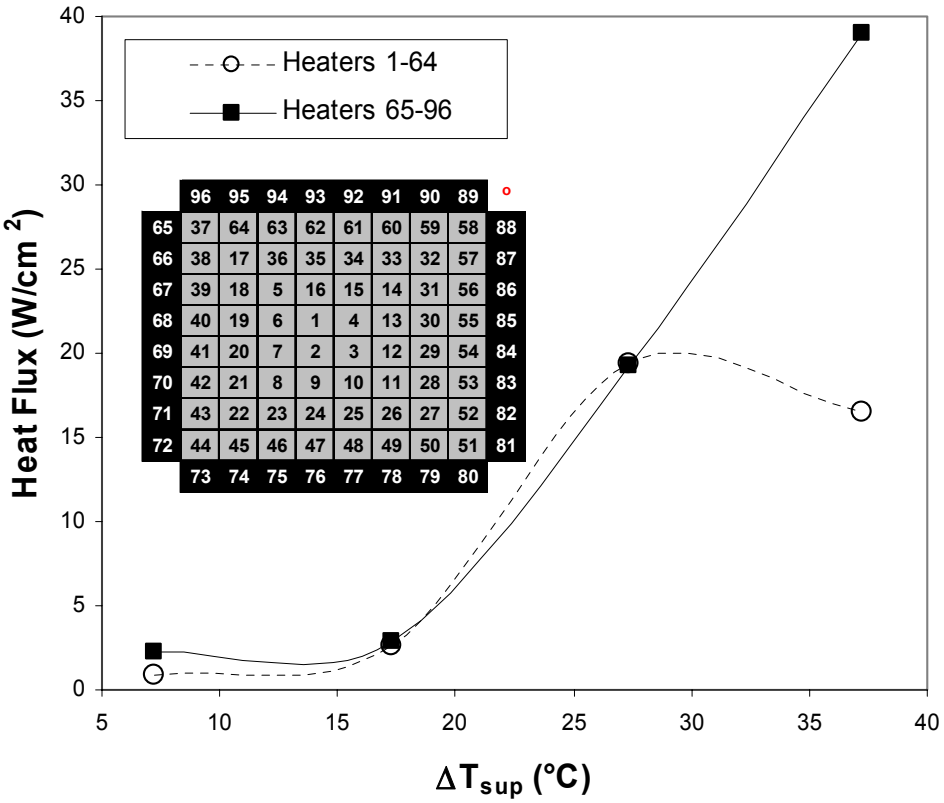

Figure 4.11: High-g surface averaged heat transfer from interior heaters (1-64) and exterior heaters (65-96), ΔT_{sub} = 9°C.

be removed from the surface. This causes occasional dryout of the interior portion of the array reducing the time and surface averaged heat transfer. The rapid formation and departure of vapor causes a stronger liquid flow from the edge of the array which enhances the heat transfer in this region. It is posited that the heat transfer from the edge region (near the edge of the primary bubble) levels off as the wall superheat is increased further and the surface averaged heat transfer from the total array begins to decrease indicating CHF. It is interesting to note that for ΔT_{sat} = 41°C and ΔT_{sub} = 29°C, Fig. 4.7, multiple primary bubbles form and the heat transfer in between bubbles is similar to the heat transfer at the heater edge for ΔT_{sub} = 9°C, Fig. 4.6. Such trends indicate the mechanism for CHF in high-g.

4.2.3 1.62 x 1.62 mm^2, 36 Heater Array

Boiling curves for the 36 heater array are shown in Fig. 4.12. Boiling images over the entire range of conditions investigated are shown in Fig. 4.13. At low wall superheats, the process is again dominated by natural convection and agrees with predictions. Trends similar to the 2.7 x 2.7 mm^2 array boiling curve are observed and the heat transfer was measured to be almost identical over the ranges investigated. See the previous section for an in-depth discussion of the boiling dynamics on the surface.

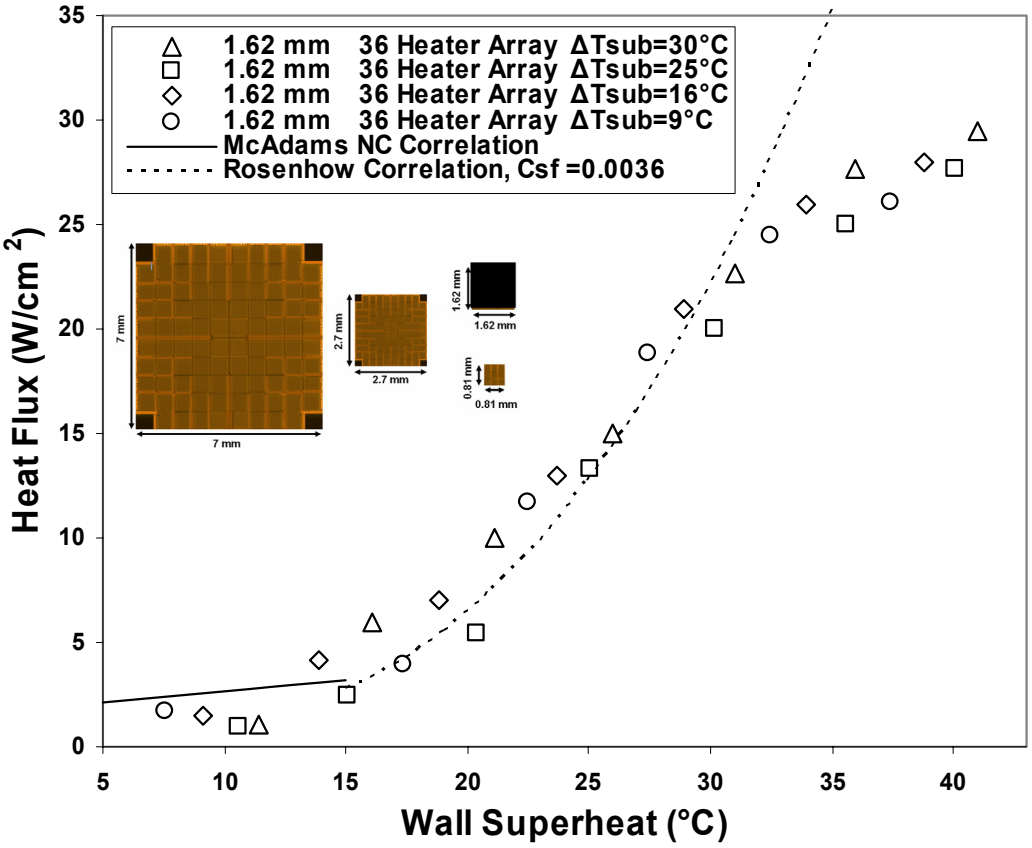

Figure 4.12: High-g boiling curves for a 1.62 x 1.62 mm^2 heater array.

Similar to the larger heater arrays, the formation of a primary bubble occurred at higher wall superheats and this bubble periodically departed the surface allowing the entire heater to be rewetted with liquid. Although the bulk liquid subcooling had a

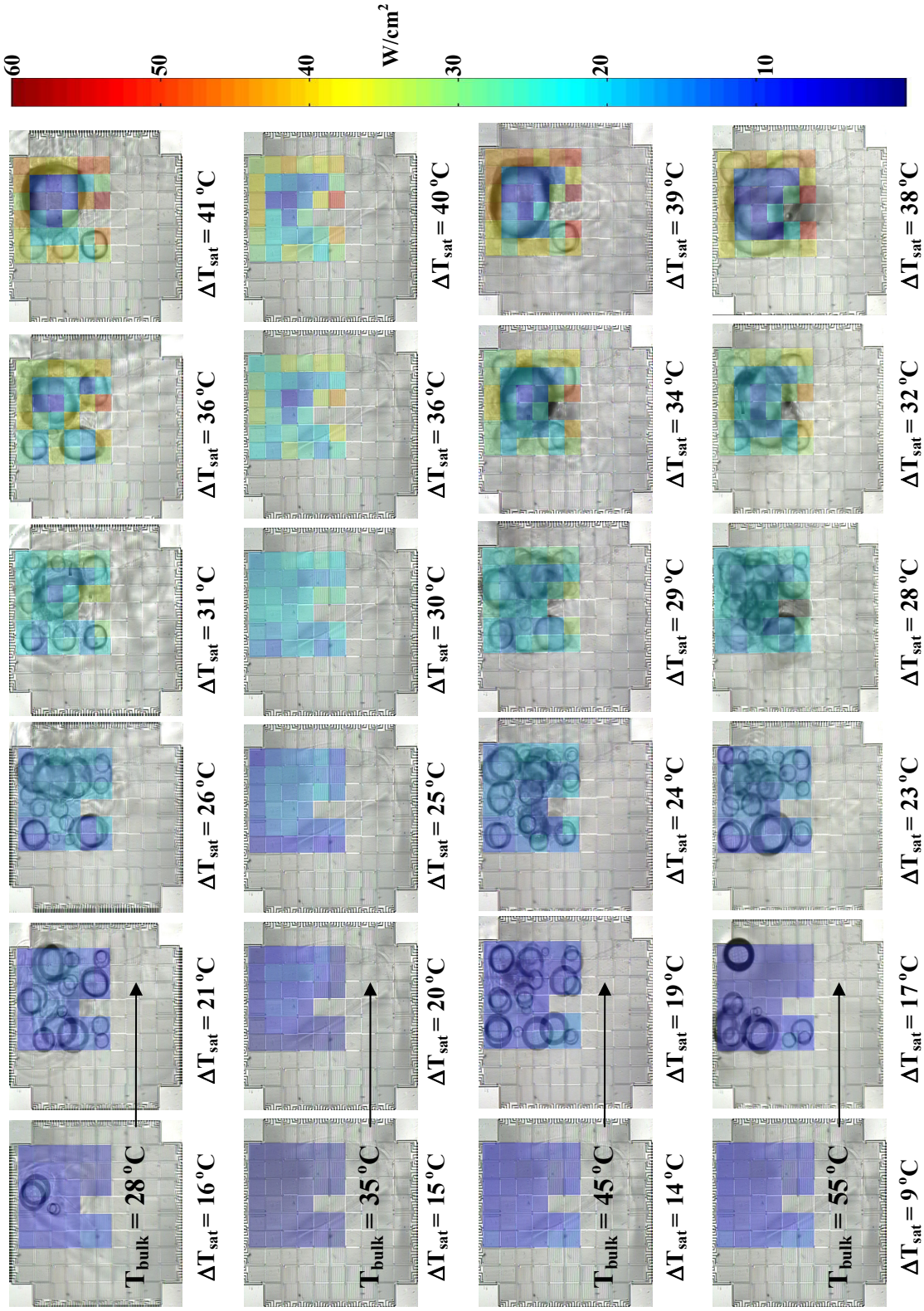

Figure 4.13: Time-averaged, spatially resolved heat flux maps of boiling process for 36 heater array in **high-g** at various ΔT_{sat} and T_{bulk}.

negligible effect on the surface and time averaged heat flux, the size of the primary bubble was measurably smaller for higher subcoolings, as observed for the 96 heater case, Fig 4.13. The formation of a primary bubble is again predicted from Taylor instability theory at higher wall superheats because the heater size is much smaller than $\frac{1}{2}\lambda_d$.

The time resolved heat flux data allowed the primary bubble departure frequency to be measured at higher wall superheats. The departure frequency was determined from $q_{total}(t)$, as discussed in the data reduction section. For cases in which the departure frequency was less than 20 Hz, the measured value was corroborated by the frequency obtained from the side view video images. Although the subcooling level was measured to have a negligible effect on time and space averaged heat flux, increased subcooling was shown to dramatically reduce the departure frequency of the primary bubble as shown on Fig. 4.14. As seen in this figure, the bubble departure frequency increases by over 100% as the bulk subcooling decreases from ΔT_{sub}= 31°C to ΔT_{sub}= 9°C at a superheat of 32°C. An increase in the bulk subcooling increases condensation at the cap of a growing primary bubble, reducing its growth rate. The longer time needed for the bubble to reach departure size results in a decreased departure frequency, decreasing the time-averaged heat transfer. It appears this effect is compensated by a larger heat transfer to the rewetting fluid due to a larger temperature difference between the heater surface and the bulk liquid at higher subcoolings (sensible heating effect). This can be seen from Fig. 4.15 where at low subcoolings, Fig. 4.15a, a higher frequency signal is measured indicating a higher departure frequency. At higher subcoolings, Fig. 4.15b, although the departure frequency is reduced (as indicated from a lower frequency signal), the peaks in

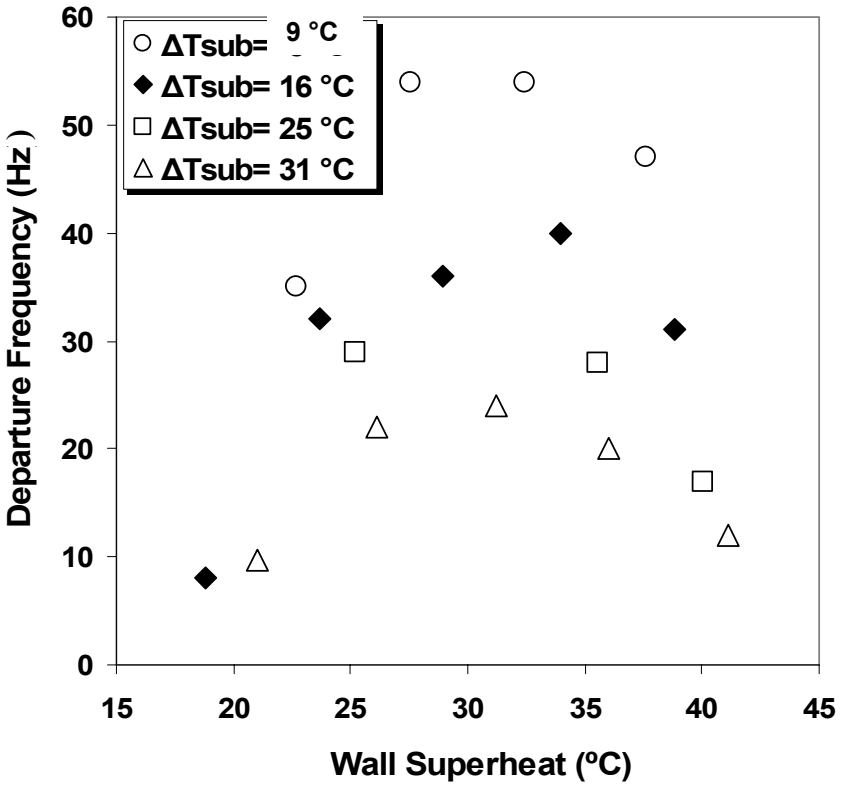

Figure 4.14: Primary bubble departure frequency in high-g for a 36 heater array (1.62 x 1.62 mm^2).

the heat transfer are 20-30% higher and wider compared to the lower subcooling case. If a peak in heat transfer in Fig. 4.15 is associated with a rewetting event (post bubble departure) then there exists a time in which the rewetting liquid will increase to the saturation temperature of the fluid, at which point it is assumed vapor formation occurs which is followed by dryout of the interior heaters and low heat transfer. The total heat required from the heater to bring the rewetting fluid up to the saturation temperature is estimated by Eq. 4.9. Furthermore, if the heat transfer just after primary bubble departure is approximated by a semi-infinite conduction model, the time required to heat the rewetting fluid to the saturation temperature (given by Eq. 4.9) is estimated by Eq. 4.10.

$$q_{sens} = mc_p\left(T_{sat} - T_{rewet}\right) \tag{4.9}$$

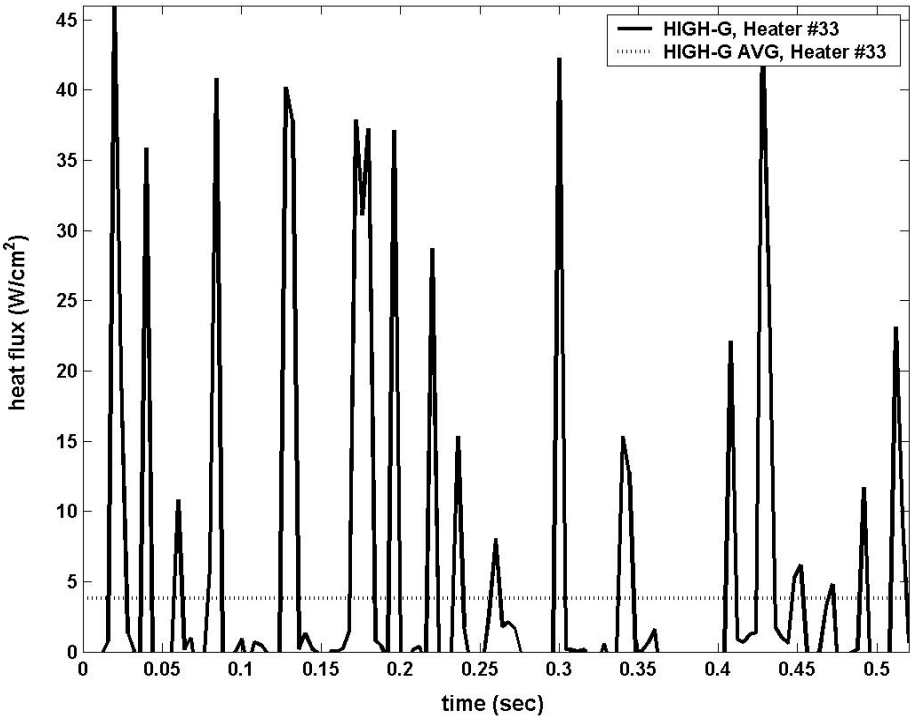

a) $\Delta T_{sub} = 9°C$

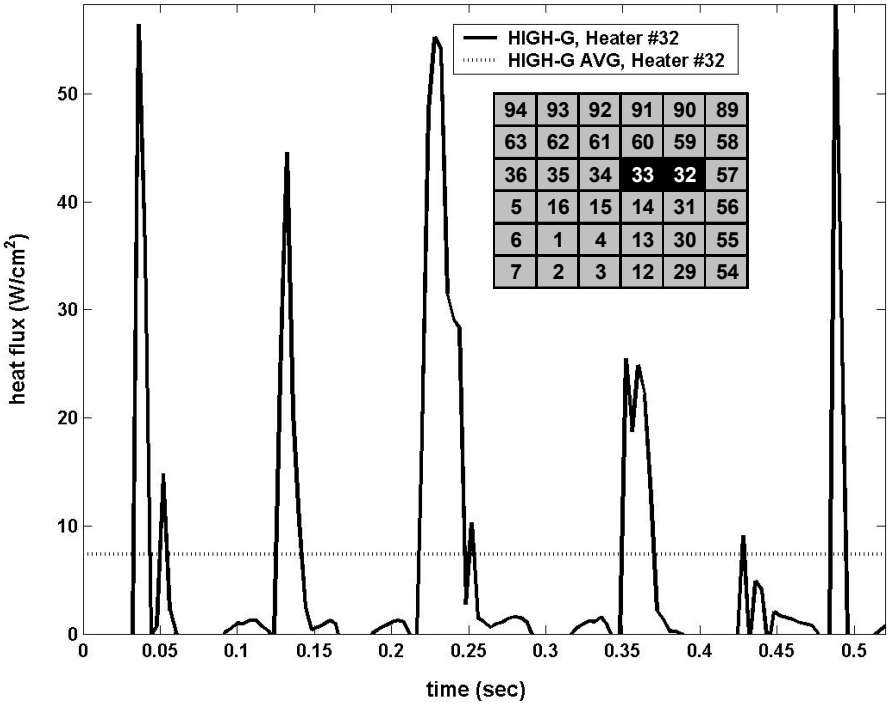

b) $\Delta T_{sub} = 30°C$

Figure 4.15: High-g time resolved heat flux from interior heaters in the 1.62 x 1.62 mm^2 array. $T_{wall} = 100°C$.

$$q_{sens} = \int_0^{t_{sens}} \frac{A_{heat} k_l (T_{wall} - T_{rewet})}{\sqrt{\pi \alpha t}} dt = \frac{2 A_{heat} t_{sens}^{0.5} k_l (T_{wall} - T_{rewet})}{\sqrt{\alpha \pi}}$$

$$t_{sens} = q_{sens}^2 \left[\frac{(2 A_{heat} k_l)(T_{wall} - T_{rewet})}{\sqrt{\pi \alpha}} \right]^{-2} = \frac{\left[mc_p (T_{sat} - T_{rewet}) \right]^2}{\left[\frac{(2 A_{heat} k_l)(T_{wall} - T_{rewet})}{\sqrt{\pi \alpha}} \right]^2} \qquad (4.10)$$

This equation was derived by integrating the semi-infinite conduction heat flux and solving for the time required to sensibly heat the fluid to T_{sat} .

Considering the two cases shown in Fig. 4.15, if the rewetting temperature is estimated to be the bulk liquid temperature and the rewetting liquid mass is assumed the same in both cases, the estimated time required to bring the rewetting fluid up to the saturation temperature (from Eq. 4.10) is 4.5 times longer for ΔT_{sub} = 30°C (Fig. 4.15b) than for the ΔT_{sub} = 9°C case (Fig. 4.15a). From Fig. 4.15 it is observed that the width of the heat flux spike in the ΔT_{sub} = 30°C case is approximately four times that for the ΔT_{sub} = 9°C case. This calculation supports the idea that the measured spike in heat flux may be due to rewetting fluid on the heated surface and the primary mechanism of heat transfer is transient conduction over this short time period. Experimental data taken by Kim and Demiray (2004) also support this idea.

As measured for the 2.7 x 2.7 mm^2 array, the edge and corner heat transfer was measured to be much higher than the center heat transfer at higher wall superheats. This trend again indicates the mechanism for CHF for these heater sizes, Fig. 4.16. First, dryout of the center of the array occurs due to high rate of vapor generation. Second, most of the time and surface averaged heat transfer eventually occurs at the edges of the heater array as the wall superheat is increased. Also note that the primary bubble tends to

break down into multiple primary bubbles as the subcooling is increased, Fig. 4.17. This trend was also observed for the 2.7 x 2.7 mm^2 array and is again attributed to increased condensation at the primary bubble cap as the bulk subcooling level increases reducing the primary bubble size until surface tension acts to pull the bubble apart. Also note as

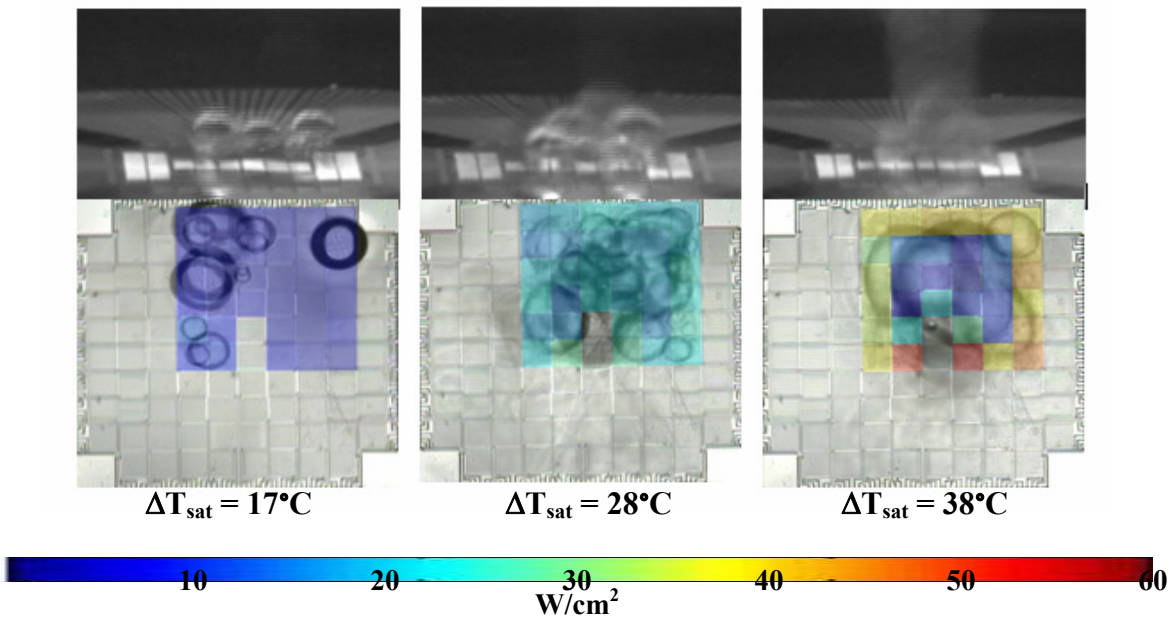

Figure 4.16: Bottom and side view images of a 36 heater array at low subcoolings, ΔT_{sub} = 9°C.

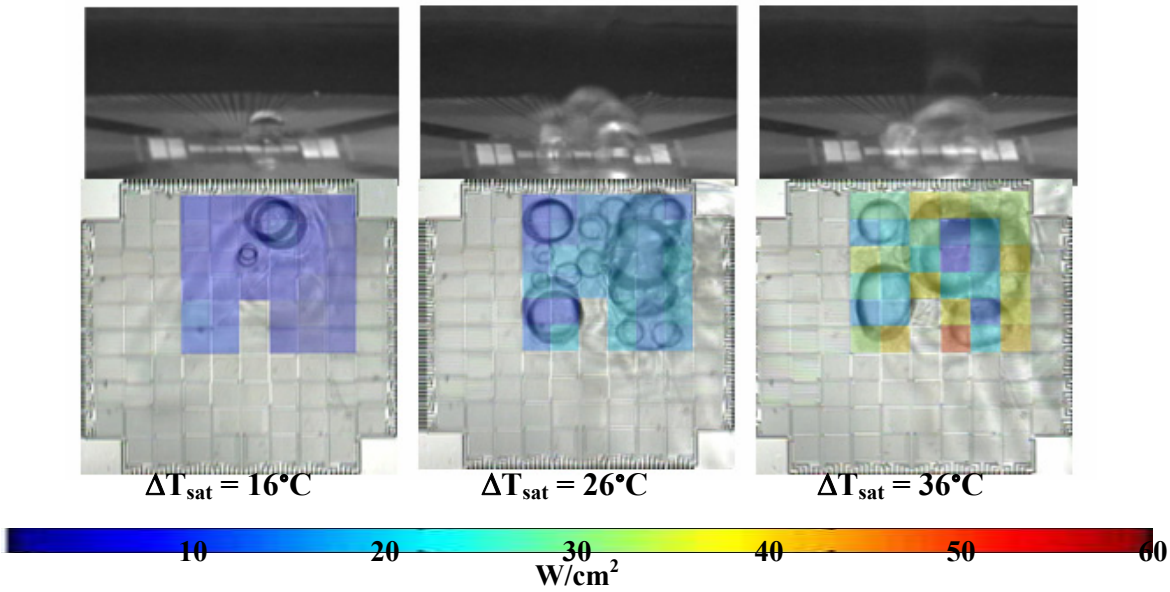

Figure 4.17: Bottom and side view images of a 36 heater array at high subcoolings, ΔTsub = 30°C.

the primary bubble breaks down, interior regions of the array are wetted which can enhance the time averaged heat transfer, Fig. 4.18.

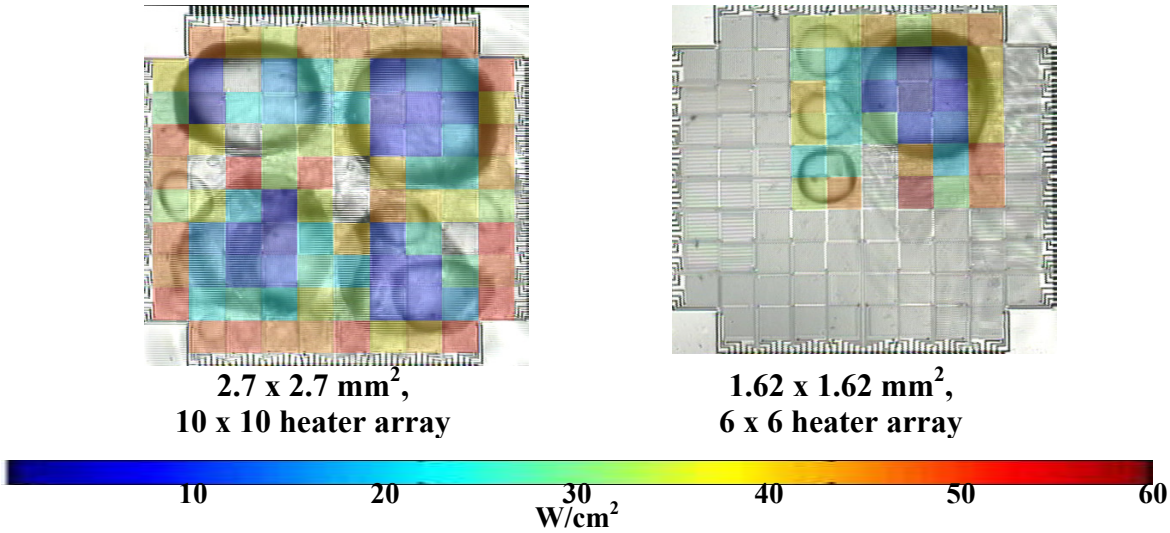

Figure 4.18: High-g time averaged boiling heat transfer at high bulk subcooling, ΔT_{sub} = 30°C and high wall superheat, ΔT_{sat} = 41°C.

Based on the departure frequency shown in Fig. 4.14, an estimate of the amount of heat transfer due to condensation can be obtained if it is assumed that the measured heat transfer is due to a combination of three energy removal modes during the ebullition cycle. These modes include: sensible heating of the rewetting fluid after bubble departure (q_s), latent heat transfer (q_e) from the heater surface which is responsible for the formation of a bubble of mass m_v, and condensation from the bubble (q_c) while the bubble is in contact with the heater surface. For the analysis that follows, these variables were calculated in joules and the heat transfer rate was determined by summing the three modes and then multiplying this value by the measured bubble departure frequency. The three different modes are graphically depicted in Fig. 4.19. As mentioned above, these heat transfer modes occur cyclically with a frequency shown in Fig. 4.14 at various

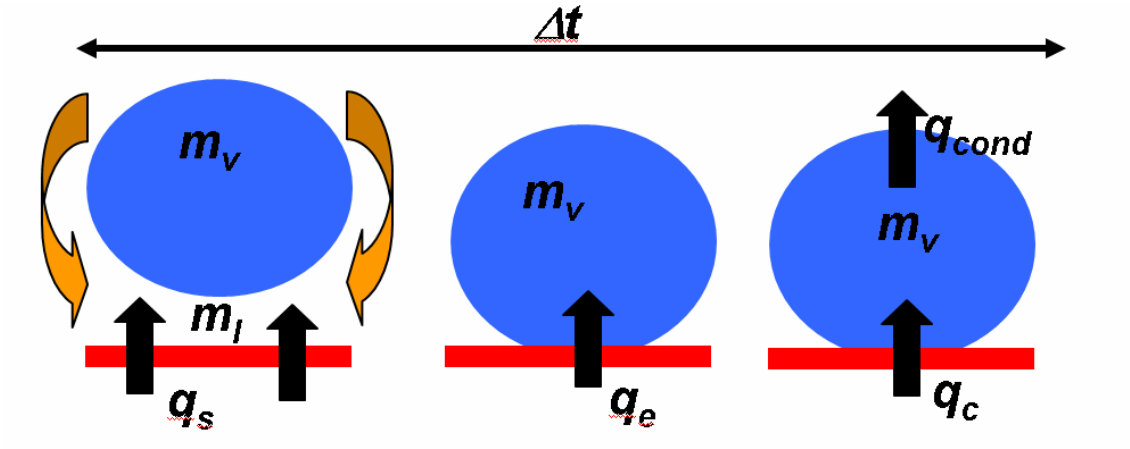

Figure 4.19: Boiling heat transfer modes in high-g.

subcoolings. A complete cycle occurs over time Δt which is equal to the inverse of the measured bubble departure frequency. If these three modes are the only contributors to the measured heat transfer, an estimate of the heat transfer due to condensation can be obtained from Eq. 4.11. In this equation, the total sensible heat transferred to the fluid is

$$q''_{meas} = q_s + q_e + q_c \Rightarrow q_c = q''_{meas} - \frac{\rho_v V_b f\left(c_p \Delta T_{sub} + h_{fg}\right)}{A_{heat}} \qquad (4.11)$$

assumed to be that required to bring the bulk fluid temperature up to the saturation temperature. V_b is the volume of the primary vapor bubble that is generated and *f* is the measured primary bubble departure frequency. V_b was calculated based on the bubble departure diameter measured just after the bubble leaves the heater surface.

As seen in Table 4.1, for pool boiling under nearly saturated bulk conditions, the primary mode of heat transfer is latent heat while for highly subcooled bulk conditions, condensation accounts for the majority of heat transfer from the surface. It should be noted that these results are for cases where a distinct primary bubble forms in high-g. Lastly, existing CHF correlations do not accurately account for the measured peak heat transfer as discussed for the 2.7 x 2.7 mm^2 array.

ΔT_{sub} (°C)	ΔT_{sat} (°C)	q_s (W/cm²)	q_e (W/cm²)	q_{meas} (W/cm²)	q_c (W/cm²)
9	*38*	*2.83*	*24*	*26.1*	*~0*
28	41	2.65	6.5	29.5	20.35

Table 4.1: Condensation heat transfer at two different subcoolings.

4.2.4 0.8 x 0.8 mm^2, 9 Heater Array

Boiling curves for the 9 heater array in high-g are presented in Fig. 4.20. A set of images of boiling from the 0.81 x 0.81 mm^2 array are shown in Fig. 4.21. At low wall superheats, the images show few active nucleation sites and the process is again dominated by natural convection. At higher superheats, the images clearly indicate the formation of a single primary bubble surrounded very occasionally by satellite bubbles, similar to what is observed in low-g for larger heaters. The measured heat transfer at low

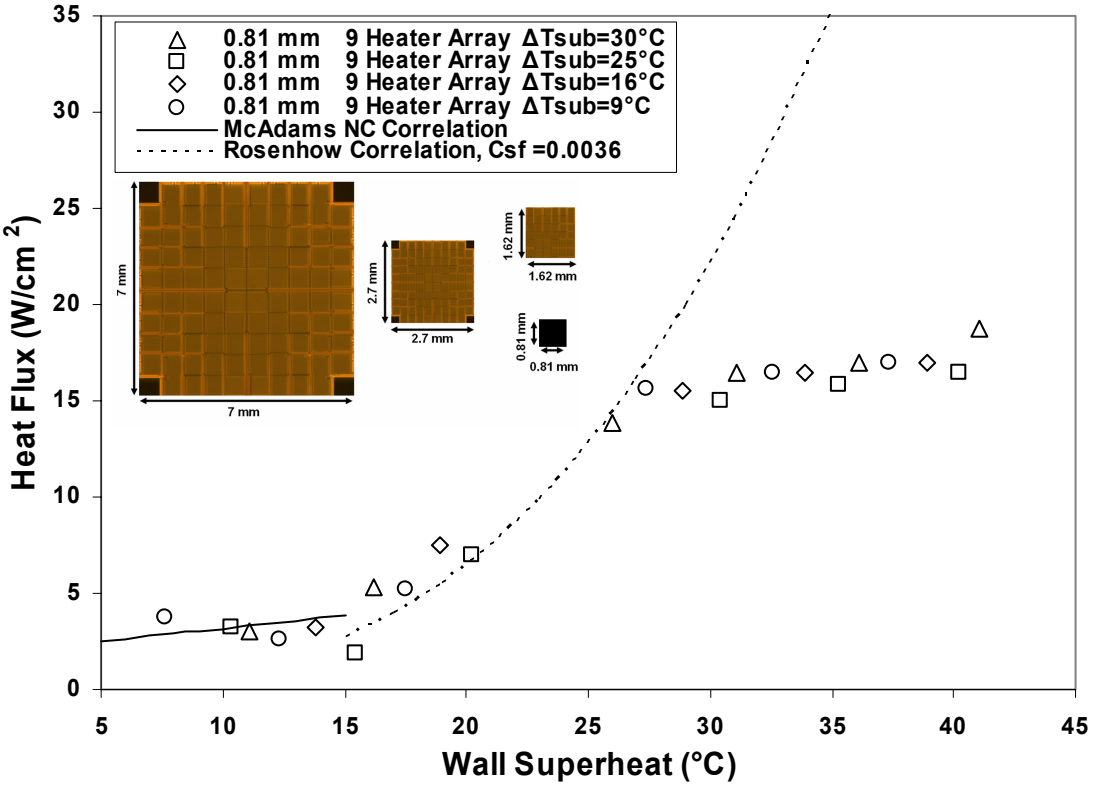

Figure 4.20: High-g boiling curves for a 0.81 x 0.81 mm^2 heater array.

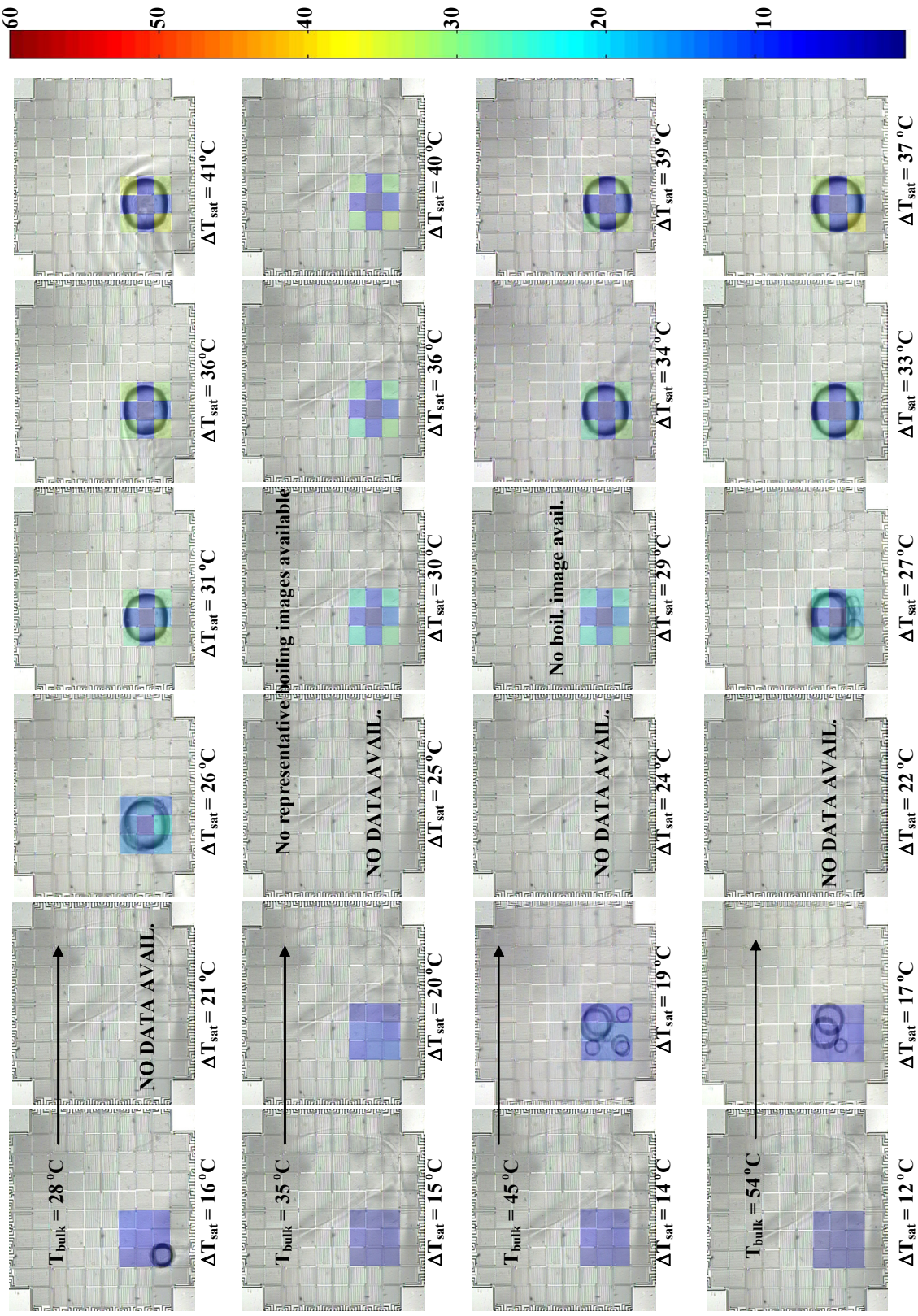

Figure 4.21: Time-averaged, spatially resolved heat flux maps of boiling process or 9 heater array in **high-g** at various ΔT_{sat} and T_{bulk}.

wall superheats agrees fairly well with the Rosenhow correlation but deviates significantly at higher wall superheats $\Delta T_{sat} > 25°C$. Primary bubble departure from the heater surface was not observed except for one case (ΔT_{sat}=37 °C, ΔT_{sub}= 8 °C) in which departure was infrequent (< 1 Hz). Surface tension clearly dominated the boiling dynamics over the superheat and subcooling ranges investigated.

The boiling curves shown in Fig. 4.20 indicate what appear to be two distinct boiling regimes. At low wall superheats, $\Delta T_{sat} < 25°C$, multiple bubbles tend to form on the 3 x 3 heater array and tend to coalesce with a larger primary bubble which dominates the boiling activity, Fig. 4.21 - 4.22. As indicated by the presence of multiple bubbles on the surface, there appears to be few active nucleation sites and vapor appears to be

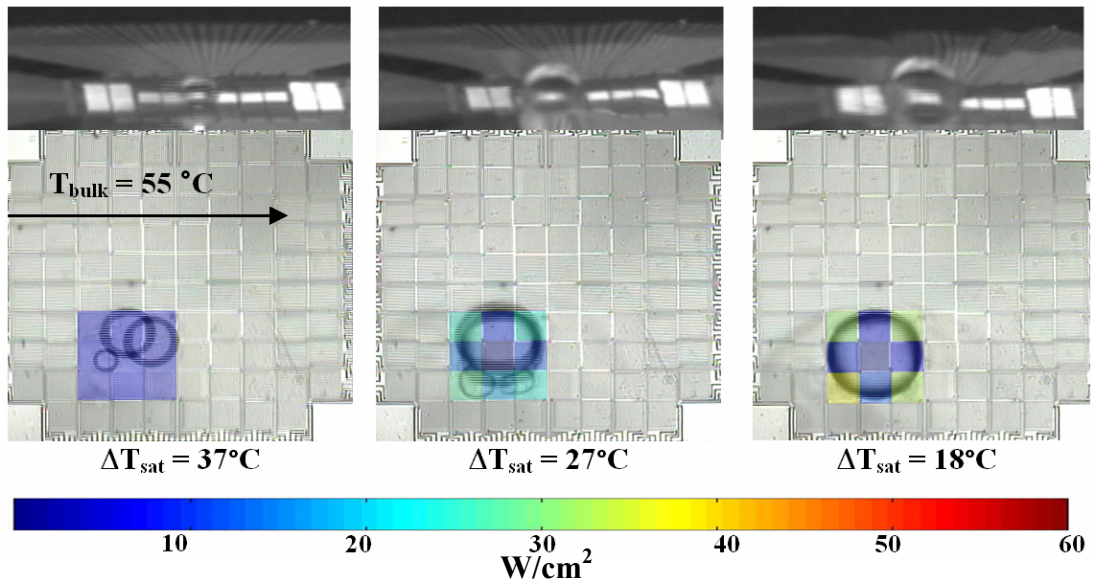

Figure 4.22: High-g boiling images from a 0.81 x 0.81 mm^2 heater array, ΔT_{sub} = 9°C.

generated at a small rate. Heat transfer in this regime appears to be due primarily to the movement of the individual bubbles on the heated surface which tends to enhance local mixing. At higher wall superheats, $\Delta T_{sat} > 25°C$, another boiling regime appears to occur

and is characterized by the formation of a single primary bubble on the heated surface. Coalescence of the satellite bubbles with the primary bubble, surface tension, and increased condensation at the cap of the bubble due to natural convection prevented the primary bubble from reaching the size required for departure. A strong jet was observed above the bubble indicating the presence of natural convection and/or thermocapillary convection which served to regulate the primary bubble size by enhancing condensation at the bubble cap. The condensing vapor flux was balanced by vapor addition from smaller coalescing bubbles at its base. The occasional departure mentioned previously may indicate that the bubble is close to the required isolated bubble departure diameter for the specified operating conditions. At first glance, the primary bubble appeared to be an isolated bubble. Further analysis showed the primary bubble has a number of interesting characteristics. First, it appears to be fed by microscopic bubbles that form around the edge of the array and coalesce with it, Fig. 4.23. Second, it remains relatively stable in both size and position throughout high-g.

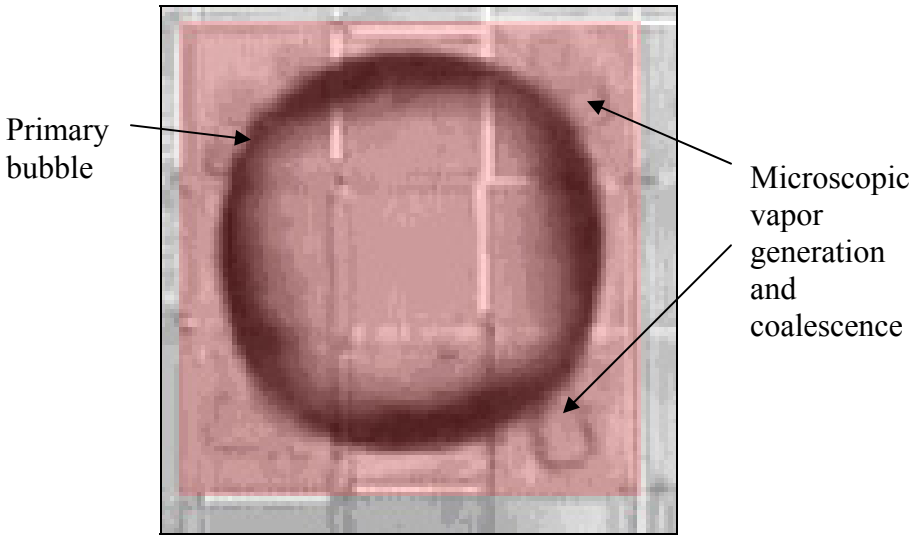

Figure 4.23: High-g boiling from a 0.81 x 0.81 mm^2 heater array. $T_{bulk} = 28°C$, $\Delta T_{sat} = 34°C$. Colored area represents powered heaters.

Due to the stability and size of the primary bubble on the heated surface, the mechanism of heat transfer is not solely dominated by buoyancy driven flows but is instead a combination of thermocapillary and natural convection. As mentioned in Chapter 1, for small bubbles that do no depart the heated surface, experiments have shown thermocapillary convection to be the dominant heat and mass transport mechanism and buoyancy effects play a much smaller role (Wang et al, 2005).

From the side view images, an estimate of the force balance acting on the bubble can be calculated. The surface tension and coalescence force that counteracts buoyancy can be estimated based on the primary bubble size to be $\geq 3 \times 10^{-6}$ N. This force is calculated based on the buoyancy force acting on a bubble, $F_b = \Delta\rho_{lv} V_b g$ where V_b is calculated from the bubble diameter measured from the bottom view images. Side view images of the bubbles in high-g show a contact angle of approximately 90 degrees with a resulting surface tension force of approximately 20×10^{-6} N. This surface tension force is an order of magnitude larger than the buoyant force acting on the bubble and therefore explains why the bubble remains on the heated surface.

Increased subcooling was measured to have a negligible effect on heat transfer over the ranges tested. This tends to indicate that the thermocapillary and/or buoyancy driven flow above and around the bubble is not strongly influenced by the level of bulk subcooling. The heat transfer from the array at higher wall superheats appears to be the result of a competition between increase in heat transfer associated with the satellite bubble region and the decrease in heat transfer due to growth of the dry area under the stable primary bubble. Further analysis of the boiling images indicates that the primary bubble acts as a pump, bringing liquid in from the side of the heater array and pumping it

out at the top of the vapor bubble where it is transported upward due to natural convection and the momentum of thermocapillary flow.

The primary bubble shape and position on the heater caused local dryout over the center of the array. The heat transfer from the heater under and outside of the primary bubble is shown in Fig. 4.24. The presence of the primary bubble causes very large heat transfer from the edge of the array due to presence of strong thermocapillary and/or buoyancy driven flows toward the center of the bubble. In addition, *interior* heaters (8,22-24,46, Fig. 4.24), or heaters that are >50% covered by a primary bubble appear to reach a surfaced average CHF at relatively low superheat.

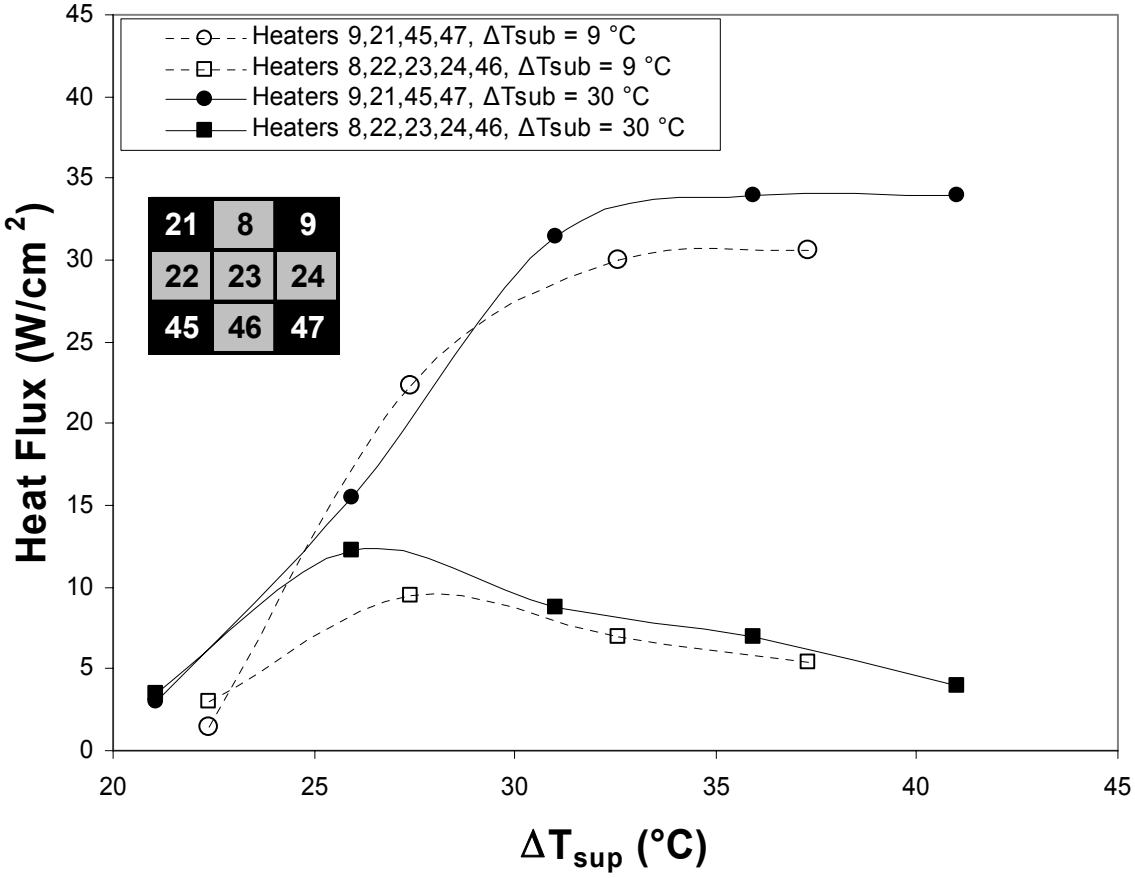

Figure 4.24: High-g surfaced averaged boiling heat flux from representative heaters in the 0.81 x 0.81 mm^2 heater array. ΔT_{sub} = 9°C.

It should be noted that the heater array size is close to the predicted bubble departure diameter from correlations and is significantly smaller than the Taylor wavelength, lending support to the idea that boiling at such scales is not governed by the models and methods presented in Chapter 1. The mechanisms for CHF are clearly not Taylor and Helmholtz instabilities as predicted from Zuber model and others.

4.3 COMPARISON OF BOILING CURVE AND HEATER SIZE RESULTS

Boiling curves for all four square heater arrays investigated in high-g are shown in Fig. 4.25. At low wall superheats, the data is in good agreement with natural convection correlations for a horizontal heated surface facing upward for all subcoolings and heater sizes as mentioned previously. The fact that natural convection correlations are in good agreement with the experimental data serves additionally to validate the substrate conduction estimation method described in the previous chapter. At higher wall superheats, there appears to be a negligible subcooling dependence on the heat flux over the ranges tested for all heater sizes. This may be attributed to the fact that CHF was not measured for all the cases studied, although it can be approximated based on the trends in the data. These findings agree with classical boiling models, correlations, and experimental data which show a negligible subcooling dependence in the nucleate pool boiling regime. In addition, the data for the 1.62 x 1.62 mm^2 array shows the primary bubble that tends to form at higher wall superheats in high-g departs less frequently as the liquid subcooling increases. It is thought that a reduction in the departure frequency would cause a reduction in the heat transfer but this effect is counteracted by larger sensible heating to the rewetting fluid and additional condensation as discussed in detail previously.

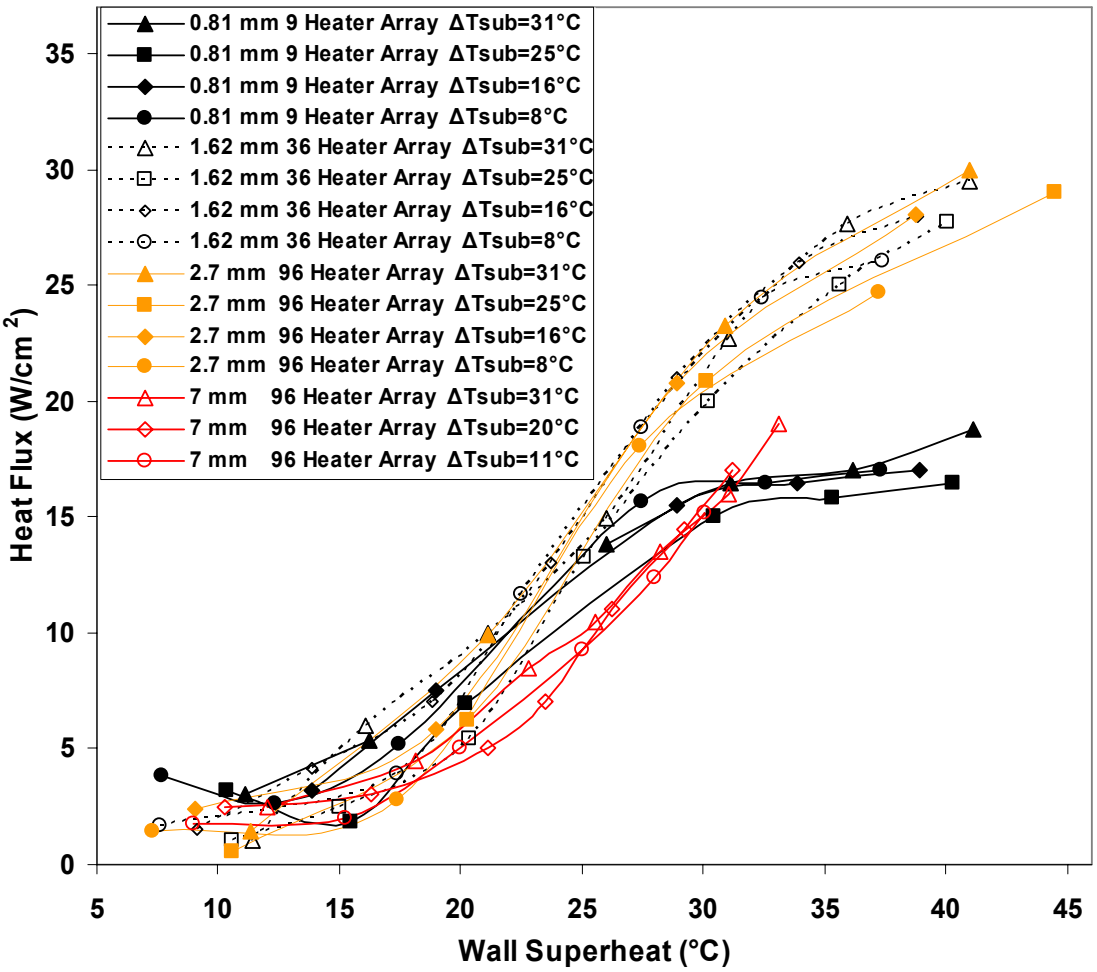

Figure 4.25: High-g boiling curves for various square heater arrays.

Depending on the size of the heater, boiling in high-g appears to be defined by at least two distinct regimes. For heater sizes smaller than the predicted isolated bubble departure diameter, surface tension dominates the process and classical models fall short of explaining the behavior. Under such conditions, the primary bubble that forms on the heater surface does not depart and the transport mechanisms appear to be a combination of thermocapillary and buoyancy driven flow. Current nucleate pool boiling correlations used to predict the heat transfer cannot explain the differences in performance seen across heater sizes indicating the need for new models and correlations that more effectively

account for appropriate length scales such as the Taylor wavelength and isolated bubble departure diameter.

Boiling from the smallest heater array is clearly surface tension dominated, although natural convection may play a role in enhancing condensation from the bubble cap which tends to regulate the primary bubble size. The corner and edge heat transfer compared to the larger arrays, 36 and 96 arrays, is slightly less due to the fact that vapor is not removed from the heated surface by bubble departure.

For heaters that are larger than the isolated departure diameter and smaller than the vapor jet diameter predicted from Taylor instability (1.62 – 2.7 mm arrays), the heat transfer at higher wall superheats was measured to be 100% higher than for the 0.81 x 0.81 mm^2 array. This enhancement is due to primary bubble departure that occurs frequently allowing rewetting of the heated surface and an enhancement in heat transfer.

For the largest heater size investigated (7 x 7 mm^2), the boiling measurements appear to fall in between the two cases mentioned above. As indicated previously, this may be due to the purity of the fluid and/or the given surface/fluid combination which may act to slightly alter the heat transfer from the surface.

In summary, the data appears to show three different boiling regimes in high-g. These regimes are directly related to the heater size relative to the bubble sizes. The important non-dimensional length scales that govern pool boiling performance in high-g are: the ratio of the heater length to the bubble departure diameter predicted from the Fritz correlation, and the ratio of the heater length to the Taylor wavelength. The heater hydraulic diameter (ratio of surface area to perimeter) may also play a significant role by determining the relative effect of heat transfer from the edge of the heater, which has

been shown to be dramatically enhanced under certain conditions. These length scales were found to be equally important across gravity levels as will be discussed in the next section.

It is hypothesized that the transition from buoyancy to surface tension dominated boiling occurs when the bubble departure diameter (D_b) and the heater size are of the same order. The largest bubbles observed for the 1.62 mm and 2.7 mm heater cases in high gravity have a diameter of approximately 0.8 mm, supporting this hypothesis. In addition, the bubble departure diameter in high-g predicted from correlations is 0.72 mm. In summary, the three distinct boiling regimes are shown in Fig. 4.26. This figure shows the three boiling regimes defined by the relative size of the heater to the predicted

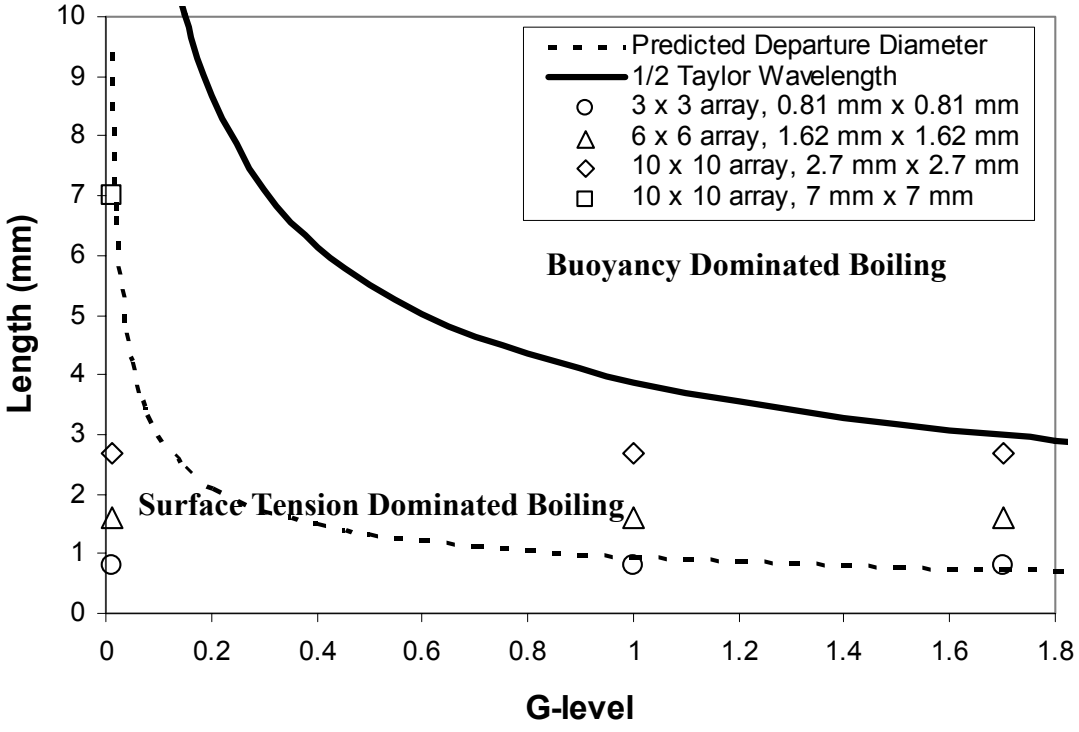

Figure 4.26: Boiling regime map.

departure diameter (Fritz correlation) and Taylor wavelength. If the heater length is smaller than both of these length scales, boiling is surface tension dominated. If the

heater is larger that both of these length scales then buoyancy dominated boiling results. The various heater sizes investigated in this thesis are shown by the symbols in Fig. 4.26.

4.4 TRANSITION FROM HIGH TO LOW-G

4.4.1 Gravitational Effects on the Bubble Departure Diameter

The gravitational environment produced aboard the KC-135 provides a transition from high-g to low-g over approximately five seconds. Although the transient gravitational environment produced does not allow a steady-state boiling process to be observed, significant information can be obtained nonetheless. Consider first the measured primary bubble departure frequency for the 0.81 mm to 2.7 mm heater arrays (Fig. 4.27-4.29). The departure frequency was reduced dramatically as the g-level declined, as expected, and can be explained by the reduction in buoyant forces acting on the bubble. It should be noted that a consistent primary bubble was not observed across gravity levels for a 7 x 7 mm^2 array because the heater size was much larger than a vapor column diameter and sufficiently high wall superheats that cause the formation of a primary bubble in high-g were not investigated.

Looking first at the g-level dependence on the primary bubble departure frequency for various heater sizes, as the gravity level is reduced, the primary bubble was observed to depart less frequently, Fig. 4.27. An interesting trend can be observed from Fig. 4.27. It appears that for the 1.62 and 2.7 mm heaters, the bubble departure frequency is a function of the ratio of the heater length, L_h, to the Taylor wavelength, λ_D. Best fit curves of the data shown in Fig. 4.27 were used to calculate the data shown in Fig. 4.28. For the few data points that can be considered, the data appears to fall along the same

curve indicating once again the importance of the Taylor wavelength on the dynamics of the primary bubble.

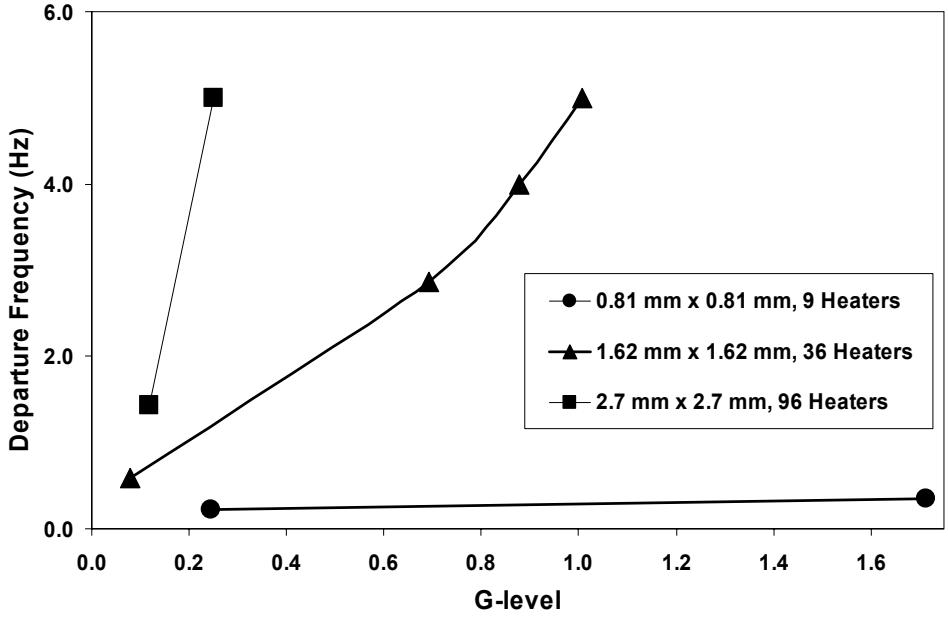

Figure 4.27: Effect of Heater Size on primary bubble departure frequency (T_{bulk} = 54°C, T_{wall} = 100°C).

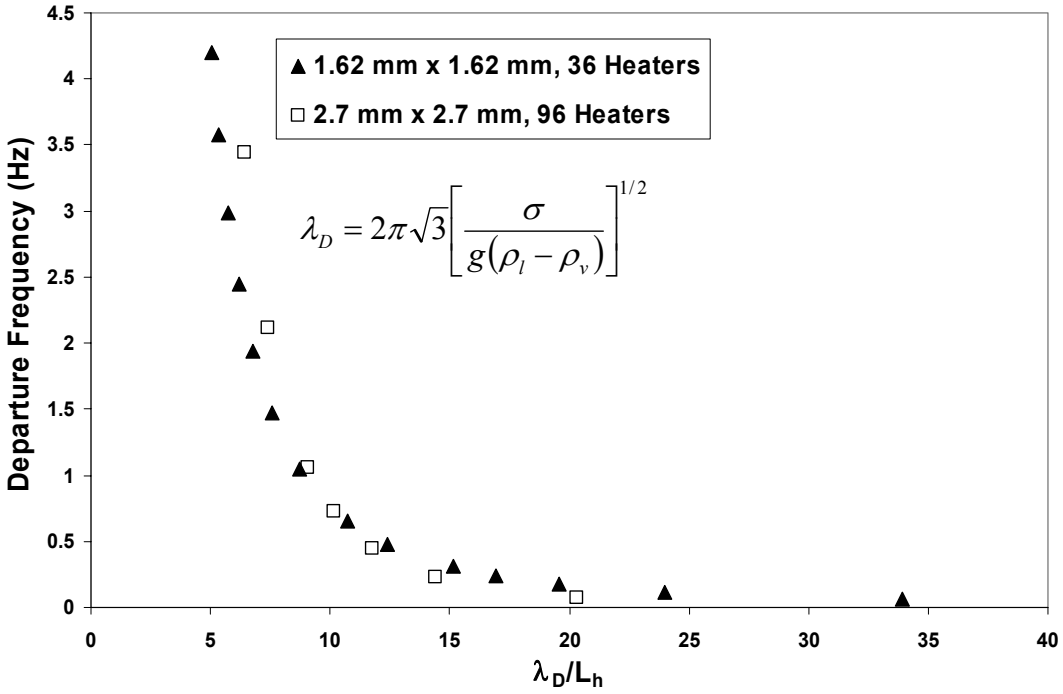

Figure 4.28: Effect of the ratio of the Taylor wavelength to heater length on primary bubble departure frequency (T_{bulk} = 54°C, T_{wall} = 100°C).

The frequency of bubble departure vs. gravity level is shown in Fig. 4.29 for the 1.62 x 1.62 mm^2 array at higher bulk subcoolings. A higher subcooling reduces the bubble departure frequency for a given wall temperature, g-level, and heater size since the size of the primary bubble decreases due to increased condensation at the top of the vapor liquid interface.

As mentioned previously, the effect of bubble coalescence at the base of the primary bubble is thought to significantly influence the primary bubble departure

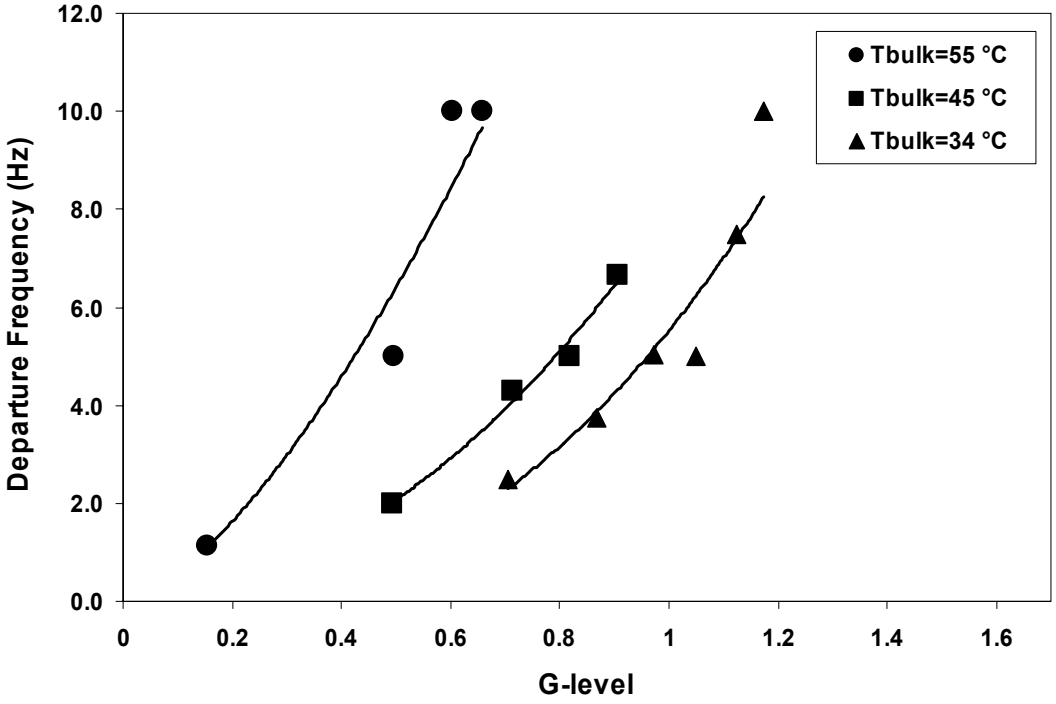

Figure 4.29: Effect of bulk fluid temperature and g-level on bubble departure frequency. Data taken from a 36 heater array (1.62 x 1.62 mm^2), T_{wall} = 95°C.

frequency. Higher wall superheats increase vapor generation from satellite nucleation sites, increasing the rate of coalescence. The dynamic effects of the coalescence process are thought to provide a net force that holds the bubble onto the surface, counteracting buoyancy as shown in Fig. 4.30.

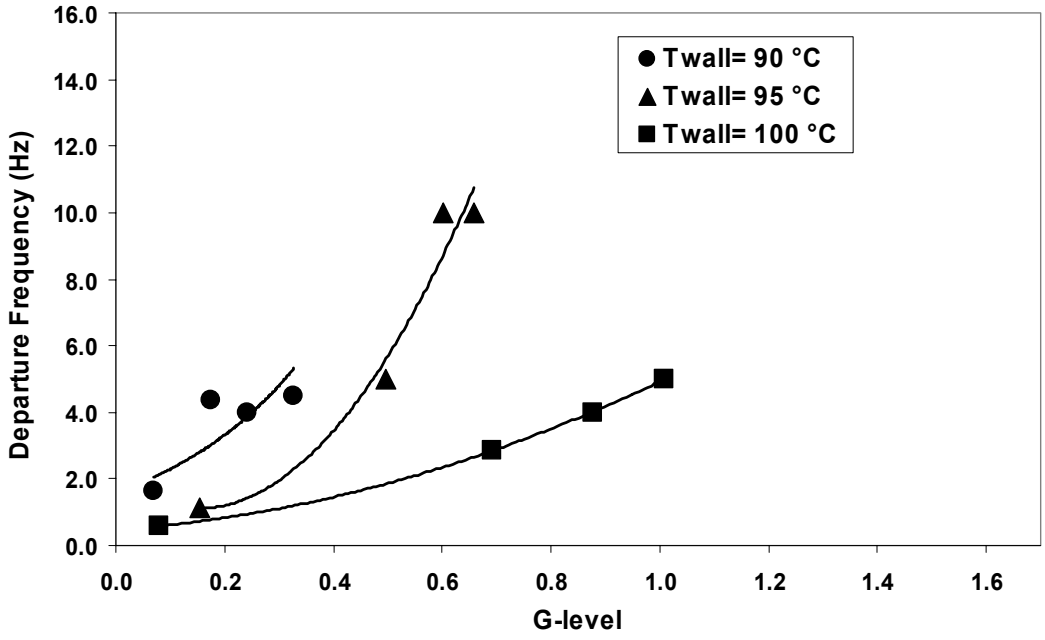

Figure 4.30: Bubble departure frequency for 1.62 x 1.62 mm^2 heater array T_{bulk} = 55°C.

4.4.2 Gravitational Effects on Primary Bubble Size

The transition from high-g to low-g also had a dramatic effect on the primary bubble diameter for the 0.81 x 0.81 mm^2 array. A plot of the gravity level vs. time with representative bottom view images of the boiling process is shown in Fig. 4.31. It is interesting to note that the boiling behavior for this heater size at all gravity levels studied is strikingly similar to what is observed in low gravity boiling for all heater sizes, Fig. 4.32. The primary bubbles in high-g were seen to be significantly smaller than those observed in low-g for the same heater size.

This boiling is dominated by the formation of a stable primary bubble that does not depart the heated surface. Surface tension clearly dominated the boiling process for a 9 heater array across gravity levels which indicates that if the heater size is smaller than the bubble departure diameter, the boiling heat flux is dramatically affected.

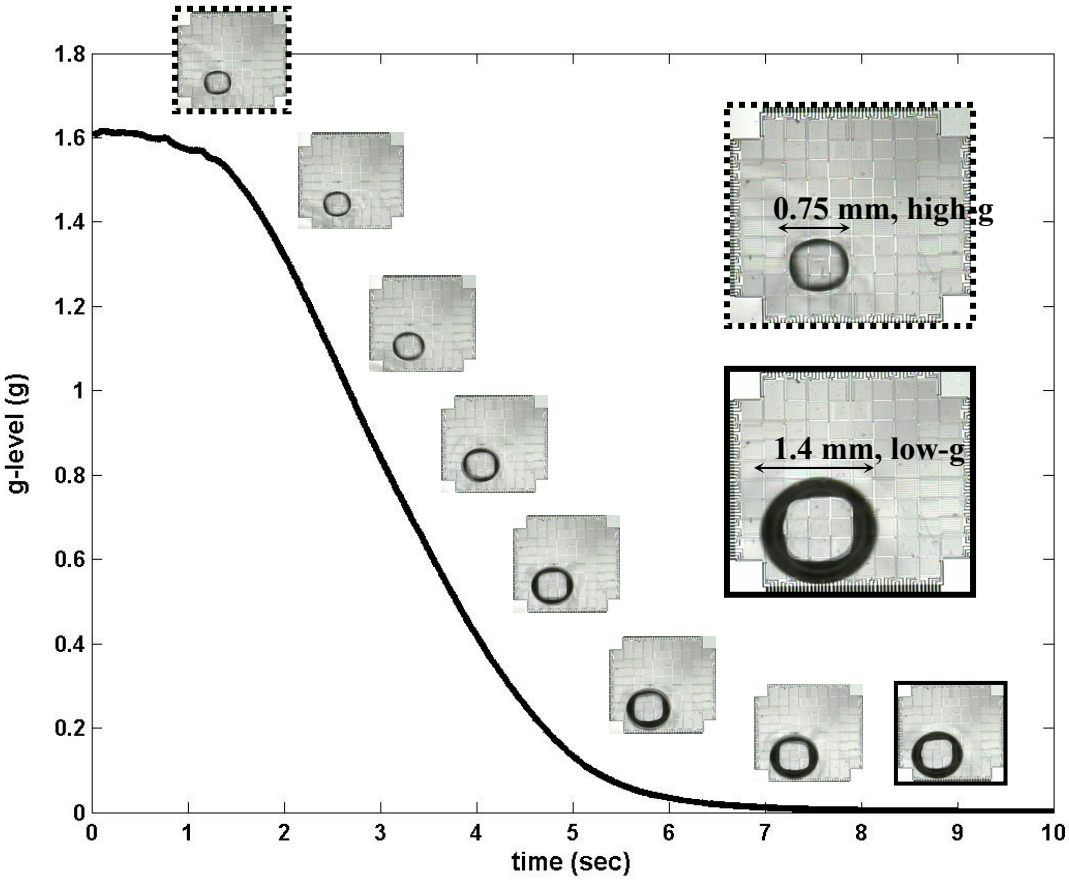

Figure 4.31: Bubble size vs. gravity level, ΔT_{sat} = 38°C, T_{bulk} = 28°C.

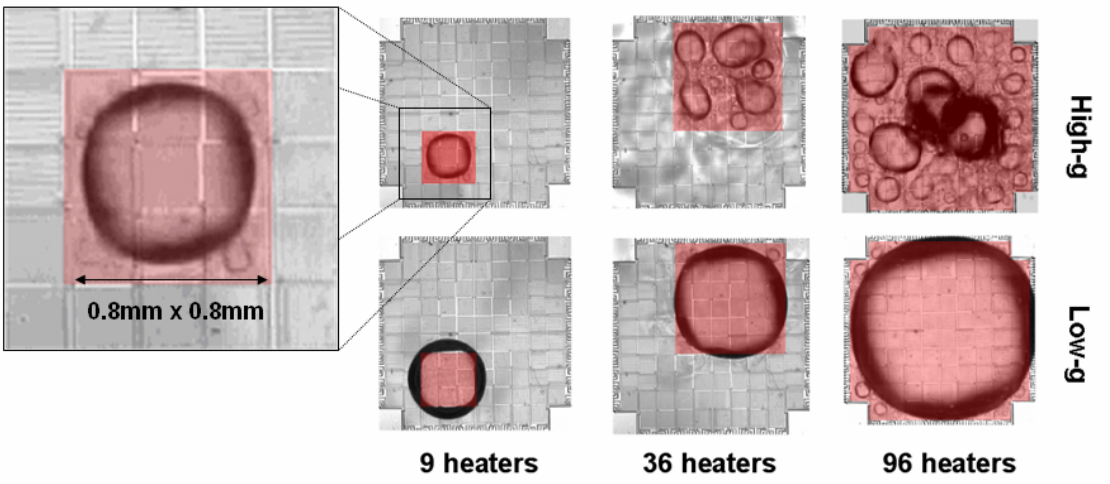

Figure 4.32: Boiling on a 3 x 3 Heater Array (.8 mm x .8 mm) at 1.6 g, T_{bulk} = 28°C, ΔT_{sat} = 34°C. Colored area represents powered heaters.

Observations showed the primary bubble (formed in high-g) increases in size as the gravity level decreases. The increase in primary bubble diameter may be due to a decrease in natural convection causing decreased condensation at the top of the bubble. At equilibrium the bubble was nearly 100% larger in low-g.

4.5 HIGH-G CONCLUSIONS

In conclusion, the data presented in this section serves to validate previous work for boiling from heater sizes larger than the isolated bubble departure diameter. In addition, the Rosenhow correlation accurately predicts the pool boiling performance at relatively low wall superheats. The primary mechanism for heat transfer during nucleate pool boiling was different for various levels of subcooling. Under near saturated bulk conditions, the majority of heat removal from the surface occurs due to sensible heating to the rewetting fluid as well as latent heat transfer required for bubble formation. Under high bulk subcoolings, the primary bubbles that formed tended to stay on the heated surface longer and large heat transfer due to condensation was identified. For large heaters, the mechanism for CHF was identified to be dryout of the interior portion of the heater which is accompanied by a strong increase in heat transfer from the edges.

High gravity boiling on small heaters can be surface tension dominated, similar to boiling in low gravity. Surface tension dominated boiling results in a dramatically lower heat flux and the transition to surface tension dominated boiling is not a function of Bo_B alone but depends additionally on wall superheat, bulk fluid subcooling, heater size, and gravity level.

Chapter 5: Low-g Boiling Results

5.1 INTRO

Buoyancy was found to be the primary bubble departure mechanism at higher g-levels. The primary effect of a reduction in the gravitational level is a reduction in the buoyant force acting on bubbles which causes them to grow large and depart the heated surface less frequently. Bubble departure from the heated surface was found to account for the majority of the heat transfer during saturated pool boiling while under highly subcooled conditions, condensation from the bubble cap was identified as the primary heat transfer mechanism in the presence of strong buoyancy driven convection around the primary bubble. Because the transport process is enhanced by bubble removal and buoyancy driven convection, it can be expected that a reduction in bubble departure frequency in addition to a reduction in buoyancy driven convection tends to reduce the time and surface averaged heat transfer. This chapter discusses in detail the heat and mass transport characteristics due to bubbles that do not depart the heater surface. In low-g, bubbles tended to grow much larger than their high-g counterparts and the heat flux in most cases were found to be dramatically reduced. Although this might be expected at first glance, physical mechanisms not thought to be significant were found to dominate the transport process. Extensive experimental data is presented throughout this chapter which serves to support the many inferences made.

This chapter is organized in a similar manner to Chapter 3. Experimental results for the square heater arrays are first presented and analyzed. The effects of bulk liquid subcooling and wall superheat are discussed in detail for each heater size. This is

followed by a brief discussion on the effects of boiling in low-g from heaters of larger aspect ratio. Lastly, information is presented which identifies the effect of dissolved gases on the boiling performance in low-g which was found to be dramatic.

Throughout this chapter, experimental data is discussed alongside analytical and numerical models. These models are meant to facilitate understanding of the phenomena in addition to providing a predictive capability for future design. Last, a summary of the significant contributions of this work and design recommendations for a passive thermal control system in space are discussed. The conclusions section discusses recommendations for future work in this area.

5.2 HEATER SIZE EFFECTS

5.2.1 7 x 7 mm^2, 96 Heater Array

Boiling curves for a 7 x 7 mm^2 heater array in low-g are shown in Fig. 5.1 for all bulk liquid subcoolings. Images of the boiling process for a 7 x 7 mm^2 array are shown in Fig. 5.2. At low wall superheats, the process is dominated by single phase conduction through the liquid. This transport process is much less efficient than the natural convection process observed in high-g at similar superheats and is the reason why a smaller heat flux is measured. In a zero-g environment, the heat transfer from the heater during single phase transport can be modeled at first approximation using a steady state conduction model assuming the liquid located a distance, x, away from the heater is at constant bulk temperature. As an example, assuming the temperature of the bulk liquid located 1 cm away from the heater surface is at T_{bulk} then the resulting heat transfer due to conduction is 0.02 W/cm^2. This value is much smaller than the measured heat flux which may be due to residual buoyancy driven fluid motion. Steady natural convection

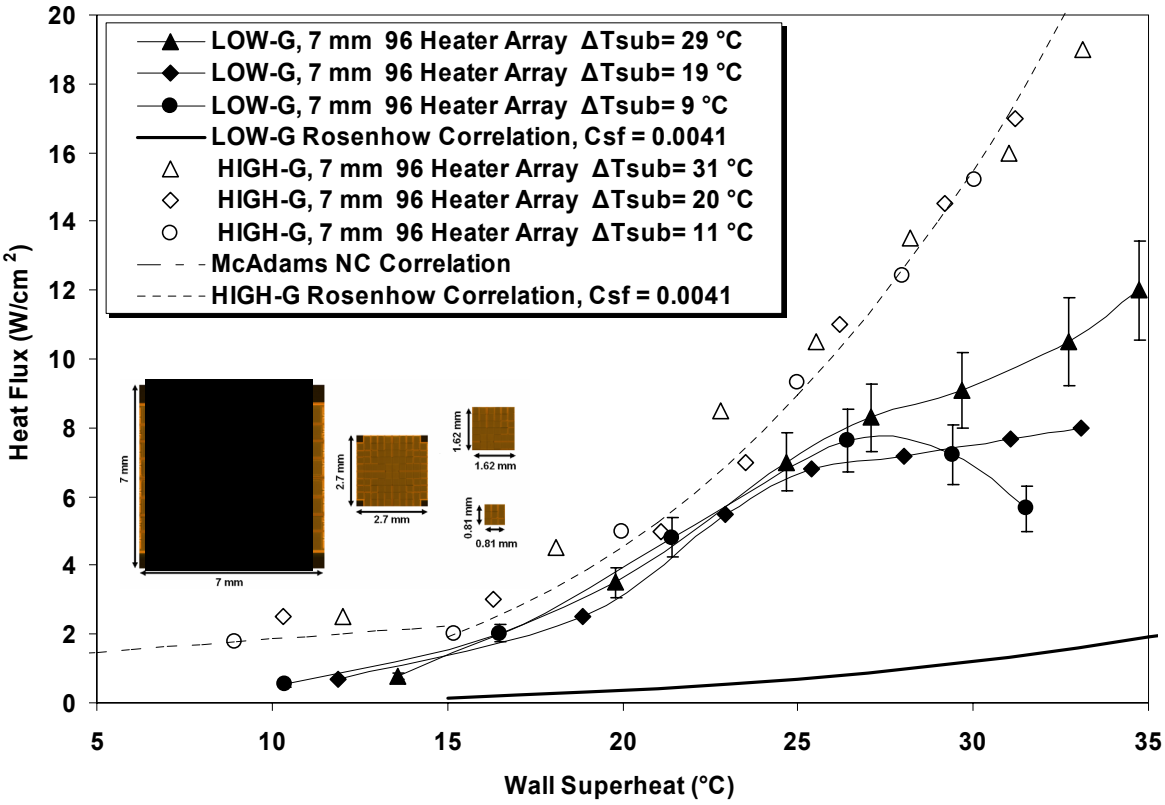

Figure 5.1: Boiling curves for a 7 x 7 mm^2 heater array in low and high-g.

that is set up in high-g may not be significantly damped out in the amount of time the g-environment transitions from high to low-g (< 5 sec). Therefore, it is concluded that the residual fluid motion within the system enhances the single phase heat transfer process in low-g. In a true microgravity environment, the steady-state time and surfaced averaged heat flux is predicted to be much smaller.

As bubble formation occurs at low wall superheats, $15^{\circ}C < \Delta T_{sat} < 25^{\circ}C$, the measured heat transfer in low-g is similar to what was measured in high-g, Fig. 5.1. This is due to the formation of small bubbles on the heater that move around and coalesce with other bubbles on the heater surface. Under such conditions, the nucleation site density was relatively small, and the formation of a primary bubble was not observed and may be

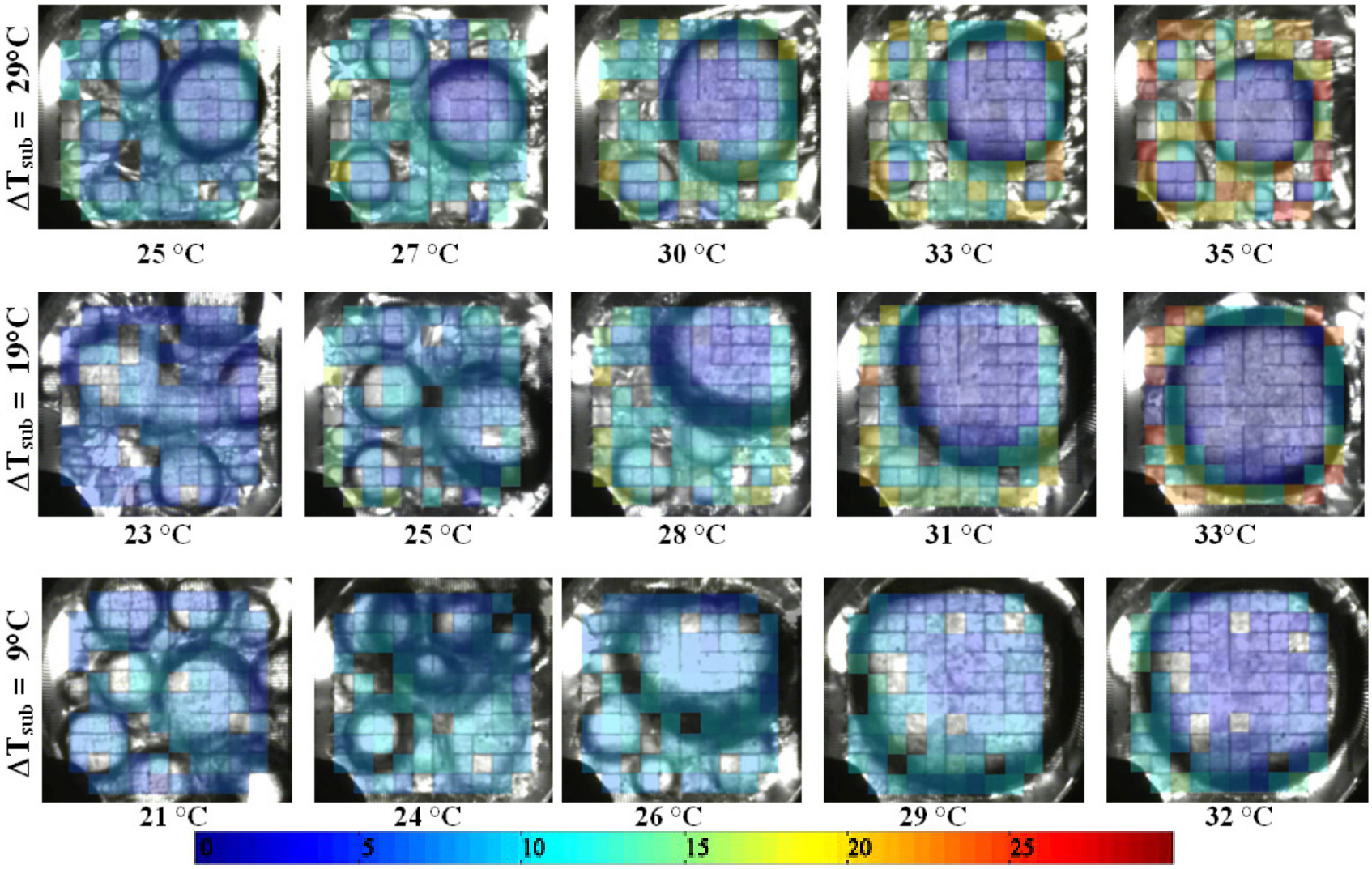

Figure 5.2: Surface resolved time averaged boiling heat transfer in low-g from a 7 x 7 mm^2 heater array

due to the fact that vapor is not generated at a sufficient rate to sustain a larger bubble on the surface, Fig 5.3. For all of the subcooling levels investigated, condensation from the

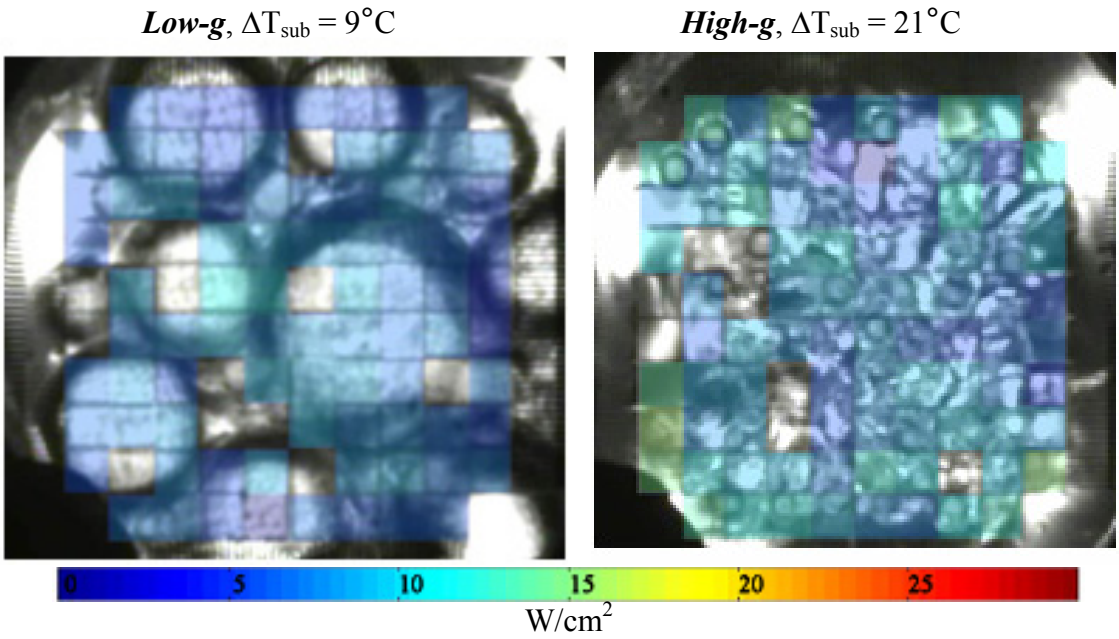

Figure 5.3: Boiling in high and low-g at low wall superheats, $\Delta T_{sat} = 21°C$.

bubbles was observed which regulates their size. The bubble coalescence process in low-g mentioned above appears to have the same effect on the heat transfer as in high-g where much smaller bubbles were observed, Fig. 5.3. As seen from Fig. 5.3, the heat transfer appears to be evenly distributed across the heater array for both g-levels and although the bubbles are much larger in low-g, the time and spatially averaged heat transfer is nearly the same and independent of subcooling. It appears that the lateral bubble motion on the surface low-g can create the same heat flux as smaller departing bubbles in high-g. In this boiling regime which can be defined as, "isolated satellite bubble regime", the bubbles act as turbulence generators and their relative movement across the heater surface allows the surrounding cooler liquid to wet the surface, enhancing the heat transfer. In low-g at low wall superheats, the primary heat transfer mechanism appears to

be single phase conduction to the rewetting liquid although an appreciable condensation component may exist. This will be discussed in greater detail for the smaller heater arrays. It is interesting to note that the Rosenhow correlation, which was shown to be a good predictor of performance in high-g, predicts a heat transfer that is much smaller than the measured value in low-g, Fig 5.1. It is clear from this data that such models need to be modified to account for the pertinent mechanisms in low-g.

At higher wall superheats, the boiling curves in low-g are strongly dependent on the level of subcooling. Consider first the lowest subcooling investigated (ΔT_{sub}=9°C). The heat transfer increases with superheat up to 26°C, then decreases at higher superheats. The primary bubble that formed at ΔT_{sat} = 26°C increased in size as the superheat increased but did not grow large enough to cover the entire heater, Fig. 5.2. The primary bubble moved around the heater surface coalescing with smaller satellite bubbles. Primary bubble movement in low-g may be due to induced liquid motion from the surrounding satellite bubbles and/or the significant g-jitter in all three axial directions aboard the KC-135. G-jitter has a much larger effect on the primary bubbles that form on the 7 mm array than on the smaller heaters. Thermocapillary effects were not observed to be significant at this particular subcooling. CHF is clearly indicated from the trend in the boiling curve and measured to be approximately 7.8 W/cm^2 at ΔT_{sat} = 27°C, Fig 5.1. The mechanism for CHF appears to be breakdown of the satellite bubble region into a single primary bubble which tends to insulate most of the heater area.

The CHF at the highest subcooling (ΔT_{sub}=29°C and 31°C) was much higher than for the case mentioned above. As indicated from Fig 5.1, CHF was not reached for this particular subcooling over the range of the wall superheats measured. Coalescence with

the primary bubble was observed to be the satellite bubble removal mechanism at all wall superheats investigated. As the wall superheat was increased from 25°C < ΔT_{sat} < 30°C, the size of the primary bubble increases slightly causing dryout over a larger portion of the array. This effect is counteracted by higher heat transfer around the primary bubble due to increasingly active nucleation sites and strong coalescence that increases as the wall superheat is increased. As the superheat is increased to 30°C, the primary bubble size reaches a maximum, but does not cause complete dryout on the heater. The heat flux continues to increase, however, due to a higher nucleation site density and heat transfer around the primary bubble. As the wall superheat is increased above 30°C, the primary bubble size decreases due to the onset of strong thermocapillary driven flows. This allowed increased satellite bubble formation and an enhancement in heat transfer. Further increases in superheat were accompanied by increases in thermocapillary convection which reduced the primary bubble size and increased the overall heat transfer. CHF was not reached since the derivative of the satellite bubble heat transfer w.r.t the wall superheat was positive, Eq. 5.1. In this equation, q"wet refers to the average heat

$$\frac{\partial \dot{q}}{\partial(\Delta T_{sat})} = q''_{wet}\frac{\partial A_{wet}}{\partial(\Delta T_{sat})} + A_{wet}\frac{\partial q''_{wet}}{\partial(\Delta T_{sat})} \geq 0 \tag{5.1}$$

flux over the satellite bubble area, A_{wet}. In addition, it is assumed that the heat transfer beneath the primary bubble is negligible. The derivatives shown in Eq. 5.1 were calculated using a backward differencing scheme. As shown in Fig. 5.4, this value is positive at ΔT_{sat} = 30°C. A comparison between high-g and low-g boiling at high subcooling is shown in Fig. 5.5. Clearly, the presence of the primary bubble in low-g causes a reduction in time and surface averaged heat transfer.

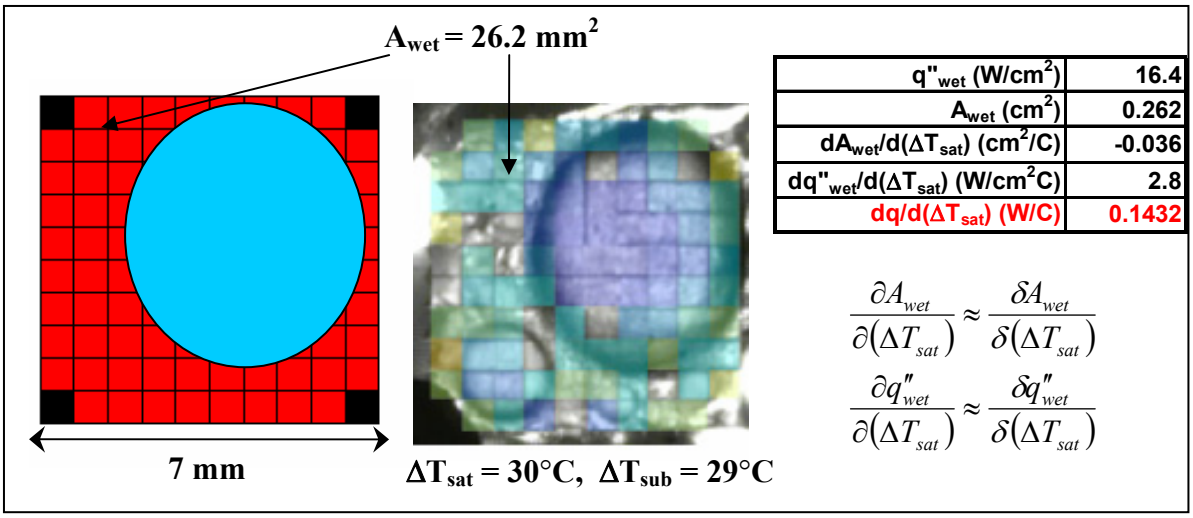

Figure 5.4: Wetted area heat transfer calculation.

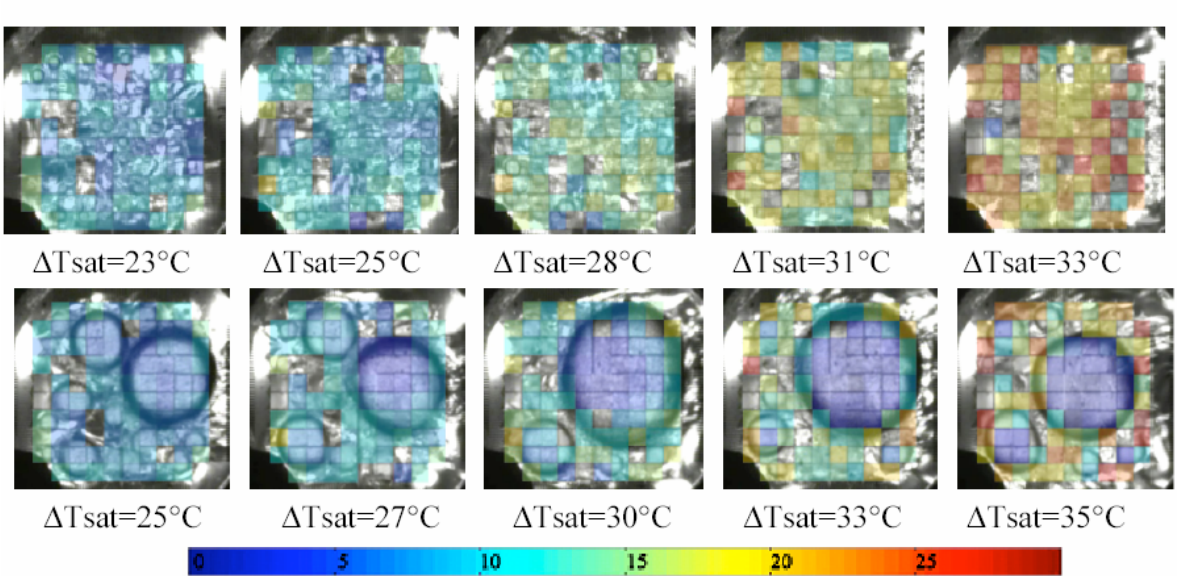

Figure 5.5: Boiling in low and high-g, ΔT_{sub} = 29°C. Top row corresponds to boiling in high-g and bottom row corresponds to boiling in low-g.

At the intermediate subcooling (ΔT_{sub}=19 °C) the boiling process is again dominated by the primary bubble. Trends similar to the high subcooling cases are observed in both the heat flux data and the images for all heater sizes. As expected, the primary bubble size falls between the high and low subcoolings sizes as does the measured time and surface averaged heat flux, Fig. 5.6.

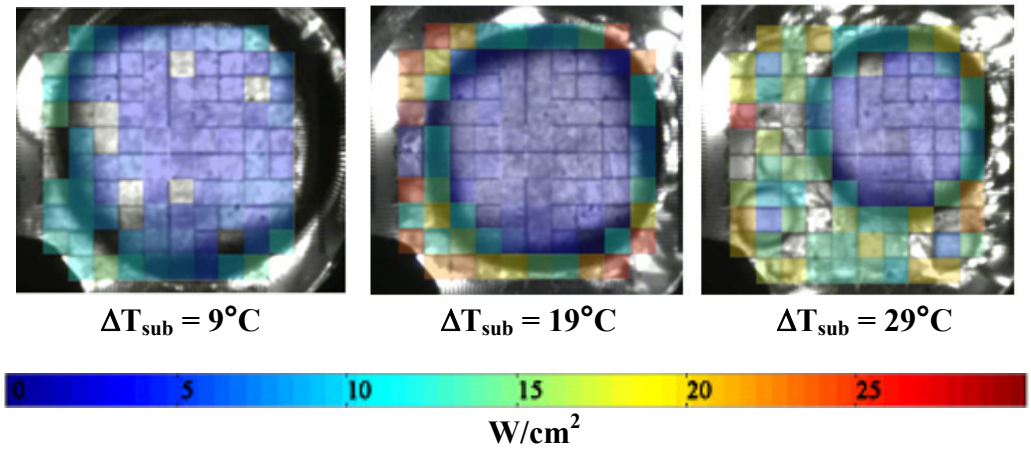

Figure 5.6: Bulk liquid subcooling effect in low-g pool boiling from a 7 x 7 mm^2 array, ΔT_{sat} = 32 - 33°C.

5.2.2 1.62 x 1.62 mm^2, 36 Heater Array and 2.7 x 2.7 mm^2, 96 Heater Array

5.2.2.1 Low Subcooling. Boiling curves for the 1.62 x 1.62 mm^2 and 2.7 x 2.7 mm^2 heater arrays are shown in Fig. 5.7. At low subcoolings (ΔT_{sub} = 6°C), a large primary bubble was observed over most of the wall superheat range investigated. At low wall superheat, ΔT_{sat} = 9°C, no bubbles were observed on the heated surface and the heat transfer mechanisms were similar to those describe previously for the larger heater. At higher wall superheats, ΔT_{sat} > 15°C, vapor generated at active nucleation sites coalesced into a stable primary bubble that caused dryout over nearly all of the heater area resulting in a very small heat transfer, Fig. 5.8-9.

Although the bubbles sizes remain nearly the same, the heat transfer from the edge of the array, heaters 65-96, appears to reach a time and surface averaged maximum at ΔT_{sat} = 30°C, Fig 5.10. This is due to two competing effects, 1). an increase in heat

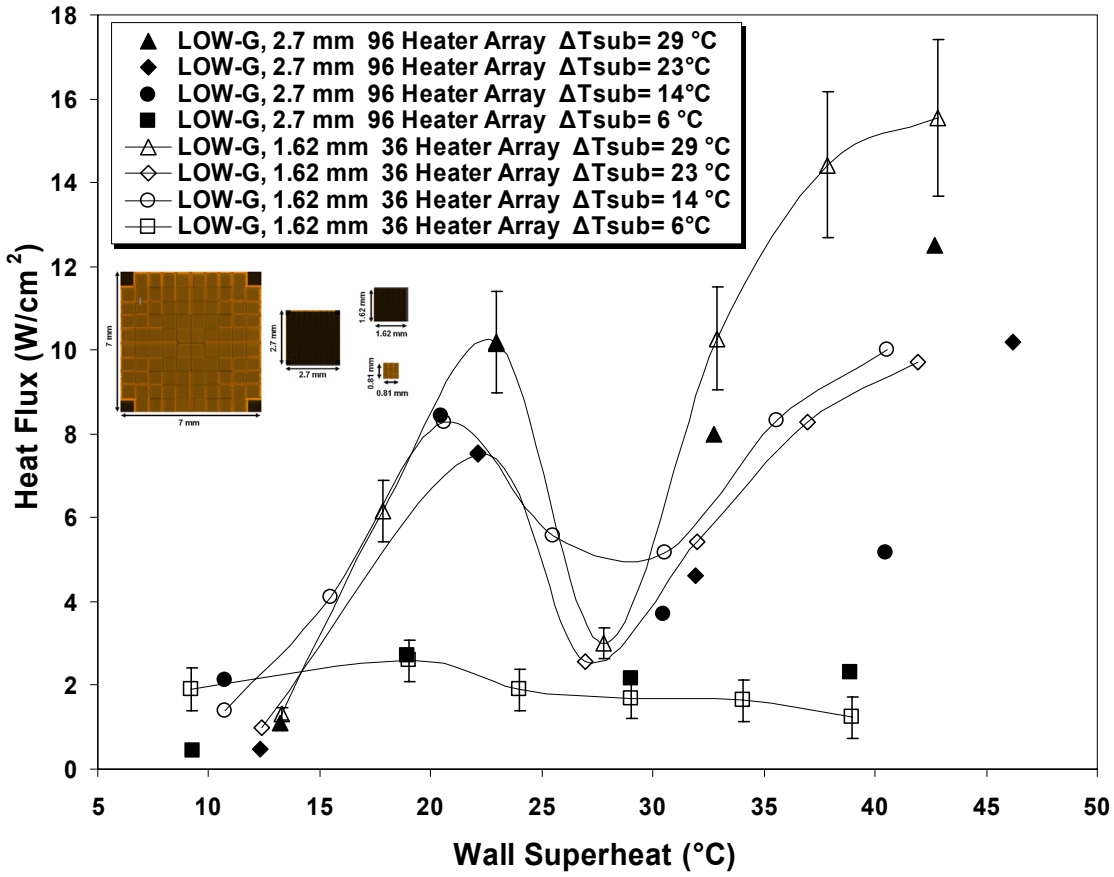

Figure 5.7: Low-g boiling curves for a 1.62 x 1.62 mm^2 & 2.7 x 2.7 mm^2 heater arrays.

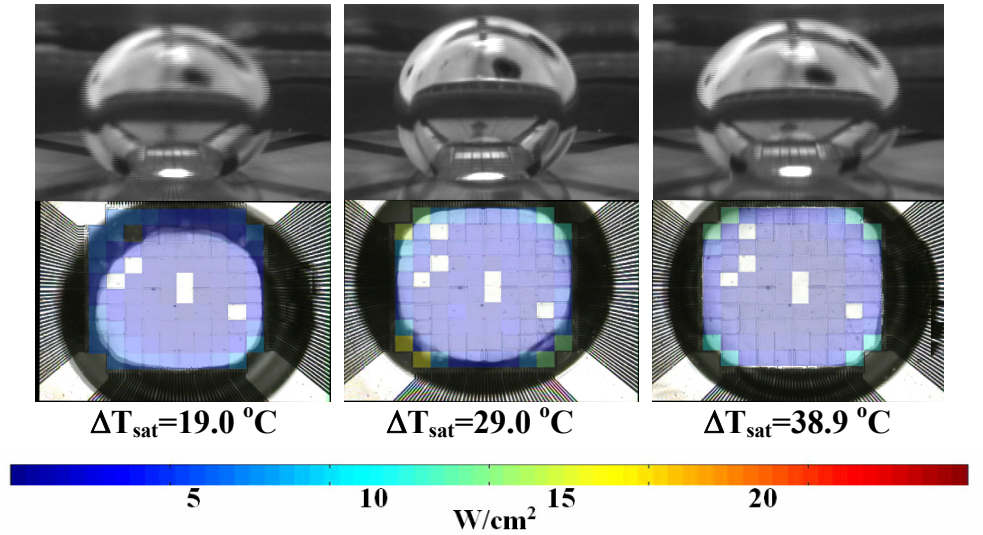

Figure 5.8: Bottom and side view time averaged low-g boiling images of a 2.7 x 2.7 mm^2 heater array at low subcooling, ΔT_{sub} = 6°C.

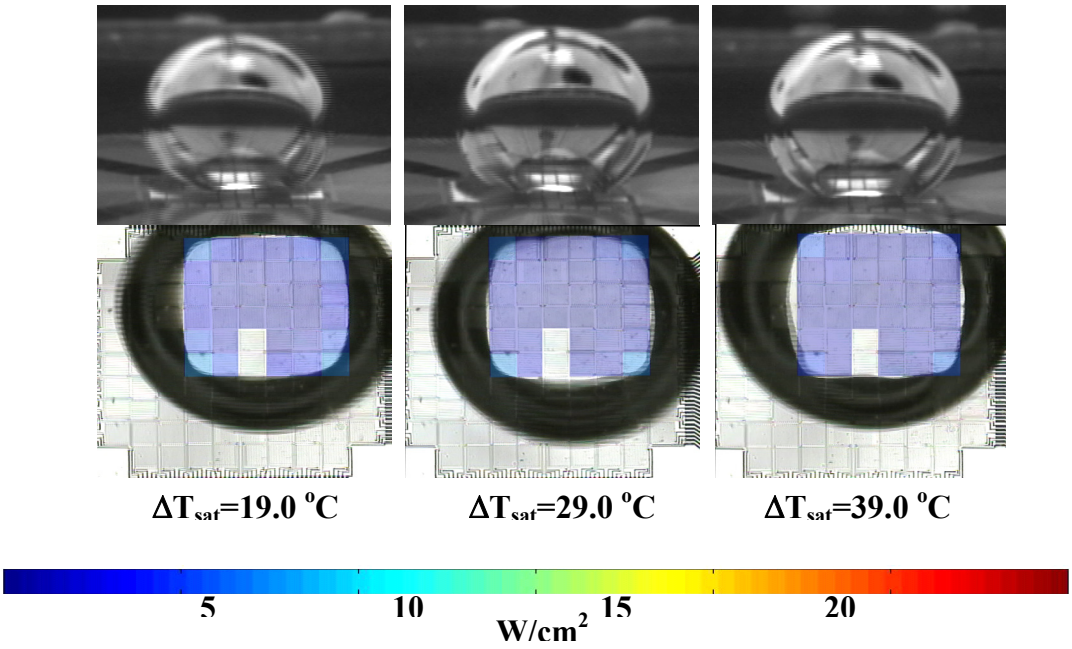

Figure 5.9: Bottom and side view time averaged low-g boiling images of a 1.62 x 1.62 mm^2 heater array at low subcooling, $\Delta T_{sub} = 6°C$.

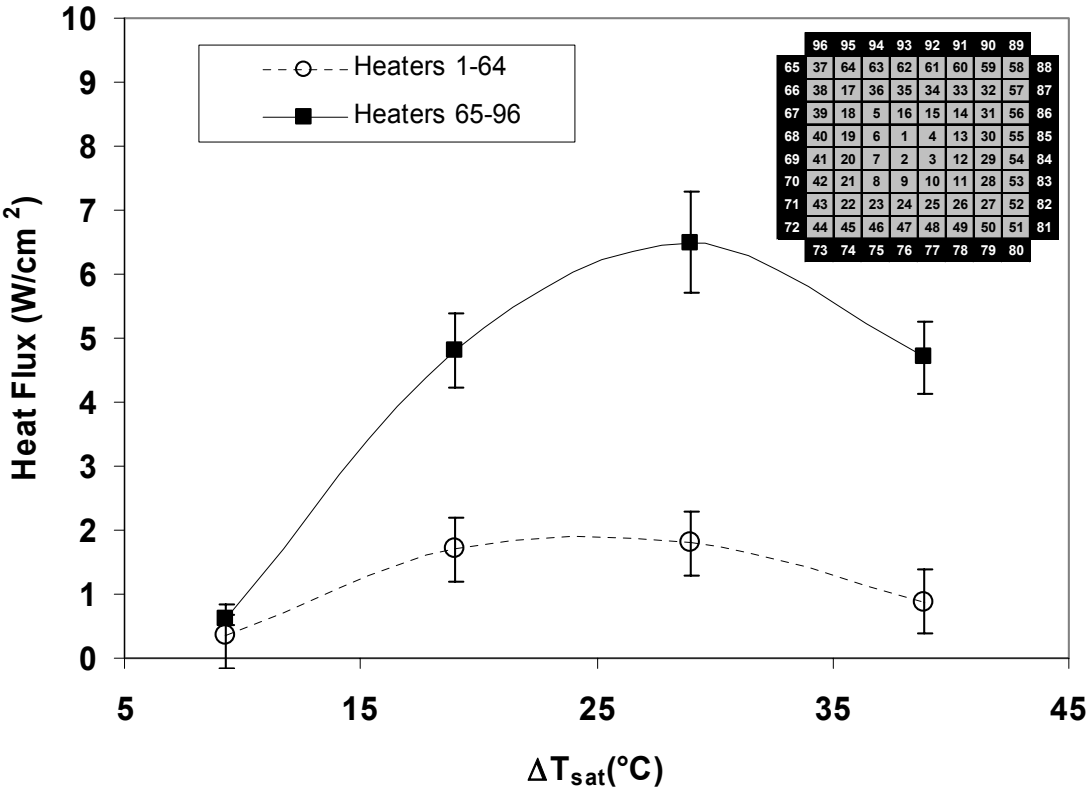

Figure 5.10: edge (black,#65-96) and center (gray, #1-64) boiling from a 2.7 x 2.7 mm^2 heater array at low subcooling, $\Delta T_{sub} = 6°C$.

transfer from the wetted heaters outside the primary bubble as the wall superheat increases, and 2). an increase in the size of the primary bubble which reduces the wetted heat transfer area as described previously for the larger heater array.

5.2.2.2 High Subcooling. As the subcooling is increased, the low-g boiling curve takes a dramatically different shape. At low wall superheats $\Delta T_{sat} < 13°C$, the heat transfer process is again dominated by conduction and residual buoyancy driven convection. Consider first the 1.62 x 1.62 mm^2, 36 heater array at the highest subcooling investigated, $\Delta T_{sub} = 29°C$, Fig 5.11. At low superheats, the primary bubble is significantly smaller than the heater size and few active nucleation sites are observed. The rapid increase in wall heat transfer as the superheat increases to 23°C (CHF) is due to an increase in the number of active nucleation sites as observed from the bottom view videos. These nucleation sites produce small bubbles that tend to coalesce with the primary bubble that forms. At CHF, the primary bubble was observed to rotate counterclockwise with a frequency of 28 rad/sec or 4.4 Hz as shown in Fig. 5.12.

Consider first heater #8 in the 2.7 x 2.7 mm^2 heater array, the colored heater in Fig. 5.12. The time resolved heat flux for this heater is shown in Fig. 5.13 a-b. Considering the movement of the primary bubble at CHF, Fig. 5.12, it is clear from the bottom view images that heater #8 is periodically completed covered by the primary bubble for approximately 0.05-0.1 seconds. During such times, heat transfer is expected to be very small. This is in good agreement with the time resolved heat flux measurement shown in Fig 5.13b which periodically goes to zero.

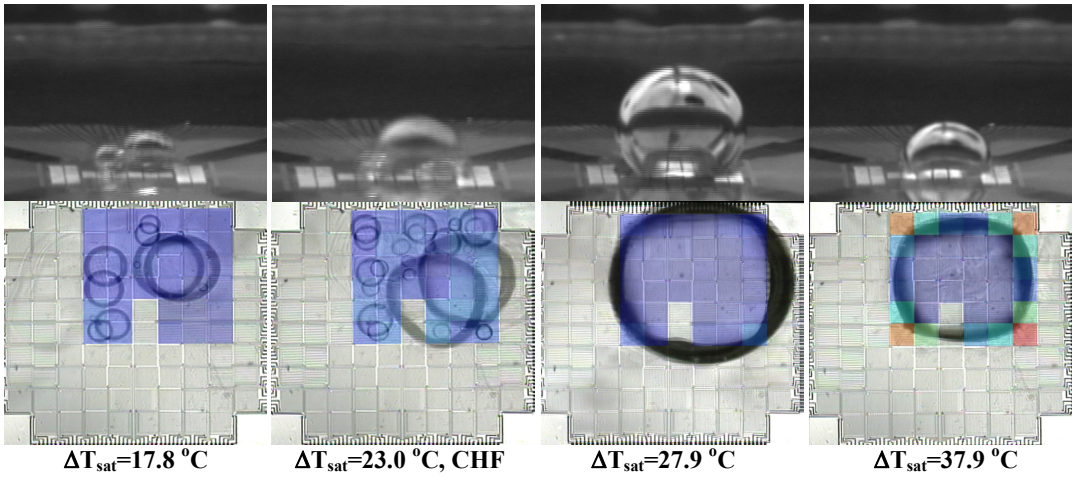

Figure 5.11: Bottom and side view time averaged low-g boiling images of a 1.62 x 1.62 mm^2, 36 heater array (a) and a 96(b) heater array at high subcooling, ΔT_{sub} = 29°C.

Such trends indicate a number of interesting findings. First, the primary bubble acts as a vapor reservoir that moves around the heater surface, pulling bubbles into it. This causes a significant heat transfer in the region where coalescence occurs. Comparing this performance to high-g, the measured time averaged heat flux appears to be nearly identical. Therefore, it can be concluded that satellite bubble coalescence with

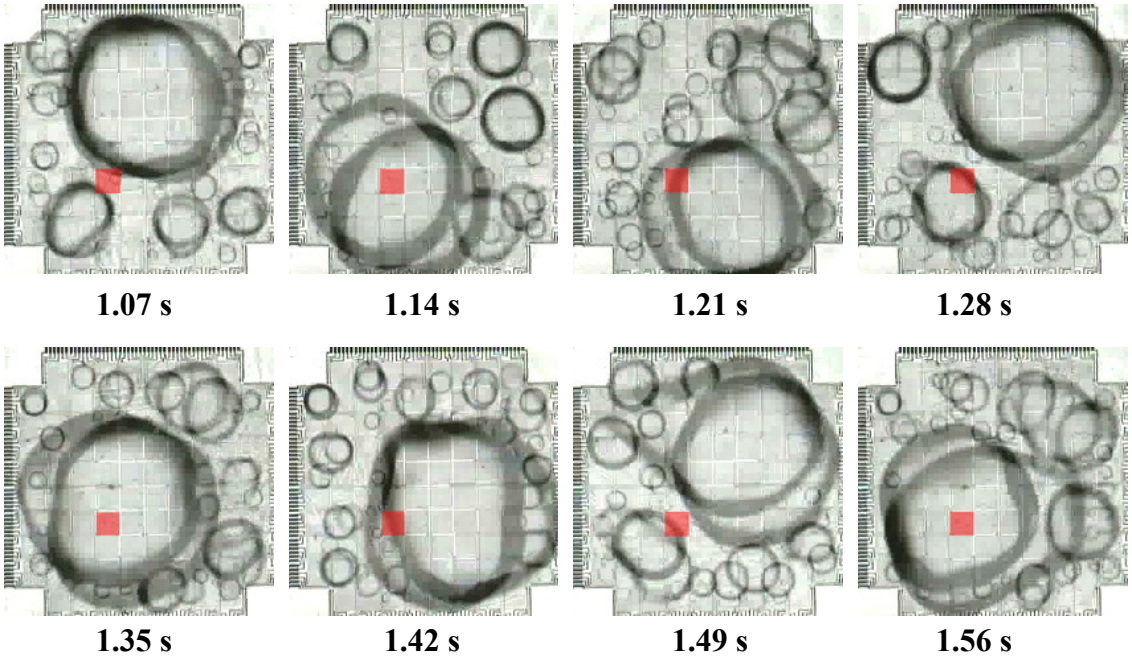

Figure 5.12: Time resolved low-g boiling images at CHF, ΔT_{sat} =23°C, ΔT_{sub} = 29°C for a 2.7 x 2.7 mm^2 heater array. Colored heater corresponds to heater # 8 in the array.

the primary bubble replaces bubble departure as the primary mechanism for heat transfer in low-g at relatively low wall superheats and high subcoolings. More importantly, it appears that the effect of the primary bubble is similar to the heat transfer mechanism in high-g indicating that high-g correlations may be able to predict the heat transfer in low-g if the gravitational term is replaced by another term that accounts for primary bubble size. It should also be noted that heat transfer from the corner of the array, heater #96 at CHF is nearly identical to heat transfer in high-g, Fig. 5.14, indicating once again that low-g mechanisms produce the same measurable behavior during high-g.

The CHF condition described extensively above can be analyzed further by considering the following scenario. At any given instant in time, the heater has a distribution of satellite bubbles on its surface as seen from Fig. 5.12. The total mass of vapor on the surface in the form of satellite bubbles at each instant in time can be

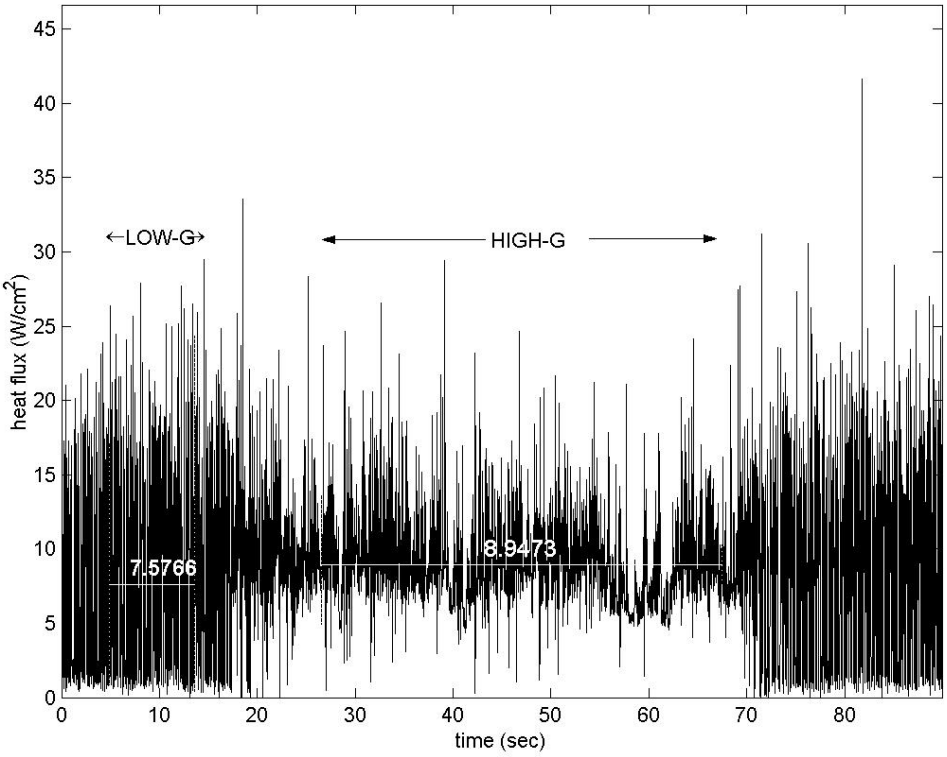

(a) Time resolved heat flux over entire parabola.

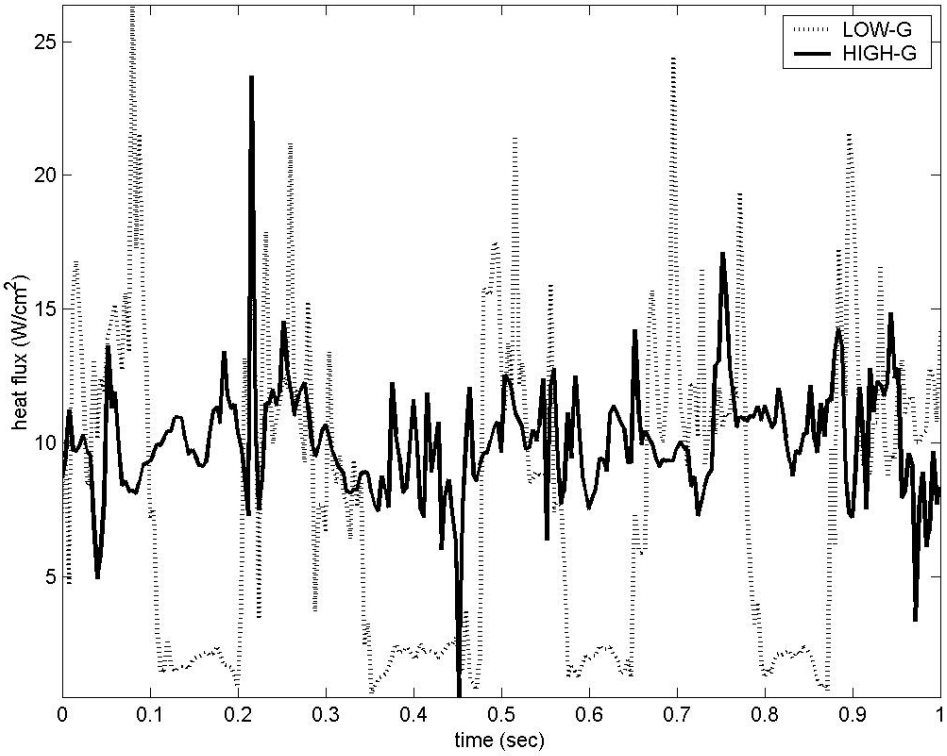

(b) Time resolved heat flux over smaller time scale.

Figure 5.13: Time resolved boiling heat flux from Heater #8 (Fig. 5.10) at CHF, ΔT_{sat} = 23°C, ΔT_{sub} = 29°C. Fig. 5.10 does not correspond to the time scale in this graph.

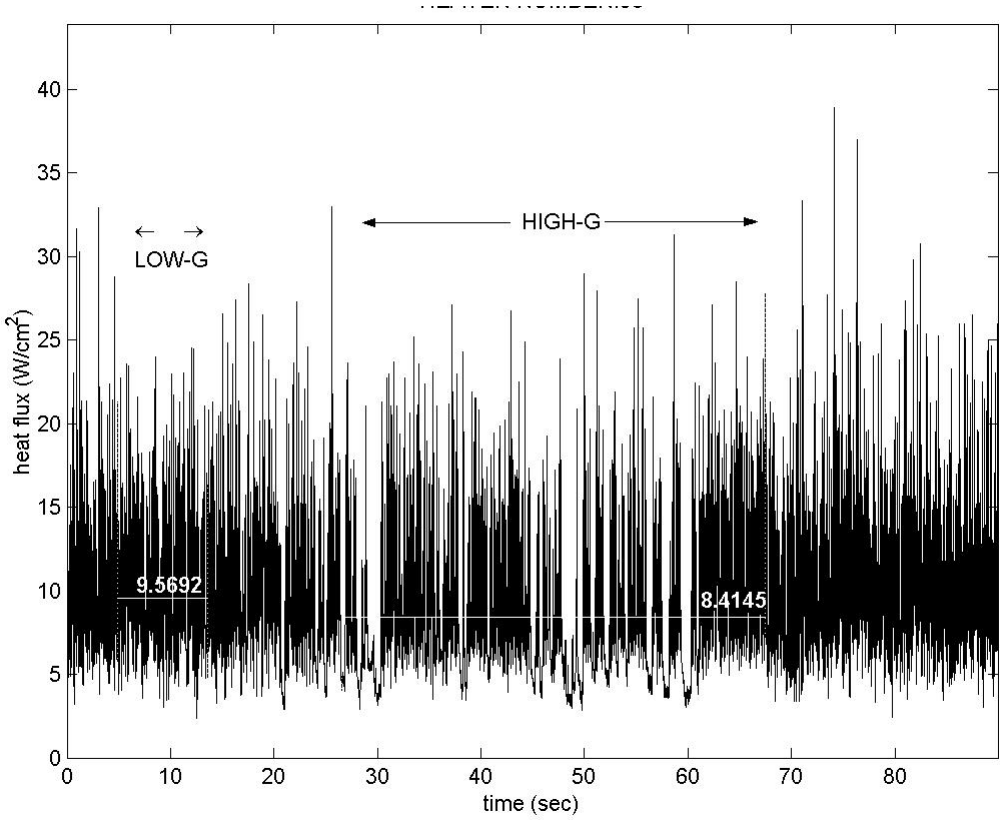

Figure 5.14: Time resolved heat transfer for heater #96, 2.7 mm array, at low-g CHF, $\Delta T_{sat} = 23°C$, $\Delta T_{sub} = 29°C$.

calculated by summing the volume of the bubbles, $V_{b,i}$, and multiplying by the density of FC-72 vapor, 16.4 kg/m^3. Furthermore, the amount of latent heat required to produce such a bubble distribution on the surface can be estimated by multiplying the mass of vapor by the latent heat of vaporization. As mentioned previously, the primary bubble rotates in a counterclockwise direction around the surface coalescing with satellite bubbles. After one complete counterclockwise revolution, the primary bubble has removed all of the satellite bubbles shown in a given picture at time, t. As the primary bubble coalesces with the satellite bubbles, it is interesting to note that the primary bubble does not increase in size. The vapor addition to the primary bubble from satellite bubble coalescence is balanced by condensation at the top of the primary bubble. In this manner, the primary bubble acts as a vapor sink. Considering the above scenario, an

estimate of the latent heat transfer from the heater surface can be obtained from Eq. 5.2. Furthermore, a more accurate estimate of the latent heat transfer to the fluid can be calculated by considering the above scenario for all images, Eq. 5.3, where k is total number of pictures and n is total number of bubbles on a given picture. The analysis described above assumes condensation from satellite bubbles to be negligible which is justifiable by the fact that they do not grow to the size of the primary bubble and therefore are in contact with higher temperature liquid which is possibly superheated. In addition, the absence of buoyancy driven convection enables condensing vapor to remain in the local vicinity of the bubble interface heating up the surrounding bulk liquid. This idea predicts a decreasing rate of condensation as time increases due to the transient increase in the bulk fluid temperature surrounding a bubble locally. This analysis also neglects coalescence between adjacent satellite bubbles which increases the latent heat transfer estimation. Performing this analysis for the image shown in Fig. 5.11 (0.21s image), results in a heat flux estimation of 0.046 W/cm^2, Table 5.1.

$$q'' = \frac{\rho h_{fg} f_p}{A_{heat}} \sum_{i=1}^{n} V_{b,i} \qquad q''_{ideal} = \frac{\sum_{j=1}^{k} \left(\frac{\rho h_{fg} f_p}{A_{heat}} \sum_{i=1}^{n} V_{b,i} \right)}{k} \qquad \text{(Eq. 5.2-5.3)}$$

It is clear from the above calculation that the amount of heat transferred to the fluid as latent heat at CHF does not account for the amount of heat transfer measured experimentally. In fact, the measured heat flux is 2.5 orders of magnitude higher than the calculated value. This indicates that the majority of heat transfer at CHF in low-g is not due to latent heat transfer but is instead due to sensible heating of the fluid that wets the heater surface as bubbles coalesce and move around the heater. This rewetting process is enhanced by the movement of the primary bubble on the heater surface which acts as a

CHF Latent Heat Calculation			
Bubble #	**D_b (mm)**	**$V_{b,i}$ (m^3)**	**q_{latent} (J)**
1	0.27	1.030E-11	1.274E-05
2	0.54	8.241E-11	1.019E-04
3	0.4	3.349E-11	4.141E-05
4	0.135	1.288E-12	1.592E-06
5	0.3	1.413E-11	1.747E-05
6	0.15	1.766E-12	2.184E-06
7	0.32	1.715E-11	2.120E-05
8	0.11	6.966E-13	8.612E-07
9	0.135	1.288E-12	1.592E-06
10	0.27	1.030E-11	1.274E-05
11	0.135	1.288E-12	1.592E-06
12	0.2	4.187E-12	5.176E-06
13	0.13	1.150E-12	1.421E-06
14	0.13	1.150E-12	1.421E-06
15	0.1	5.233E-13	6.470E-07
16	0.35	2.244E-11	2.774E-05
17	0.23	6.367E-12	7.872E-06
18	0.27	1.030E-11	1.274E-05
19	0.27	1.030E-11	1.274E-05
20	0.135	1.288E-12	1.592E-06
21	0.35	2.244E-11	2.774E-05
22	0.54	8.241E-11	1.019E-04
23	0.3	1.413E-11	1.747E-05
24	0.135	1.288E-12	1.592E-06
25	0.27	1.030E-11	1.274E-05
26	0.6	1.130E-10	1.398E-04
27	0.6	1.130E-10	1.398E-04
		F_p (Hz)	**4.4**
		A_{heat} (cm^2)	**0.069984**
		q" (W/cm^2)	***0.046***

Table 5.1: Latent heat flux calculation at CHF.

single phase turbulence generator. This finding is also in agreement with the results presented for the larger 7 mm heater array.

As the superheat is increased above CHF to 28°C, a sharp decrease in heat transfer occurs due to increased dryout of the heater. Considering the CHF condition described previously, if the rate of vapor addition from the satellite bubbles increases due to an increased satellite bubble density, the condensation from the primary bubble is unable to condense enough vapor to maintain a constant primary bubble size. Therefore

the primary bubble tends to grow which decreases satellite bubble formation allowing the bubble to reach a larger stable size. At this point, vapor generation is balanced by condensation from the bubble cap which serves to regulate the primary bubble size. As the superheat is increased above 32°C, a strong increase in thermocapillary convection was observed from the side view video images. The mechanism for the sudden increase in thermocapillary driven flow is currently unknown but may be due to the increased vapor generation from the edge of the array that occurs at higher wall superheats or it may be related to the presence of dissolved gases in the liquid, as suggested by Straub (2001). Similar trends in the heat transfer data are observed for the lower subcooling cases, T_{bulk} = 35° C and T_{bulk} = 45°C, Fig. 5.15-16.

For the 2.7 mm 96 heater array, coalescence was again observed to be the primary mechanism for CHF at higher subcoolings (similar to the 36 heater array). Although strong thermocapillary convection was observed at high subcoolings and high superheats, data was not obtained with sufficient superheat resolution to determine whether a local maximum occurs after CHF (as was observed for the 36 heater array).

A comparison between boiling in high and low-g for these heater sizes is shown in Fig. 5.17-18. As mentioned previously, correlations do not account for the nearly identical performance at low wall superheats and do not predict the trends at higher wall superheats during the presence of strong thermocapillary flow. At the highest superheat and subcooling, (ΔT_{sat} = 43°C, ΔT_{sub} = 29°C), the heat flux surpassed CHF, suggesting that thermocapillary convection can limit the rise in heater temperature even for an applied heat flux greater than CHF.

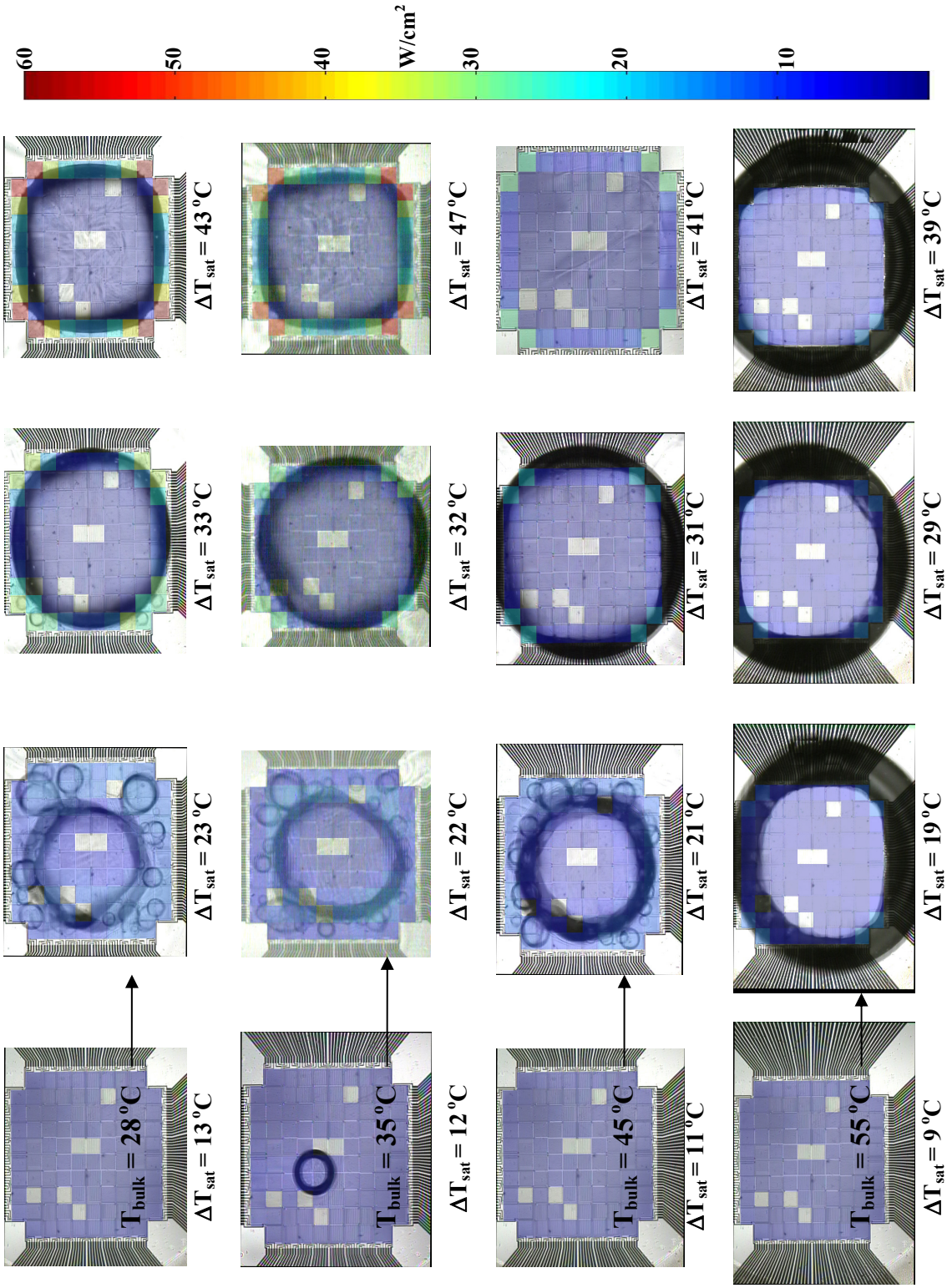

Figure 5.15: Time-averaged, spatially resolved heat flux maps of boiling process for 96 heater array in low-g at various ΔT_{sat} and T_{bulk}.

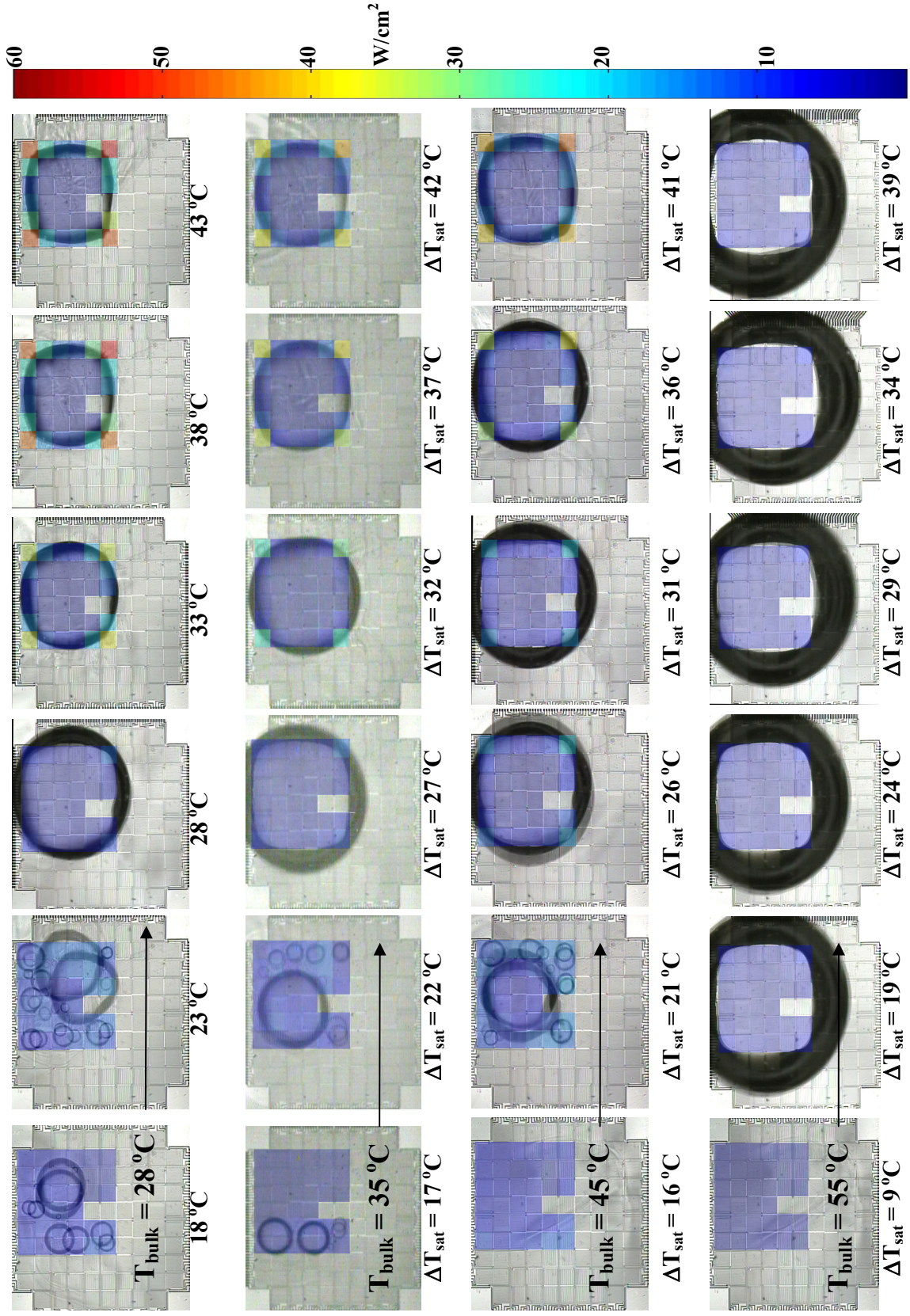

Figure 5.16: Time-averaged, spatially resolved heat flux maps of boiling process for 36 heater array in **low-g** at various ΔT_{sat} and T_{bulk}.

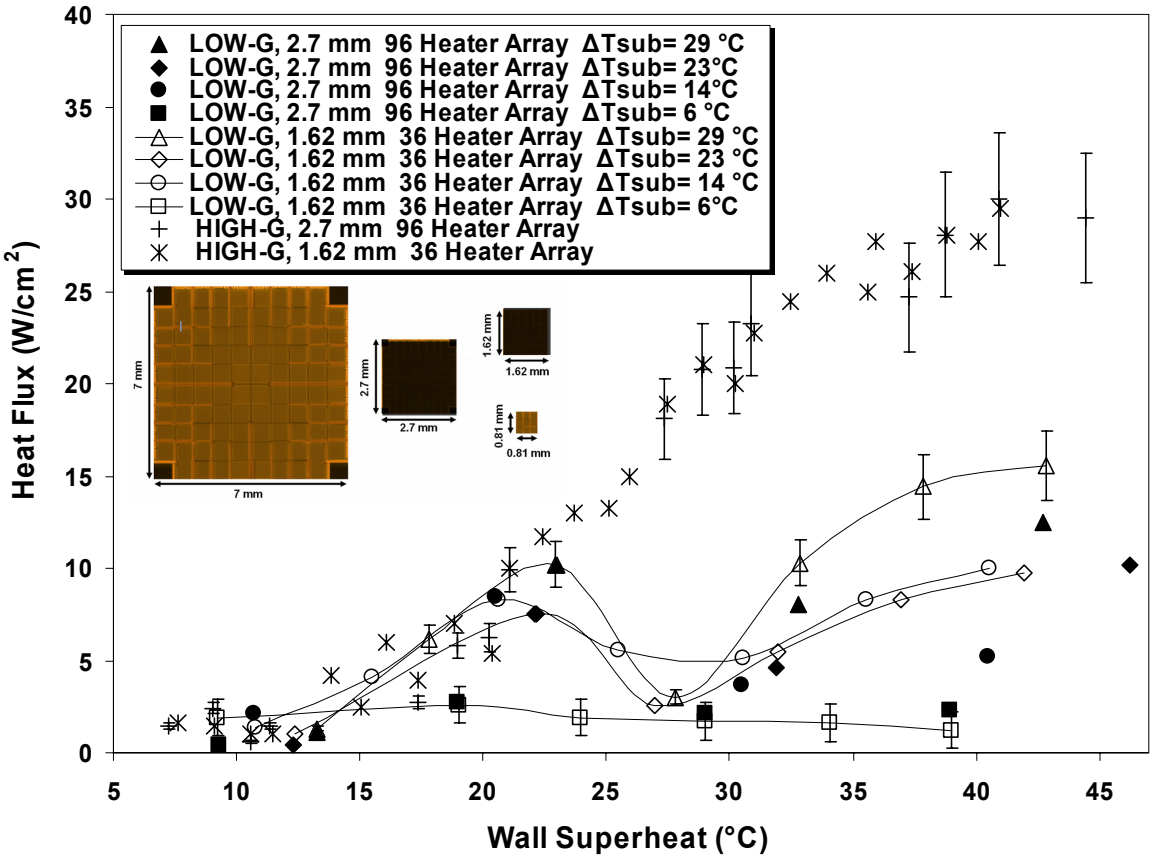

Figure 5.17: Boiling Curves for a 1.62 mm and 2.7 mm heater arrays.

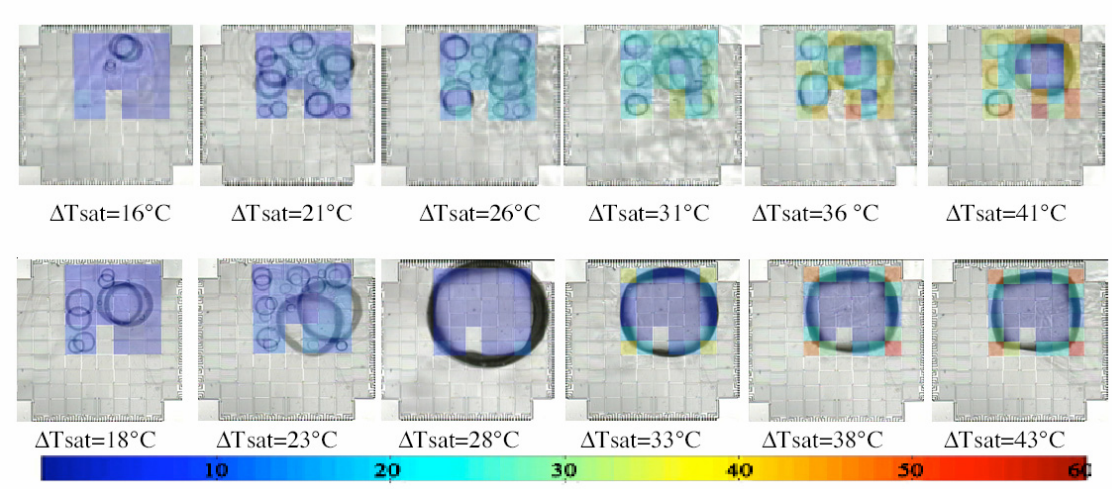

Figure 5.18: Boiling behavior on a 6 x 6 array, 1.62 x 1.62 mm^2 powered array for high-g (top row) and low-g (bottom row). Heat flux is in W/cm^2.

5.2.2.3 Thermocapillary Convection. The formation of very strong thermocapillary convection was observed at high subcoolings and high wall superheats. Fig. 5.19 plots

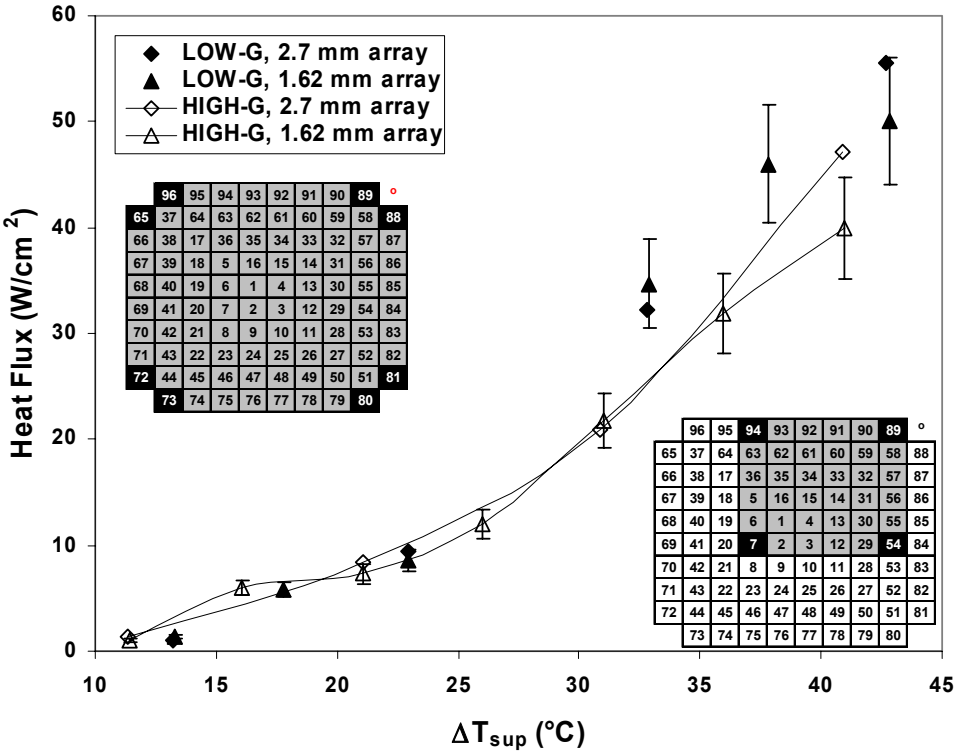

Figure 5.19: time and surface averaged heat flux from the wetted area in high and low-g T_{bulk} = 28°C, ΔT_{sub} ranges from 29-30°C. Wetted heaters are highlighted in black.

the heat flux measured in the wetted area for both high and low-g. The wetted heaters are those that are completely outside of the primary bubble dryout region. It is interesting to note that the heat transfer in the wetted area in low-g is slightly larger than in high-g, indicating that the rate of vapor generation and removal is more efficient in low-g than in high-g. The primary bubble is able to sustain a large vapor influx from around its edges as thermocapillary convection is increased. At certain wall superheats, ΔT_{sat} = 33°C and ΔT_{sat} = 37°C, the wetted area heat transfer is slightly larger in low-g than in high-g. The time resolved heat flux plot for heater #96, corner heater, is shown in Fig. 5.20a-b. As indicated from the heat flux trace in low-g, the corner heaters are always outside the

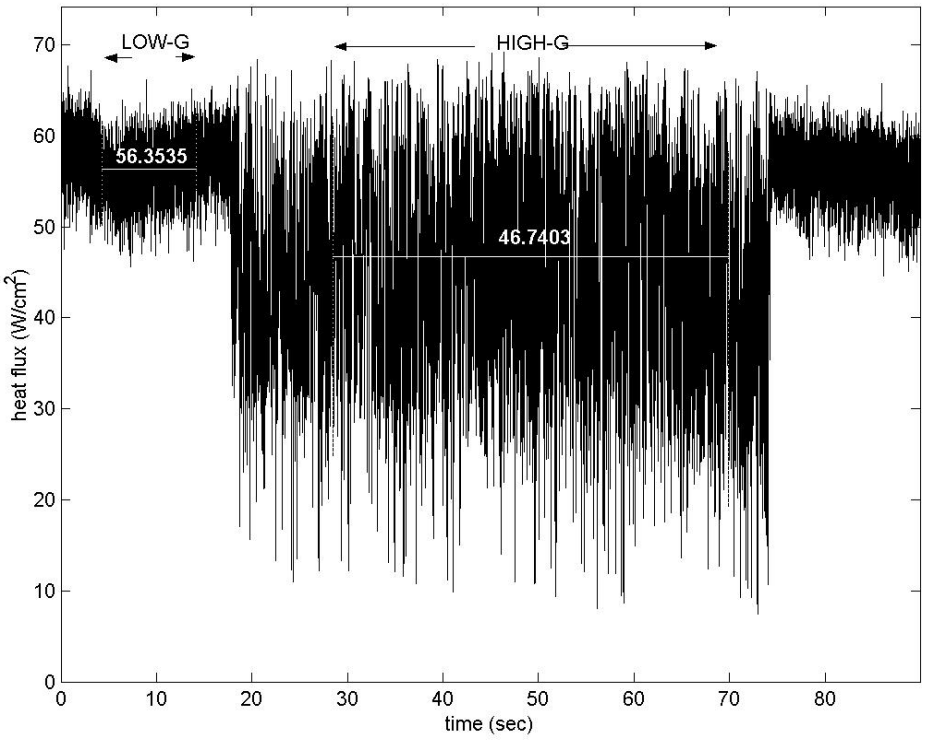

(a) Time resolved boiling in high and low-g throughout parabolic maneuver.

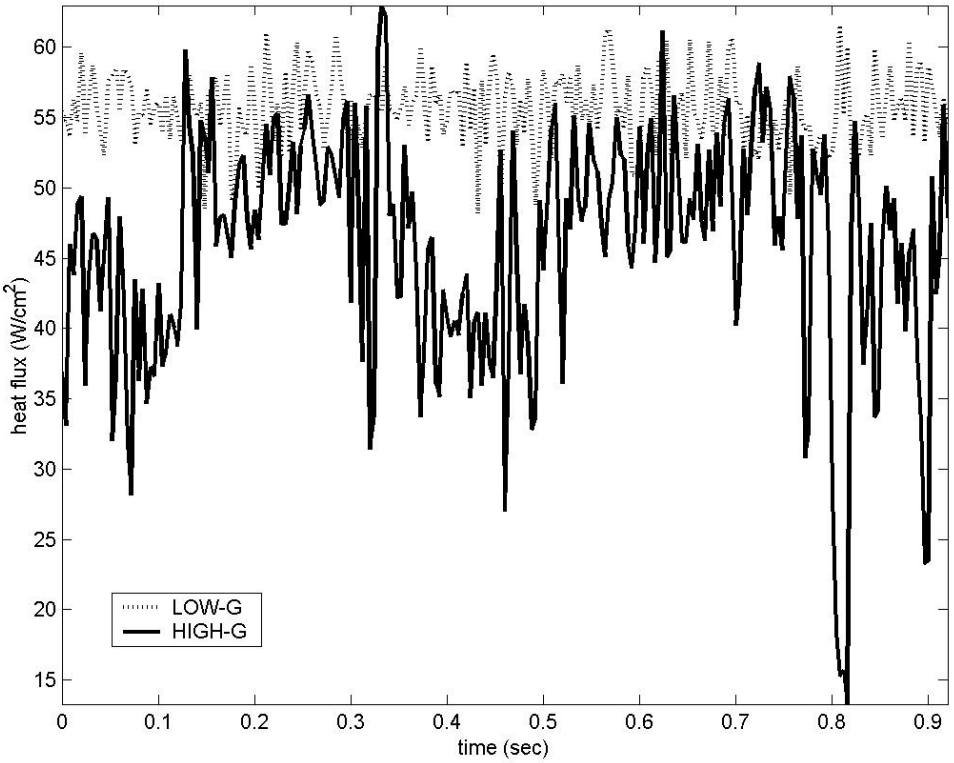

(b) Time resolved boiling over one second.

Figure 5.20: 2.7 x 2.7 mm^2 heater, T_{wall} =100°C, T_{bulk} = 28°C heater #96 (corner heater).

primary bubble area and continuously wetted with bulk liquid. As shown in Fig 5.21a, vapor generated in this region is removed by the primary bubble allowing continuous thin film vapor generation throughout low-g. In high-g, the corner heater is occasionally partially covered with a bubble and this causes the heat transfer to drop dramatically, Fig 5.21b. When this bubble departs a spike in the heat transfer is measured.

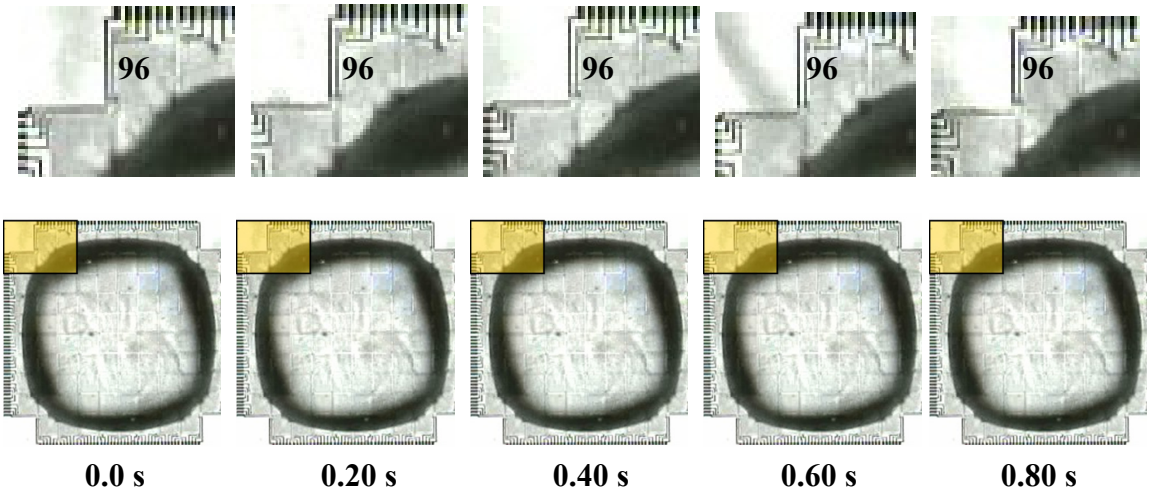

(a) Low-g time resolved image sequence. $\Delta T_{sat} = 43°C$, $\Delta T_{sub} = 29°C$

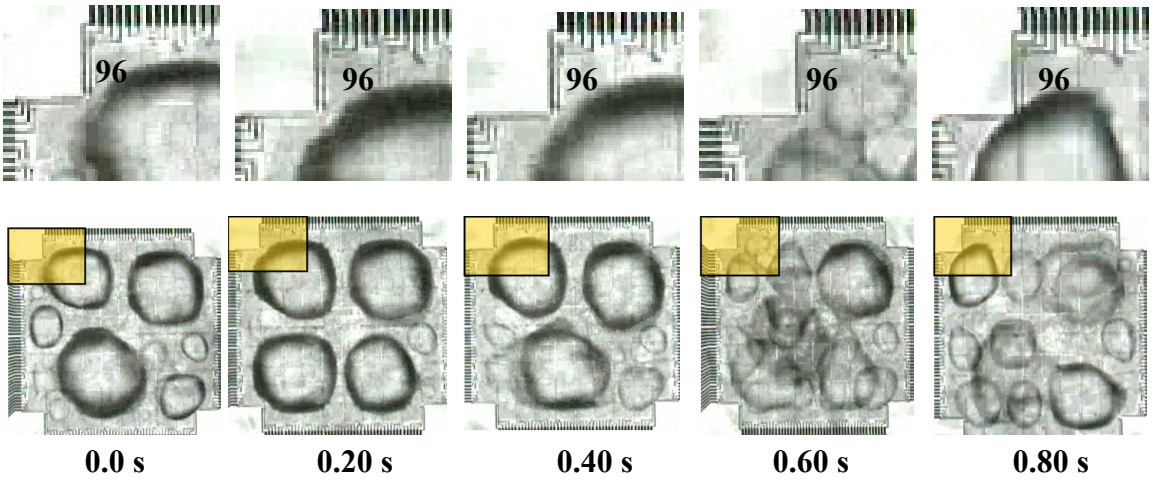

(b) High-g time resolved image sequence. $\Delta T_{sat} = 41°C$, $\Delta T_{sub} = 30°C$.

Figure 5.21: Time resolved boiling images in high-g (b) and low-g (a).

At high wall superheats and bulk subcoolings, the presence of strong thermocapillary convection was observed. Analyzing the wetted area in low-g further shows a number of interesting trends. First, the effect of bulk liquid subcooling on wetted area heat transfer is shown in Fig. 5.22. In high-g the time averaged wetted area heat flux is independent of bulk subcooling. This agrees with the data presented in the previous chapter which showed that subcooling had a negligible effect on the boiling heat flux in the nucleate boiling regime and agrees with the work of other researchers presented in Chapter 1. In low-g, a nearly linear dependence of subcooling on wetted area heat flux is observed. This indicates that the bulk liquid subcooling in low-g influences the thermocapillary flow as mentioned previously. The data from various subcoolings and wall superheats is plotted in Fig. 5.23 showing that the data tends to

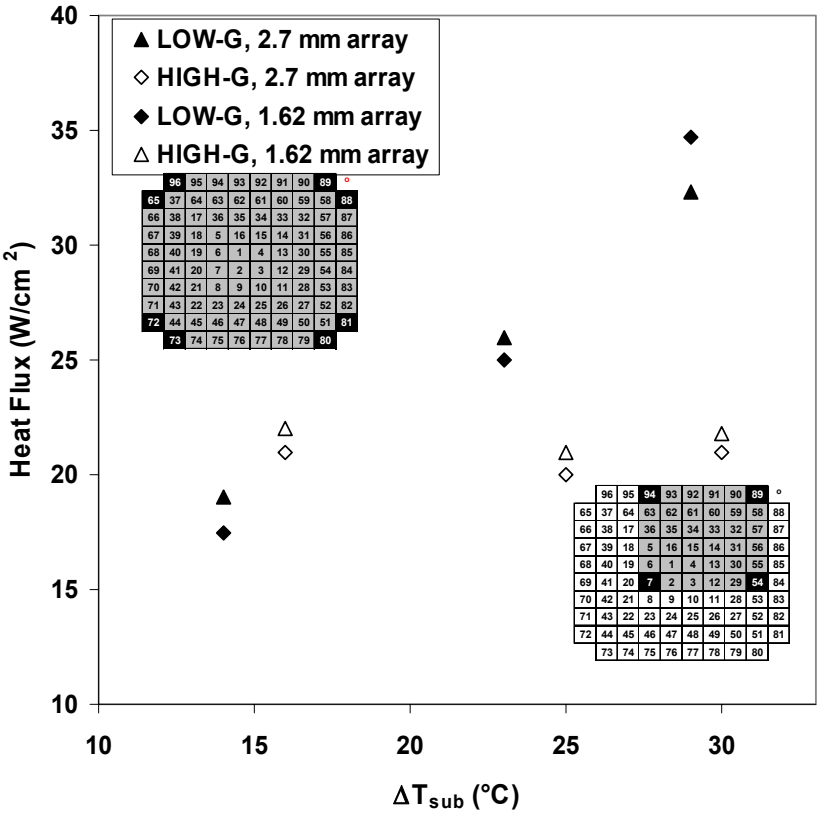

Figure 5.22: Wetted area heat flux at various subcoolings for T_{wall} = 90°C.

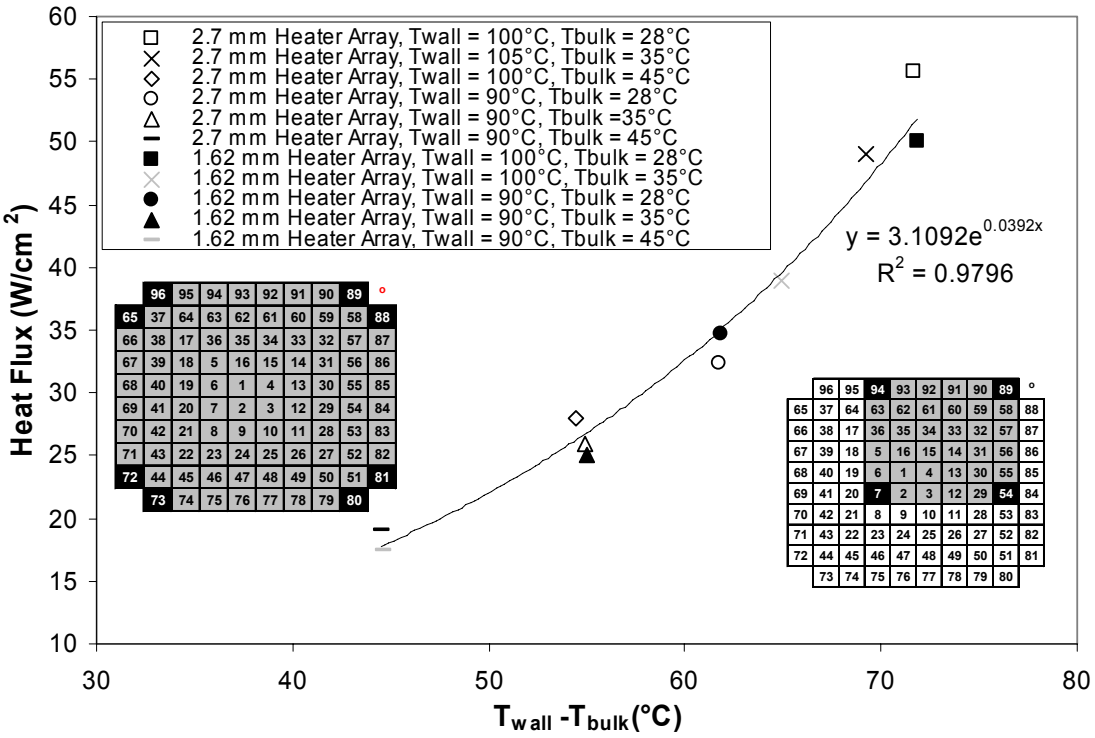

Figure 5.23: Low-g time and surface averaged heat transfer from the wetted area for various heater arrays and different wall superheats and subcoolings.

collapse onto a single curve indicating that the driving temperature difference for such flows is the wall temperature minus the bulk temperature. The heat transfer coefficient obtained from the wetted area and the wall temperature minus the bulk temperature, which appears to be the driving temperature difference, is shown in Fig. 5.24. It can be inferred that increased subcooling enhances the thermocapillary flow rate around the bubble which acts to enhance the heat transfer coefficient in the wetted area.

Further information about the thermocapillary phenomenon can be obtained by considering a number of different analytical models. An estimate of the liquid velocity around the primary bubble during thermocapillary convection can be obtained by considering the bubble shape and heat transfer measured. This model will be referred to as the "latent heat transfer model". If it is assumed that all of the measured heat flux

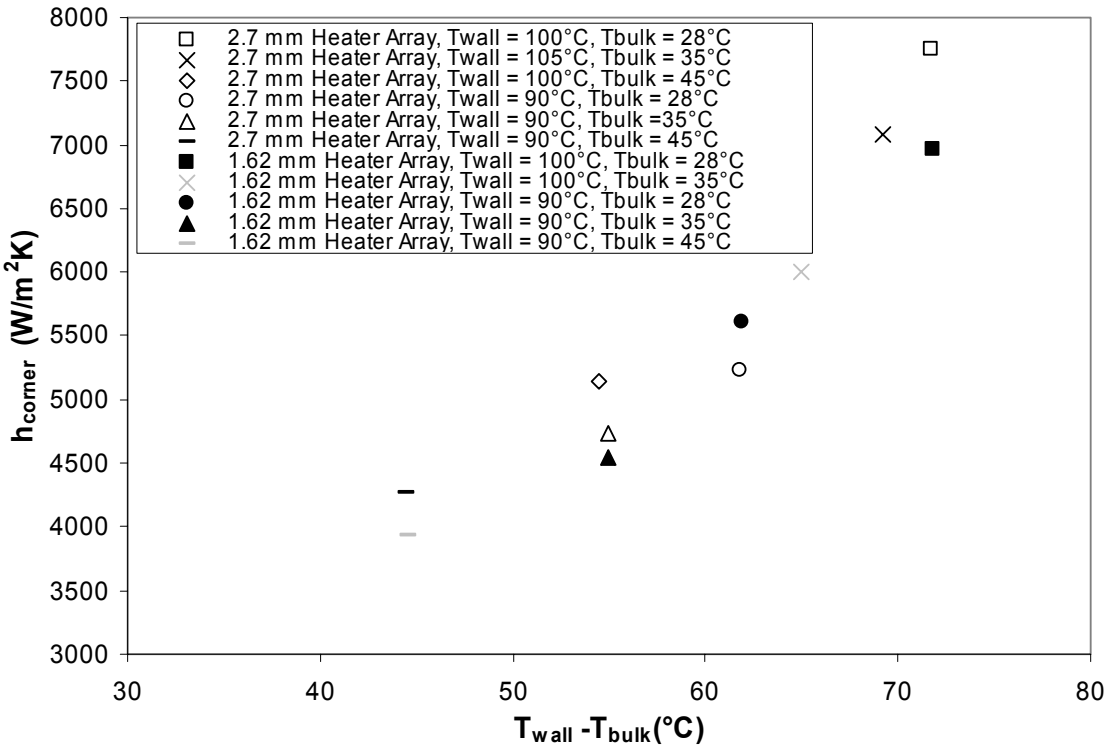

Figure 5.24: Low-g time and surface averaged heat transfer coefficient from the wetted area.

from the wetted heater area goes into latent heat transfer, the vapor generated near the base of the bubble must condense somewhere along the primary bubble surface area, Fig. 5.25. From the bottom view images, the wetted area can be calculated by subtracting the heater area by the primary bubble dryout area. The area for vapor condensation to occur across the primary bubble interface is assumed to be some fraction of the total surface area of the primary bubble, f. It is assumed that the majority of the primary bubble area has condensation occurring across it and vapor is only generated in a small region near the contact line. From the equations shown in Fig. 5.24, an estimate of the average liquid velocity normal to the bubble interface can be obtained, 2.5 mm/s < v_{liq} < 10 mm/s. These equations represent a simple energy balance near the heater surface and assumes all of the measured heat transfer goes into vapor generation and a mass balance over the

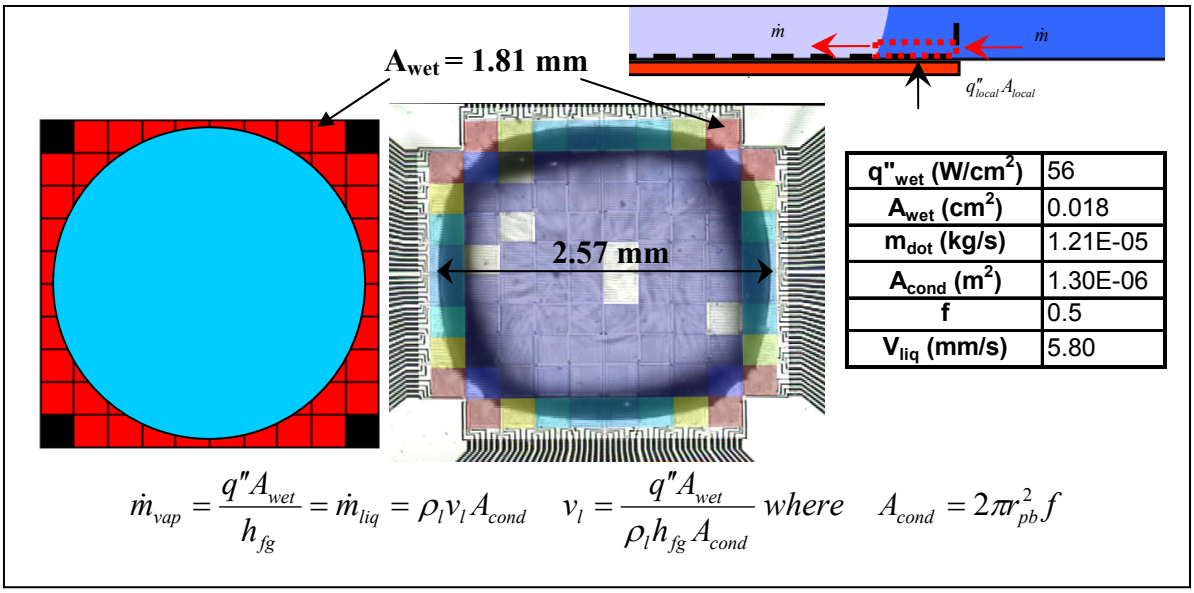

q''_{wet} (W/cm^2)	56
A_{wet} (cm^2)	0.018
m_{dot} (kg/s)	1.21E-05
A_{cond} (m^2)	1.30E-06
f	0.5
V_{liq} (mm/s)	5.80

Figure 5.25: Thermocapillary convection velocity analytical model example for following condition, 2.7 x 2.7 mm^2 heater array, ΔT_{sat} = 43°C, ΔT_{sub} = 29°C.

same region equates the vapor mass flux to the liquid mass flux. The calculated velocity values provide a good analytical estimate of the minimum liquid velocity directly above the bubble interface and is in good agreement with experimentally measured values (15 mm/s -140 mm/s, Wang et. al, 2005). During the presence of thermocapillary convection, the actual liquid velocity above the bubble is expected to be higher than this value due to the presence of thermocapillary stresses which provide additional impetus for flow.

The second analytical model developed, referred to as the "sensible heating model", was created based on the experimental results shown in Fig. 5.23 which identifies the bulk fluid temperature and wall temperature as the driving temperature difference for thermocapillary flow. This model assumes the primary bubble acts as a heat pump bringing in liquid from the bulk fluid at its base and pumping the fluid along the two-phase interface until it is expelled at the top of the bubble in a saturated thermodynamic state. A diagram of the model is shown in Fig. 5.26. This model

predicts a zero liquid velocity in low-g under bulk saturated conditions which is similar to what was observed at the lowest subcooling measured experimentally. This model assumes the heat transfer is directly proportional to the bulk subcooling level which has been shown to strongly influence the strength of thermocapillary convection, Fig 5.26.

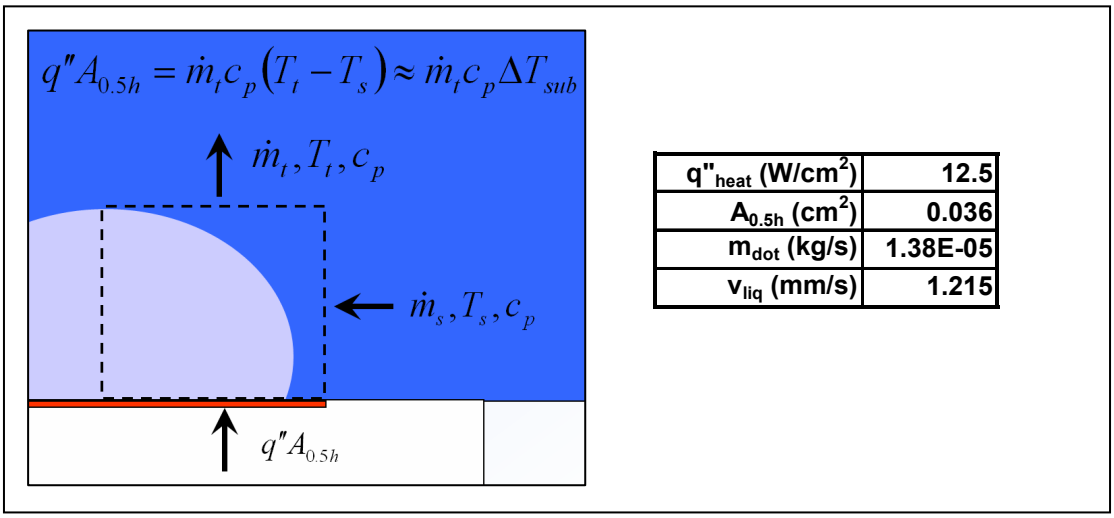

q''_{heat} (W/cm^2)	12.5
$A_{0.5h}$ (cm^2)	0.036
m_{dot} (kg/s)	1.38E-05
v_{liq} (mm/s)	1.215

Figure 5.26: Sensible analytical model for the liquid velocity above the vapor bubble. Example for following condition, 2.7 x 2.7 mm^2 heater array, ΔT_{sat} = 43°C, ΔT_{sub} = 29°C.

5.2.3 0.8 x 0.8 mm^2 (9 heater array)

Images of the boiling behavior for a nine heater array are shown in Fig. 5.27. Boiling curves for the nine heater array in low-g are presented in Fig. 5.28. At low wall superheats, ΔT_{sat} < 15 °C, the transport process was dominated by single phase conduction and convection to the bulk fluid. For the nine heater array, a primary bubble was observed to form and cause dryout over significant portions of the heater surface. Subcooling was found to have little effect on the size of the dry area. At low wall superheats, the primary bubble oscillated laterally on the surface. The cause of such oscillations is currently unknown but may be due to g-jitter aboard the aircraft. The magnitude of oscillations decreased with increasing wall superheat and the size of the dry

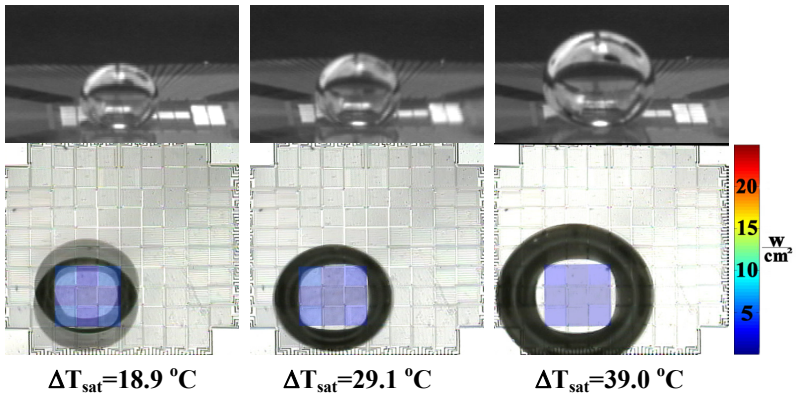

Figure 5.27: Low-g time averaged boiling images from a 0.81 x 0.81 mm^2 heater array.

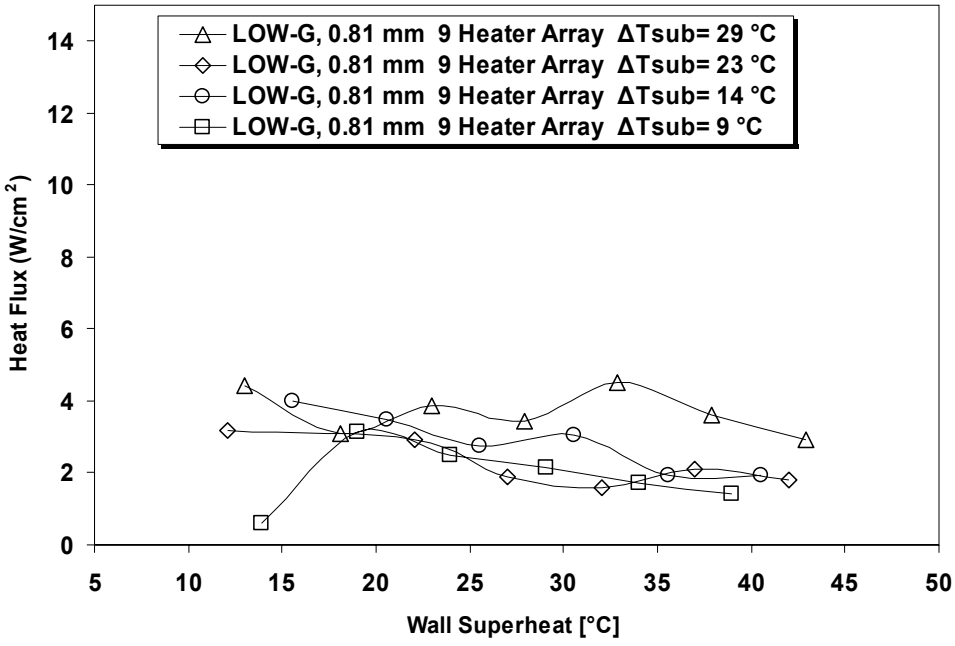

Figure 5.28: Low-g boiling curves for a 0.81 x 0.81 mm^2 heater array.

area increased, resulting in a lower average heat flux. CHF appears to occur at very low superheats immediately following boiling incipience. Also, in contrast to boiling from larger heaters, the onset of thermocapillary convection was not observed. This may be due to the heater size and amount of satellite bubble formation in addition to the size of the primary bubble which is much smaller and therefore may not grow large enough to grow out of the superheated liquid layer. This observation suggests that if the growing primary bubble is within the superheated region, then the onset of thermocapillary convection cannot occur. Furthermore, this also suggests that the superheated boundary layer thickness is an important scaling parameter and its value relative to the heater length appears to strongly influence thermocapillary behavior. A complete listing of the boiling images from this array is shown in Fig 5.29.

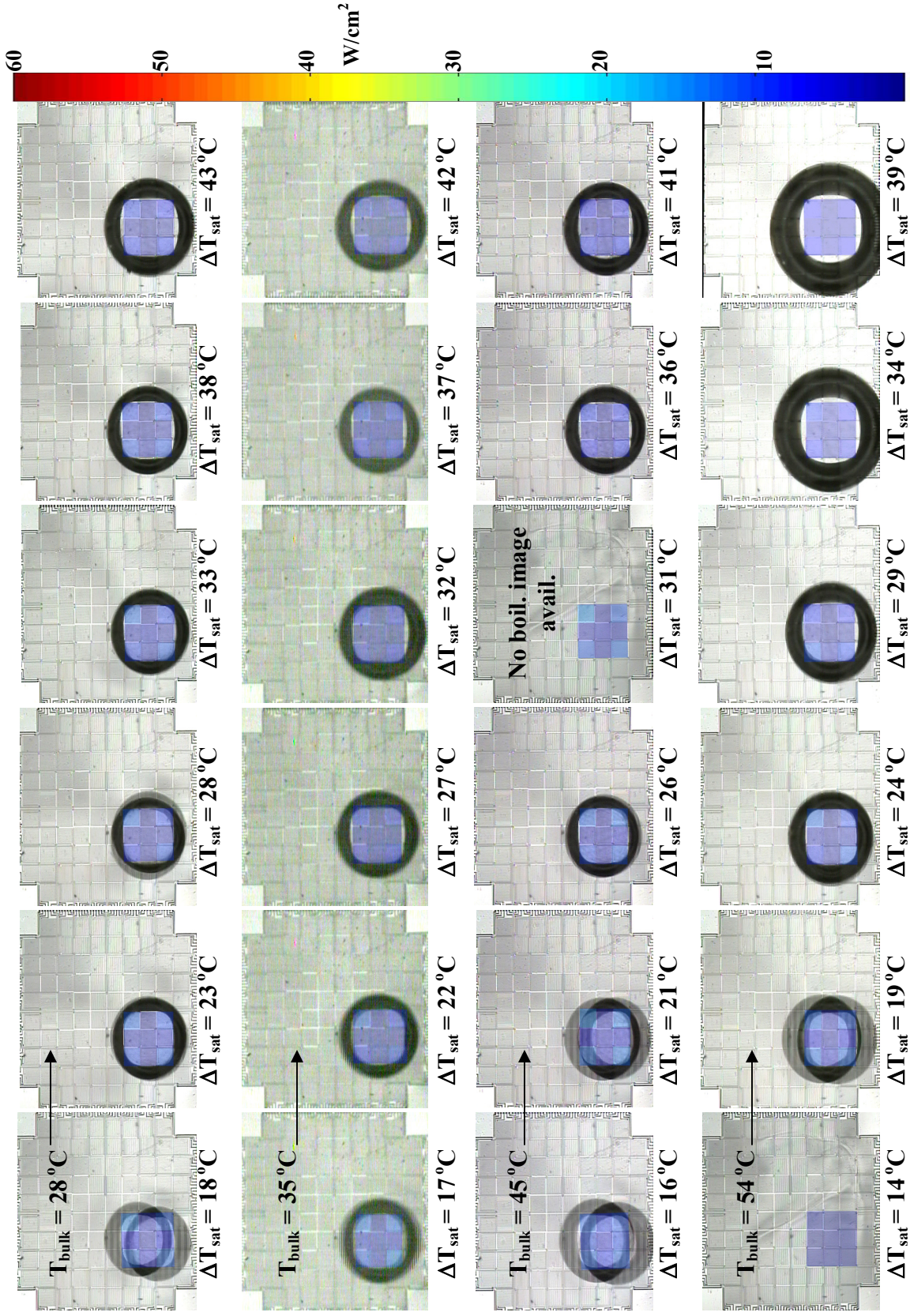

Figure 5.29: Time-averaged, spatially resolved heat flux maps of boiling process for a 9 heater array in low-g at various ΔT_{sat} and T_{bulk}.

5.3 LOW-G HEATER SIZE EFFECTS SUMMARY

Boiling curves from all of the square heaters investigated in this study are shown in Fig. 5.30. It appears that low-g boiling behavior on square heaters appears to be dominated by the dynamics of the primary bubble. At low wall superheats (ΔT_{sat} < 18°C), boiling performance appears to be constant across gravity levels. At higher wall superheats, boiling performance is significantly reduced in low-g. Increased subcooling decreases

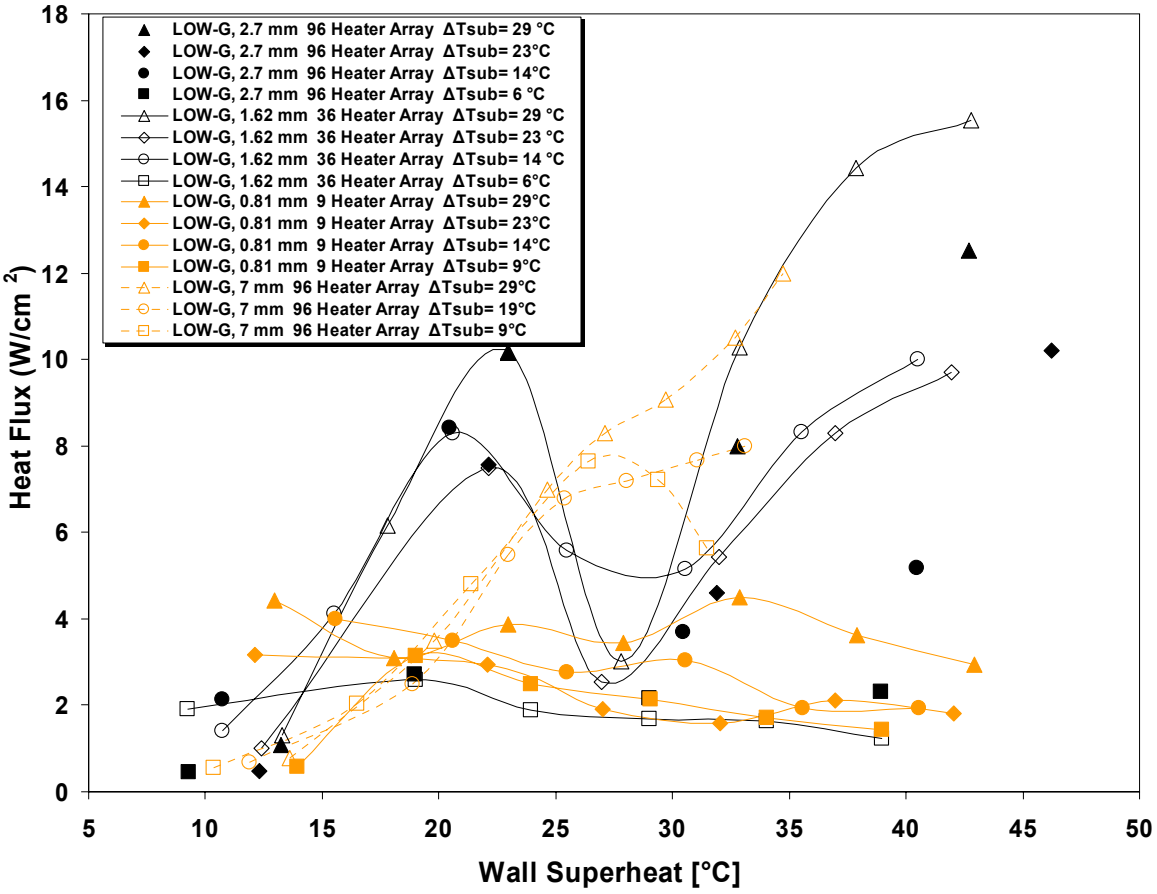

Figure 5.30: Low-g boiling curves for various heater sizes and subcoolings.

the size of the primary bubble, allowing satellite bubbles to form with a corresponding increase in heat transfer. CHF for the intermediate sized heaters, appeared to be a result

of the competition between increasing heat transfer associated with the satellite bubbles and the decrease in heat transfer due to growth of the dry area under the primary bubble as the wall superheat increases. It was shown that the primary mode of heat transfer at CHF was single phase conduction to the rewetting fluid. Depending on the heater size, there appears to be an initial CHF which is dominated by satellite bubble coalescence. This is attributed to heater dryout and the reduction of bubble removal mechanisms such as buoyancy. Increased subcooling appears to delay the reduction in boiling performance (compared to high-g) to higher wall superheats. Thermocapillary convection may be responsible for the post-CHF increase in heat flux observed on the two intermediate sized heaters (2.7 mm-6x6 and 2.7 mm-10x10) at higher subcoolings. For the largest heater (7 mm-10x10), CHF was not observed at high subcoolings although the thermocapillary mechanism was still dominant.

Multiple models were presented that predict the liquid flow velocity above the bubble at higher wall superheats and subcoolings (post CHF). It is thought that increased subcooling causes increased condensation at the bubble cap, resulting in a smaller bubble, which in turn increases the temperature gradient along the surface of the bubble. This leads to an increase in the strength of the thermocapillary convection, which brings cold liquid to the bubble cap increasing condensation and causing the bubble to shrink even further. The ultimate size of the primary bubble results from a balance between vapor removal by condensation and vapor addition by evaporation at the base which is primarily due to coalescence with the satellite bubbles.

The size of the heater appears to strongly affect the primary bubble size and onset of thermocapillary motion through its effect on the superheated boundary layer near the

surface. As indicated, the boiling performance for the smallest heater 0.8 x 0.8 mm^2 is very different from boiling from larger heaters in low-g.

In a low-g environment, the thermal boundary layer during the initial growth of the bubble near the heater can be modeled using a single phase axisymmetric transient conduction model. Assuming no vapor generation, the model is shown in Fig 5.31. In this figure, boundary 4 represents the heater which is at bulk temperature at time =0 and then set to T_{wall} for t>0. Boundaries two and five are constant temperature boundaries where $T = T_{bulk}$. Boundary 1 is an insulated boundary and boundary 3 is an axisymmetric boundary. The length of boundary four relative to the length of all other boundary is sufficiently small such that the effects of boundary 2 and 5 are negligible over the time scales considered. The transient conduction model was developed and

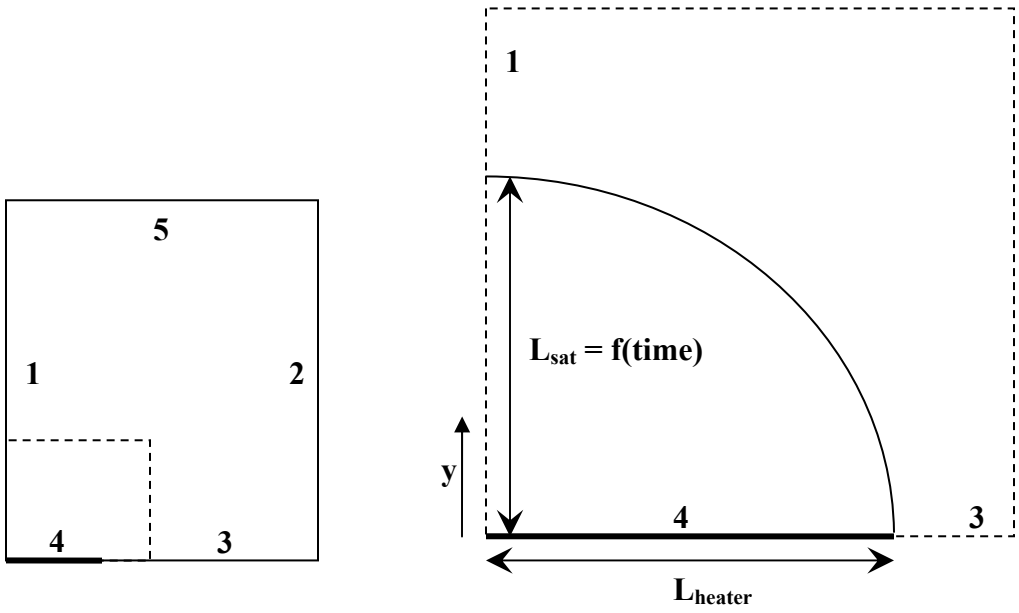

Figure 5.31: 2-D axisymmetric model of the thermal boundary layer near the heater surface in low-g.

analyzed using FEMLAB. In Fig 5.31, the two pertinent length scales should be noted, L_{heater}, or the length of the heater array, and L_{sat}, or the superheated boundary layer

thickness which is defined as the vertical distance away from the heater element where the temperature of the liquid is above the saturation temperature. It should also be noted that L_{sat} is a function of time.

Different numerical results were obtained by varying L_{heater} to correspond to the actual heater lengths encountered in this experiment. Representative results obtained in FEMLAB at a given time are shown in Fig. 5.32. In this figure a hemispherical boundary is drawn on the contour plot which would represent the maximum size of a growing

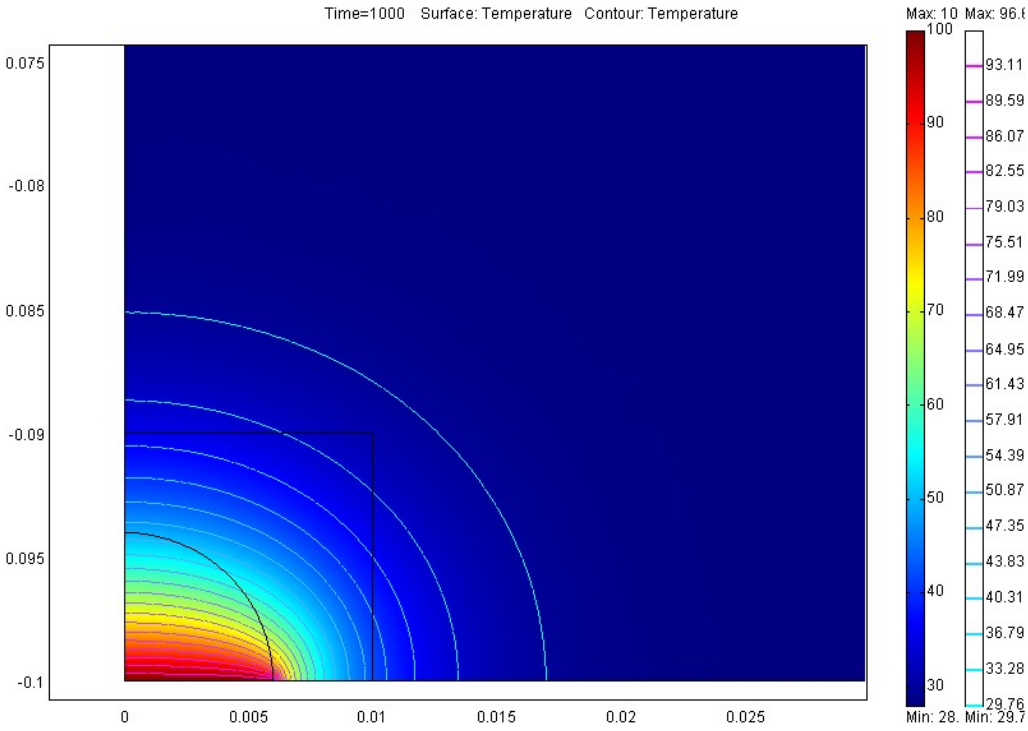

Figure 5.32: Axisymmetric transient conduction results for a 7 mm heater at t = 1000 s. The x and y axis represent the distance in meters, and the colors represent the temperature, T_{wall} = 100°C. T_{bulk} = 28°C.

bubble on the heater surface (constrained from growing larger than the heater). A growing bubble is constrained from growing by two different mechanisms. Firstly, if the bubble reaches a diameter the size of the heater array, it is constrained from further

growth and secondly, the bubble may reach a height above the heater (bubble radius) where cool liquid at the two-phase interface prevents further growth by allowing significant condensation.

A plot of the thermal boundary layer development as a function of time is shown in Fig. 5.33. It is significant to note that the boundary layer does not develop in a hemispherical manner. This has profound effects for a hemispherically growing bubble that is on the heated surface. Firstly, consider the various length scales mentioned above,

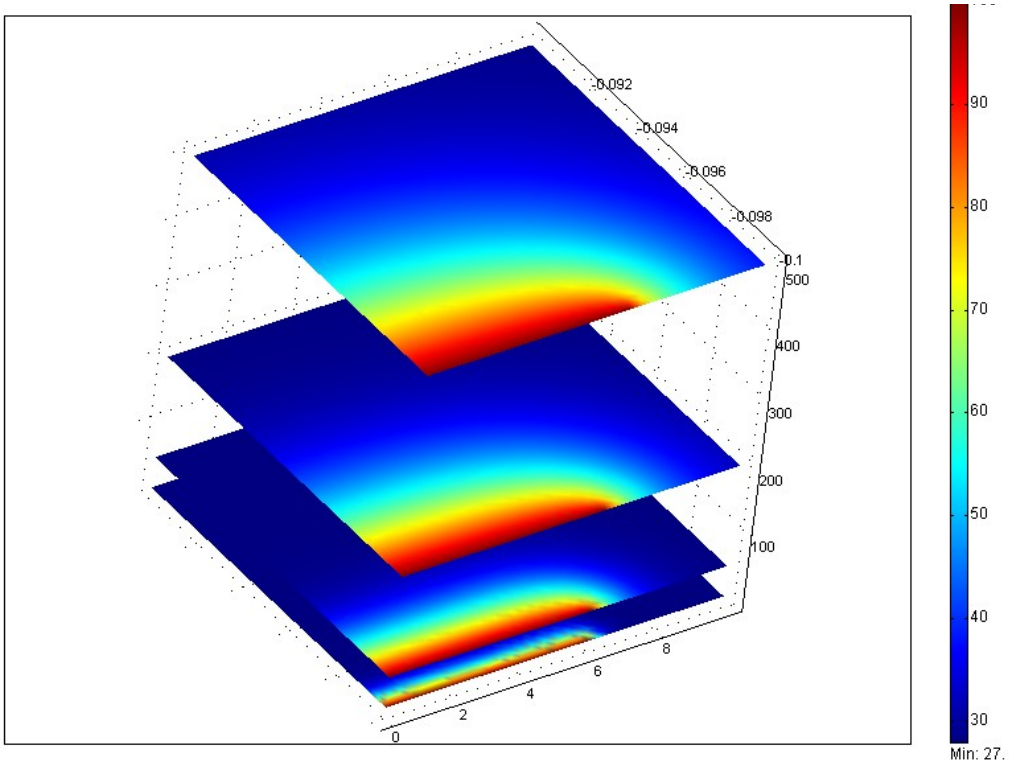

Figure 5.33: Time resolved boundary layer development. Colors represent temperatures and the vertical axis represents various times.

L_{sat} and L_{heater}. A non-dimensional number can be defined which is the ratio of these lengths. This value is plotted as a function of time in Fig. 5.33 for the various heater lengths investigated experimentally. It is interesting to note that the growth of the

superheated region is much faster for the smaller heater array than for the larger heaters. Furthermore, it is assumed that a hemispherically growing bubble on the surface is limited in radius by L_{sat} or L_{heater}, whichever is smaller. In Fig 5.34, for the smallest heater array, L_{sat} is equal to L_{heater} in a much smaller time than for the larger heater arrays which may explain why the bubbles for this array cause dryout over the heater array for all conditions investigated. The experimentally measured bubble shapes for this heater are shown in Fig 5.35. It is clear from the data that the bubbles that grow from a 0.8 x 0.8 mm^2 heater array are much less hemispherical than the bubbles observed from the larger arrays. It can be inferred that the bubble wants to continue to grow vertically above the heater surface but is constrained from growing laterally by the heater boundary. This indicates that the bubble has not reached sufficient height to allow significant

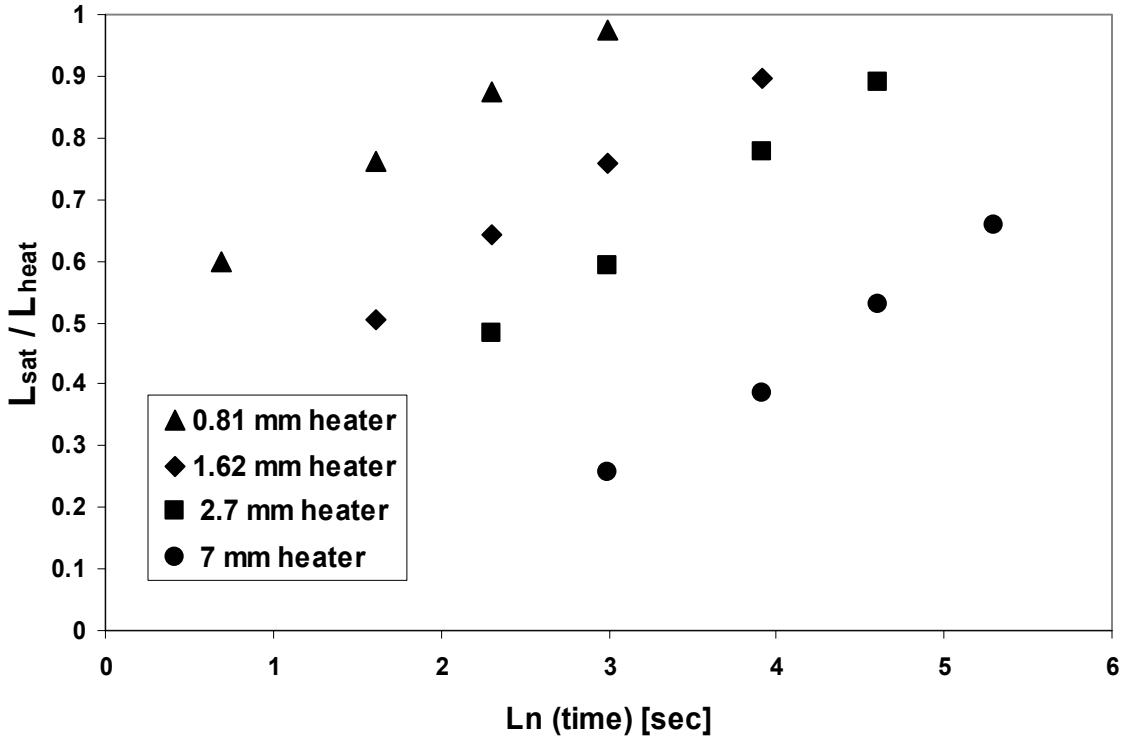

Figure 5.34: Development of the superheated boundary layer for various heaters (numerical results obtained using FEMLAB).

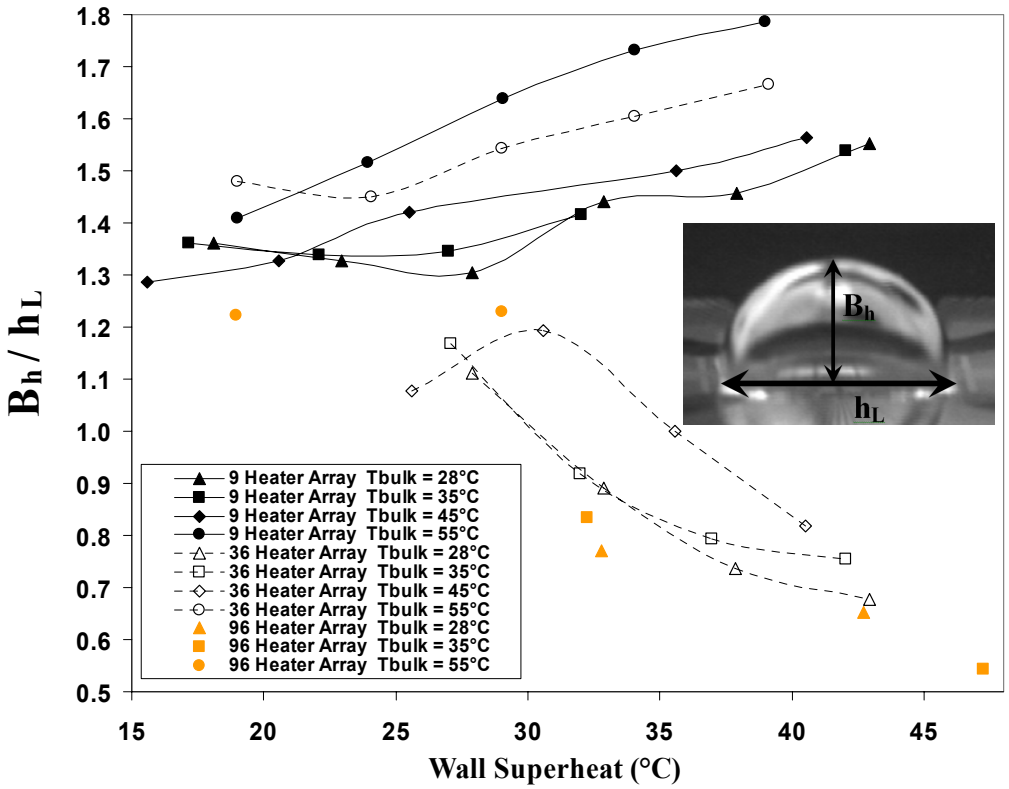

Figure 5.35: Primary bubble geometric characteristics for different heaters.

condensation to occur above the bubble. It appears that the constraining mechanism on bubble size is not growth of the superheated boundary layer but is instead the heater length.

For the 7 mm heater array the observation is completely the opposite. Firstly, note that CHF was not observed experimentally for this array at high subcoolings as opposed to the two intermediate sized heaters where CHF was defined as the breakdown of the satellite bubbles into a single primary bubble on the heater surface. For the 7 mm heater array, a single primary bubble was never observed to cover the entire array. This might again be explained by Fig 5.34 which shows that for a 7 mm array, the time required for the thermal boundary layer to grow to the size of the heater length is very large. In other words, it appears the constraining bubble growth mechanism is the development of the superheated boundary layer and not the heater length.

The above model is valid for short times after nucleation where the bubble begins to grow and remains inside the superheated region. Once the bubble reaches a stable size, which occurs at later times, thermocapillary motion and additional mass fluxes across the vapor bubble interface (condensation) may significantly affect the thermal and velocity boundary layers around the bubble. For the larger heaters, strong thermocapillary motion was observed at higher wall superheats and it is acknowledged that the model presented is less valid. The above analysis should be used instead to understand the growth of the boundary layer around the small heater array, 0.81 x 0.81 mm^2, where liquid motion was not observed and dryout occurred under all conditions. A more vigorous model would account for evaporation, condensation and thermocapillary effects along a two-phase interface. In summary, it appears that the size of the primary bubble compared to the heater size determines the heat transfer. The wall superheat, heater size, subcooling, and the development of thermocapillary convection all impact the size of the bubble that forms.

In conclusion, as the heater gets larger, it takes a much longer time for the thermal boundary layer thickness, measured directly above the center of the heater, to reach a length equal to the heater length. If the growing bubble extends out of the superheated layer, condensation and thermocapillary effects become increasingly significant. As an example, consider a hemispherically growing bubble. As the bubble grows, if the bubble quickly extends out of the superheated region and begins to condense before the bubble can reach a diameter that is equal to the heater length then the governing length scale is the superheated boundary thickness (as is in the larger heater, 7 mm). In contrast, consider a hemispherically growing bubble that reaches a diameter that is equal to the

heater length and is within the superheated boundary layer. Under such conditions, the bubbles is constrained from further lateral growth by the heater and grows vertically within the superheated boundary layer. If the heater is completely covered by vapor, the bubble may not extend out of the superheated region (as in the small heater case, 0.81 mm).

5.4 HEATER ASPECT RATIO EFFECTS

5.4.1 Comparison of 2 x 2, 1.4 x 1.4 mm^2 array and Baseline Heater (1.62 x 1.62 mm^2)

The 2x2 array on the 7x7mm^2 heater was of similar overall size (1.92 mm^2) to that used to obtain the baseline data, 1.62 x 1.62 mm^2 (Fig. 5.7). At low superheats (ΔT_{sat} < 29.5°C) nucleation did not occur and the heat transfer was due to conduction and convection to the fluid. G-jitter in the three coordinate directions during the low-g portion of parabolic flight and undamped natural convection may have caused small scale convection within the test chamber. Compared to the baseline boiling curve, differences can be attributed to a lower wall superheat used to initiate boiling in the larger 7 mm case compared to the baseline case. In those cases where nucleation did occur at low wall superheats, a clear reduction in active nucleation sites compared to the baseline case was observed. This may be attributed to the fact that these two heater arrays were made approximately two years apart and the oxide deposited on the surface may not have the same structure. The width and length of the serpentine resistance elements were also different, perhaps leading to a different surface morphology. Lastly, the extensive degassing process used for the larger array may have resulted in a deactivation of nucleation sites that might have been active if a small amount of gas were present.

An increase in superheat to 29.5°C resulted in the formation of a stable primary bubble which caused dryout over most of the heated surface, similar to what was observed for the baseline data at a similar superheat. Increasing the superheat to 34.7°C increased the strength of the thermocapillary convection and reduced the primary bubble size, allowing additional wetting of the heater edges and corners. The ratio of wetted to heated area was measured from the images to be from the images to be 68% for the 2x2 array, and 31% for the baseline data at similar superheats. The increase in wetted area is directly proportional to the increase in the heat transfer (roughly 50%).

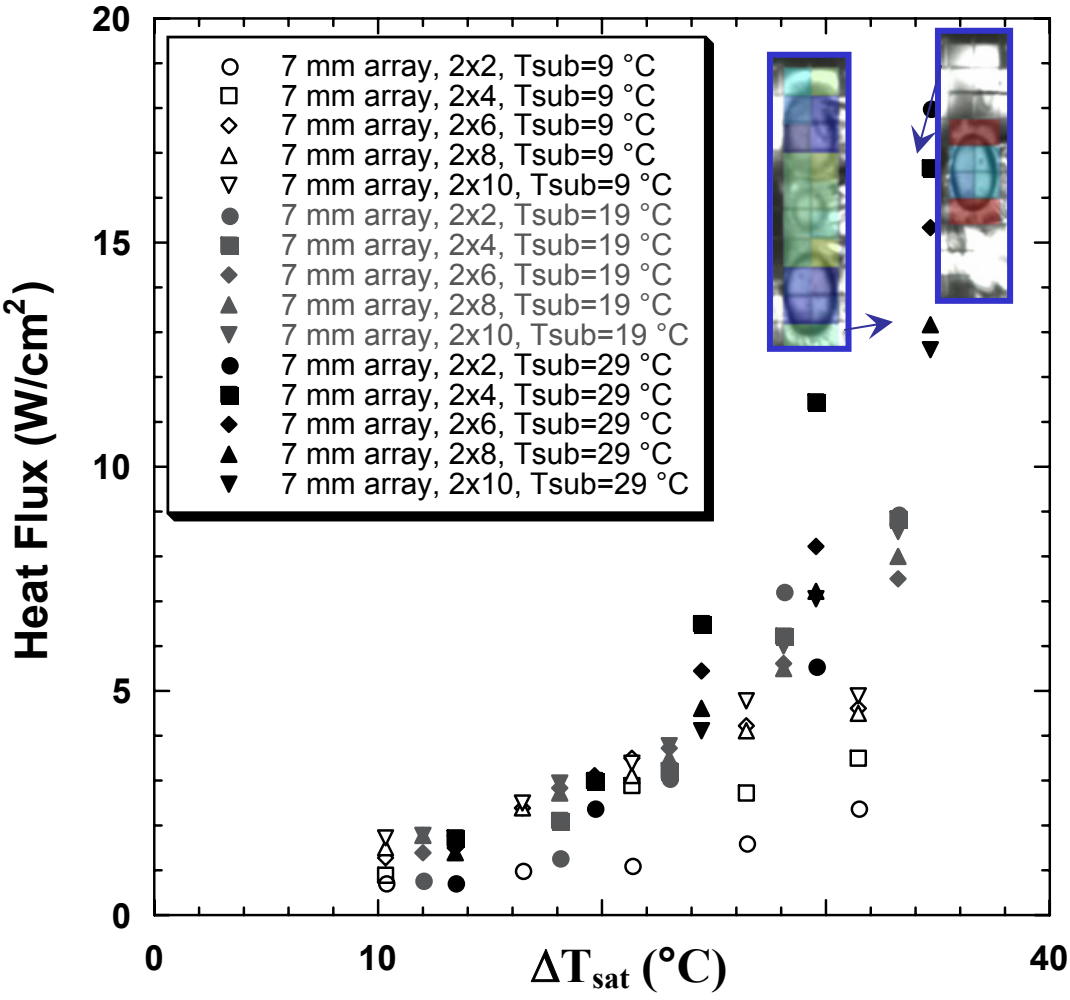

Figure 5.36: Boiling curves for various aspect ratio heaters at various bulk subcoolings.

5.4.2 Aspect Ratio Effects

Boiling curves for heaters of various aspect ratio (2x2, 2x4, 2x6, 2x8, and 2x10 heaters powered on the 7 mm array) at three subcoolings (9°C, 19°C, and 29°C) are shown on Fig. 5.36. Images of the boiling behavior obtained through the heater array are shown on Fig. 5.37. In general, higher subcoolings for a given aspect ratio result in higher overall heat transfer. The boiling behavior at various subcoolings is described below. The heater aspect ratio was changed by varying the number of heaters powered (2x2, 2x4, 2x6, 2x8, 2x10, and 10x10) on a 7x7 mm^2 array.

5.4.2.1 Low subcooling. For all aspect ratios at low superheats (<20°C), the nucleation site density was very low as described above. The heat transfer process is this regime is dominated by conduction and convection to the bulk liquid. At low subcooling, the heat flux appears to increase with increasing aspect ratio, especially at higher superheats. Thermocapillary motion around the bubble was observed to be very weak. For example, at ΔT_{sat}=31.4°C (Fig. 5.38), it can be seen that large increases in the wetted area fraction occur as the aspect ratio increases from 2x2 to 2x6. On non-square heaters, surface tension acts to pull the bubble away from the ends of the array, allowing liquid to partially rewet the surface and the bubble shape becomes less spherical. As seen from the images, the wetted area fraction increases from nearly 0% (2 x 2 array) to 25% (2 x 6 array) and correspondingly larger increases in heat flux are observed. The wetted area fraction increases less dramatically between 2x6 and 2x8 (25-28%) with smaller increases in heat flux. On the 2x10 array, two large bubbles are observed, Fig. 5.38, which may result in a nominally larger increase in wetted area and larger heat transfer. In the absence of thermocapillary effects, larger aspect ratio heaters may enhance the heat

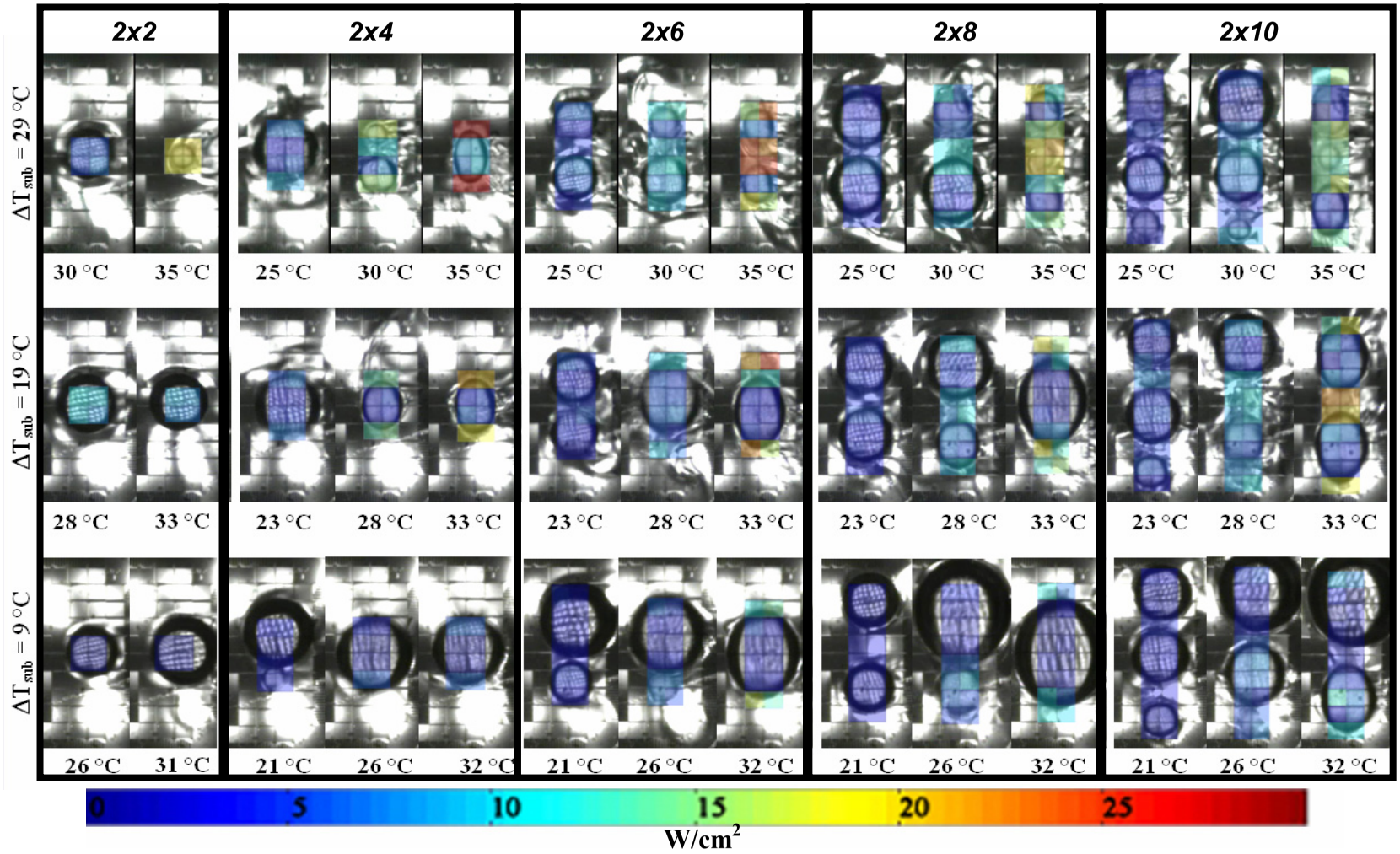

Figure 5.37: Images of boiling on heaters of various aspect ratio. The superheat at which the images were obtained are listed below each image. Each heater in the array has been shaded according to the time average wall heat transfer.

transfer by allowing multiple bubbles to form on the surface increasing the wetted area. Also, the presence of multiple bubbles allows bubble coalescence which has been shown to account for the majority of the heat transfer in low-g near CHF. The aspect ratio can have a dramatic effect on the heat transfer by affecting the shape of the bubble which dictates the wetted area fraction.

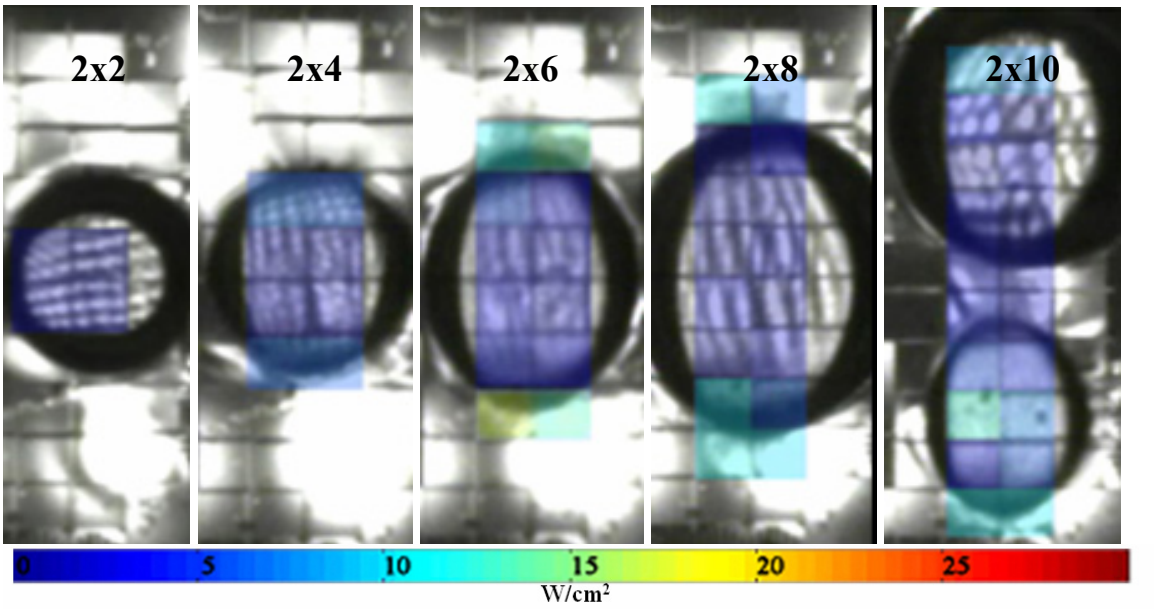

Figure 5.38: Time averaged heat transfer from heaters of various aspect ratio, ΔT_{sub} = 9°C, ΔT_{sat} = 32°C.

5.4.2.2 High Subcooling. At low superheats (<20°C), the nucleation site density was very low as described above. At higher wall superheats, the heat transfer tends to decrease as the aspect ratio is increased from 2x4 to 2x10. At a superheat of ~24.6°C, a single oblong bubble is observed on the 2x4 array. This bubble moved slightly back and forth on the surface as it merged with smaller bubbles nucleating at the ends of the array, accounting for the higher heat transfer at the ends. As the aspect ratio increases, the single bubble split into two bubbles (2x6 and 2x8) due to surface tension effects. On the

2x10 array, the increased heater area allows for additional nucleation sites, but similar heat transfer levels are observed. At high subcooling (ΔT_{sub}= 29°C) the heat flux increases slightly with aspect ratio at low superheats (<20°C). Visual observations indicated that the nucleation site density was very low under such conditions. At higher superheats, the heat flux decreases as the aspect ratio increases, contrary to what was observed at low subcooling. Heat fluxes up to 30 W/cm^2 are seen around the three phase bubble interface.

Bubble motion for a superheat of ~29.7°C is shown on Fig. 5.39. Boiling on the 2x4 array was the result of the interplay between thermocapillary convection and bubble coalescence. The thermocapillary convection decreased the size of the primary bubble, allowing additional bubbles to form. Two bubbles occasionally merged into a single bubble at the center of the heater (which subsequently shrinks due to thermocapillary convection) allowing new bubbles to nucleate at the ends. The large bubble then merges with one of the growing bubbles, and the cycle repeats.

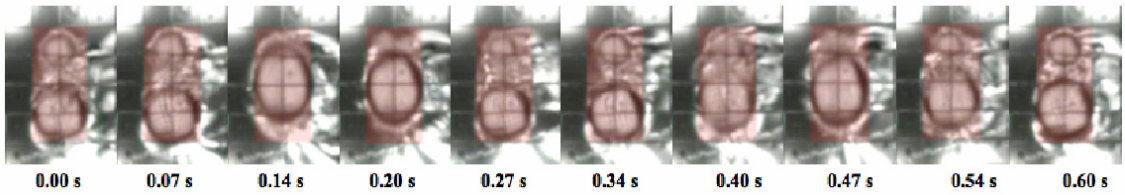

(a) 2x4 heater array

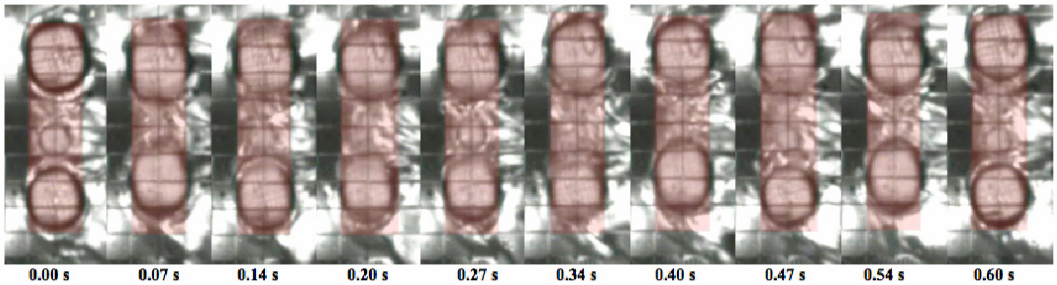

(b) 2x8 heater array

Figure 5.39: Time lapse images for the (a) 2x4 and (b) 2x8 arrays at ΔT_{sat} = 29.7°C.

To a first approximation, the trends in the high subcooling data might be due to the increasing two dimensionality of the flow field around the heater. The 2x2 array experiences thermocapillary convection from all four sides of the array equally, causing the primary bubble size to shrink to its minimum value. As the aspect ratio increases, thermocapillary convection from the ends of the array become less important, and the bubble is cooled only on two sides.

Thermocapillary convection dominated boiling is observed at the highest superheat (34.7°C). The size of the bubbles on all of the heaters decreases as the superheat is increased, which is due to increased thermocapillary flow causing enhanced condensation on the top of the bubbles. More of the heater surface is wetted by liquid, allowing nucleation to occur. The nucleating bubbles merge with the larger bubbles, resulting in higher heat transfer. The large bubbles on the 2x4 and 2x6 arrays were stable, while the large bubbles on the 2x8 and 2x10 arrays occasionally merged with the nucleating bubbles, disturbing the steady thermocapillary convection that had been developed and decreasing the heat transfer from the edges.

5.4.2.3 Intermediate Subcooling. At the intermediate subcooling (ΔT_{sub}= 19°C), the data tends to collapse onto a single curve. This case represents a case where both thermocapillary convection and surface tension are important.

5.4.3 Summary of Heater Aspect Ratio Effects

With varying aspect ratios, there appears to be two boiling mechanisms at play: thermocapillary convection and surface tension. In both cases, as the wetted area increases so does the heat transfer. At low subcooling, it appears that the heat transfer increases due to an increase in wetted area fraction when surface tension acts to pull the

bubble away from the heater edges at higher aspect ratios. At high subcooling, thermocapillary convection causes the primary bubble to shrink due to increased condensation, resulting in more wetted area.

At high wall superheats and subcoolings, boiling performance appears to decrease with an increase in aspect ratio. Again as for the square heaters, strong thermocapillary convection was observed even for gas concentrations in the liquid <3 ppm. The origins for the thermocapillary convection are not known, but may be due to contaminants in the liquid. The effect of heater aspect ratio on the boiling performance is shown in Fig. 5.40. It is predicted that as the aspect ratio is increased above the measured values, multiple bubbles would form on the heater surface causing the performance to be independent of the heater aspect ratio.

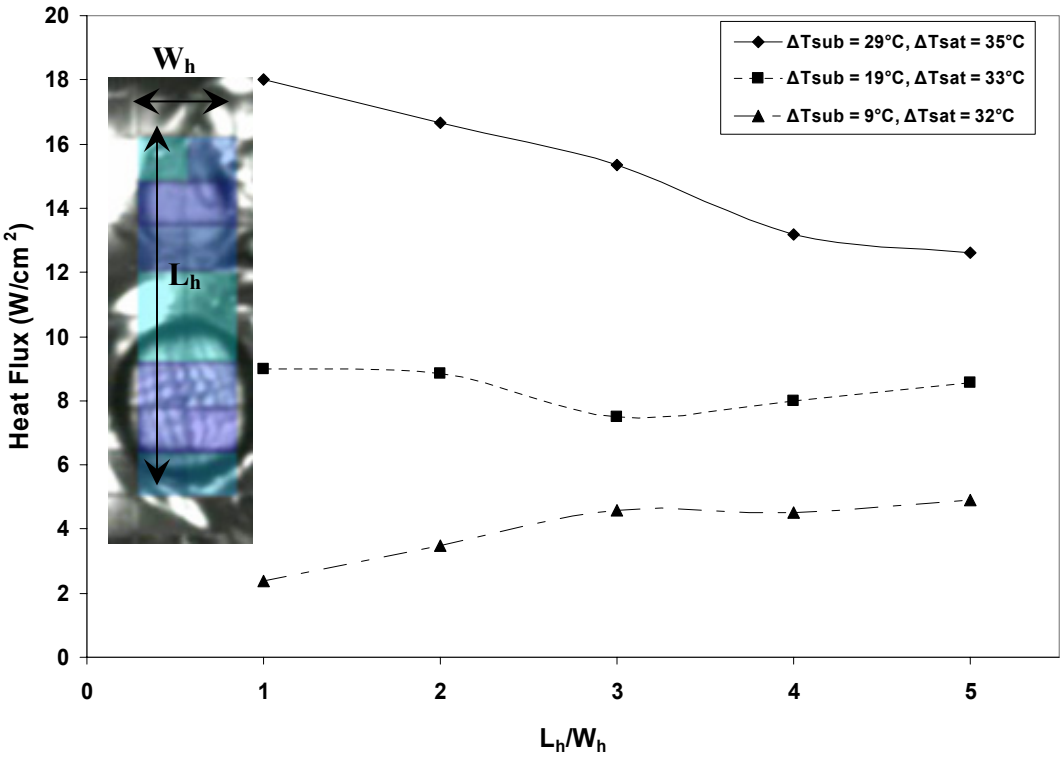

Figure 5.40: Heater aspect ratio effects on boiling heat transfer in low-g at relatively high wall superheats.

5.5 DISSOLVED GAS EFFECTS

The effect of dissolved gas content was investigated during a single flight week in October, 2003 by conducting experiments with pure fluid (n-perfluorohexane) that was completely degassed (< 3 ppm) for two days, and then opening the boiling chamber to allow ingassing to occur until an equilibrium gas concentration was reached at room temperature and pressure (Cg = 3600 ppm).

The boiling performance with very small gas concentrations has been discussed in detail throughout this chapter. All of the data previously shown was taken with a negligible gas concentration in the working fluid. For cases where the liquid gas concentration is very high, the boiling characteristics and performance are dramatically different. In a gassy system, the bubbles tended to grow much larger and cause dryout over a larger portion of the heater surface, Fig 5.41b. The reason for this may be due to the dissolution of gas as vapor is generated near the contact line. As more and more gas is released into the bubble, the bubble grows larger until its size has reached sufficient surface area for gas diffusion back into the liquid, balancing the rate of gas addition near the contact line. It is thought that the bubble that forms is predominately a gas bubble and the partial pressure of vapor inside the bubble is quite small. Boiling curves at the two different dissolved gas concentrations are shown in Fig 5.42. In high-g, it appears that the dissolved gas level has little effect on the measured heat transfer or on the qualitative boiling dynamics as observed from the side view images. Since conduction to rewetting liquid after bubble departure was shown to be the dominate mechanism in high-g, higher gas concentrations, although they may affect the bubble composition, do not seem to interrupt the bubble growth and departure process.

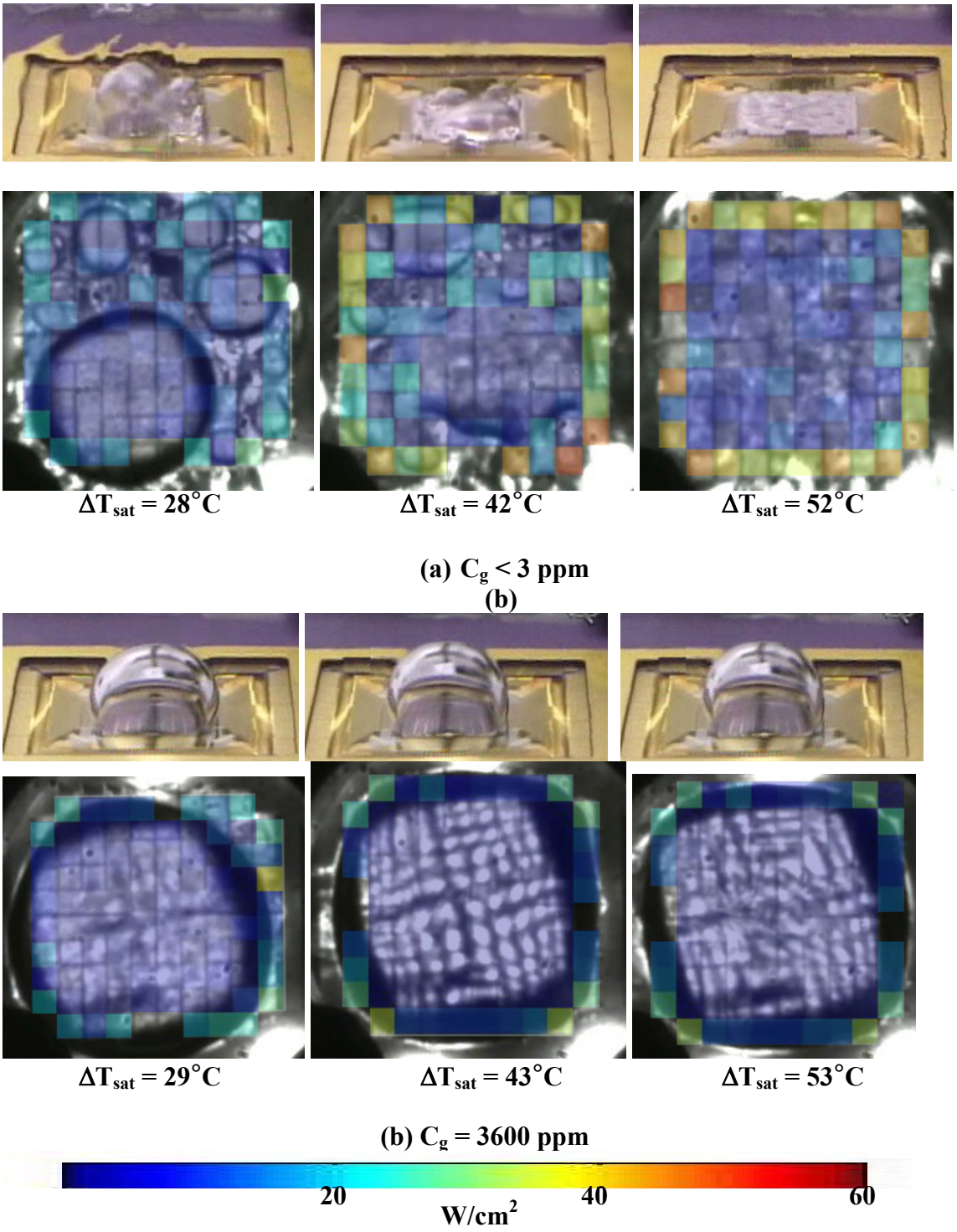

Figure 5.41: Time resolved boiling images from a 7 x 7 mm2 heater array at low and high gas concentrations in the fluid a,b, ΔT_{sub} = 28°C.

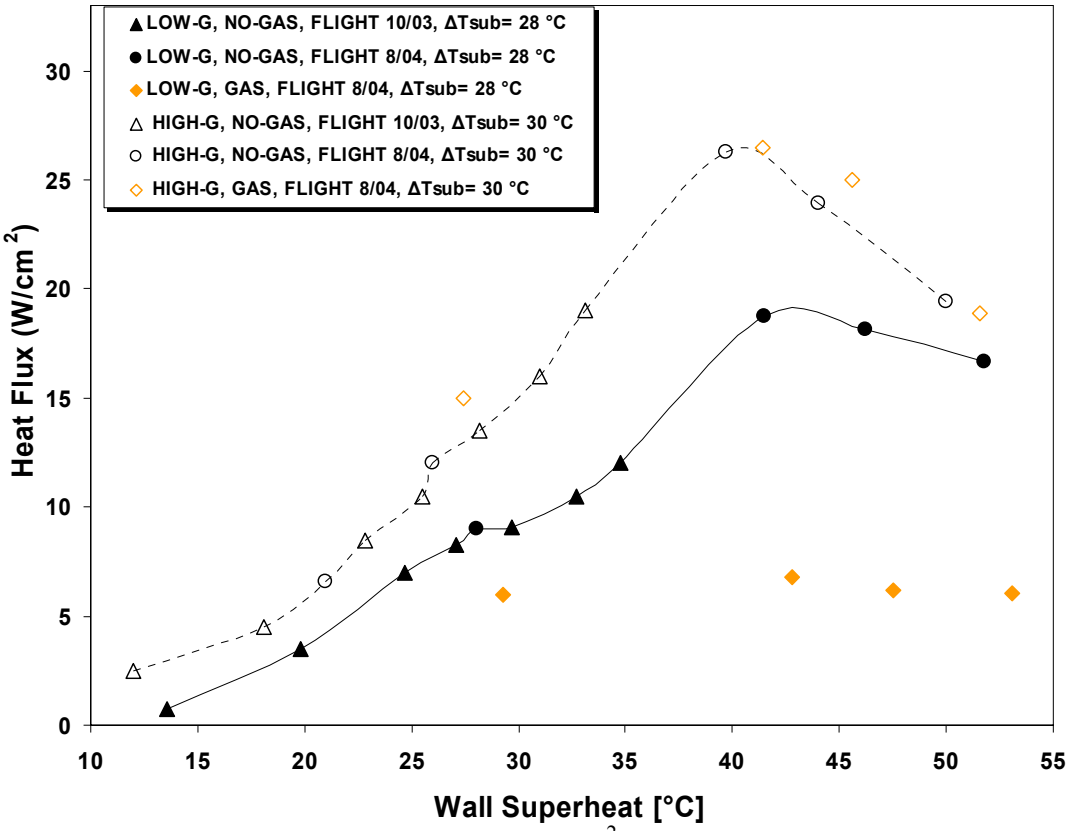

Figure 5.42: Boiling curves for a 7 x 7 mm^2 heater array for various dissolved gas concentrations.

In low-g, at higher wall superheats a single large primary bubble forms for high gas concentrations and the heat transfer is small and independent of wall superheat. For a degassed fluid, the boiling performance is quite different. It appears the a thin film of vapor is located on the heater surface post CHF and a strong liquid jet above the heater was observed and is attributed to thermocapillary convection. It is interesting to note that for negligible gas concentrations in low-g, CHF is 19 W/cm^2 or 70% of the high-g CHF, 27 W/cm^2. This value is much higher than expected and is not predicted from any contemporary correlations. The dramatic enhancement in CHF for negligible gas concentrations is due to the dynamics of the boiling process which causes a thin vapor region to form near the heater and strong thermocapillary convection carries the

condensing vapor away from the heater at a high rate accounting for the large heat transfer measured.

At the highest wall superheat investigated in low and high-g, ΔT_{sat} = 50-52°C, there appears to be no difference in the boiling performance for a degassed fluid, Fig 5.43. For this particular case, the boiling regime is in the transition region and surprisingly the boiling dynamics in high and low-g are identical. This indicates that a degassed fluid might provide significant enhancement in heat flux at high wall superheats and subcoolings for a passively cooled two-phase system in space.

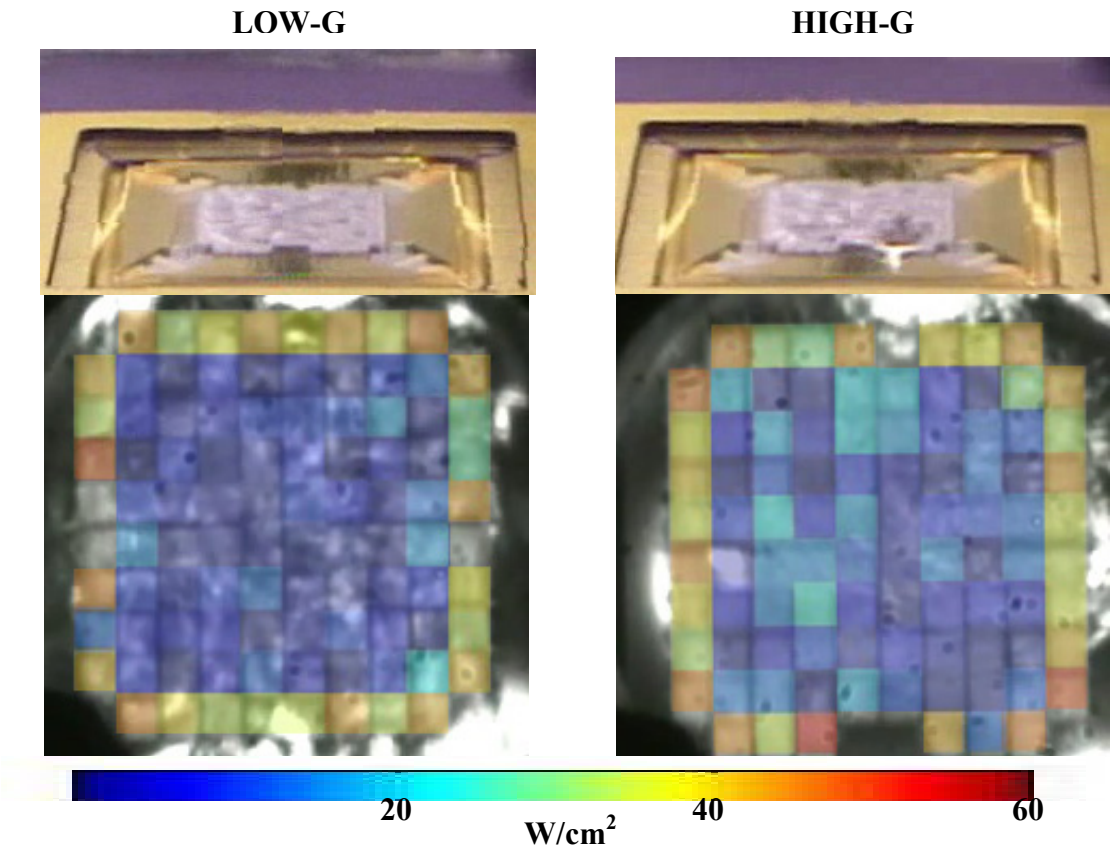

Figure 5.43: Time resolved boiling in high and low-g for a degassed fluid, C_g = 3 ppm. ΔT_{sat} = 50 – 52°C, ΔT_{sub} = 28°C.

Chapter 6: Summary of Gravitational Effects on Pool Boiling

At low wall superheats, boiling performance appears to be independent of gravity level although the heat and mass transfer mechanisms are different. In high-g, buoyancy dominates the process which is characterized by the ebullition cycle. In low-g, satellite bubble coalescence is responsible for the heat transfer.

At higher wall superheats, boiling performance is significantly reduced in low-g. This is attributed to heater dryout and the reduction of bubble removal mechanisms such as buoyancy. Increased subcooling appears to delay the reduction in boiling performance (compared to high-g) to higher wall superheats. The heater size appears to strongly affect thermocapillary induced heat transfer that occurs post CHF.

Surface tension dominated boiling was observed in both high and low-g under certain conditions. In high-g, if the heater size is smaller than the isolated bubble departure diameter predicted from the Fritz correlation then bubble departure does not occur and the formation of a single primary bubble is observed. The transport process is dominated by natural convection and thermocapillary transport around the primary bubble interface. In low-g, surface tension dominated boiling occurred under all of the conditions investigated. The absence of buoyancy means that thermocapillary convection around the primary bubble is the dominant heat and mass transport mechanism.

It appears that the primary bubble dominates the boiling performance in low-g. If the primary bubble grows in size to completely dryout the heater surface then low heat transfer results. Contrastingly, the smaller the primary bubble relative to the heater surface, the larger the heat transfer. The effect of bulk liquid subcooling was found to have a more dramatic relative effect on heat transfer in low-g. This is attributed to the

strong dependence of thermocapillary convection on the bulk liquid subcooling level in low-g. Thermocapillary effects are less significant in high-g due to the presence of buoyancy driven convection around the bubble which tends to compensate for a reduction in thermocapillary convection at lower subcoolings.

In low-g, CHF appeared to be a result of the competition between increasing heat transfer associated with the satellite bubble and the decrease in heat transfer due to the growth of the dry area under the primary bubble as the wall superheat increases.

It is hypothesized that the primary bubble size in microgravity is affected by a number of parameters including the thickness of the superheated boundary layer and the heater length. For a growing bubble in microgravity, the bubble is constrained from growing either vertically or laterally depending on the thickness of the superheated boundary layer or the heater length. For smaller heaters, it appears that the heater length determines the maximum size of the primary bubble while for larger heaters, the superheated boundary layer thickness determines the size. If the heater size is the dominant parameter affecting bubble size then thermocapillary convection may be very small and low heat transfer results.

The presence of dissolved gases in the system was shown to have a dramatic effect on boiling performance in low-g. The presence of non-condensables changes the composition of a growing bubble. Consider a binary system of n-perfluorohexane and nitrogen. As a bubble forms on the surface and grows, nitrogen is carried into the bubble along with vapor. At equilibrium, the bubble reaches a size whereby vapor and gas addition at its base is balanced by vapor and gas removal near the top of the interface. Gas transport across the bubble interface is governed by diffusion and is directly

proportional to the concentration gradient of gas near the bubble interface. The equilibrium gas concentration in the bubble causes it to grow larger than it would if no gas was present. This larger bubble causes increased dryout of the heater surface and a reduction in heat transfer. In high-g, the composition of the bubble is less significant due to buoyancy effects. The bubble departure size, departure frequency (and heat transfer) are unaffected by the composition of the bubble in this case because the density of the two components are nearly identical.

Thermocapillary flow is important due to its local transport of the hot thermal boundary layer near the heater. It appears that the thermocapillary flow velocity near the bubble can be approximated if the heat flux and bubble size are known. It was also observed that during thermocapillary dominated boiling, heat transfer from the wetted region in low-g is comparable to heat transfer in high-g under similar conditions. The driving temperature difference for the flow was found to be the wall temperature minus the bulk temperature.

Although very strong thermocapillary flow was observed throughout these experiments, its origins are not known. It is believed that the thermocapillary motion observed in these experiments is not due to dissolved gas effects as suggested by Straub (2000) since the gas concentration was reduced to well below 3 ppm and strong liquid jets above the bubbles were still observed. Its presence may instead be due to contaminants in the system. Although reasonable care was taken to clean the system, it was not possible to remove all contaminants. Contaminants may have been introduced into the system from the O-rings used to seal the system, or the small amount of silicone RTV used to seal the PGA containing the heater array to the bottom of the test chamber.

Chapter 7: Contributions and Future Scope

7.1 CONTRIBUTION TO THE STATE OF THE ART

This thesis provides a much needed basis for future research concerning two-phase flows in space. In addition to providing an in-depth discussion of the boiling process in a variable gravity environment, this effort has identified some of the pertinent pool boiling mechanisms in low-g including thermocapillary convection and bubble coalescence. A comprehensive discussion of the CHF mechanisms in low-g was presented and provides a firm groundwork for future two-phase thermal design in space. In addition, contributions to the state of the art include:

1) Development of an optimized sensor capable of heat flux and temperature measurement at the small scale
2) Development of analytical and numerical methods for interpreting sensor data
3) Characterization of pool boiling in the absence of ebullition cycle behavior
    a. Applicability of classical models was determined
4) Identification of pertinent scaling parameters
5) Fundamental boiling mechanisms in low gravity identified and analyzed

7.2 FUTURE WORK

7.2.1 Numerical

A number of numerical investigations were presented in this thesis. Although these models provide support for the experimental observations made, additional models could be developed which account for: a dynamic bubble interface, energy and mass

transport across the two-phase interface, surface tension effects near the three-phase contact line, and the effects of multiple components in the fluid. In addition, statistical thermodynamic modeling (molecular dynamic simulations) could serve to identify the governing mechanisms for the onset of thermocapillary flow.

7.2.2 Experimental

This thesis focused on a single fluorocarbon fluid. Additional research should be conducted that investigates the performance of various other fluids including organic and inorganic compounds. The selection of such fluids would have to meet the most stringent of design specifications for testing in space. These specifications, noted earlier in this thesis, are extensive and may require redundant safety systems and containment vessels that could prove costly for future space experimentation.

The effect of g-jitter on bubbles is still unclear. This effect needs to be quantified entailing experimentation aboard microgravity platforms that are more robust and significantly more expensive than the KC-135.

The thermocapillary phenomenon is discussed throughout this thesis. Future experimentation should focus on the origin of such flows. This would entail measurements (temperature, pressure, velocity) near the two-phase interface.

In conclusion, while some recent studies shed light on the complex phenomena governing pool boiling in microgravity, these studies are mostly qualitative in nature and inconclusive at best. This effort provides a discussion of extensive experimental measurements taken aboard the KC-135. Analytical and numerical models were also presented which aid understanding of the phenomenon. Additional efforts are needed to

build upon the solid foundation established and will hopefully lead to new aerospace designs characterized by enhanced efficiency and optimized functionality.

Bibliography

Abe Y., Iwasaki A., (1999) "Single and Dual Vapor Bubble Experiments in Microgravity," Proceeding of the Microgravity Fluid Physics and Heat Transfer Conference, Sept. 19-24, Kahuku, Hawaii.

Baboi, N. F., Bologa, M. K., and Klyukanov, A. A., (1968) "Some Features of Ebullition in an Electric Field," Appl. Electr. Phenom., (USSR), Vol. 20, pp. 57-70.

Bakhru, N., and Lienhard, J.H., (1972) "Boiling from Small Cylinders," Int. J. Heat Mass Transfer, Vol. 15, pp. 2011-2025.

Beckman, W.A., and Merte, H., Jr., 1965, "A Photographic Study of Boiling in an Accelerating System," ASME Journal of Heat Transfer, Vol. 87, No. 3, pp. 374-380.

Bergles, A.E., and Rohsenhow, W.M., 1964, "The Determination of Forced-Convection Surface-Boiling Heat Transfer," ASME Journal of Heat Transfer, Vol. 86, p. 365.

Bromley, L.A. (1950) "Heat Transfer in Stable Film Boiling," Chem. Eng. Prog. Symp. Ser. 46, pp. 221-227.

Cole, R, and Shulman, H L, Bubble departure diameters at subatmospheric pressures, Chem Eng Prog Symp Ser, vol 62, no 64, pp 6-16, 1966.

Cole, R, and Rosenhow, W M, Correlation of bubble departure diameters for boiling of saturated liquids, Chem Eng Prog Symp Ser, vol 65, no 92, pp 211-213, 1968.

Cooper, M.G. (1984) "Saturation Nucleate, Pool Boiling–a Simple Correlation," Institution of Chemical Engineers Symposium Series, Vol. 86, pp. 785-792.

DiMarco, P. and Grassi, W., (1999) "About the Scaling of Critical Heat Flux with Gravity Acceleration in Pool Boiling," XVII UIT National Heat Transfer Conference, Ferrara, June 30-July 2.

DiMarco, P. and Grassi, W., (1992) "Gravity and Electric Field Effects on Pool Boiling Heat Transfer," Proceeding of the VIIIth European Symposium on Materials and Fluid Sciences in Microgravity, Brussels, ESA SP-333:783-788.

Eschweiler, J.C., Benton, A.M., and Preckshot, G.W., 1967, "Boiling and Convective Heat Transfer at High Accelerations," Chemical Engineering Progress Symposium Series, No. 79, Vol. 63, pp.66-72.

Flourinert Liquids, "Properties, Product & Contact Guide," 3M.

Fritz, W. (1935) "Berechnungen des Maximalvolumens von Dampfblasen", Phys. Z., Vol. 36, pp. 379-384.

Forster, H. K., and Greif, R., (1959) "Heat Transfer to a Boiling Liquid – Mechanisms and Correlations," J. Heat Transfer, Vol. 81, pp. 45.

Gaertner, R. F. Photographic Study of Nucleate Pool Boiling on a Horizontal Surface, Journal of Heat Transfer, Feb. 1965, pp. 17-29.

Gunther, F. C., and Kreith, F., (1956) "Photographic Study of Bubble Formation in Heat Transfer to Subcooled Water," Prog. Rept. 4-120, Jet Propulsion Lab., California Institute of Technology, Pasadena, CA, March.

Haramura, Y, and Katto, Y. (1983) "A New Hydrodynamic Model of the Critical Heat Flux, Applicable Widely to Both Pool and Forced Convective Boiling on Submerged Bodies in Saturated Liquids," Int. J. of Heat and Mass Transfer, Vol. 26, pp. 389-399.

Hartman, Thomas, G. "Phase I of PFH/FC-72 Pyrolysis Study: GC-MS & GC-FID Impurity Profiling of FC-72 and Aldrich Lot #18025DB n-Perfluorohexane (PFH) Samples. Rutgers University, 2004.

Incropera, Frank, and David Dewit, Fundamentals of Heat and Mass Transfer. Fifth Edition, John Wiley & Sons: NewYork, 2002.

Ivey, H.J. and Morris, D.J. (1962) "On the Relevance of the Vapor-liquid Exchange Mechanism for Subcooled Boiling Heat Transfer at High Pressure," British Rep. AEEW-R-137, Atomic Energy Establishment, Winfrith.

Kao, Y.S.; Kenning, D.B.R. 1972: Thermocapillary flow near a hemispherical bubble on a heater wall. J. Fluid Mech. 53, 715-735.

Keshok, E.G.; Siegel, R. (1964): "Forces Acting on Bubbles in Nucleate Boiling Under Normal and Reduced Gravity Conditions; NASA TN D-2299, Washington D. C.

Kim, J., Benton, J.F., and Wisniewski, D. (2002) "Pool Boiling Heat Transfer on Small Heaters: Effect of Gravity and Subcooling," International Journal of Heat and Mass Transfer, Vol. 45, pp. 3919-3932.

Koerner, W., 1970, "The Influence of High Acceleration on Boiling Heat Transfer," Chemie-Ingenieur-Technik, Vol. 42, No. 6, pp. 409-414

Kotake, Susumu, (1969) "Effects of Reduced Gravity on Nucleate Boiling. Bulletin of JSME., Vol. 12, No. 54, pp. 1459-1466

Kutateladze, S.S., (1962) "Heat Transfer During Condensation and Boiling," translated from a publication of the State Scientific and Technical Publishers of Literature and Machinery, Moscow-Leningrad, as AEC-TR-3770.

Liepmann, H. W., Roshko, A. Elements of Gasdynamics. John Wiley & Sons Inc. 1957, library of Congress Catalog Card Number: 56-9823.

Lienhard, J. H., Dhir, V. K., and Reheard, D. M., Peak pool boiling heat flux measurements on finite horizontal flat plates, J. Heat Transfer, vol. 95, pp. 477-482, 1973.

Marek, R. & J. Straub. 2001. The origin of thermocapillary convection in subcooled nucleate pool boiling. Int. J. Heat Mass Transfer 44: 619-632.

Martin, H., "Heat and Mass Transfer between Impinging Gas Jets and Solid Surfaces," in J.P. Hartnett and T.F. Irvine, Jr., Eds., Advances in Heat Transfer, Vol. 13, Academic Press, New York, 1977.

Miettinen, Nonlinear Multiobjective Optimization, Kluwer Academic Publishers, 1999.

McAdams, W. H., *Heat Transmission*, 3rd ed., Mc-Graw-Hill, New York, 1954, Chap. 7.

McGrew, J.L., Bamford, T.R. "Marangoni flow: an additional mechanism in boiling heat transfer, Science 153 (3740) (1966) 1106-1107.

Mikic, B., and Rohsenow, W. M., 1968, "A New Correlation of Pool Boiling Data Including the Effect of Heating Surface", ASME Paper No.: 68-WA/HT-22.

Merte , H., Lee, H.S., Ervin, J.S., 1994, "Transient Nucleate Pool Boiling in Microgravity-Some Initial Results," Microgravity Science and Technology, VII, 2, July 1994, pp. 173-179.

Moore, F. D., and Mesler, R. B., A.I.Ch.E. J. 7, 620 (1961)

Oka T., Abe Y., Mori Y.H, Nagashima A., 1995, Pool Boiling of n-Pentane, CFC-113 and Water under Reduced Gravity: Parabolic Flight Experiments with a Transparent Heater, J. Heat Transfer, Trans. ASME, Vol. 117, pp. 408-417.

Ostrach, S., 1982, "Natural Convection Heat Transfer in Cavities and Cells", Proceedings 7th International Heat Transfer Conference, Vol. 1, pp. 365-379.

Raake, D., and J. Siekmann, 1989. Temperature and velocity fields due to surface tension driven flow. Experiments in Fluids, 7, 164-172.

Rohsenhow, W.M. (1962) "A Method of Correlating Heat Transfer Data for Surface Boiling of Liquids," Transactions of the ASME, Vol. 84, pp. 969.

Rule, T.D. and Kim, J., (1999) "Heat Transfer Behavior on Small Horizontal Heaters During Pool Boiling of FC-72," Journal of Heat Transfer, Vol. 121, No. 2, pp. 386-393.

Rule, Toby, (1997) "Design, Construction, and Qualification of a Microscale Heater Array for Use in Boiling Heat Transfer," Master's Thesis, Washington State University.

Shatto, D. and Peterson, GP, "Pool Boiling Critical Heat Flux in Reduced Gravity," ASME J. Heat Transfer, Vol. 121, No.4, 1999, pp. 865-873.

Steinbichler, M., Micko, S., and Straub, J. (1998) "Nucleate boiling heat transfer on a small hemispherical heater and a wire under microgravity", Proceedings of the 11th International Heat Transfer Conference, Kyongju, Korea, Vol. 2, pp. 539-544.

Stephan and Abdelsalam (1980), "Heat Transfer Correlations for Natural Convection Boiling," Int. J. Heat Mass Transfer 23, pp. 73-87.

Straub, J., Picker, G., Winter, J., and Zell, M. (1997) "Effective Cooling of Electronic Components by Boiling Phase Transition in Microgravity", Acta Astronautica, Vol. 40, No. 2-8, pp. 119-127.

Straub, J. (2000) "Origin and Effect of Thermocapillary Convection in Subcooled Boiling: Observations and Conclusions from Experiments Performed in Microgravity," presented at the 2001 Engineering Foundation Conference on Microgravity Transport Processes in Fluid, Thermal, Biological and Materials Sciences II, Banff, CA, Paper MTP01-41.

Thomas, V.A., N.S. Prasad and C. Ananda Mohan Reddy, "Microgravity research platforms – A study," Current Science, Vol. 79, No. 3, August 2000.

Trefethen, L., "On the Jet Propulsion of Bubbles in a heater liquid," Tufts University Mechanical Engineering Rep., 61-8-1, 1961.

Ulucakli M.E., Merte H, "Nucleate Boiling with High-Gravity and Large Subcooling," Journal of Heat Transfer Transactions of ASME, Vol. 112: pp. 451-457, May 1990.

Wang H., X. F. Peng, D. M. Christopher, W. K. Lin, C. Pan, "Investigation of bubble-top jet flow during subcolled boiling on wires", International Journal of Heat and Fluid Flow, Vol. 26: pp. 485-494, 2005

Yaddanapudi, N., and Kim, J., "Single Bubble Heat Transfer in Saturated Pool Boiling of FC-72", Multiphase Science and Technology, Vol. 12, No. 3-4, pp. 47-63, 2001.

You, Simon, Bar-Cohen, and Hong, (1995) Effect of dissolved gas content on pool boiling of a highly wetting fluid, Journal of Heat Transfer, Vol. 117, pp. 687-692.

Zhang, N., Chao, D.F., Yang, W.J., "Heat Transfer Performance of pool boiling on Metal-Graphite Composite Surfaces," Proceedings of the Fifth Microgravity Fluid Physics and Transport Phenomena Conf., NASA Glenn Research Center, Cleveland, OH, CP-2000-210470, pp. 1459-1461, Aug. 9, 2000.

Zuber, N., (1959) "Hydrodynamics of Boiling Heat Transfer," AEC Report AECU-4439.

Appendix A: TEDP Report

Prepared by:

Jungho Kim (PI)
Christopher Henry
University of Maryland
Dept. of Mechanical Engineering
College Park, MD 20742
(301) 405-5437 (O)
(301) 314-9477 (FAX)
kimjh@eng.umd.edu

Technical Grant Monitor: Mr. John McQuillen
(216)-433-2876
John.B. McQuillen@nasa.gov

Support Provided by NASA MSAD Under
Grant No. NCC3-783

FLIGHT WEEK: July 2005

A.1 CHANGE PAGE

Doc. Version	Date	Process Owner	Description
Basic	Aug, 2004	J. Kim/C.D. Henry	TEDP submitted for KC-135 flight
Revision 1	June, 2005	J. Kim/C.D. Henry	• Revised according to NASA TEDP 0205 requirements. • Maximum Temperature Raised to 120 deg C • Added PIV capability (laser) • Integrated power supply and monitor into a single test apparatus. • Removed UPS and replaced with surge suppressor

A.2 QUICK REFERENCE DATA SHEET

Principal Investigator: Jungho Kim

Contact Information: University of Maryland, Dept. of Mechanical Engineering, College Park, MD 20742, 301-405-5437 (O), kimjh@eng.umd.edu.

Experiment Title: Pool Boiling Heat Transfer Mechanisms in Microgravity

Flight Date(s): July 2005

Overall Assembly Weight (lbs.): Test Package (est. *256*)

Assembly Dimensions (L x W x H): Test Package: 24"wide x 24" deep x 42" high,

Equipment Orientation Requests: Facing back of aircraft

Proposed Floor Mounting Strategy (Bolts/Studs or Straps): Bolts,/Studs

Gas Cylinder Requests (Type and Quantity): Air, 1 per day

Overboard Vent Requests (Yes or No): No

Power Requirement (Voltage and Current Required):
Aircraft AC Power: 110 VAC *(<6.5A)*
Aircraft DC Power: 28VDC (<4A)

Free Float Experiment (Yes or No): No

Flyer Names for Each Proposed Flight Day: Christopher Henry, *Jonathan Coursey, Hitoshi Sakamoto*, Jungho Kim

Camera Pole or Video Support: *No*

A.3 FLIGHT MANIFEST

Minimum number of personnel required to operate test apparatus during flight: 2

Trained Test Operators:

1) Christopher Henry, experienced test operator having previously flown aboard the KC-135 during: March 2004 (GRC), October 2003 (GRC), May 2003 (GRC), July 2002 (GRC).

2) Jungho Kim (PI), PI and experienced test operator having previously flown aboard the KC-135 during: March 2004 (GRC), October 2003 (GRC), May 2003 (GRC), July 2002 (GRC).

3) Jonathan Coursey, flew aboard KC-135 during: July 2002 (GRC)

4) Hitoshi Sakamoto, never flown aboard KC-135

A.4 EXPERIMENT BACKGROUND

Experimental Purpose

The physics of systems incorporating phase change processes needs to be better understood in order to provide a predictive capability for design. The current work aims to identify, measure, characterize, and model the fundamental heat transfer mechanisms associated with the boiling process in space.

Experiment History

The experiment is a follow-up of a previous experimental system that included a microgravity payload to study subcooled pool boiling heat transfer. This payload was flown on a Terrier-Orion sounding rocket in December, 1999 from NASA Wallops. The

test was considered to be very successful, with the exception of obtaining video data. The payload was therefore repackaged to fly on the KC-135, and was flown in April, 2000 from GRC. Additional data was taken in January 2001 from JSC and May, 2001 using the same test rig, but with slight modifications. The modifications include the addition of a PI supplied accelerometer in place of SAMS-FF, a temperature controller on the boiling chamber to vary the liquid subcooling, the addition of high-speed digital video, and a low-pressure air jet for cooling the bottom of the microheater array. This system was then transferred into a flight qualified rack supplied by NASA and flown in 2002, 2003, and 2004.

In this series of tests, we have integrated the experimental system into a single test apparatus. A Sorenson 35 volt DC power supply, and LCD monitor have been integrated into the payload eliminating the need for an additional rack for instrumentation purposes. This dramatically reduces the space required aboard the KC-135 during flight. In addition, Particle Image Velocimetry (PIV) experimental capabilities have been incorporated into the test apparatus. The goal of this technique is to provide experimental information regarding the velocity field in the fluid around a stationary bubble in low-g under the influence of thermocapillary convection. This is achieved by seeding the fluid with glass microspheres and illuminating a plane of these spheres using a class II laser. High-speed video images are then used to track the particle motion providing information about the velocity and vorticity fields. We will be performing a series of tests to look at the effect of heater size and thermocapillary convection on microgravity boiling heat transfer. The effective heater size will be varied by turning on and off a different number

of heaters in the array. This series of experiments are in direct support to a space flight experiment (BXF/MABE) being developed by NASA Glenn.

A.5 EXPERIMENT DESCRIPTION

The experimental test apparatus aims to characterize pool boiling mechanisms in a variable gravity environment. The experimental system uses a microheater array (2.7 mm x 2.7 mm) to measure time and spatially resolved heat flux during pool boiling. The heaters are made up of an array of 96 individually controlled heater elements that are maintained as an isothermal surface through the use of feedback control circuits. PIV measurement techniques have been incorporated into the system. The experimental fluid (n-perfluorohexane) has been seeded with glass microspheres (app. 1-10 μm diameter) at relatively small concentration levels. During the experiments, the particles become entrained in the liquid flow field around growing bubbles and, if illuminated, reflect light allowing high-speed cameras to track their position with time. Successive images can be correlated using various software algorithms providing information about the velocity and vorticity field. A plane of particles is illuminated by a class II laser directly in the center of the boiling chamber.

Visualization of the bubbles during their growth and departure with high-speed cameras will be correlated to periods of high heat transfer – this should lead to better understanding of the mechanisms by which heat is transferred during boiling. Boiling curves will be obtained at various subcooling levels under low and high gravity. The scientific objectives of the project are:

1) Obtain microgravity data with a test package hard mounded to the floor of the aircraft.

2) Obtain and correlate microscale heater data with video data.

3) Obtain PIV measurements of the liquid flow field around the primary bubble.

4) Compare data and observations against existing models and develop new mechanistic models where appropriate.

This test will be operated with the test apparatus mounted to the floor of the aircraft. Data will be obtained regarding:

1) The time required for the heat transfer from the surface to reach a steady state after exposure to a microgravity environment.
2) Boiling curves under various subcooled conditions, including critical heat flux.
3) Low-speed visualization of bubbles using a regular CCD camera, and high-speed visualization using a Phantom digital camera.
4) The effect of heater size on boiling heat transfer.
5) Thermocapillary convection and its effects on heat and mass transfer in low-gravity

The maximum temperature within the test rig will never exceed *120 °C*. Temperatures this high may occur at small areas on the heater surface (2.7 mm x 2.7 mm) for very short periods of time (< 2 sec) in order to initiate nucleate boiling. This situation poses minimal risk to operators because the system is hermetically sealed and inaccessible. Three sides of the boiling chamber are inaccessible to the user and the front side of the boiling chamber has a video camera in front of it, making unintentional contact unlikely.

A.6 EQUIPMENT DESCRIPTION

The experimental package consists of a single main component. This component is a PI built sounding rocket payload mounted in a NASA supplied **Vertical Equipment Rack (VER)**. This component also contains a PI supplied monitor, keyboard, and DC power supply. A photograph of the test package along with the components is shown on Fig. A.1. The components are described in greater detail in Tables 1and 2. The total weight of the package is approximately 256 lb. The dimensions of the test section are 24”x24”x42”.

The ideal test operator location during experimentation is to sit fore or aft of the experimental package. To satisfy the structural requirement, the VER handles must also face fore and aft. Straps bolted to the floor of the aircraft will be used to restrain the test operators during the microgravity maneuvers.

Table A.1: Description of components in VER.

Type	Description	Component Description & Considerations
Experimental	Test rig	Sounding rocket payload. This contains the boiling chamber, the high-speed camera for taking pictures from below, a computer, flash disk, control electronics, keyboard, class II laser, and temperature readout. This structure is very rigid, and has survived numerous vibration tests in preparation for the sounding rocket flight. The structure was designed to handle 50g loads in all directions.
Experimental	Frame	This flight qualified frame was supplied by NASA. It bolts directly to the floor of the aircraft using four bolts at each corner. The frame will have lexan panels on each side to prevent damage to the payload from aircraft personnel, and will also keep any loose parts within the frame envelope.
Experimental	DC Power Supply	This is a Sorenson LH35-10 capable of supplying 35 V, 10 A.
Experimental	Computer Monitor	This is a flat panel 15" LCD monitor. Power required: 110 VAC, 1.2 A.

The experiment will not free float. The current test package (VER) will be mounted in the same orientation. Lexan panels are attached to the each side of the VER to prevent unintentional damage to the test rig. The lexan is 0.1"" thick, and bolted to holes in the VER. These panels are to prevent unintentional contact with the test rig by research personnel–they are *not* structural.

The test fluid to be used will be either FC-72 or n-perfluorohexane, which is the mail constituent of the FC-72. Approximately 3 liters of one of the fluids will be used. Both fluids are completely inert at the temperatures encountered in this experiment. A hazards analysis and MSDS' for these fluids are included later in this report.

Equipment to be taken on-board the flight other than the main components listed above include a pen, notepad, hand held digital video camera with power supply, a laptop computer to acquire data from the high-speed camera, and a small digital still camera. A list of equipment for each flight is given below:

1). VER

4). Clipboard with checklists

5). Pens (4)

6). 2 digital video cameras

7). Videotapes (4)

8). PCMCIA flash disks (2)

9). Digital still camera

10). Laptop

The VER has handles by which it can be carried onto the plane and moved about. The VER can be handled by 2 people if necessary. The experiment can be located in any

location aboard the aircraft that provides enough room around the experiment for 2 people. During setup and disassembly aboard the aircraft, a tool box containing various tools will be brought aboard the aircraft if troubleshooting of the experimental system is required. The tool box is completely inventoried and this inventory will be checked anytime the tool box is taken off the aircraft. A clipboard, and laptop can be secured

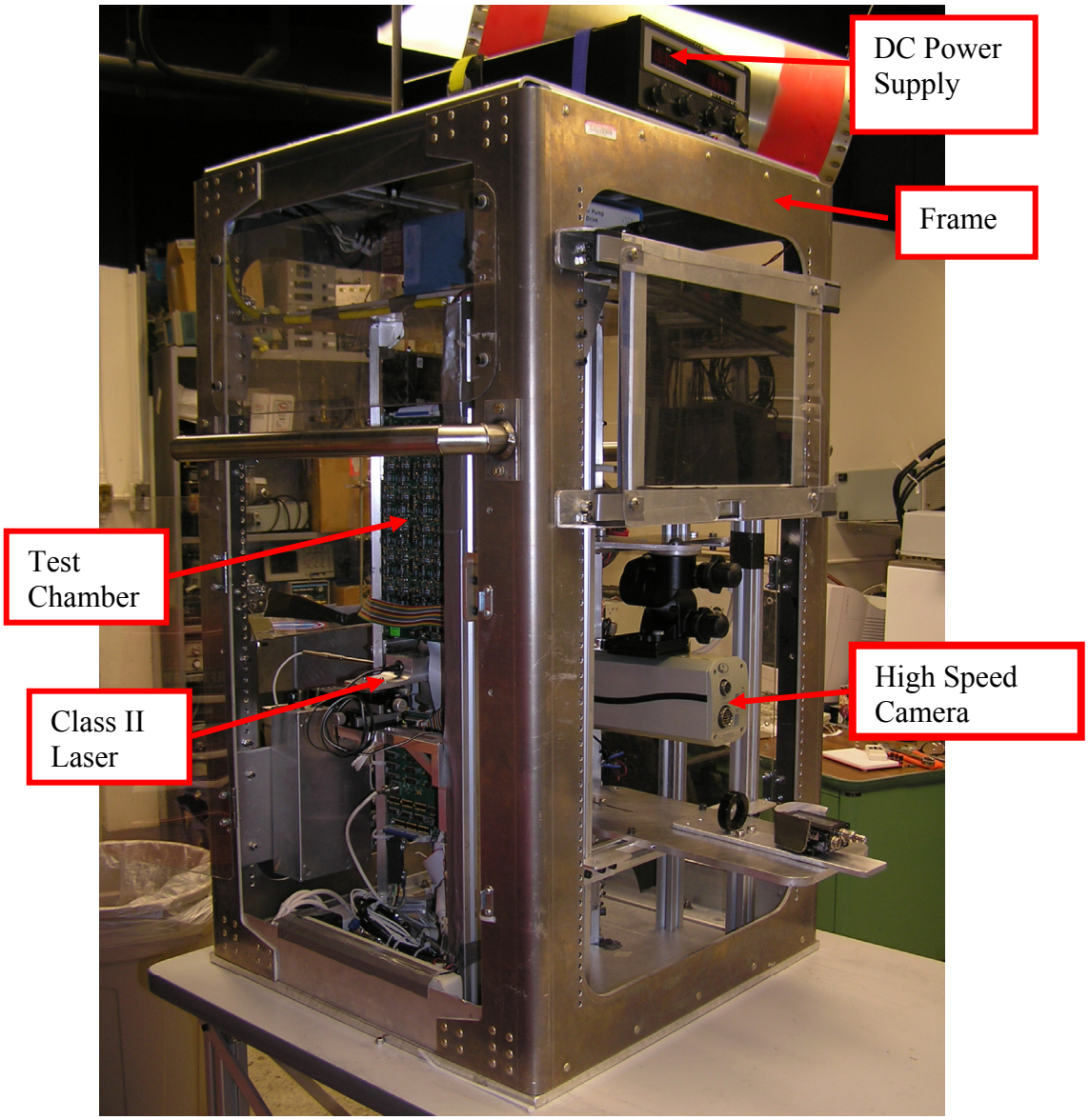

Figure A.1: Photograph of modified test package (the VER) and its components.

to the floor of the aircraft with VELCRO during flight. The remaining items will be carried in a backpack. This backpack will be stored in storage bins provided by the aircraft facility for takeoff and landing. During the flight, the equipment in the backpack will be taped or velcro'd to the floor, held by hand (e.g. video cameras and pens), or placed in pockets in the flight suits.

A.7 STRUCTURAL VERIFICATION

This report summarizes the testing that has been conducted on the VER. Included in this report is a listing of flight load requirements, component weights, results of the stress test, and turning moment calculations. This report concludes that the VER structure is well within flight regulations set forth in *AOD 33897, Rev A: Experiment Design Requirements and Guideline -NASA 932 C-9B.*

For the purposes of this test, the sounding rocket payload will be considered to be an independent and structurally sound member of the VER. The sounding rocket payload was designed to withstand 50 g loads in all directions, has undergone severe vibration testing, and has successfully withstood rocket launch with no damage to any of the systems. For these reasons, and since no modifications have been made to the core payload, it will be considered a structurally sound and rigid component of the test package, and no further analysis of the payload will be performed. The VER the test rig is housed in was sent to us by NASA, and is flight certified. An analysis of the frame is included in the appendix for reference. The frame we are using is actually stronger than the analysis suggests since the basebar and original baseplate were replaced by a 24" x 24" x 1/2" aluminum plate. The new plate is much wider than originally analyzed, and is capable of handling much higher shear loads. The sounding rocket payload is in exactly

the same configuration it was in when it flew on the Terrier-Orion except that the VCR is not being used. *AOD 33897, Rev. A* outlines five possible flight load scenarios that must be considered in conducting a structural analysis. These five scenarios are listed in Table A.3. The component weights are listed in Table 4. The rack capabilities, per *Vertical Equipment Rack: Structural Analysis for Use on Aircraft* are summarized in Table A.5.

Scenario	Load	Direction
One	9g	Forward
Two	3g	Aft
Three	2g	Lateral
Four	2g	Upward
Five	6g	Downward

Table A.2: Maximum Flight Loads

Table A.3: Component weights & moment arms about base

Component	**Weight (lbs)**	**Component's Center of Gravity (in)**	**Moment arm (in·lbs)**
Test rig	146	24	3504
Frame	57	22	1254
DC Power Supply & mounting plate	45	44	1980
High Speed Camera	5	14	70
Monitor	3	30	90
Total	**256**	**27**	**6898**

Table A.4: VER Rack capabilities

Allowable weight (lbs)	500
Actual Weight (lbs)	256
Rig C.G. from floor of rack (in)	27
Rig turning moment	7071

The philosophy behind the testing is a follows. Because both the test rig and the VER are structurally sound, a test only needs to be performed to ensure that the connections between the two are sound. Since stress testing on the actual test rig was risky, a model of the test rig was built that mounts to the frame in **exactly** the same way as the test rig. The exact same bolts and holes are used in both the model and test rig. A photograph of the model is shown on Figure A.2. The model was mounted in the VER, as shown in Figure 3. The model is bolted directly to the 1/2" thick base plate of the VER using four 5/16" steel bolts. The top of the test rig is bolted to a 0.25" thick aluminum plate using eight 5/16" steel bolts. The corners of this plate are attached to existing holes on the VER using 1/4" aluminum angle using 1/4" steel bolts.

Stress testing for the forward direction (9 g) for the test rig (146 lbs.) was performed using an Instron SRV017 machine. The model/frame was mounted as shown in Figure 4, and model loaded at a rate of 1000 lb/min up to 1600 lbs through the steel pipe shown on Figure A.3. This pipe imparted the load directly to the model. The load was held at 1600 lbs for a few seconds. The test rig weighs no more than 150 lbs, so the 1600 lb loading represented at least 10 g of loading. No creaking or cracking of the test rig was observed during the test. Because the test rig is mounted in the frame symmetrically in the forward and aft directions, the load capability in the aft direction is similar to that in the forward direction.

Stress testing in the other directions (lateral, and upward) for the test rig (146 lbs.) was performed by having two people (Combined weight of 325 lbs) stand on the model close to the center of gravity of the model after the model was rotated to various orientations. Testing in the lateral and upward directions is shown in Fig. A.5. The

weight of the two people combined with the weight of the model resulted in a loading in each direction that was close to 3 g.

Stress testing in the downward direction was not performed. Because the test rig is mounted directly to the bottom of the frame (which is mounted to the floor of the aircraft) there is nothing that can break. The center of gravity of the test rig is 27 inches from the floor of the rack. This results in a turning moment of the test rig about the baseplate of 6912 in-lbs (assuming a 1-g loading in the forward and aft direction). A high speed camera and side view camera will be used in this series of tests, similar to what was done in April 2001. As part of the TEDP for that series of flights, the camera mounting was stress tested by placing the appropriate weights in all three directions.

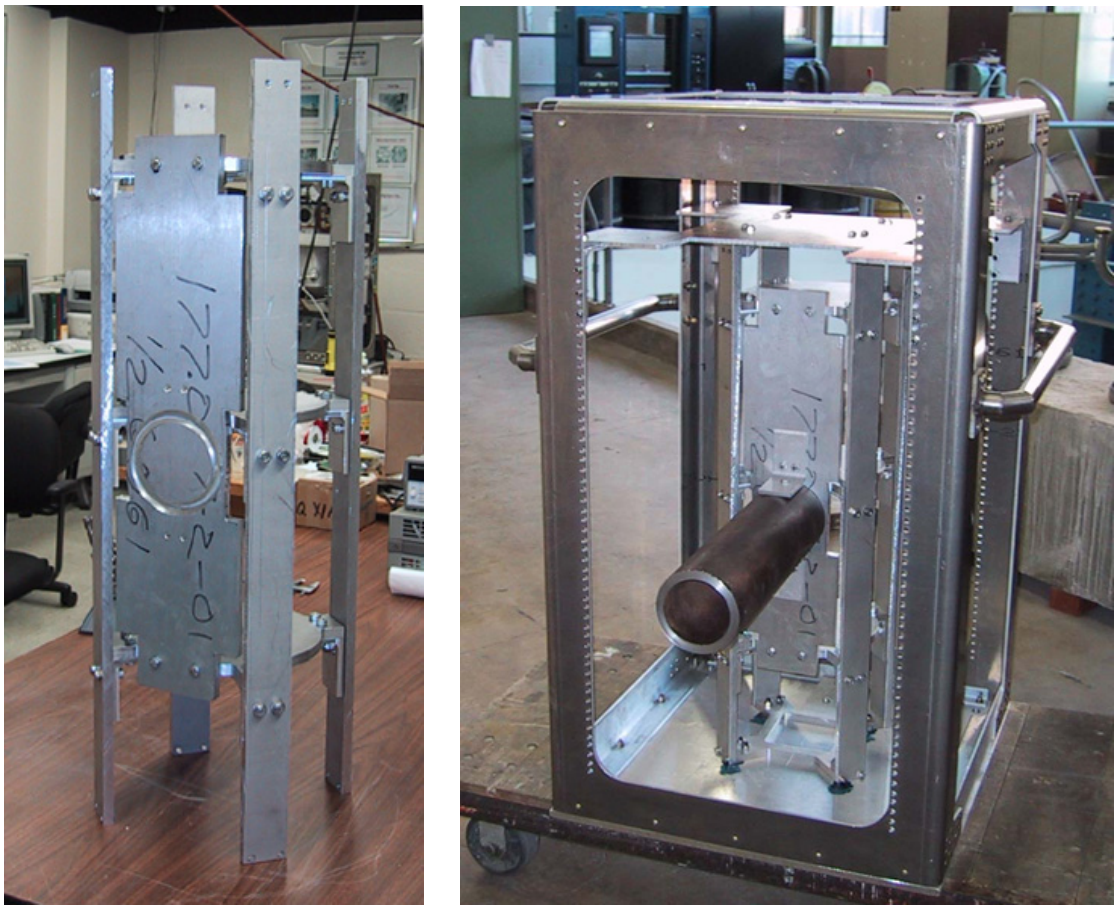

Figure A.2-3: Model of test rig used for stress testing & model of test rig mounted in the frame.

Figure A.4: Testing of model/frame in forward (9 g) direction.

(a) (b)

Figure A.5: Stress testing in various directions: (a) lateral, and (b) upward.

Stress analysis for monitor:

The 15" LCD monitor is held in place between two aluminum U-channel (1-1/4" x 0.125") brackets which are themselves held in place by two 1/4" bolts to the VER. The mass of the LCD monitor and brackets is less than 4 lbs. For a 10g loading, the stress the two bolts are subjected to can be computed to be

$$\frac{4x10\ lbs}{\left(\pi\frac{(0.25\ in)^2}{4}\right)(2\ bolts)} = 410\ psi$$

which is roughly two hundred times smaller than their yield strength. Two additional bolts on either side of the monitor prevent the monitor from sliding back and forth within the channels. These bolts also hold a 1/8" thick lexan sheet in front of monitor to protect it from unintended impact.

Stress analysis for power supply:

The power supply (Sorensen LH35-10) weighs 45 lbs, and is mounted onto a 6061 Al top-plate (24"x24"x1/8") using two nylon straps (minimum 800 lb ultimate tensile load). It is positioned on the top plate by four Al angle brackets, each of which is bolted to the top-plate using two 1/4" bolts. The stress the bolts would experience under a 10g load is the weight of the power supply distributed over two bolts:

$$\frac{45x10\ lbs}{\left(\pi\frac{(0.25\ in)^2}{4}\right)(2\ bolts)} = 4600\ psi$$

The stresses on the bolts are about seventeen times smaller than their yield strength. The top-plate is attached to the VER using four 1/4" bolts. The mass of the top plate is 3.2

lbs. The stress these bolts would experience under a 10 g load is the sum of the weight of the power supply and the top-plate distributed over four bolts:

$$\frac{48x10\ lbs}{\left(\pi\frac{(0.25\ in)^2}{4}\right)(4\ bolts)} = 2400\ psi$$

The stresses on the bolts are about thirty times smaller than their yield strength. The top plate was also stressed over 6g's in the downward direction by having two people stand on it (total weight 330 lbs).

Stress analysis for laser mount:

The mounting apparatus for the laser consists of a laser mounting block which is bolted to a micro-positioner (using three -1/8" bolts). The micro-positioner is bolted (using two 1/4" diameter bolts) to a cantilever beam with a diagonal support member (both 6061 Al). This system is then bolted to the experimental system by two 1/4" bolts, see Figure below.

The laser mounting block, micro-positioner, and cantilever beam weighs 2 lb, 4 lb, and 1 lb respectively. Analyzing first the mounting block, the maximum shear stress a given 1/8" bolt would experience is 600 psi well below the yield strength (10g loading assumed). A similar analysis at the micropositioner and cantilever levels results in a maximum stress of 350 psi and 611 psi respectively.

The cantilever support system is designed to withstand a 6g downward loading as shown in the figure below. Under such conditions a maximum load of 36 lb is supported. Under such conditions the maximum stress within the support structure will occur along the diagonal support member (400 psi, cross sectional area 0.125 in^2). This number is 140 times below the yield strength limits of 6061 Al (58,000 psi).

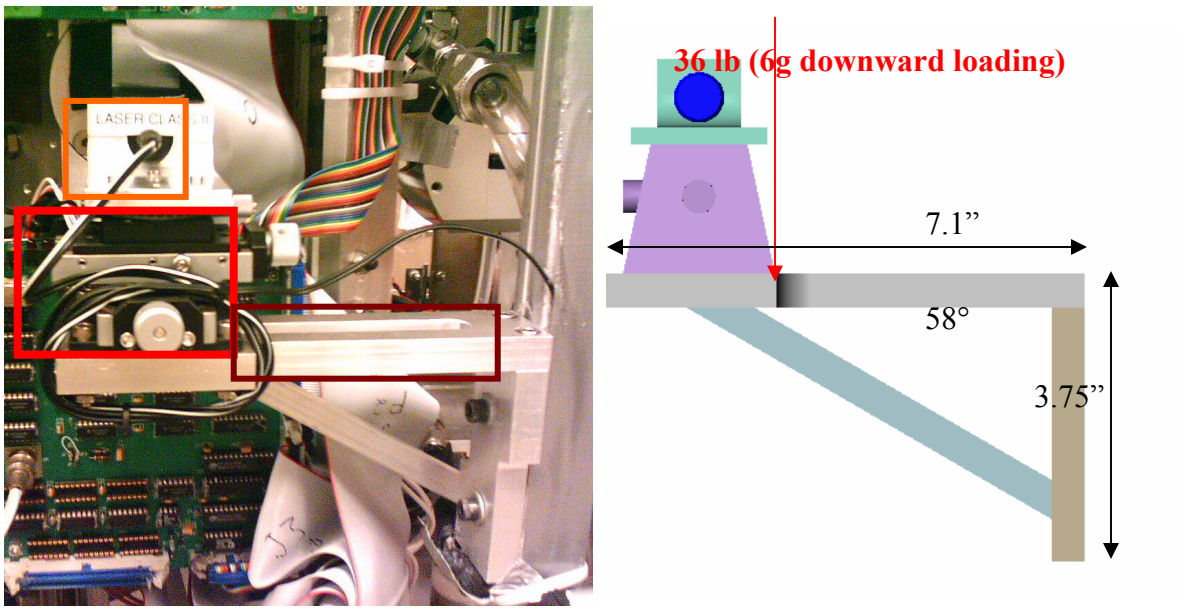

Figure A.6: Laser mounting system: laser mounted block (orange square), micro-positioner (red square), cantilever support (maroon square).

A.8 ELECTRICAL LOAD ANALYSIS

An electrical schematic of the test apparatus is shown in Fig.A.7. Lists of the components along with their electrical characteristics are listed in Table A.8 The total current draw on the aircraft 110 VAC source is no more than 5.3A. Total power required is less than 700 W.

A PID temperature controller is used to control the temperature of the liquid in the boiling chamber. The output of the RTD in the boiling chamber is input to the temperature controller. The output of the temperature controller is a 0–5 V pulse width modulated signal to a solid state relay (SSR) that determines whether or not current flows through the heaters surrounding the boiling chamber.

Both the sounding rocket payload (Test Apparatus) and the heaters are protected using a slo-blo fuse rated at 10A. All wire gauges shown interior to the test apparatus are either 16-18 gauge and are well within the load limits specified in Table 8. 14 gauge wires are used to connect the test apparatus to the aircraft power supply.

The wires in the test apparatus were sized according to Table 7:

Table A.5: Wire Gauges	
Current (A)	Wire size (Ga)
< 0.25	22
< 0.50	20
< 1	18
< 5	16
< 12	14

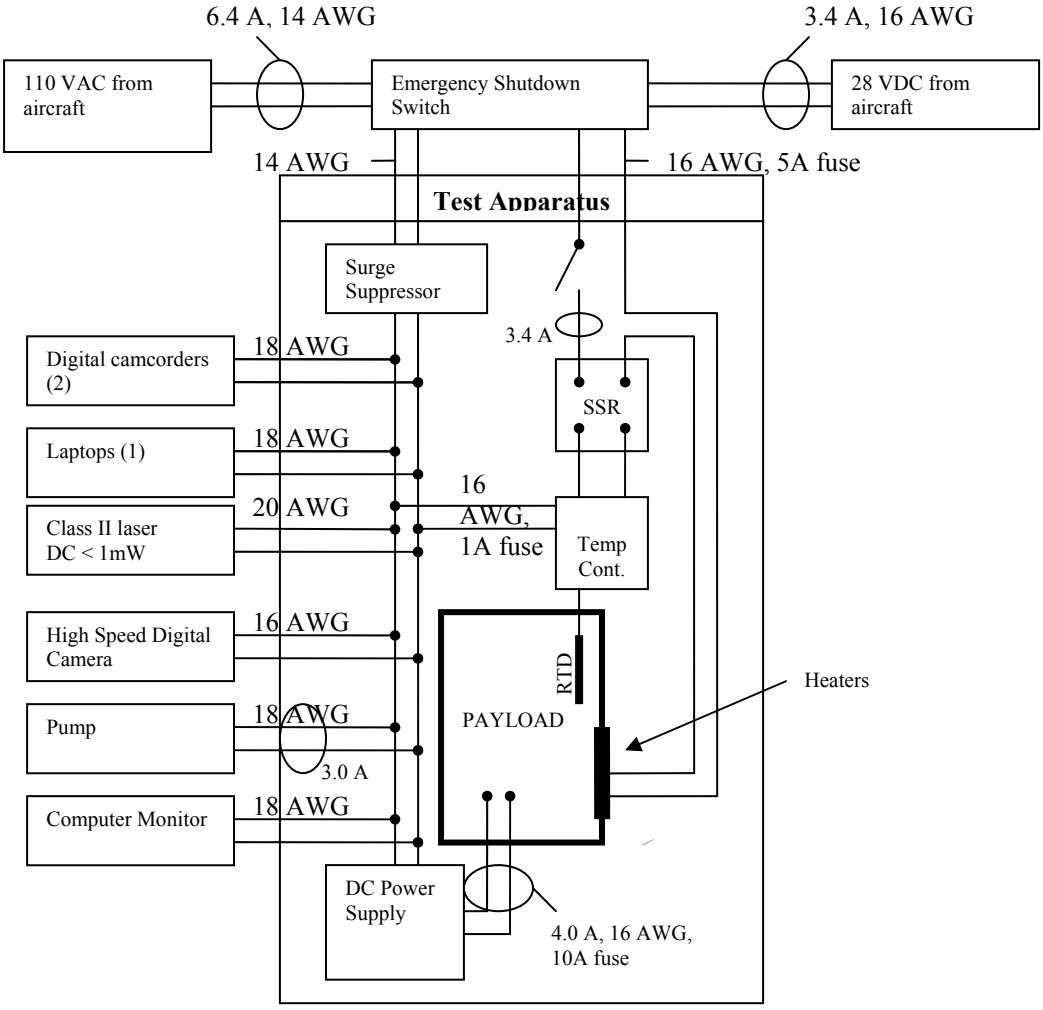

Figure A.7: Electrical schematic.

These wire sizes are more conservative than those suggested in the JSC User's Guide. Two mini digital video cameras will be used to record images of the boiling process. These cameras are manufactured by Canon (model Elura).

A.9 LOAD ANALYSIS

The total current draw on the rack 28 VDC power supply no more than 4.0 A. The total current draw on the aircraft 28 VDC source is no more than 3.4 A.

Power Source Details	**Load Analysis**
Name: 110 VAC	2 video cameras: 0.03 Amps Monitor: 1.2 Amps High-speed camera: 0.25 Amps Laptop: 0.15 Amps *Laser: 0.005*
Description: Aircraft 110 VAC	DC Power Supply: 1.5 Amps
	Micropump: 3.0 Amps
Wire Gage: ***14***	*Total power:* ***550 W***
Outlet Current: ***20.0 A***	*Total current draw:* ***5.0 A***

Power Source Details	**Load Analysis**
Name: Aircraft 28 VDC Power	Heaters for boiling chamber: 3.4 Amps
Description: 28 VDC from aircraft	
Wire Gage: ***14***	Total power: **96 W**
Outlet Current: ***20.0 A***	Total current draw: **3.4 Amps**

Table A.6: Components and their power requirements.

The master kill switch for the experiment is on the top of the VER. By depressing this red knob, all power to the experiment is cut off. The experiment has been designed to allow for a sudden loss of power without permanent damage to the experimental system and automatically defaults to a safe configuration. Alternatively, power to the VER can be turned off by turning off the power strip located at the bottom of the rig and turning off the power to the SSR. For the payload, an alternate kill switch is on the DC

power supply. The Micropump utilizes a 2A fuse. There is also a switch on the front that is easily accessible to shut the pump off in an emergency. The wire size used by the pump is regulated by the pump manufacturer.

A.10 PRESSURE VESSEL CERTIFICATION

The only chamber that experiences a pressure differential is the dome/boiling chamber, figure 8. This chamber has been pneumatically tested to 37 psia (over night) by pressurizing the chamber around the bellows. The pressure difference on the boiling chamber (the chamber containing the FC-72) will be 22.4 psig (37.1 psia).

The chamber will be sealed off while the aircraft is on the ground so that the pressure will be 14.7 psia, and all tests will be performed at this pressure. In the event of a catastrophic decrease in cabin pressure at altitude, the pressure around the boiling chamber could decrease to 3.5 psia. The maximum pressure differential possible during

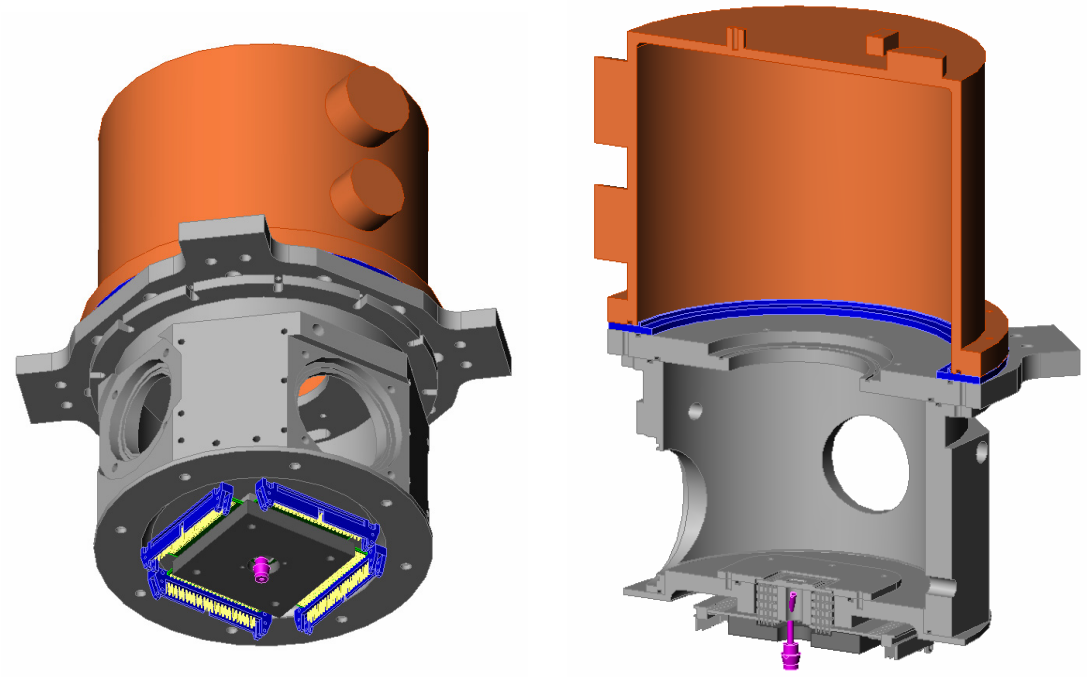

Figure A.8: Low-pressure air cooling jet schematic (Courtesy of J. Benton).

the flight is therefore 11.2 psig. Since this is 2 times smaller than the pressure difference at which the chamber will be tested, the risk of the boiling chamber failing and releasing FC-72 or normal perfluorohexane is very small. Even if the test fluid is released into the cabin, the it poses no health risks since there are no toxicity limits below the temperatures at which we are operating. As an added measure of protection, a pressure relief valve (Nupro SS-RL3S4) has been installed onto the dome to relieve the pressure whenever the dome pressure exceeds the cabin pressure by 10 psig.

The other pressure system being used on this flight is the low-pressure air impingement nozzle. This system is shown is Figure A.8. The system consists of a K-bottle of compressed air, a pressure regulator, a flexible hose, a needle valve, and a nozzle. The pressure downstream of the regulator will be maintained at 5 psig or less. A certified hose and pressure regulator to connect the K-bottle to the needle valve and nozzle will be supplied by NASA. The nozzle exits to the cabin.

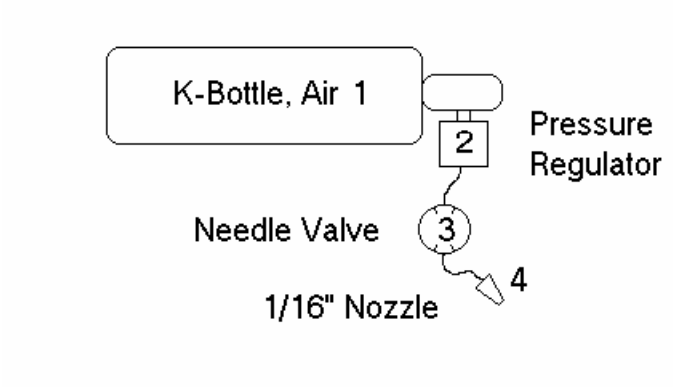

Figure A.9: Low-pressure air cooling jet schematic.

Table A.7: Pressure System Component	MAWP (psi)	Relief Valve Setting (psi)	Regulator Setting (psi)	Supplied/Built By
1. Air K-Bottle	2200	N/A	N/A	GRC
2. Pressure Regulator	2200	N/A	15	Victor MF43011
3. Needle Valve	400	N/A	N/A	Hoke
4. Nozzle	500	N/A	N/A	Custom Built
Dome/boiling chamber	37 psia	10 psig	N/A	Custom build

A.11 LASER CERTIFICATION

A diode type class II laser manufactured by Diode Laser Concepts will be used as part of the PIV measurement system. The laser has internal electronics that provide static, surge, and reverse polarity protection. The laser operates at 5 VDC and draws a maximum total power of 1 mW. Included as part of the laser assembly is a lens that converts the laser beam into a sheet of laser light at an angle of 45°. The laser wavelength is 635 nm. The line width is 1mm @ 1 meter and the fan angle is 10°.

The laser is used to illuminate a plane of the boiling fluid, and the light reflected off neutrally buoyant glass microspheres is imaged using a high-speed camera. Power to the laser is controlled by a switch located on the front of the experimental test rig and will be used only during parabolic maneuvers. The laser light is completely enclosed by the experimental system. Black protective mats have been attached to all viewport holes on the experimental system so that minimal laser radiation leaves the experimental chamber. No protective eyewear is required due to the laser class and since minimal laser radiation leaves the boiling chamber. The laser will be aligned and fixed in place prior to travel to NASA facilities and therefore no alignment is necessary during the flight week.

A.12 PARABOLA DETAILS AN D CREW ASSISTANCE

We will be testing with both the test apparatus and the instrumentation rack attached to the aircraft floor for all flights. Accelerometers on the package will be used to measure the g-levels the package experiences. Data will be taken using an on-board data acquisition system throughout the parabolas for every other parabola. Ideally, a one minute window will be provided prior to the start of microgravity periods after aircraft turns for camera preparation and manual data recording. Thirty or more standard parabolas per day are desired. No crew assistance is required to operate the test equipment. A block diagram of the relevant procedures are shown in Fig. A.10.

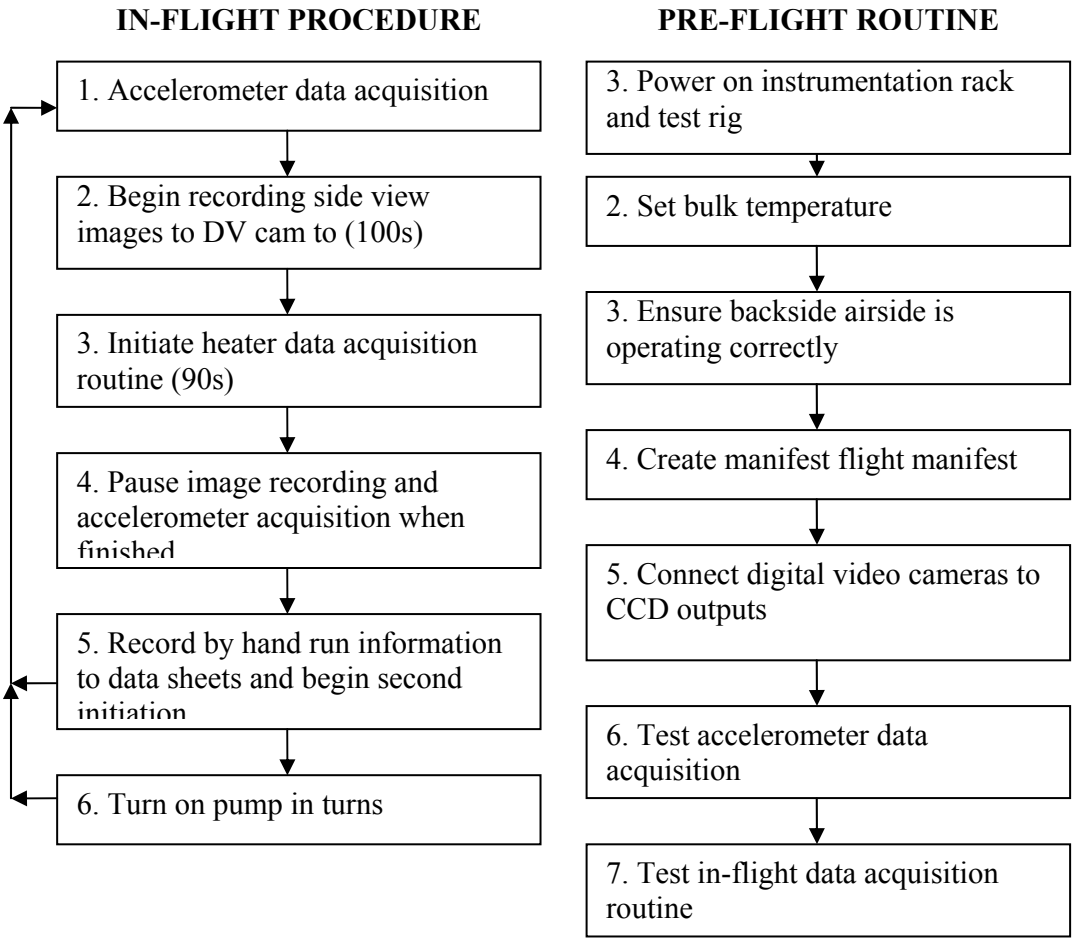

Figure A.10: In-flight operational procedure (left), pre-flight routine (right). I have some updated sheets of this to put in the Appendix.

A.13 HAZARDS ANALYSIS REPORT GUIDELINES

HAZARD SOURCE CHECKLIST

Enumerate or mark N/A
_N/A_ Flammable/combustible material, fluid (liquid, vapor, or gas)
__5__ Toxic/noxious/corrosive/hot/cold material, fluid (liquid, vapor, or gas)
__1__ High pressure system (static or dynamic)
_N/A_ Evacuated container (implosion)
_N/A_ Frangible material
_N/A_ Stress corrosion susceptible material
__3__ Inadequate structural design (i.e., low safety factor)
_*8*_ High intensity light source (including laser)
_N/A_ Ionizing/electromagnetic radiation
_N/A_ Rotating device
_N/A_ Extendible/deployable/articulating experiment element (collision)
_N/A_ Stowage restraint failure
_N/A_ Stored energy device (i.e., mechanical spring under compression)
_N/A_ Vacuum vent failure (i.e., loss of pressure/atmosphere)
_N/A_ Heat transfer (habitable area over-temperature)
_N/A_ Over-temperature explosive rupture (including electrical battery)
__6__ High/Low touch temperature
__7__ Hardware cooling/heating loss (i.e., loss of thermal control)
_N/A_ Pyrotechnic/explosive device
_N/A_ Propulsion system (pressurized gas or liquid/solid propellant)
_N/A_ High acoustic noise level
_N/A_ Toxic off-gassing material
_N/A_ Mercury/mercury compound
_N/A_ Other JSC 11123, Section 3.8 hazardous material
_N/A_ Organic/microbiological (pathogenic) contamination source
__4__ Sharp corner/edge/protrusion/protuberance
_N/A_ Flammable/combustible material, fluid ignition source (i.e., short circuit; under-sized wiring/fuse/circuit breaker)
__2__ High voltage (electrical shock)
_N/A_ High static electrical discharge producer
_N/A_ Software error or compute fault
_N/A_ Carcinogenic material
_____ Other:_____
_____ Other:_____

Appendix B: Optimization of a Constant Temperature Microheater Array Feedback Control Circuit

B.1 PROBLEM DEFINITION

The primary goal of this optimization analysis is to maximize the temperature resolution of the heater array while maximizing a user defined operational temperature range. Such results serve two purposes: Firstly, the goal of experimental research is to maintain the highest fidelity in measurement and, secondly, the microheater array operates ideally when there is a minimum temperature difference between adjacent heaters. A minimum temperature difference reduces lateral substrate conduction between heaters providing a better estimate of the heat transfer due to boiling. In addition, lateral substrate conduction can cause adjacent heaters to "turn off" during the boiling process which is problematic because the array no longer provides an isothermal boundary condition locally making it difficult to infer information about the boiling process.

The control circuit mentioned previously can be modeled analytically based upon electrical circuit theory. A single and multiobjective formulation is presented alongside a host of linear and nonlinear constraints. This set of mathematical equations defines the optimization formulation that is solved using a number of methods in Matlab. A parametric investigation is performed on a number of the design parameters providing additional information about the optimized solution.

A schematic of the feedback control circuit is shown in Fig. 2.1. The circuit is characterized by three main electronic components: resistors, an operational amplifier, and a transistor. Resistors, represented by R_1, R_3, $R_{4,}$ $R_{5,}$ $R_{h,}$ and the digital potentiometer (R_{DP}), define a wheatstone bridge that characterizes the performance of the control circuit. R_1, R_3, $R_{4,}$ $R_{5,}$ are metal film resistors with a manufacturer specified tolerance of 1% and are rated at 0.6 Watts. High tolerance metal film resistors are used for their

relative insensitivity to temperature, high power dissipation, and commercial availability. These resistors, in addition to R_{DP}, form the set of design variables which are optimized in the analysis that follows. R_{DP} is a dual digital potentiometer consisting of two digitally controlled potentiometers manufactured by Dallas Semiconductor. It consists of 512 resistive sections providing a resistance range of 0 – 20 kΩ. R_h represents the resistance of a specific heater element. As mentioned previously, each heater element can be modeled as an equivalent temperature dependent resistance (R_h has a temperature coefficient of

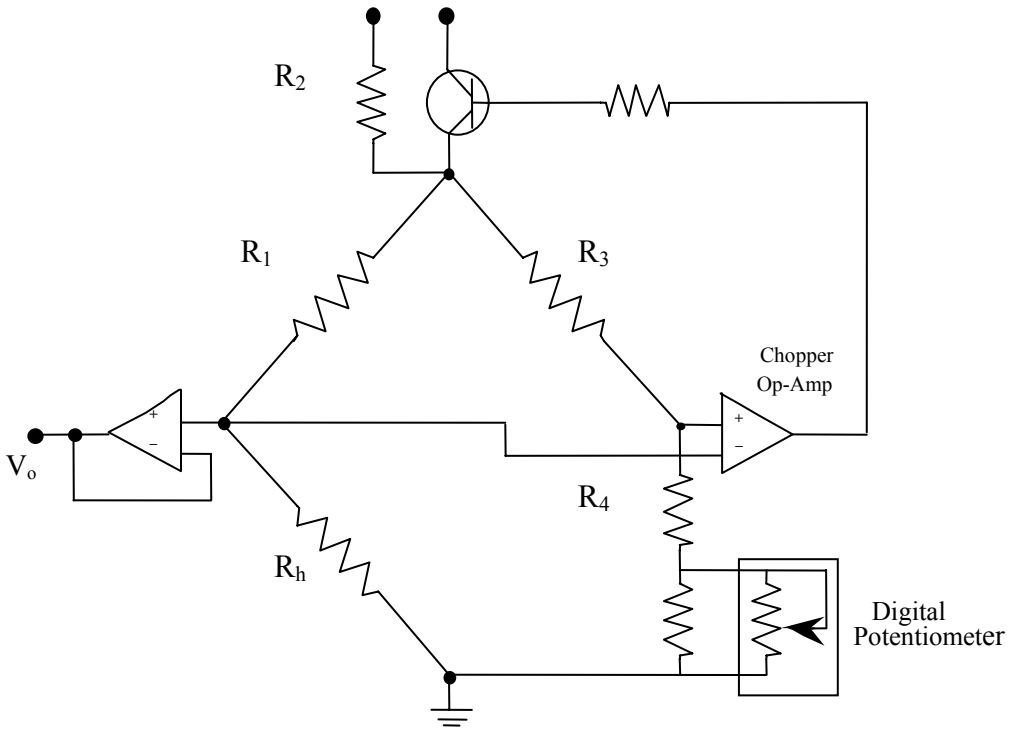

Figure B.1: Feedback Circuit Schematic

resistance 1000 times larger that the metal film resistors described above). The circuit regulating op-amp, labeled "Chopper Op-Amp" in Fig B.1, is a high-voltage, high-performance operational amplifier. An additional op-amp is used to measure the voltage,

V_o, across the heater element but does not directly influence the performance of the control circuit. The transistor shown in Fig. B.1 is a high current, low voltage, NPN switching transistor that is used to provide power to the heater elements. It is important to note that the analysis presented subsequently applies to a single heater and its respective feedback control circuit. Similar analysis can be performed for each heater in the array to obtain an optimized heater array.

The control circuit operates in the following manner: The chopper op amp is used to sense an imbalance in the wheatstone bridge, represented by R_1, R_3, R_4, R_5, R_h, and R_{DP}. If an imbalance exists, the op-amp outputs a proportional voltage to the gate of the transistor allowing additional current to flow from the 24 volt source through the bridge. This current causes an increase in the temperature of the heater (joule heating) with a corresponding increase in resistance. The resistance of the heater will continue to rise until a new equilibrium state is reached corresponding to a balance in the wheatstone bridge. This entire process occurs very quickly, in approximately 66μs, and much faster than the dynamic behavior of the heater boundary surface. Based on these functional characteristics, the heater resistance can be controlled by controlling R_{DP}. During data acquisition, the time-varying voltage across the heater resistance, V_o in Fig. B.1, is measured and used along with the heater resistance at the given temperature to determine the total power dissipated by the heater to maintain it at constant temperature.

In summary, the design variables are defined as $\mathbf{R_1, R_3, R_4, R_5, R_{DP}}$ (see Fig. B.1). The optimization goal involves optimizing these variables for maximum temperature resolution of a given heater in the array subject to constraints described subsequently. All design variables are approximated as continuous variables.

B.2 FORMULATION

B.2.1 Objective Function 1: Maximize Temperature Resolution

As mentioned previously, under steady state operation a balance exists in the wheatstone bridge. Written mathematically, Eq. 1 characterizes this behavior. In Eq. 1, R_h is written as the dependent variable and R_{DP} as the independent variable as described in the previous section. Taking the derivative of Eq. B.1 with respect to R_{DP} yields the differential change in heater resistance with respect to a differential change in R_{DP}, Eq. B.2.

$$\frac{R_1}{R_h} = \frac{R_3}{R_4 + R_5 R_{DP} \Big/ \left(R_5 + R_{DP}\right)} \quad \Rightarrow \quad R_h = \frac{R_1 R_4}{R_3} + \frac{R_1 R_5 R_{DP}}{R_5 R_3 + R_{DP} R_3} \tag{B.1}$$

$$\frac{\partial R_h}{\partial R_{DP}} = \frac{R_1 R_5}{R_3 R_5 + R_3 R_{DP}} - \frac{R_1 R_5 R_{DP} R_3}{\left(R_5 R_3 + R_{DP} R_3\right)^2} \Rightarrow \partial R_h = \frac{R_1 R_5 \partial R_{DP}}{R_3 R_5 + R_3 R_{DP}} - \frac{R_1 R_5 R_{DP} R_3 \partial R_{DP}}{\left(R_5 R_3 + R_{DP} R_3\right)^2} \tag{B.2}$$

Since R_{DP} can only be adjusted in 512 equal increments, the minimum possible change in the digital potentiometer resistance is given as 39 Ω. This value also describes the maximum resolution control of the wheatstone bridge. Substituting this value into Eq. B.2 defines the minimum increase in heater resistance for a minimum change in R_{DP}, Eq. B.3. Stated differently, Eq. 3 represents the smallest theoretical change in heater resistance for a step change in digital potentiometer setting.

$$\Delta R_h = \frac{R_1 R_5 \Delta R_{DP}}{R_3 R_5 + R_3 R_{DP}} - \frac{R_1 R_5 R_{DP} R_3 \Delta R_{DP}}{\left(R_5 R_3 + R_{DP} R_3\right)^2} = \frac{39 R_1 R_5}{R_3 R_5 + R_3 R_{DP}} - \frac{39 R_1 R_5 R_{DP} R_3}{\left(R_5 R_3 + R_{DP} R_3\right)^2} \tag{B.3}$$

In addition to Eq. B.3, the heater resistance is also strongly dependent on temperature. The temperature dependence on the resistance of the heater was measured experimentally and is characterized by the temperature coefficient of resistance, α.

Using this parameter, a resistance-temperature relation can be formulated, Eq. 4, where R_{ref}, T_h, T_{ref}, and ΔT, represent some arbitrary metal reference resistance (corresponding to the reference temperature), heater temperature, reference temperature, and change in temperature (T_h-T_{ref}) respectively. These additional variables are considered design parameters and appear in the optimization formulation summary at the end of this section. Differentiating Eq. B.4 with respect to ΔT, yields Eq. B.5. Equation B.5 states that a differential change in heater temperature is proportional to the differential change in resistance.

$$T_h = \frac{\left(R_h \big/ R_{ref} - 1 \right)}{\alpha_h} + T_{ref} \quad \Rightarrow \quad R_h = R_{ref}(1 + \alpha \Delta T) \tag{B.4}$$

$$\frac{dR_h}{d(\Delta T)} = \alpha R_{ref} = \frac{dR_h}{dT_h} \quad \Rightarrow \quad dT_h = \frac{dR_h}{R_{ref}\alpha} \tag{B.5}$$

From the previous analysis, dR_h can only be controlled to a minimum value specified by Eq. B.3. Substituting ΔR_h for dR_h (Eq. B.3 into Eq. B.5) yields the temperature resolution of the heater element, Eq. 6. Equation 6 represents the minimum possible theoretical temperature change for a step change in digital potentiometer resistance (temperature resolution or uncertainty). Therefore, the optimization objective involves the minimization of Eq. B.6, or in simplified form Eq. B.7.

$$\Delta T_h = \frac{1}{\alpha_h R_{ref}} \left[\frac{39 R_1 R_5}{R_3 R_5 + R_3 R_{DP}} - \frac{39 R_1 R_5 R_{DP} R_3}{\left(R_5 R_3 + R_{DP} R_3 \right)^2} \right] = \frac{39 R_1 R_5}{\alpha_h R_{ref} R_3} \left[\frac{1}{R_5 + R_{DP}} - \frac{R_{DP}}{\left(R_5 + R_{DP} \right)^2} \right] \tag{B.6}$$

$$\min \ \Delta T_h = \frac{39 R_1 R_5^2}{\alpha_h R_{ref} R_3 \left(R_5 + R_{DP} \right)^2} \tag{B.7}$$

B.2.2 Objective Function 2: Maximize Temperature Range (Single Objective Constr. 4)

The second objective considers the maximum operating temperature of the heater. Substituting Eq. B.1 into Eq. B.4 for R_h and setting R_{DP} to 20000 (the maximum controllable potentiometer resistance), the high temperature limit is obtained, Eq. B.8. As a constraint, Eq. B.8 states that the maximum temperature that the heater can operate at must be greater than or equal to T_{high}, or the user specified high temperature limit. This constraint is written as an inequality constraint for the single objective formulation. Ideally, the user would like the largest possible temperature range. Therefore, T_{high} is a design parameter and, written in standard form, this constraint is given by Eq. B.9. Formulating Eq. B.8 as a second objective results in Eq. B.10 (note: the second objective function shown in Eq. B.10 is transformed using the epsilon constraint method to a single objective formulation, constraint g_4, introducing design parameter T_{high}).

$$T_{high} \le \frac{R_1 R_4}{\alpha_h R_3 R_{ref}} + \frac{20000 R_1 R_5}{\alpha_h R_5 R_3 R_{ref} + 20000 \alpha_h R_3 R_{ref}} - \frac{1}{\alpha_h} + T_{ref} \tag{B.8}$$

$$g_4: \quad T_{high} - \frac{R_1 R_4}{\alpha_h R_3 R_{ref}} - \frac{20000 R_1 R_5}{\alpha_h R_5 R_3 R_{ref} + 20000 \alpha_h R_3 R_{ref}} + \frac{1}{\alpha_h} - T_{ref} \le 0 \tag{B.9}$$

$$\max T_{high} = \frac{R_1 R_4}{\alpha_h R_3 R_{ref}} + \frac{20000 R_1 R_5}{\alpha_h R_5 R_3 R_{ref} + 20000 \alpha_h R_3 R_{ref}} - \frac{1}{\alpha_h} + T_{ref} \tag{B.10}$$

B.2.3 Inequality Constraint 1: Low Temperature Control

The lowest temperature that a given heater element can be controlled to is determined by substituting Eq. B.1 into Eq. B.4 for R_h and setting R_{DP} to zero theoretically (experimentally this would be a very low value). Setting R_{DP} equal to zero approximates the low end temperature control range. Performing this manipulation and simplifying results in Eq. B.11 with T_{low} representing the lowest controllable heater temperature. Stating Eq. B.11 as a constraint in standard form says that the optimized circuit design must be able to operate to atleast a temperature defined by T_{low}, Eq. B.12. T_{low} is a user specified design parameter. Additional information regarding the operational temperature range of the heater element is given by Eq. B.13. This equation is for the user's reference and is introduced later in this report and does not enter into the optimization formulation.

$$T_{low} = \frac{\left(R_1 R_4 \big/ R_3 R_{ref} - 1 \right)}{\alpha_h} + T_{ref} \tag{B.11}$$

$$g_1 : \quad \frac{\left(R_1 R_4 \big/ R_3 R_{ref} - 1 \right)}{\alpha_h} + T_{ref} - T_{low} \le 0 \tag{B.12}$$

$$T_{range} = T_{high} - T_{low} = \frac{20000 R_1 R_5}{\alpha_h R_5 R_3 R_{ref} + 20000 \alpha_h R_3 R_{ref}} = \frac{R_1 R_5}{\alpha_h R_3 R_{ref}} \left(\frac{20000}{R_5 + 20000} \right) \tag{B.13}$$

B.2.4 Inequality Constraint 2: Minimize Power Dissipation Across Right Side of Bridge

A physical constraint that arises due to the circuit operation considers the amount of current flow through each side of the wheatstone bridge. Ideally, the user would like

to have the largest current flow through the heater element R_h. This situation further validates the assumption that the metal film resistors on the right side of the bridge do not change resistance because very little current will flow through them and thus a negligible amount of heat is generated. In addition, this allows large amounts of power to be dissipated through the heater which can occur during times of large boundary heat flux conditions. The larger the voltage present across the heater, the larger the range of boundary conditions the heater can accommodate. In order to ensure that a small amount of power is dissipated by the right side of the bridge, the resistance $R_3 + R_4$ should be significantly higher that $R_1 + R_{ref}$. Stated mathematically, Eq. B.14 represents this constraint with C_{min} being the minimum value of this ratio chosen by the user.

$$g_2: \qquad C_{\min} - \frac{R_3 + R_4}{R_1 + R_{ref}} \leq 0 \tag{B.14}$$

B.2.5 Inequality Constraint 3: Maximum Voltage Drop Across R_1

The voltage drop across R_1 should not be too high as to decrease the maximum performance of the heater array. Under high heat flux conditions, the heater resistance may require a large voltage to regulate its temperature. If the voltage drop across R_1 is too large, this will not occur. The voltage drop across a resistor in series with another is represented by Eq. B.15. Defining a maximum voltage drop permissible across R_1, V_{drop}, and substituting in Eq. 1 for R_h, an additional constraint is formulated, Eq. 16.

$$V_{drop} \geq {}^{24R_1}\!\!\diagup\!\!{}_{\left(R_1 + R_h\right)} \tag{B.15}$$

$$g_3: \qquad \frac{24}{\left(1 + \frac{R_4}{R_3} + \frac{R_5 R_{DP}}{R_5 R_3 + R_{DP} R_3}\right)} - V_{drop} \leq 0 \tag{B.16}$$

B.2.6 Inequality Constraint 5: Op-amp Sensitivity (R_1 Bound)

The chopper op-amp has a minimum sensitivity (voltage difference) for accurate operation. The maximum sensitivity in the wheatstone bridge occurs when R_1 and R_h are approximately equal. If the ratio of these two resistances becomes extremely large or small, the op amp is incapable of detecting the voltage difference and thus cannot compensate for an imbalance in the bridge. Therefore, an additional constraint on the system is required (Eq. B.17). Similar to equation B.14, design parameter D_{min} is the lowest user specified ratio of R_1 and R_{ref} and is dependent on the specifications of the op-amp. This equation can be restated as the lower bound of the design variable R_1, Eq. B.18.

$$D_{\min} - \frac{R_1}{R_{ref}} \leq 0 \tag{B.17}$$

$$g_5 : \quad R_1 \geq R_{ref} D_{\min} \tag{B.18}$$

B.2.7 Inequality Constraints 6-11: Additional Design Variable Bounds

All design variables must be real numbers greater than or equal to zero. In addition, R_1, R_3, and R_4 have maximum bounds specified by the design parameters R_{1Ubnd}, R_{3Ubnd}, and R_{4Ubnd} respectively. R_5 can be any real number greater than zero and R_{DP} has a maximum value of 20,000. Equations B.19-B.24 represent additional design variable bounds.

$$\begin{aligned} g_6 - g_{11} : \qquad & R_1 \leq R_{1Ubnd}, \quad 0 \leq R_3 \leq R_{3Ubnd}, \\ & 0 \leq R_4 \leq R_{4Ubnd}, \quad 0 \leq R_5 \leq \infty, \\ & 0 \leq R_{DP} \leq 20000 \end{aligned} \tag{B.19-B.24}$$

B.2.8 Equality Constraint 1: Define Optimized Temperature

A brief analysis of Eq.7, the optimization objective function, provides some insight into this next constraint. Firstly, Eq. 7 is nonlinear w.r.t R_{DP} indicating that the temperature resolution increases with the inverse of the quadratic of R_{DP}. This means that the heater temperature resolution will increase with an increase in heater temperature. It can be shown that the temperature uncertainty is monotonically decreasing w.r.t R_{DP} for $R_{DP} > 0$, Eq. B.25. This indicates that the worst temperature resolution always occurs for a digital potentiometer setting of zero.

$$\frac{\partial(\Delta T_h)}{\partial R_{DP}} = \frac{78 R_1 R_5}{\alpha_h R_{ref} R_3}\left[\frac{R_{DP}}{(R_5 + R_{DP})^3} - \frac{1}{(R_5 + R_{DP})^2}\right] = \frac{-78 R_1 R_5^2}{\alpha_h R_{ref} R_3 (R_5 + R_{DP})^3} \qquad \text{(B.25)}$$

Since R_{DP} is controlled by the user and can take on 512 incremental values between 0 and 20 k Ω, a particular heater temperature, T_{opt}, is defined which corresponds to the heater temperature being optimized. This constraint forces R_{DP} to take on a single value corresponding to T_{opt} and eliminates the semi-infinite behavior of this variable, Eq. B.26. The monotonic behavior of the objective function w.r.t R_{DP} indicates that all temperatures above T_{opt} will have a temperature resolution that is *guaranteed* to be better than the temperature resolution at T_{opt}. This characteristic aids the user in selecting this critical design parameter value.

$$h_1: \quad -\frac{R_1 R_4}{\alpha_h R_3 R_{ref}} - \frac{R_{DP} R_1 R_5}{\alpha_h R_5 R_3 R_{ref} + R_{DP} \alpha_h R_3 R_{ref}} + \frac{1}{\alpha_h} - T_{ref} + T_{opt} = 0 \qquad \text{(B.26)}$$

In summary, equality constraint 1 (Eq. B.26), reduces the optimization goal from optimizing the temperature resolution over the entire temperature range, to optimizing a

single heater temperature value. This constraint was formulated as such because in the particular research context that the author is involved, excellent temperature resolution is not required at the low temperature limit, T_{low}, but is instead desired over a temperature range from T_{opt} to T_{high}. The solution therefore optimizes the temperature resolution at T_{opt} and because of the monotonic nature of the objective function w.r.t R_{DP}, all temperatures between T_{opt} and T_{high} are guaranteed to have a temperature resolution better or equal to the temperature resolution at T_{opt}.

B.2.9 Optimization Formulation Summary

In summary, customization of the feedback control circuits is governed by an optimization formulation that seeks to minimize the temperature resolution of a single heater, Eq. B.6, and maximize the high temperature limit, Eq. B.10, subject to the non-linear inequality constraints, g_1-g_3 (Eq. B.12, B.14, B.16), non-linear equality constraint, h_1 (Eq. B.26), and the design variable bounds, g_5-g_{11} (Eq. B.18-B.24). The representative multiobjective and single objective optimization formulations are summarized on the following pages (note: the single objective formulation applies the epsilon constraint method to the multiobjective formulation).

Design Variables (resistor values, see Fig 1.2):
R_1 [Ω], R_3 [Ω], R_4 [Ω], R_5 [Ω], R_{DP} [Ω]

Design Parameters:

α_h: temperature coefficient of resistance of the heater [Ω / Ω ^oC]
R_{ref}: reference resistance of the heater array at reference temperature [Ω]
T_{ref}: reference temperature corresponding to reference resistance [^oC]
C_{min}: constant used to minimize power dissipated across the right side of the wheatstone bridge
D_{min}: minimize ratio defined by the operation of the chopper op-amp (see 1.2).
T_{high}: the highest temperature that the heater must reach [^oC]
T_{low}: the lowest temperature the heater must be able to operate at [^oC]
T_{opt}: the temperature being optimized [^oC]

R_{1Ubnd}: upper bound of R_1 [Ω]
R_{3Ubnd}: upper bound of R_3 [Ω]
R_{4Ubnd}: upper bound of R_4 [Ω]
V_{drop}: max voltage drop across R_1 [V]

Single-Objective Optimization Formulation:

Objective Function:

$$\Delta T_h = \frac{39 R_1 R_5^2}{\alpha_h R_{ref} R_3 \left(R_5 + R_{DP}\right)^2} \tag{B.7}$$

Subject to:

$$g_1: \quad \frac{\left(R_1 R_4 \big/ R_3 R_{ref} - 1\right)}{\alpha_h} + T_{ref} - T_{low} \le 0 \tag{B.12}$$

$$g_2: \quad C_{\min} - \frac{R_3 + R_4}{R_1 + R_{ref}} \le 0 \tag{B.14}$$

$$g_3: \quad \frac{24}{\left(1 + \frac{R_4}{R_3} + \frac{R_5 R_{DP}}{R_5 R_3 + R_{DP} R_3}\right)} - V_{drop} \le 0 \tag{B.16}$$

$$g_4: \quad T_{high} - \frac{R_1 R_4}{\alpha_h R_3 R_{ref}} - \frac{20000 R_1 R_5}{\alpha_h R_5 R_3 R_{ref} + 20000 \alpha_h R_3 R_{ref}} + \frac{1}{\alpha_h} - T_{ref} \le 0 \tag{B.9}$$

$$g_5 - g_{11}: \quad R_{ref} D_{\min} \le R_1 \le R_{1Ubnd}, \quad 0 \le R_3 \le R_{3Ubnd}, \quad 0 \le R_4 \le R_{4Ubnd}, \quad 0 \le R_5 \le \infty, \quad 0 \le R_{DP} \le 20000 \tag{B.18-24}$$

$$h_1: \quad -\frac{R_1 R_4}{\alpha_h R_3 R_{ref}} - \frac{R_{DP} R_1 R_5}{\alpha_h R_5 R_3 R_{ref} + R_{DP} \alpha_h R_3 R_{ref}} + \frac{1}{\alpha_h} - T_{ref} + T_{opt} = 0 \tag{B.26}$$

Multiobjective formulation:

Objective Function:

$$\min\ \Delta T_h = \frac{39 R_1 R_5^2}{\alpha_h R_{ref} R_3 \left(R_5 + R_{DP}\right)^2} \tag{B.7}$$

$$\max T_{high} = \frac{R_1 R_4}{\alpha_h R_3 R_{ref}} + \frac{20000 R_1 R_5}{\alpha_h R_5 R_3 R_{ref} + 20000 \alpha_h R_3 R_{ref}} - \frac{1}{\alpha_h} + T_{ref} \tag{B.10}$$

Subject to:

$$g_1: \quad \frac{\left(R_1 R_4 \big/ R_3 R_{ref} - 1\right)}{\alpha_h} + T_{ref} - T_{low} \le 0 \tag{B.12}$$

$$g_2: \quad C_{\min} - \frac{R_3 + R_4}{R_1 + R_{ref}} \le 0 \tag{B.14}$$

$$g_3: \quad \frac{24}{\left(1 + \frac{R_4}{R_3} + \frac{R_5 R_{DP}}{R_5 R_3 + R_{DP} R_3}\right)} - V_{drop} \le 0 \tag{B.16}$$

$$g_5 - g_{11}: \quad R_{ref} D_{\min} \le R_1 \le R_{1Ubnd}, \quad 0 \le R_3 \le R_{3Ubnd}, \quad 0 \le R_4 \le R_{4Ubnd}, \quad 0 \le R_5 \le \infty, \quad 0 \le R_{DP} \le 20000 \tag{B.18-24}$$

$$h_1: \quad -\frac{R_1 R_4}{\alpha_h R_3 R_{ref}} - \frac{R_{DP} R_1 R_5}{\alpha_h R_5 R_3 R_{ref} + R_{DP} \alpha_h R_3 R_{ref}} + \frac{1}{\alpha_h} - T_{ref} + T_{opt} = 0 \tag{B.26}$$

B.3 ASSUMPTIONS

The formulation derived previously incorporated a number of assumptions in addition to assuming the ideal behavior of the op-amp and transistor. Firstly, the circuit leads are assumed to have a zero resistance. Parasitic effects associated with inductance and capacitance within the circuits is assumed to have a negligible effect on the circuit performance. Design variables R_1, R_3, R_4, and R_5 are assumed to have negligible temperature dependence. This is a valid assumption for R_3, R_4, and R_5 but significant power may be dissipated through R_1 causing a measurable change in its resistance. A more robust model would account for slight changes in this resistance due to joule heating.

The heater resistance is assumed to be solely dependent on temperature. In reality, thermal fatigue of the heater array can cause wire bond detachment, cracking of the heater substrate, voids to form between the substrate and epoxy adhesive, and many other problems which can lead to operational transients. This assumption defines what it means to be an ideal heater (one that has uniform temperature and no time varying thermal properties). The heater properties have been measured experimentally and the heater itself has been sufficiently tested so that the ideal heater assumption is valid.

For the following analysis, all design variables are assumed to be continuous variables. In reality, the commercial market only sells discrete resistors. It is assumed that multiple resistors can be put together in parallel or series combinations so that, practically speaking, the continuous assumption is valid. Theoretically, R_{DP} is a discrete variable, but can be modeled as a continuous variable with little loss in modeling accuracy.

It should be noted that the nature of the current control circuit design allows resistors to be removed and installed quite easily. Through hole mounted sockets are used on printed circuit boards which eliminates the need for any additional soldering. Therefore, optimized resistance values can be installed and modified with little effort and the performance can be validated experimentally with relative ease.

B.4 METHODS, RESULTS, AND DISCUSSION

The presence of the nonlinear equality constraint, h_1, makes it difficult to obtain any significant insight into the problem using monotonicity analysis. Nonetheless, the monotonic behavior w.r.t the different design variables for the temperature resolution objective function, ΔT_h or T_{unc}, is shown for positive valued design variables, Eq. B.27-B.30.

$$\frac{\partial T_{unc}}{\partial R_1} = \frac{39R_5^2}{a_h R_{ref} R_3 \left(R_5 + R_{DP}\right)^2} \geq 0 \tag{B.27}$$

$$\frac{\partial T_{unc}}{\partial R_3} = \frac{-39R_1R_5^2}{a_h R_{ref} R_3^2 \left(R_5 + R_{DP}\right)^2} \leq 0 \tag{B.28}$$

$$\frac{\partial T_{unc}}{\partial R_5} = \frac{78R_1R_5R_{DP}}{a_h R_{ref} R_3 \left(R_5 + R_{DP}\right)^3} \geq 0 \tag{B.29}$$

$$\frac{\partial T_{unc}}{\partial R_{DP}} = \frac{-78R_1R_5^2}{a_h R_{ref} R_3 \left(R_5 + R_{DP}\right)^3} \leq 0 \tag{B.30}$$

As mentioned previously, the mulitobjective formulation was converted to a single objective optimization problem using the epsilon constraint method. This was achieved by introducing an additional design parameter, T_{high}, which was used to convert

the second objective, Eq. B.10, to a constraint, g_4 (Eq. B.9) which was varied over a specified range to obtain the Pareto frontier. A representative optimum was chosen based on user preferences and is elaborated on later in this report.

An initial point sensitivity analysis was performed to assess the affect of the initial point on the optimization results. It was observed that the initial point strongly affects the optimized solutions and further discussion will be provided in the next section. A parametric investigation was performed on the design parameters T_{low}, and T_{opt} and their affect on the optimized design is presented subsequently. These design variables were chosen to be parametrically varied because it was observed that the constraint g_1 was active at the optimum and furthermore, h_1, has a strong dependence on T_{opt}. Lastly, a custom optimization solution algorithm, based on the exterior penalty method, was developed and used to verify the results obtained using the Matlab function, "fmincon". As will be shown, both methods agree very well with one another adding to the validity of the solutions presented herein.

Before proceeding any further, it is necessary to define the different values chosen for the design parameters. The lower bounds for design variables, R_3, R_4, R_5, R_{DP}, were chosen to be a very small value, as shown in Table B.1, which avoids any singularity issues associated with the objective or constraint functions. In addition, consideration was given to avoid lower boundary values which became active constraints at the optimized solution. Similar reasoning was applied to the upper boundary limits on the design variables where all resistances except R_5 were specified to be less than 1 MΩ. R_5 can naturally tend toward infinity without degrading the performance of the circuit. The design parameters α, R_{ref}, and T_{ref} were determined based on the physical characteristics

of the heater array and confirmed experimentally. C_{min} and D_{min} were chosen from experience, where adequate performance of the circuit has been observed. V_{drop} was chosen based upon the maximum operating boundary conditions that are applied to heater. It has been shown through experimentation that the heater can require up to 14 volts in order to accommodate large heat flux boundaries and therefore, V_{drop} was to chosen to be 10 volts (24V – 14V).

For the particular boiling fluid being studied (FC-72), the saturation temperature is 56 ^{o}C at atmospheric pressure. Of particular interest are the boiling characteristics at temperatures higher than 70 ^{o}C. Therefore, the temperature resolution below this value is not significant and the baseline T_{opt} value was chosen as 70 ^{o}C. The low operational temperature limit, T_{low}, was chosen to allow for adequate operation of the heater under ambient room temperature conditions with some margin added for safety. Operation of the heater at room temperature provides time saving diagnostic capabilities that can be used to quickly characterize the heater prior to data acquisition. T_{high} was chosen based on reliability and safety considerations (120 ^{o}C). Most industrial electronic devices are rated to 125 ^{o}C which makes this a good temperature limit while providing a suitable range for the superheat of the fluid during boiling to be studied. Lastly, T_{high}, T_{low}, and T_{opt} were parametrically studied over a range of values shown in Table 1. The baseline, or user preferred, case is the default design parameter vector used while varying the parametric variables in question.

Table B.1: Design parameter values

		Baseline		Parametric Study
LOWER BOUND	R_1	89.4		**T_{opt}: 20, 30, 40, 50, 60, 70, 80, 90, 100, 110, 120**
	R_3	0.000001		
	R_4	0.000001		
	R_5	0.000001		
	R_{DP}	0.000001		
UPPER BOUND	R_{1Ubnd}	500		**T_{low}: 10, 15, 20, 25, 30, 35, 40, 45, 50, 55, 60, 65**
	R_{3Ubnd}	1000000		
	R_{4Ubnd}	1000000		
	R_5	inf		
	R_{DP}	20000		
DESIGN PAR.	α	0.003		**T_{high}: 71, 75, 77.5, 80, 82.5, 85, 90, 95, 100, 105, 110, 115, 120, 130, 140,**
	R_{ref}	298		
	T_{ref}	24.7		
	C_{min}	20		
	D_{min}	0.3		
	T_{high}	120		
	T_{low}	10		
	T_{opt}	70		
	Vdrop	10		

B.5 SINGLE OBJECTIVE RESULTS USING "fmincon"

As mentioned above, the Matlab function, "fmincon" was used to solve the single objective optimization formulation. This function finds the constrained minimum of a scalar function of several variables starting at an initial point estimate. It takes a number of input arguments including the function to be minimized, nonlinear equality and equality constraints, variable bounds, and others.

B.5.1 Initial Point Sensitivity

After programming the single objective formulation into Matlab and solving for a number of different initial points, it was observed that each optimized output was

quantitatively different. After verifying the Matlab output solutions were feasible, it was determined that a rigorous initial point sensitivity analysis was required to characterize the outputs. The approach developed shares many similarities to Monte Carlo analysis.

The first step involved obtaining a representative set of initial points that spanned the entire range of the variable bounds. Considering the fact that there exist 5 variables and a low, medium, and high, value for each variable was desired, the number of different combinations one can obtain from this set is 125. Adding additional robustness, 250 randomly distributed initial value sets were computed in Matlab (for a single design parameter vector, ex. "Baseline") and the optimized solution of each was determined using "fmincon".

The initial design points, used as an input into the "fmincon" function were calculated by first generating a uniformly distributed random number from zero to one in Matlab and then applying that value on a percentage basis to the design variable bounding limits. Since the high limit bounds are so large for the design variables, a random permutation vector between 2 and 6 was also generated at each iteration to represent the exponent of the high limit (Ex. 10^2, 10^3, 10^5, 10^6, 20000). This ensured that low value combinations could be obtained in the simulation and provides a better representation of the initial value space. This additional step enabled a more random distribution to be obtained. The process as described above was repeated for all five design variables until a single initial point vector was generated. An iterative process was then used to obtain an initial point matrix with the total number of rows equal to the total number of initial point vectors, 250 (Eq. B.31). This matrix was input into Matlab and a solution was obtained for each initial point vector.

The 250 optimized solutions obtained were then plotted on a histogram to observe the distribution of objective function values, Fig. B.2. The majority of the optimized solutions fall very close to the global minimum (lowest optimized objective value) of the formulation. The minimum of these 250 results was then chosen as the "representative" optimum or the design that most closely represents the global optimum for the particular formulation. In the parametric analysis that follows, this modified Monte Carlo procedure was conducted for each design parameter vector.

$$\begin{bmatrix} R_{1,1} & R_{1,3} & R_{1,4} & R_{1,5} & R_{1,dp} \\ \vdots & \vdots & \vdots & \vdots & \vdots \\ R_{i,1} & R_{i,3} & R_{i,4} & R_{i,5} & R_{i,dp} \\ \vdots & \vdots & \vdots & \vdots & \vdots \\ R_{250,1} & R_{250,3} & R_{250,4} & R_{250,5} & R_{250,dp} \end{bmatrix} \qquad \text{(B.31)}$$

$i = initial\ \ point\ vector\ number$

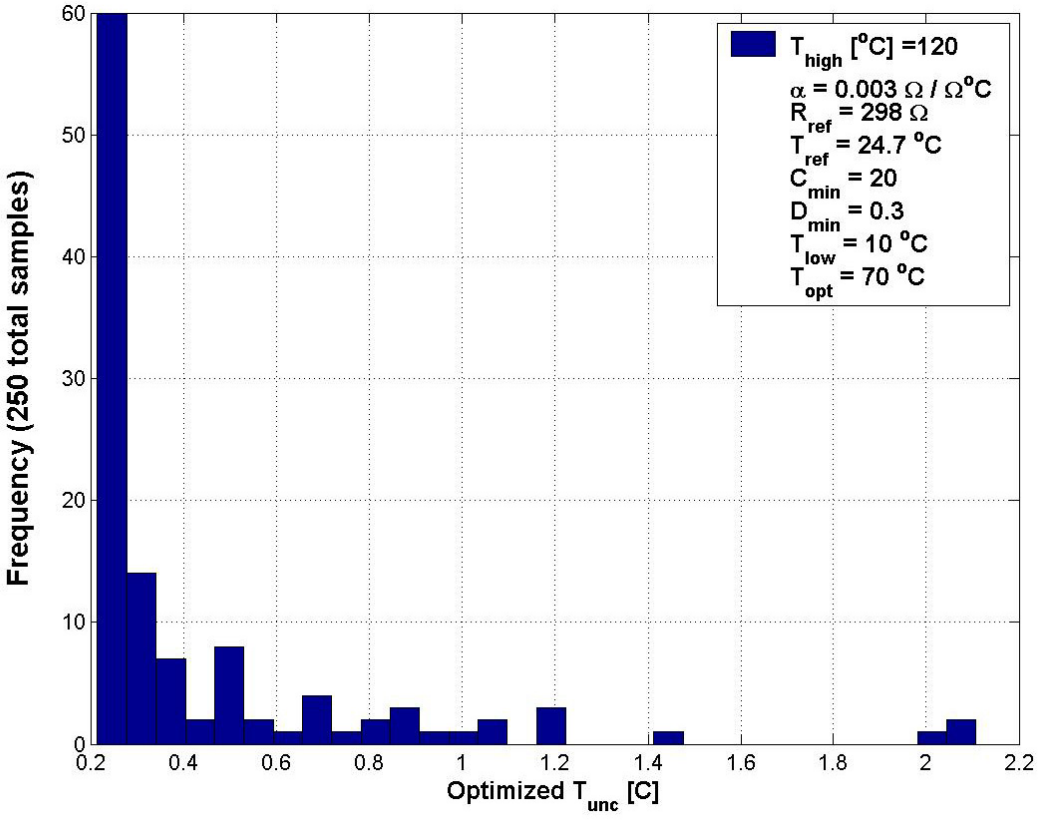

Figure B.2. Example objective function distribution for different initial points

B.5.2 Pareto Frontier

As mentioned previously, the multiobjective formulation was converted to a single objective problem using the epsilon constraint method. The epsilon constraint method is an A posteriori method used to solve multiobjective optimization problems and is of the form:

$$\begin{aligned} &\min imize\ f_l(x) \\ &subject\ to \quad f_j(x) \le \varepsilon_j \quad for\ all\ j = 1,.....,k \quad j \neq l \\ &\qquad\qquad x \in S \end{aligned}$$

Where S is the feasible design space.

The Pareto frontier provides the solution to the multiobjective optimization formulation in k variable space (where k is the total number of objective functions). A decision vector x* ε S is Pareto optimal if there does not exist another decision vector x such that f_i (x) less than or equal to f_i (x*) for all i = 1,….k, and f_j (x) < f_j (x*) for atleast 1 index j [2]. In order to obtain a single optimum design from the Pareto solution set, a user weighting method was applied to the objectives. For the particular problem under investigation, the Pareto frontier is shown in Fig. B.3. From this graph it is clear than the objective space in nonconvex. In addition, the constraint, g_4 (epsilon constraint) was active for all the optimal solutions obtained which helps to validate the choice of the second objective.

Applying user preferences to Fig. B.3, a single design is chosen based on the "baseline" design parameter vector from Table. B.1. This design has a number of interesting characteristics as shown in Fig. B.4. In this figure, the x-axis represents the temperature of the heater and the y-axis is the single objective function value or T_{unc}.

When compared to the current design, it is clear that the optimal design performs much better at temperatures above 70 ^{o}C. It should be noted that at 70^{o}C, a slight (< 1%) enhancement in performance in observed. Table B.2 provides additional information regarding the optimal and current designs and Table B.3 summarizes the Pareto results.

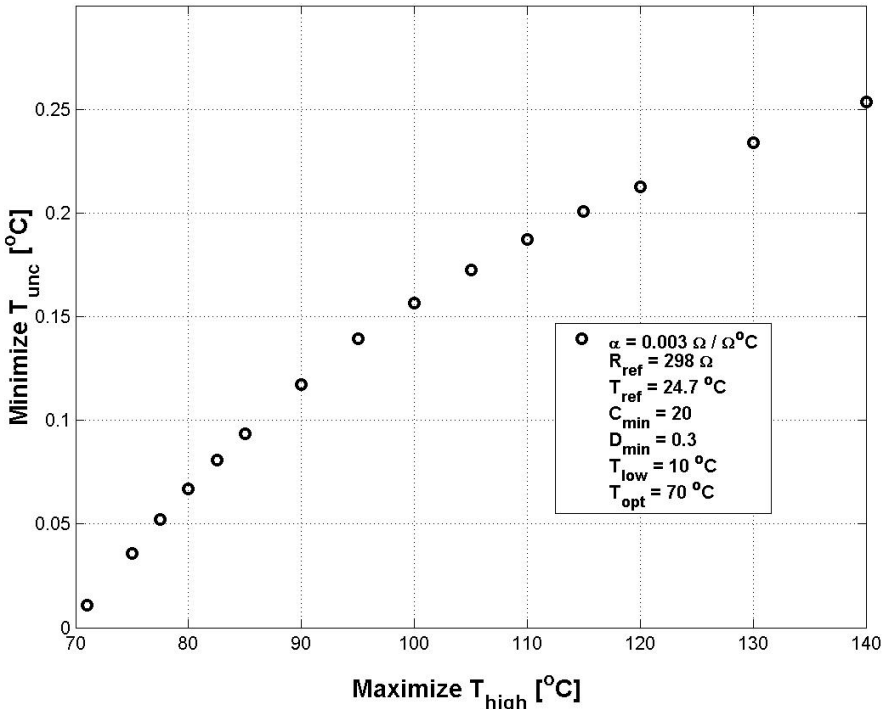

Figure B.3: Pareto frontier

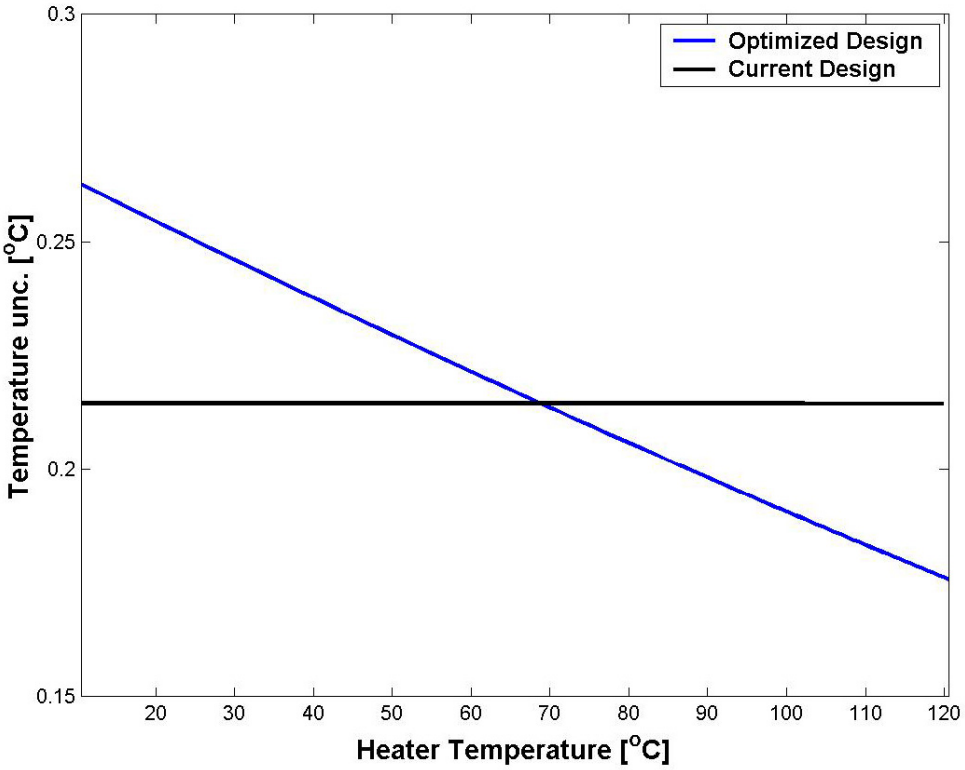

Figure B.4: User specified optimal design ("baseline" design parameter values).

Table B.2: Current vs. optimal design comparison (single-objective formulation).

		OPTIMUM DESIGN	CURRENT DESIGN
DESIGN VARIABLES	R_1 [Ω]	*167*	237
	R_3 [kΩ]	*27.733*	47.6
	R_4 [kΩ]	*47.379*	57
	R_5 [kΩ]	*89.786*	1000000
	R_{dp} [kΩ]	*9.906*	10.7
OBJECTIVE FUNCTION	F	*0.2127*	0.2157
CONSTRAINTS	g_1	*0*	0
	g_2	*-142*	-175.3975
	g_3	*-2.08*	-0.099
	g_4	*0*	-2.025
	h_1	*1E-13*	*1E-13*

Table B.3: Pareto results

MATLAB INPUTS	INITIAL POINT	R_1	246.4	474.02	187	310	410	311	120	168.61	474.3	365	466	253.98
		R_3	4033.1	423810	20363	523110	650	64	34150	18231	1780.4	323	5311	479940
		R_4	4851	70	3930	770	250	84	675030	60	893.9	11141	91653	85.912
		R_5	49.8	6910	345	6480	296700	76373	30	810	457.6	69189	86592	56.331
		R_{DP}	5844.3	15520	3010	4590	7880	13268	1114	17738	440.2	2839	19241	12020
	LOWER BOUND	R_1	89.4	89.4	89.4	89.4	89.4	89.4	89.4	89.4	89.4	89.4	89.4	89.4
		R_3	1E-06	1E-06	1E-06	1E-06	1E-06	1E-06	1E-06	1E-06	1E-06	1E-06	1E-06	1E-06
		R_4	1E-06	1E-06	1E-06	1E-06	1E-06	1E-06	1E-06	1E-06	1E-06	1E-06	1E-06	1E-06
		R_5	1E-06	1E-06	1E-06	1E-06	1E-06	1E-06	1E-06	1E-06	1E-06	1E-06	1E-06	1E-06
		R_{DP}	1E-06	1E-06	1E-06	1E-06	1E-06	1E-06	1E-06	1E-06	1E-06	1E-06	1E-06	1E-06
	UPPER BOUND	R_1	500	500	500	500	500	500	500	500	500	500	500	500
		R_3	1E+06	1E+06	1E+06	1E+06	1E+06	1E+06	1E+06	1E+06	1E+06	1E+06	1E+06	1E+06
		R_4	1E+06	1E+06	1E+06	1E+06	1E+06	1E+06	1E+06	1E+06	1E+06	1E+06	1E+06	1E+06
		R_5	inf	inf	inf	inf	inf	inf	inf	inf	inf	inf	inf	inf
		R_{DP}	20000	20000	20000	20000	20000	20000	20000	20000	20000	20000	20000	20000
	DESIGN PAR.	α	0.003	0.003	0.003	0.003	0.003	0.003	0.003	0.003	0.003	0.003	0.003	0.003
		R_{ref}	298	298	298	298	298	298	298	298	298	298	298	298
		T_{ref}	24.7	24.7	24.7	24.7	24.7	24.7	24.7	24.7	24.7	24.7	24.7	24.7
		C_{min}	20	20	20	20	20	20	20	20	20	20	20	20
		D_{min}	0.3	0.3	0.3	0.3	0.3	0.3	0.3	0.3	0.3	0.3	0.3	0.3
		T_{high}	**71**	**75**	**80**	**85**	**82.5**	**77.5**	**90**	**95**	**105**	**115**	**120**	**140**
		T_{low}	10	10	10	10	10	10	10	10	10	10	10	10
		T_{opt}	70	70	70	70	70	70	70	70	70	70	70	70
		Vdrop	10	10	10	10	10	10	10	10	10	10	10	10
MATLAB OUTPUT (GLOBAL OPTIMUM)	DESIGN VAR.	R_1	241.78	240.13	242	238	89.898	164	231	211.36	106	89.553	167	129.61
		R_3	4957	6893	12628	17759	5758	6811	20035	28752	13907	14722	27733	22305
		R_4	5840	8176	14875	21243	18246	11802	24707	38750	37422	46830	47379	49021
		R_5	1184	1820	3911	6667	5239	2857	8992	21396	25235	67567	89786	1E+11
		R_{DP}	15406	10004	9912	1000	9982	10000	9640	11073	9777	10142	9906	9231
	OBJ. FUNC.	F1	**0.0108**	**0.036**	**0.0669**	**0.0936**	**0.0807**	**0.052**	**0.1172**	**0.1393**	**0.1725**	**0.2006**	**0.2127**	**0.2535**
	CONSTR.	g_1	0	0	0	0	0	0	0	0	0	0	0	0
		g_2	0	-8	-31	-52.7	-41.9	-20.3	-64.581	-112.52	-107.1	-138.82	-141.62	-146.8
		g_3	0	-0.04	0	-0.09	-4.96	-2.15	-0.2652	-0.7747	-4.2825	-4.979	-2.0795	-3.3548
		g_4	0	0	0	0	0	0	0	0	0	0	0	0
		h_1	1E-13	1E-13	1E-13	1E-13	1E-13	1E-13	1E-13	1E-13	1E-13	1E-13	1E-13	1E-13

B.5.3 Parametric Study

Results of the parametric investigation of T_{low} are shown in Fig. B.5 and Table B.5 (located in Appendix III). In all of the cases studied, g_1 was active at the optimum, Fig. B.5. T_{low} appears to have a linear affect (monotonically decreasing) on the optimized objective function value T_{unc} over the range studied.

The second parametric investigation focused on the affect of T_{opt}. T_{opt} has a very interesting affect on the optimal solution as seen in Fig. B.6. For low values (near T_{low}), T_{low} appears to have no effect on the optimum. At larger values, near T_{high}, strong dependence on the optimized objective function is observed. Table B.6 (Appendix III) details the results of this parametric investigation.

Lastly, the optimization effects of T_{low}, T_{high}, and T_{opt} can be represented in a non-dimensional form combining all of effects presented in this section and the previous one. If the non-dimensional values shown in Eqs. B.32, B.33 are defined, and the results from Tables B.3, B.5 and B.6 are written in terms of Eq. B.32, B.33, then Fig B.7 results. Tabular non-dimensional results are presented in Appendix III, Table B.8. The important observation is that the non-dimensional results collapse onto the same curve. This indicates that if the temperature range and optimization temperature is chosen, the optimal temperature resolution can be taken directly from the graph (although a complete solution would have to be obtained using one of the solution methods described herein). This provides the user with a powerful predictive means of determining the optimal design.

$$T_{rnage,non} = \frac{T_{opt} - T_{low}}{T_{high} - T_{low}} = \%range \qquad \Delta T_{non} = \frac{T_{unc}}{T_{flat}} = \frac{T_{unc}}{T_{range}/512} = \%res \qquad \text{(B.32,B.33)}$$

The matlab code used to obtain the results presented herein is available in Appendix D.

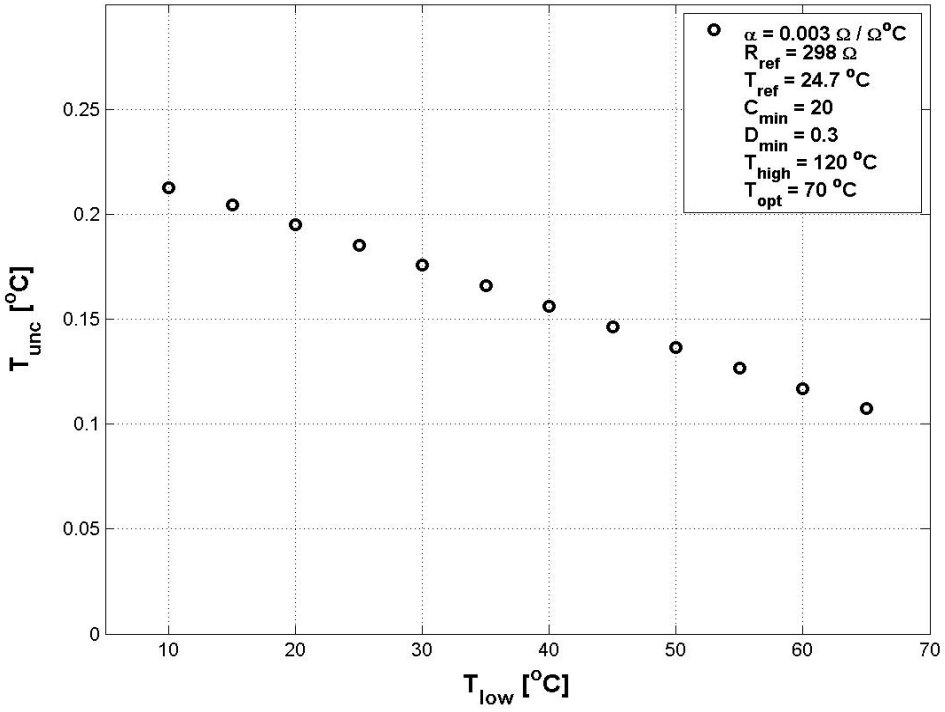

Figure B.5. Parametric effect of T_{low} on optimum solution.

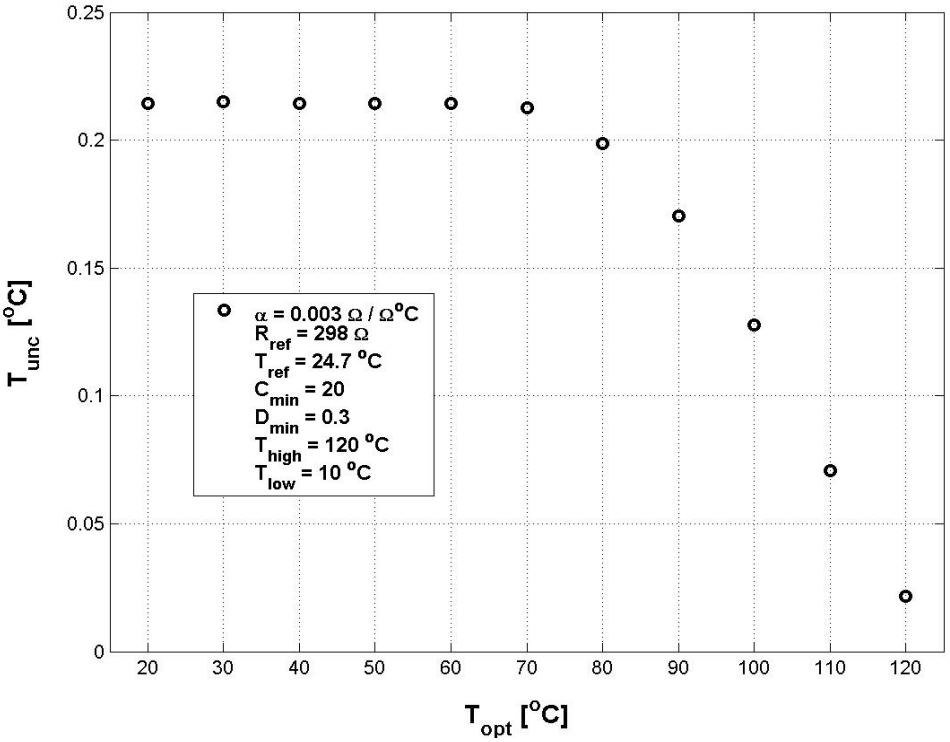

Figure B.6. Parametric effect of T_{opt} on optimum solution.

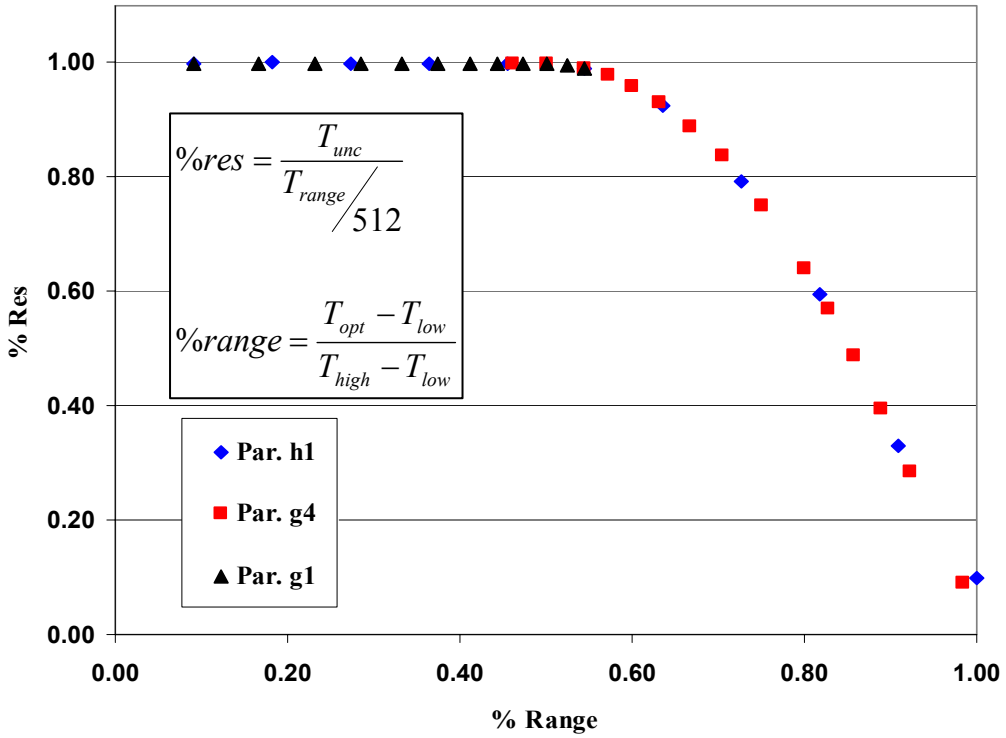

Figure B.7. Non-dimensional results (Par. g4, Par. g1, and Par. h_1 represent the results obtained from Tables 3, 5, and 6 respectively in non-dimensional form).

B.6 EXTERIOR PENALTY METHOD

A second optimization solution method was developed based on the exterior penalty approach. This method involves converting the constrained single objective formulation to an unconstrained optimization problem which can then be solved using a number of well-developed unconstrained optimization techniques. The method is classified as a transformation method for this reason. The Penalty method considers the transformation of the constrained formulation to unconstrained form given by Eq. B.34, where ΔT_h is the objective function (Eq. B.7) and g(x) and h(x) are vectors defined in the single objective formulation presented previously.

$$P(R,t) = \Delta T_h + \Omega\left(t, g(x), h(x)\right) \tag{B.34}$$

For small penalty terms, Matlab was unable to obtain a solution, Fig. B.8. As the penalty term is increased above 100, the optimized solution reaches a steady value. The entire unconstrained exterior penalty formulation can be found in Appendix II. As can be seen in Table B.4, the optimization results obtained using this exterior penalty approach agree very well with the results obtained in Matlab using "fmincon" (detailed results can be found in Table B.7, Appendix III).

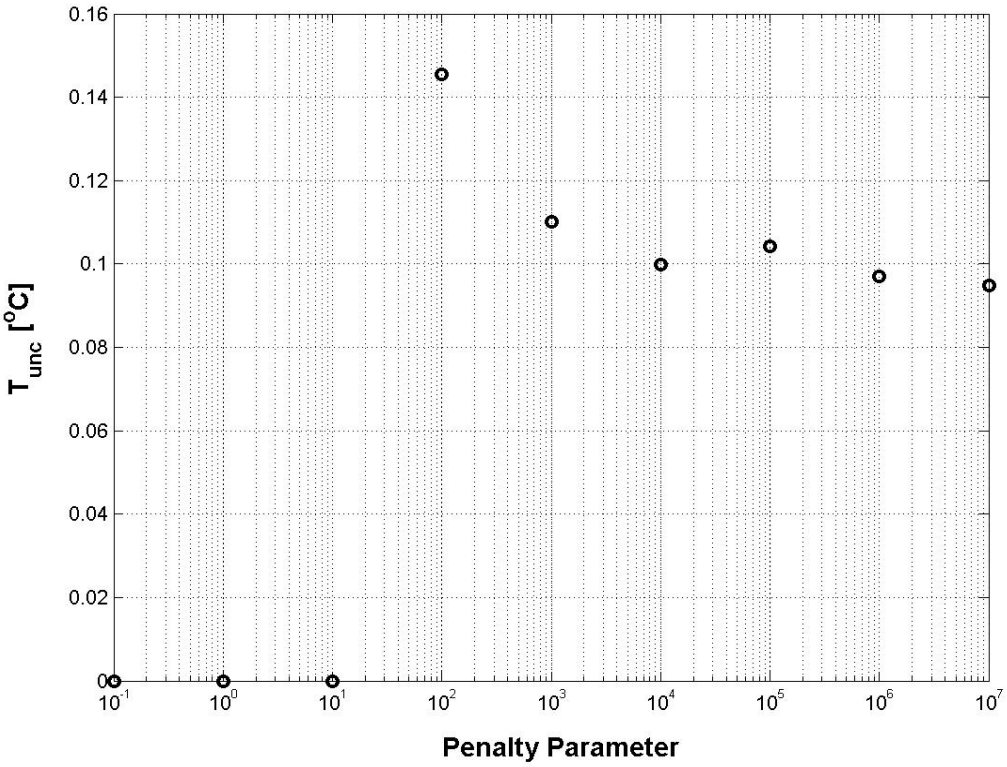

Figure B.8. Affect of the penalty term on the unconstrained optimization results.

Table B.4. Exterior penalty and "fmincon" comparison

T_{opt} [^oC]	T_{unc} ("fmincon") [^oC]	T_{unc} EP [^oC]	% DEV
71	0.0108	0.0114	5.56%
75	0.036	0.0365	1.39%
80	0.0669	0.0686	2.54%
85	0.0936	0.0947	1.18%
82.5	0.0807	0.0825	2.23%
77.5	0.052	0.0547	5.19%
95	0.1393	0.1386	0.50%
105	0.1725	0.1729	0.23%
120	0.2127	0.2129	0.09%
140	0.2535	0.2535	0.00%

Appendix C

C.1 FINAL HEATER RESISTANCE VALUES

Card #	Circuit #	Heater #	R_h (Ω)	R_1 (Ω)	R_2 (Ω)	R_3 (Ω)	R_4 (Ω)	R_5 (Ω)
0	0	17	199	66.5	48800	26200	76800	200000
	1	65	195	64.8	48800	26200	76800	200000
	2	18	11		48800	26200	76800	200000
	3	38	199	66.3	48800	26200	76800	200000
	4	66	193	64.7	48800	26200	76800	200000
	5	6	170	55.9	48800	26200	76800	200000
	6	39	193	64.7	48800	26200	76800	200000
	7	67	170	55.9	48800	26200	76800	200000
	8	19	217	71.3	48800	26200	76800	200000
	9	40	191	63.2	48800	26200	76800	200000
	10	68	210	69.6	48800	26200	76800	200000
	11	1	225	74.7	48800	26200	76800	200000
	12	2	226	74.8	48800	26200	76800	200000
	13	69	210	69.6	48800	26200	76800	200000
	14	41	192	63.2	48800	26200	76800	200000
	15	20	219	71.2	48800	26200	76800	200000
	16	70	172	57.5	48800	26200	76800	200000
	17	42	194	64.6	48800	26200	76800	200000
	18	7	200	66.4	48800	26200	76800	200000
	19	71	194	64.9	48800	26200	76800	200000
	20	43	200	66.2	48800	26200	76800	200000
	21	21	227	74.7	48800	26200	76800	200000
	22	72	196	64.8	48800	26200	76800	200000
	23	22	200	66.2	48800	26200	76800	200000
1	0	44	218	73	48800	26200	76800	200000
	1	73	198	64.6	48800	26200	76800	200000
	2	8	221	73	48800	26200	76800	200000
	3	45	201	66.5	48800	26200	76800	200000
	4	74	189	63.3	48800	26200	76800	200000
	5	23	225	74.7	48800	26200	76800	200000
	6	46	220	73	48800	26200	76800	200000
	7	75	207	68	48800	26200	76800	200000
	8	24	223	74.7	48800	26200	76800	200000
	9	76	215	71.3	48800	26200	76800	200000
	10	47	202	67.9	48800	26200	76800	200000
	11	9	239	78.6	48800	26200	76800	200000
	12	10	230	76.9	0	26200	76800	200000
	13	48	202	66.2	48800	26200	76800	200000
	14	77	222	73.1	48800	26200	76800	200000
	15	25	224	74.9	48800	26200	76800	200000
	16	78	209	69.6	48800	26200	76800	200000
	17	49	221	73.1	48800	26200	76800	200000
	18	26	226	74.8	48800	26200	76800	200000
	19	79	192	63.1	48800	26200	76800	200000
	20	50	221	73.2	48800	26200	76800	200000
	21	11	223	74.9	48800	26200	76800	200000
	22	80	201	66.3	48800	26200	76800	200000
	23	51	222	73	48800	26200	76800	200000

Card #	Circuit #	Heater #	R_h (Ω)	R_1 (Ω)	R_2 (Ω)	R_3 (Ω)	R_4 (Ω)	R_5 (Ω)
2	0	27	204	67.8	48800	26200	76800	200000
	1	81	201	66.2	48800	26200	76800	200000
	2	28	228	76.8	48800	26200	76800	200000
	3	52	203	68.2	48800	26200	76800	200000
	4	82	198	66.8	48800	26200	76800	200000
	5	12	203	67.9	48800	26200	76800	200000
	6	53	197	64.9	48800	26200	76800	200000
	7	83	174	57.5	48800	26200	76800	200000
	8	29	220	73	48800	26200	76800	200000
	9	54	196	64.9	48800	26200	76800	200000
	10	84	215	71.3	48800	26200	76800	200000
	11	3	227	74.9	48800	26200	76800	200000
	12	4	227	74.9	48800	26200	76800	200000
	13	85	213	71.5	48800	26200	76800	200000
	14	55	195	64.9	48800	26200	76800	200000
	15	30	220	73.2	48800	26200	76800	200000
	16	86	174	57.6	48800	26200	76800	200000
	17	56	196	64.9	48800	26200	76800	200000
	18	13	202	66.1	48800	26200	76800	200000
	19	87	196	64.8	48800	26200	76800	200000
	20	57	202	66.6	48800	26200	76800	200000
	21	31	228	76.8	48800	26200	76800	200000
	22	88	199	66.6	48800	26200	76800	200000
	23	32	203	68.2	48800	26200	76800	200000
3	0	58	219	73.4	100065	26200	76800	200000
	1	89	199	66.6	100054	26200	76800	200000
	2	14	222	73.1	100110	26200	76800	200000
	3	59	202	66.1	100079	26200	76800	200000
	4	90	190	63.3	100053	26200	76800	200000
	5	33	226	74.9	100044	26200	76800	200000
	6	60	220	73.2	100064	26200	76800	200000
	7	91	207	68.2	100133	26200	76800	200000
	8	34	208	69.8	100051	26200	76800	200000
	9	92	219	73	100007	26200	76800	200000
	10	61	INF	0	100036	26200	76800	200000
	11	15	231	76.5	100032	26200	76800	200000
	12	16	230	76.6	100073	26200	76800	200000
	13	62	200		100058	26200	76800	200000
	14	93	220	73.1	100076	26200	76800	200000
	15	35	222	73.1	100060	26200	76800	200000
	16	94	207	67.8	100037	26200	76800	200000
	17	63	219	73.2	99998	26200	76800	200000
	18	36	225	74.7	100050	26200	76800	200000
	19	95	188	61.8	100041	26200	76800	200000
	20	64	200	66.3	100055	26200	76800	200000
	21	5	221	73.2	100046	26200	76800	200000
	22	96	196	64.9	100031	26200	76800	200000
	23	37	217	71.6	100058	26200	76800	200000

C.2 COMPRESSIBLE FLOW THEORY

For one-dimensional compressible flow, the variation of density makes the continuity and momentum equations interdependent. Under adiabatic, inviscid, and equilibrium conditions the field equations simplify to: Under steady conditions, the continuity equation simplifies to:

$$\frac{\partial}{\partial x}(\rho v A) = 0 = vA\frac{\partial \rho}{\partial x} + \rho v\frac{\partial A}{\partial x} + \rho A\frac{\partial v}{\partial x} = \frac{1}{\rho}\frac{\partial \rho}{\partial x} + \frac{1}{A}\frac{\partial A}{\partial x} + \frac{1}{v}\frac{\partial v}{\partial x} = \frac{d\rho}{\rho} + \frac{dv}{v} + \frac{dA}{A}$$

For 1-D steady compressible flow neglecting body forces terms, the momentum equation becomes:

$$v\frac{\partial v}{\partial x} = -\frac{1}{\rho}\frac{\partial p}{dx} \Rightarrow vdv + \frac{dp}{\rho} = 0 \Rightarrow \frac{v^2}{2} + \int\frac{dp}{\rho} = const.$$

the energy equation for an ideal gas becomes:

$$h + \frac{1}{2}v^2 = const. \Rightarrow dh + vdv = 0 = c_p dT + vdv \Rightarrow c_p T + \frac{1}{2}v^2 = const.$$

combining the energy and momentum equations it can be shown along with the second law of thermodynamics that:

$$dh - \frac{dp}{\rho} = 0$$

$$Tds = dh - \frac{dp}{\rho}$$

$$ds = \left(dh - \frac{dp}{\rho}\right)\frac{1}{T} = 0 \Rightarrow s = const.$$

This shows that compressible flow under the assumptions stated above is isentropic. The speed at which waves propagate through the fluid is equal to the speed of sound. It is related to the compressibility of the fluid by:

$$a^2 = \left(\frac{\partial p}{\rho}\right)_s$$

For an ideal gas,

$$p = const.\rho^{\gamma} \Rightarrow a^2 = \frac{\gamma p}{\rho} = \gamma RT$$

And the Mach number is used to represent compressibility effects. Combining the momentum and continuity equations and introducing the Mach number it can be shown:

$$\frac{dv}{v} = -\frac{dA/A}{1 - M^2}$$

Therefore M = 1 only at the throat of a tube and cannot go supersonic unless the throat diverges downstream. Combining the energy equation and substituting in for T gives (assuming a reservoir initially with no velocity:

$$\frac{1}{2}v^2 + \frac{a^2}{\gamma - 1} = \frac{a_o^2}{\gamma - 1}.$$

This can be simplified to:

$$\frac{a_o^2}{a^2} = \frac{T_o}{T} = (1 + \frac{\gamma - 1}{2}M^2)$$

$$\frac{p_o}{p} = (1 + \frac{\gamma - 1}{2}M^2)^{1/(\gamma - 1)}.$$

$$\frac{\rho_o}{\rho} = (1 + \frac{\gamma - 1}{2}M^2)^{1/(\gamma - 1)}.$$

because and ideal gas that is isentropic becomes:

$$\frac{p}{p_o} = \left(\frac{\rho}{p_o}\right)^{\gamma} = \left(\frac{T}{T_o}\right)^{\gamma/\gamma - 1}$$

P/Po must be 0.5532 in order to justify Ma = .96.

Appendix D: Data Reduction and Optimization Programs

D.1 DATA REDUCTION PROGRAMS

D.1.1 Program name: qfluxdet.m

Description: This program is used to convert heater, pressure, and accelerometer voltages to SI units.

```
%THIS FILE ASSUMES THE DATA FILES HAVE BEEN CONVERTED FROM BINARY TO TEXT FORMAT CORRECTLY AND ARE STORED ON
   THE CURRENT MACHINE IN THE FILE FORMAT SPECIFIED
%THIS PROGRAM ANALYZES HEAT TRANSFER DATA FROM THE MICROHEATER ARRAY (2.7 mm or 7 mm) IN VARIOUS GRAVITATIONAL
   ENVIRONMENTS (INPUTS FROM USER)
%THIS PROGRAM IS BROKEN UP INTO 8 DISTINCT TASKS SUMMARIZED AS THE FOLLOWING:
%  1)  IDENTIFY RUN AND FILE CHARACTERISTICS
%  2)  CONSTRUCT VOLTAGE FILENAME AND IMPORT HEATER INFORMATION
%  3)  CONVERT UPLOADED WALL TEMP TO ACTUAL CALIBRATED WALL TEMPERATURE
%  4)  BREAK UP MATRIX OF REFERENCE RESISTANCES INTO WORKING VECTORS
%  5)  UPLOAD VOLTAGE TEXT FILES AND CREATE HEAT FLUX MATRIX
%  6)  ANALYZE PRESSURE, ACCELEROMETER, AND TIME VECTORS AND CONCATENATE TO FLUX MATRIX
%  7)  WRITE DATA TO APPROPRIATE FILES
%  8)  CREATE SCREEN OUTPUTS
%  9)  DISPLAY OVERALL OUTPUT
%THIS PROGRAM ANALYZES ONE DAYS DATA (FOR KC-135 DATA) AND LOOPS THROUGH EACH RUN NUMBER FOR THE SPECIFIED DATE

%%%
```

```
%%%
```

```
    lght='9_16heaters';
  elseif  gheatsize == 2
    lght='25_36heaters';
  end
  workshe=strcat('Tbulk',bt,'_',lght);
  datas=xlsread('C:\MATLAB\BOILINGDATA\OneGRunHistory.xls',workshe);          %imports run info for 1G data
end

%%%
```

```
end
if ((environ == 1) | (environ == 2))
   disp('UPLOADING REFERENCE RESISTANCE CHARACTERISTICS');disp('-------------------------------------');
   if (heater == 1)
      heat_res_area=xlsread('C:\MATLAB\work\MicrogravityDataAnalysis\MatlabInput\Chrisdatareduction\PlatinumHeater\refresarea.xls');
      accwall_temp=1.002*wall_temp+.3987;                    %calibration curvefit (5/24/02)
      accwall_temp_unc = 2;
   elseif ((environ == 1) & (heater == 2) & (date > 102000) & (rem(date,2) == 1) & (rem(date,5) > 0) & (date < 110000))
      heat_res_area=xlsread('C:\MATLAB\work\MicrogravityDataAnalysis\MatlabInput\Chrisdatareduction\SevmmHeater\refresareaSevenmm1003.xls');
      accwall_temp=1.0152*wall_temp-0.0882;                   %calibration curvefit (9/4/03)
      accwall_temp_unc = 2;
   elseif ((environ == 1) & (heater == 2) & ((date == 080304) | (date == 080404) | (date == 080504) | (date == 080604)))
      accwall_temp = wall_temp;
      accwall_temp_unc = 2;
      heat_res_area=xlsread('C:\MATLAB\work\MicrogravityDataAnalysis\MatlabInput\Chrisdatareduction\SevmmHeater\refresareaSevenmm0804.xls');
      disp('ANALYZING 7 MM HEATER DATA FOR AUGUST 2004 KC-135 FLIGHT');disp('-------------------------------------');
   end
   %INSERT elseif STATEMENT FOR FUTURE FLIGHT DATA
   %%%%
```

```
%%%
```

```
    newvoltage = voltage;                                   %conversion factor for voltage reading
    conv_vect = [9      10      15      16      21      23      26      28      3       4       31      33      36      18      1       2
        44      8       24      25      11      51      12      29      30      13      58....
         14     34      35      5       37      6       19      20      7       22      45      46      76      77      49      50      27
        52      53      84      85      56      57      32      59      60      92      93....
         63     64      17      38      39      68      69      42      43      73      74      75      47      48      78      79      80
        81      82      83      54      55      86      87      88      89      90      91....
         61     62      94      95      96      65      66      67      40      41      70      71      72 97 98 99 100];       %conversion
vector because heater orientation was different
    for i = 1:100
       newvoltage(:,conv_vect(i)) = voltage(:,i)*1.3629;
    end
    clear voltage i
    voltage = newvoltage;
  end
  %INSERT elseif STATEMENT FOR FUTURE FLIGHT DATA DECODING OR ADDING A FACTOR
  %%%%
```

```
press_vol=voltage(:,98);                                    %pressure signal
acc_press=1*press_vol/.742;                                 %converts pressure voltage to actual pressure (ATM)
disp('FILTERING HIGH FREQUENCY PRESSURE SIGNAL');disp('--------------------------------------');
pressure=sgolayfilt(acc_press,1,1001);                      %filters out high frequencies (applies a Savitzky-Golay FIR smoothing filter)
accel=sgolayfilt(voltage(:,100),1,1001);                    %smooths accelerometer data
figure;subplot(2,2,1);plot(pressure);ylabel('pressure (ATM)');title(titl);
subplot(2,2,2);plot(acc_press);subplot(2,2,4);plot(voltage(:,100));ylabel('acc. voltage');subplot(2,2,3);plot(accel);

pressure2=cat(1,[0;0],pressure);acc_press2=cat(1,[0;0],acc_press);voltage2=cat(1,[0;0],voltage(:,100));accell2=cat(1,[0;0],accel);
time1=[0:1:(length(acc_press2))-3]'/freq;time = cat(1,[0;0],time1);        %time in seconds
datatowrite=cat(2,time,qwrite,acc_press2,pressure2,voltage2,accell2);

%%%
```

```
    save(writefilen3,'qwrite','time','acc_press2','pressure2','voltage2','accell2','accwall_temp','bulktemp','heatersize','onheaters');
  end

  %%%%
```

```
%hold on
%plot(voltage(:,9),'r')
%plot(voltage(:,23),'b')
%plot(voltage(:,8),'k')
%xlabel('Data Point')
%ylabel('Voltage (V)')
%axis([0 22500  2 9])
%legend('heater 9','heater 23','heater 8')
%plot(voltage(:,22))
%plot(voltage(:,23))
%plot(voltage(:,24))
%plot(voltage(:,45))
%plot(voltage(:,46))
```

D.1.2 Program name: FLIGHTSUBCOND.m

Description: This program analyzes the heat flux data created using "qfluxdet.m" in both gravitational environments and provides additional analytical capabilities.

```
%THIS PROGRAM ASSUMES THAT qfluxdet has already been executed and the matlab files already exist

%                                   $$$$$$$$IMPORTANT$$$$$$$
%MODFIFY THIS PROGRAM AT THE SUBSTRATE CONDUCTION BASELINE (LINES 240 - 270 AND ANALYZE THE SATURATION BASELINE
DATE FIRST (TO CREATE THE SUB BASELINES)
%                                   $$$$$$$$$$$$$$$$$$$$$$$$
%   1)  IDENTIFY RUN AND FILE CHARACTERISTICS
%   2)  IDENTIFY GRAVITATIONAL ENVIRONMENT
%       2.1)  IDENTIFY GRAVITATIONAL ENVIRONMENT "IF" 1-G DATA
%       2.2)  IF HEATER NUMBER IS 28 AND GREATER THAN 200 [W/CM2] THEN DELETE IT (10/03 DATA ONLY)
%   3)  DETERMINE SUBSTRATE CONDUCTION
%       3.1)  SAVE SUBSTRATE CONDUCTION VALUES IF THE BULK TEMPERATURE IS NEAR SATURATION TEMPERATURE, OTHERWISE
IMPORT
%       3.2)  CALCULATE 3RD-7th BASELINES BASED ON BULK 55 SUBSTRATE CONDUCTION AT SAME WALL TEMPERATURE FOR EDGE
HEATERS AND CORNER HEATERS
%       3.3)  SAVE SUBSTRATE CONDUCTION BASELINES TO FILE FOR FUTURE ANALYSIS
```

```
%  4) CALCULATE TIME RESOLVED BOILING HEAT FLUXES FOR EVERY SUBSTRATE CONDUCTION BASELINE IDENTIFIED
%     4.1) FILTER OUT HEATERS THAT ARE ON AND SHOULD NOT BE ON
%     4.2) CALCULATE AVERAGE HEAT FLUX IN MICROGRAVITY AND HIGH-G
%  5) CALCULATE WALL SUPERHEAT AND SUBCOOLING
%  6) CALCULATE AND DISPLAY HEAT FLUX IMAGES
%  7) WRITE HEAT FLUX DATA TO FILE
%  8) CREATE A PLOT OUTPUTS
%  9) CREATE SINGLE FIGURE OUTPUT FOR SAVING

%%%
```

```
   pause(20);
end

%%%
```

```
    [micrange1(2),micrange1(2)],[.8,1.5],'r:',[micrange2(1),micrange2(1)],[.8,1.5],'r:',[micrange2(2),micrange2(2)],[.8,1.5],'r:')
    axis([0 length(pressure) min(pressure(5:length(pressure)))-0.05 max(pressure)+0.05]);ylabel('Pressure(atm)');xlabel('Data Point');
    title('COMPUTER IDENTIFIED G-ENVIRONMENT LIMITS');legend('Pressure','high-gravity limits','low-gravity limits')

    xaxisp = [1:length(pressure)]/250-15;
    pzero = (pressure-min(pressure))
    glev = pzero.*((1+(1.8/max(pzero)-1)/max(pzero))*pzero);
    figure;plot(xaxisp,glev);xlabel('time (sec)');ylabel('g-level (g)');
  end
  if (max(mictime)-min(mictime))/250 < 30
    micrange1=[min(mictime)+250,max(mictime)-250];micrange2=0;
    %highgtime = [10000 9000];
    highrange=[min(highgtime)+750,max(highgtime)-100];figure
    hold on
    plot(pressure);
    plot([highrange(1),highrange(1)],[.8,1.5],'k:',[highrange(2),highrange(2)],[.8,1.5],'k:',[micrange1(1),micrange1(1)],[.8,1.5],'r:',...
      [micrange1(2),micrange1(2)],[.8,1.5],'r:');
    axis([0 length(pressure) min(pressure(5:length(pressure)))-0.05 max(pressure)+0.05]);ylabel('Pressure(atm)');xlabel('Data Point');
    title('computer identified microgravity time');legend('Pressure','high-gravity limits','low-gravity limits')
  end
  if micrange2(1) > 0;
    disp('LOW-G DATA RANGE [DATA POINT]: ');disp([micrange1;micrange2]);disp('-------------------------------------');
    disp('HIGH-G DATA RANGE [DATA POINT]: ');disp([highrange]);disp('-------------------------------------');
  else
    disp('LOW-G DATA RANGE [DATA POINT]: ');disp([micrange1]);disp('-------------------------------------');
    disp('HIGH-G DATA RANGE [DATA POINT]: ');disp([highrange]);disp('-------------------------------------');
  end
  select=menu('Do you like the computer defined limits?','yes','no');
  if select == 2
    micrange1=(input('SPECIFY MICROGRAVITY LIMITS:  '));
    micrange2= [0 0];
    highrange=(input('SPECIFY 2G LIMITS:  '));disp('-------------------------------------');
  end
  clear dif1 dpress highgtime i j k nn
  close all
else
```

```
%%%
```

```
   highGmin=min(data(highrange(1):highrange(2),:));                    %should be the same as micrange average
end

%%%
```

```
map=[0 96 95 94 93 92 91 90 89 0;65 37 64 63 62 61 60 59 58 88;66 38 17 36 35 34 33 32 57 87;67 39....
      18 5 16 15 14 31 56 86;68 40 19 6 1 4 13 30 55 85;69 41 20 7 2 3 12 29 54 84;70 42 21 8 ....
      9 10 11 28 53 83;71 43 22 23 24 25 26 27 52 82;72 44 45 46 47 48 49 50 51 81;0 73 74 75 76....
      77 78 79 80 0];qsci_map = zeros(10,10);qsci_map2 = qsci_map;
subconduction=zeros(1,length(data(1,:)));subconduction2=subconduction;
base_diff=highGmin-micromin;
jj=1;base2=0;
for i=1:length(heat_numb)
   if (automate == 1)
      subconduction(i)=micromin(i);subcondunc(i)=2.5;
      if base_diff(i) >= 0
         subconduction2(i)=micromin(i);
      elseif base_diff(i) < 0
         subconduction2(i) = highGmin(i);
         base2(jj,1:3)=[onheaters(1,i),highGmin(i),micromin(i)];jj=jj+1;
      end
   elseif (automate == 2) & (onheaters(1,i) > 0)
      num=int2str(onheaters(1,i));figure;hold on;
      plot(micrange1(1):micrange1(2),data(micrange1(1):micrange1(2),i));xlabel('DATA POINT');
      ylabel('LOW-G HEAT FLUX [W/cm^{2}]');phrase=strcat('Heater Number:  ',num);title(phrase);
      plot([micrange1(1),micrange1(2)],[totalmicro(2,i),totalmicro(2,i)],'r');
      axis([micrange1(1) micrange1(2) micromin(i) micromax(i)])
      subconduction(i)=input('ENTER qsc,i FOR SPECIFIED HEATER:  ');
      disp('--------------------------------------');
      subconduction2(i)=subconduction(i);
   end
   %MODIFY SUBSTRATE CONDUCTION MATRIX
   for j=1:10
      for k=1:10
         if (heat_numb(1,i) == map(j,k));
            qsci_map(j,k) = subconduction(i);
            qsci_map2(j,k) = subconduction2(i);
         end
      end
   end
end
clear i j k automate jj base_diff
```

```
disp('THE FOLLOWING HEATERS HAD LOWER BASELINE IN HIGH-G (IF A LOT THEN MODIFY PROGRAM):  ');disp(base2);
disp('AUTOMATED SUBSTRATE CONDUCTION VALUES IDENTIFIED (qsci_map, ROUNDED): ');disp(round(qsci_map));
disp('AUTOMATED SUBSTRATE CONDUCTION VALUES W/HIGH-G MIN (qsci_map2, ROUNDED): ');disp(round(qsci_map2));
disp('--------------------------------------');

%%%
```

```
if (filexis > 0)
   load(upfile)
   B55_mapmod = B55_map;
   disp('-------------------------------------');disp('SATURATION qsci BASLINE UPLOADED SUCCESSFULLY');
   disp('-------------------------------------');
else
   disp('SATURATED SUBSTRATE CONDUCTION BASELINE DATA HAS NOT BEEN ANALYZED YET !!!!!!')
   disp('YOU SHOULD EXIT THE PROGRAM AND ANALYZE THE SATURATION BASELINE DATE FIRST !!!!!!')
   pause(20)
end
clear filexis subfile base2

%%%
```

```
      end
   end
   clear i j k
end
qsci_map3=(qsci_map.*dummy_map)+(round(B55_mapmod)).*(uno-dummy_map);
qsci_map4=(qsci_map2.*dummy_map)+(round(B55_mapmod)).*(uno-dummy_map);
qsci_map5=(qsci_map.*dummy_map)+(round(B55_mapmod)).*(uno-dummy_map)+.15*((round(B55_mapmod)).*(uno-dummy_map));
qsci_map6=(qsci_map2.*dummy_map)+(round(B55_mapmod)).*(uno-dummy_map)+.15*((round(B55_mapmod)).*(uno-dummy_map));
qsci_map7=round(B55_mapmod);

%DECODE qsci_map 3,4,5,6,7 BACK FOR BOILING CALCULATION
subconduction3=zeros(1,length(onheaters(1,:)));subconduction4=subconduction3;
subconduction5=subconduction3;subconduction6=subconduction3;
subconduction7=subconduction3;
for i=1:length(heat_numb)
   for j=1:10
      for k=1:10
         if (map(j,k) == heat_numb(1,i))
            subconduction3(i)=qsci_map3(j,k);
            subconduction4(i)=qsci_map4(j,k);
            subconduction5(i)=qsci_map5(j,k);
            subconduction6(i)=qsci_map6(j,k);
            subconduction7(i)=qsci_map7(j,k);
         end
      end
   end
end
%USER MODIFIED SUBSTRATE CONDUCTION BASELINE (IF DESIRED, ASSUMES SOME ANALYSIS HAS ALREADY BEEN DONE)
subconduction8 = subconduction7;qsci_map8 = qsci_map7;
select2=menu('DO YOU WANT TO ADD A MODIFIED SUBSTRATED CONDUCTION BASELINE','yes','no');
if select2 == 1
   disp('THIS IS THE COMPUTER DEFINED SUBCONDUCTION BASELINE 1 (first row (sub) second row (heat #) and wall temp:
');disp([subconduction;onheaters]);
   disp(accwall_temp);
   subconduction8 = (input('INPUT NEW BASELINES VECTOR (MAKE SURE VECTOR ELEMENT CORRESSPONDS TO CORRECT HEATER
ELEMENT:  '));
   disp(subconduction8)
```

```
    disp('-------------------------------------');disp('-------------------------------------');
    for i=1:length(heat_numb)
        for j=1:10
            for k=1:10
                if (heat_numb(1,i) == map(j,k));
                    qsci_map8(j,k) = subconduction8(i);
                end
            end
        end
    end
end
clear i j k
%COLORMAP PLOT AUTOMATED SUBSTRATE CONDUCTION MAP
figure;range=[0 40];colormap;
subplot(4,2,1);imagesc(qsci_map,range);colorbar('vert');title('AUTOMATED SUBSTRATE CONDUCTION');axis square;axis tight;axis off
subplot(4,2,2);imagesc(qsci_map2,range);colorbar('vert');title('AUTOMATED SUBSTRATE CONDUCTION (q_{sc,i}map2');axis square;axis tight
subplot(4,2,3);imagesc(qsci_map3,range);colorbar('vert');title('AUTOMATED MIDDLE (BULK 55 CORNER AND EDGE) (q_{sc,i}map3');axis square;axis
tight;axis off
subplot(4,2,4);imagesc(qsci_map4,range);colorbar('vert');title('AUTOMATED SUBSTRATE CONDUCTION (q_{sc,i}map2');axis square;axis tight
subplot(4,2,5);imagesc(qsci_map5,range);colorbar('vert');title('AUTOMATED MIDDLE (BULK 55 + 15% CORNER AND EDGE (q_{sc,i}map5');axis
square;axis tight;axis off
subplot(4,2,6);imagesc(qsci_map6,range);colorbar('vert');title('AUTOMATED SUBSTRATE CONDUCTION (q_{sc,i}map2');axis square;axis tight
subplot(4,2,7);imagesc(qsci_map7,range);colorbar('vert');title('BULK 55 (q_{sc,i}map7');axis square;axis tight;axis off
figure;range2 = [0 55];
imagesc(qsci_map3,range2);colorbar('vert');title('AUTOMATED MIDDLE (BULK 55 CORNER AND EDGE) [q_{sc,i}map3]');axis square;axis tight;axis off

%%%
```

```
%%%
```

```
%TIME RESOLVED MICROGRAVITY BOILING HEAT FLUX (HAVE TIME VECTOR IN HERE)
timeUG = time(micrange1(1):micrange1(2));
boilUG1 = boilf1(micrange1(1):micrange1(2),:);boilUG2 = boilf2(micrange1(1):micrange1(2),:);
boilUG3 = boilf3(micrange1(1):micrange1(2),:);boilUG4 = boilf4(micrange1(1):micrange1(2),:);
boilUG5 = boilf5(micrange1(1):micrange1(2),:);boilUG6 = boilf6(micrange1(1):micrange1(2),:);
boilUG7 = boilf7(micrange1(1):micrange1(2),:);boilUG8 = boilf8(micrange1(1):micrange1(2),:);
%TIME RESOLVED MICROGRAVITY TOTAL BOILING POWER (WATTS)
area_mat = repmat(area,size(boilUG1,1),1);
lowg_totalheat1 = boilUG1.*area_mat;lowg_totalheat2 = boilUG2.*area_mat;lowg_totalheat3 = boilUG3.*area_mat;
lowg_totalheat4 = boilUG4.*area_mat;lowg_totalheat5 = boilUG5.*area_mat;lowg_totalheat6 = boilUG6.*area_mat;
lowg_totalheat7 = boilUG7.*area_mat;


%TIME RESOLVED HIGH-GRAVITY BOILING HEAT FLUX
timeHG = time(highrange(1):highrange(2),:);
boilHG1 = boilf1(highrange(1):highrange(2),:);boilHG2 = boilf2(highrange(1):highrange(2),:);
boilHG3 = boilf3(highrange(1):highrange(2),:);boilHG4 = boilf4(highrange(1):highrange(2),:);
boilHG5 = boilf5(highrange(1):highrange(2),:);boilHG6 = boilf6(highrange(1):highrange(2),:);
boilHG7 = boilf7(highrange(1):highrange(2),:);boilHG8 = boilf8(highrange(1):highrange(2),:);
%TIME RESOLVED HIGH-GRAVITY BOILING HEAT TRANSFER (WATTS)
clear area_mat
area_mat = repmat(area,size(boilHG1,1),1);
HIGHg_totalheat1 = boilHG1.*area_mat;HIGHg_totalheat2 = boilHG2.*area_mat;HIGHg_totalheat3 = boilHG3.*area_mat;
HIGHg_totalheat4 = boilHG4.*area_mat;HIGHg_totalheat5 = boilHG5.*area_mat;HIGHg_totalheat6 = boilHG6.*area_mat;
HIGHg_totalheat7 = boilHG7.*area_mat;

%%%
```

```
MICROMAT = [onheaters;microboilave1;microboilave2;microboilave3;microboilave4;microboilave5;microboilave6;microboilave7;microboilave8];
HIGHMAT = [onheaters;highgboilave1;highgboilave2;highgboilave3;highgboilave4;highgboilave5;highgboilave6;highgboilave7;highgboilave8];
MICROMATzero = MICROMAT;
HIGHMATzero = HIGHMAT;
%ZERO NEGATIVE AVERAGE HEAT FLUX HEATERS (IF SOME ARE NEGATIVE)
for i = 1:length(HIGHMAT(1,:))
   for j = 2:9
      if HIGHMAT(j,i) < 0
         HIGHMATzero(j,i) = 0;
      end
      if MICROMAT(j,i) < 0
         MICROMATzero(j,i) = 0;
      end
   end
end
clear i j
%CALCULATE TOTAL AVERAGE HEAT TRANSFER FROM EACH HEATER (WATTS)
TOTALMICRO =
[MICROMATzero(1,:);(MICROMATzero(2,:).*area);(MICROMATzero(3,:).*area);(MICROMATzero(4,:).*area);(MICROMATzero(5,:).*area);...
      (MICROMATzero(6,:).*area);(MICROMATzero(7,:).*area);(MICROMATzero(8,:).*area);(MICROMATzero(9,:).*area)];
TOTALHIGH = [HIGHMATzero(1,:);(HIGHMATzero(2,:).*area);(HIGHMATzero(3,:).*area);(HIGHMATzero(4,:).*area);(HIGHMATzero(5,:).*area);...
      (HIGHMATzero(6,:).*area);(HIGHMATzero(7,:).*area);(HIGHMATzero(8,:).*area);(HIGHMATzero(9,:).*area)];
%ADD ALL AVERAGE HEAT FLUX AND DIVIDE BY SUM OF AREAS (BOILING CURVE DATA POINTS)
DATAPOINTSMICRO = sum(TOTALMICRO(2:9,:),2)/(sum(area));
DATAPOINTSHIGH = sum(TOTALHIGH(2:9,:),2)/(sum(area));

%%%
```

```
   output2 = [repmat(wallsuperheat_highG,8,1) repmat(subcooling_high,8,1) DATAPOINTSHIGH];
end
disp('WALL TEMP (C), SAT TEMP (LOW-G), SAT TEMP (HIGH-G), BULK TEMP:  ');disp([accwall_temp,Tsatmicro,TsathighG,bulktemp]);
disp('---------------------------------------');
disp('---------------------------------------');
disp('RUN NUMBER:  ');disp(bbb);disp('---------------------------------------'); disp('ACTUAL HEATER SIZE: ');disp(length(onheaters));disp('HEATER SIZE
SHOULD BE: ');
disp(heatersize);disp('---------------------------------------');
disp('WALL SUPERHEAT (C),  BULK SUBCOOLING [C], LOW AVERAGE HEAT FLUX (W/cm2)  (below) HIGH AVERAGE HEAT FLUX
(W/cm2)');disp(output1);disp(output2);
disp('---------------------------------------');

%%%
```

```
            qboilhigh_map7(j,k) = HIGHMAT(8,i);
            qboilhigh_map8(j,k) = HIGHMAT(9,i);
          end
        end
    end
end

%%%
```

```
%%%
```

```
%%%
```

```
clear i j k
choice2 = menu('ANALYZE DESIRED HEATERS TO OBTAIN SURFACE AVERAGE','YES','EXIT');
k = 1;
while choice2 == 1
   choose = input('SPECIFY DESIRED HEATER TO OBTAIN SURFACE AVERAGE FLUX:  ');disp('-------------------------------------');
   for i = 1:length(choose)
      for j = 1:length(heat_numb)
         if choose(i) == heat_numb(j)
            sumarea(k) = area(j);
            qtot(k) = area(j)*highgboilave3(j);
            QTOTLOW(k) = area(j)*microboilave3(j);
            k = k+1;
         end
      end
   end
   displayavgHIGH = sum(qtot)/sum(sumarea);
   displayavglow = sum(QTOTLOW)/sum(sumarea);
   highgdisp = strcat('AVERAGE HEAT TRANSFER IN HIGH-G FOR HEATERS, :',num2str(choose),': IS:  ');
   disp(highgdisp);disp(displayavgHIGH);disp('-------------------------------------');
   lowgdisp = strcat('AVERAGE HEAT TRANSFER IN LOW-G FOR HEATERS, :',num2str(choose),': IS:  ');
   disp(lowgdisp);disp(displayavglow);disp('-------------------------------------');
   choice2 = menu('ANALYZE DESIRED HEATERS TO OBTAIN SURFACE AVERAGE','YES','EXIT');
   clear i j sumarea qtot QTOTLOW choose
end

%%%
```

```
%plot boiling heat flux
boilheatfluxseeheat = [boilf3(:,indexsave),[1:length(data)]'*1/250];
figure;plot(boilheatfluxseeheat(:,2),boilheatfluxseeheat(:,1),'k');
axis([0 length(data)/250 0 max(boilheatfluxseeheat(:,1))+5])
xlabel('time (sec)'),ylabel('heat flux (W/cm^{2})');titplot = strcat('HEATER NUMBER: ', num2str(seeheat));title(titplot)
hold on
%%%plot avg values
lowinp1 = [mean(boilf3(micrange1(1):micrange1(2),indexsave))];lowinp2 = [lowinp1;lowinp1];
lowavg = [lowinp2,micrange1'/250];
highinp1 = [mean(boilf3(highrange(1):highrange(2),indexsave))];highinp2 = [highinp1;highinp1];
highavg =[highinp2,highrange'/250];
plot(lowavg(:,2),lowavg(:,1),'w-');hold on
plot(highavg(:,2),highavg(:,1),'w-');hold on
%%%plot low-g and high-g ranges
lowlim = [0;max(boilheatfluxseeheat(:,1))+3];lowlim2  = [lowlim,repmat((micrange1(1)/250),2,1)];
plot(lowlim2(:,2),lowlim2(:,1),'w:');hold on
lowlim2  = [lowlim,repmat((micrange1(2)'/250),2,1)];
plot(lowlim2(:,2),lowlim2(:,1),'w:');hold on
highlim = [lowlim,repmat(highrange(1)/250,2,1)];
plot(highlim(:,2),highlim(:,1),'w:');hold on
highlim = [lowlim,repmat(highrange(2)/250,2,1)];
plot(highlim(:,2),highlim(:,1),'w:');hold on
%place text in screen
lowtext = num2str(lowinp1)
lowtex = strcat(lowtext);
hightext = num2str(highinp1)
text((micrange1(1)+20)/250,max(boilheatfluxseeheat(:,1))+5,lowtex)
hightext = num2str(highinp1);
text((highrange(1)+20)/250,max(boilheatfluxseeheat(:,1))+5,hightext);text((highrange(1)+200)/250,max(boilheatfluxseeheat(:,1))+5,'LOW-G')
text((highrange(1)+400)/250,max(boilheatfluxseeheat(:,1))+5,'HIGH-G');text((highrange(1)+400)/250,max(boilheatfluxseeheat(:,1))+5,'\leftarrow')
text((highrange(1)+400)/250,max(boilheatfluxseeheat(:,1))+5,'\rightarrow')

%%%ZOOM IN PLOT
figure;
%HIGH-G DATA SEQUENCE
zoomlow = boilheatfluxseeheat(micrange1(1)+20:micrange1(1)+250,:);
zoomhigh = boilheatfluxseeheat(highrange(1)+20:highrange(1)+250,:);
```

```
xax = zoomhigh(:,2)-zoomhigh(1,2);
H=plot(xax,zoomlow(:,1),'k:');hold on;G=plot(xax,zoomhigh(:,1),'k-');legend('LOW-G','HIGH-G');axis tight
title(titplot);xlabel('time (sec)');ylabel('heat flux (W/cm^{2})')
set(H,'LineWidth',2);set(G,'LineWidth',2)
%axis([0 highrange(2)+250 0 max(boilheatfluxseeheat(:,1))+3])
%figure;plot(boilUG3(:,indexsave));
%figure;plot(boilHG3(:,indexsave));
%clear i indexsave boilheatfluxseeheat

%%%plot high-g and plot avg values
figure;
%HIGH-G DATA SEQUENCE
zoomhigh = boilheatfluxseeheat(highrange(1)+20:highrange(1)+150,:);
xax = zoomhigh(:,2)-zoomhigh(1,2);
%H=plot(xax,zoomlow(:,1),'k:');
G=plot(xax,zoomhigh(:,1),'k-');hold on;
Title(titplot);xlabel('time (sec)');ylabel('heat flux (W/cm^{2})')
highinp1 = [mean(boilf3(highrange(1):highrange(2),indexsave))];highinp2 = [highinp1;highinp1];
highavg =[highinp2,highrange'/250];
xline = [0,xax(length(xax))]';
plot(xline,highavg(:,1),'k:o');hold on
hold on

seeheat = input(strcat('INPUT another HEATER NUMBER TO SEE CHARACTERISTICS: '));
   for i=1:length(onheaters)
      if onheaters(i)==seeheat
         indexsave = i;
      end
   end

   figure;boilheatfluxseeheat = [boilf3(:,indexsave),[1:length(data)]'*1/250];
zoomhigh = boilheatfluxseeheat(highrange(1)+20:highrange(1)+150,:);
xax = zoomhigh(:,2)-zoomhigh(1,2);
plot(xax,zoomhigh(:,1),'k-');hold on;
highinp1 = [mean(boilf3(highrange(1):highrange(2),indexsave))];highinp2 = [highinp1;highinp1];
highavg =[highinp2,highrange'/250];
plot(xline,highavg(:,1),'k:*');
```

```
   %legend('HIGH-G','HIGH-G AVG', 'HIGH-G, #96','HIGH-G AVG, #96');axis tight
   legend('HIGH-G','HIGH-G AVG');axis tight;xlabel('time (sec)');ylabel('heat flux (W/cm^{2})');

   choice1 = menu('ANALYZE INDIVIDUAL HEATERS','YES','EXIT');
end
```

D2. Optimization (Matlab)

```
clear all
close all
clc

%THIGH PARETO FRONTIER PLOT
T_high = [71 75   80 85 82.5 77.5    90 95 105 115 120 140 130 110 100];
Tobj = [0.0108 0.036 0.0669 0.0936 0.0807 0.052 0.1172 0.1393 0.1725 0.2006  0.2127 0.2535 0.234 0.1872 0.1564];
figure;plot(T_high,Tobj,'ko');xlabel('Maximize T_{high} [^{o}C]');axis([70 140 0 0.3])
ylabel('Minimize T_{unc} [^{o}C]');%title('Multiobjective Pareto Frontier');
legend('\alpha = 0.003 \Omega / \Omega^{o}C','R_{ref} = 298 \Omega','T_{ref} = 24.7 ^{o}C','C_{min} = 20','D_{min} = 0.3','T_{low} = 10 ^{o}C','T_{opt}
= 70 ^{o}C');grid on

%RANGE COMPARISON PLOT
%OPTMIUM @THIGH = 120
alpha = 0.003;r_ref = 298;T_ref = 24.7;
x(1) = 167;
```

```
x(2) = 27733;
x(3) = 47379;
x(4) = 89786;
R_dp = [0:156:20000];
figure;
Tsens = 39*x(1)*x(4)/(alpha*r_ref*x(2))*(1./(x(4)+R_dp)-R_dp./((x(4)+R_dp).^2));
T_range = +x(1)*x(3)/(alpha*x(2)*r_ref)+R_dp*x(1)*x(4)./(alpha*x(4)*x(2)*r_ref+R_dp*alpha*x(2)*r_ref)-1/alpha+T_ref;
plot(T_range,Tsens,'k-*');xlabel('Heater Temperature [^{o}C]');ylabel('Temperature unc. [^{o}C]');axis([min(T_range) max(T_range) 0.15 0.3]);
hold on

%COMPARE TO CURRENT DESIGN SOLUTION
x = [89.4 18179 57924 10^8 0];
Tsens2 = 39*x(1)*x(4)/(alpha*r_ref*x(2))*(1./(x(4)+R_dp)-R_dp./((x(4)+R_dp).^2));
T_range2 = +x(1)*x(3)/(alpha*x(2)*r_ref)+R_dp*x(1)*x(4)./(alpha*x(4)*x(2)*r_ref+R_dp*alpha*x(2)*r_ref)-1/alpha+T_ref;
plot(T_range2,Tsens2,'k-');
legend('Optimized Design','Current Design');

%Parametric Tlow
Tlow = [10      15      20      25      30      35      40      45      50      55      60      65];
Tobj = [0.2127  0.2043  0.195   0.1853  0.1757  0.1658  0.1561  0.1463  0.1365  0.1268  0.117   0.1073];
figure;plot(Tlow,Tobj,'ko');xlabel('T_{low} [^{o}C]');axis([5 70 0 0.3])
ylabel('T_{unc} [^{o}C]');%title('Multiobjective Pareto Frontier');
legend('\alpha = 0.003 \Omega / \Omega^{o}C','R_{ref} = 298 \Omega','T_{ref} = 24.7 ^{o}C','C_{min} = 20','D_{min} = 0.3','T_{high} = 120
^{o}C','T_{opt} = 70 ^{o}C');grid on

%Parametric Topt
Topt = [20      30      40      50      60      70      80      90      100     110     120];
Tobj = [0.2145  0.215   0.2145  0.2145  0.2145  0.2127  0.1986  0.1702  0.1277  0.0709  0.0216];
figure;plot(Topt,Tobj,'ko');xlabel('T_{low} [^{o}C]');axis([15 125 0 0.25])
ylabel('T_{unc} [^{o}C]');%title('Multiobjective Pareto Frontier');
legend('\alpha = 0.003 \Omega / \Omega^{o}C','R_{ref} = 298 \Omega','T_{ref} = 24.7 ^{o}C','C_{min} = 20','D_{min} = 0.3','T_{high} = 120
^{o}C','T_{low} = 70 ^{o}C');grid on
```

D.2 OPTIMIZATION PROGRAMS

D.2.1 Program name: Fmincon Solution Algorithm

```
%USED TO STUDY THE EFFECT OF INITIAL POINT ON OPTIMIZATION SOLUTION RESULTS
clear all;close all;clc

%DESIGN PARAMETER DEFINITION
alpha = 0.002;r_ref = 298;T_ref = 24.7;
C_min = 20;D_min = .3;T_low = 20;
T_opt = 70;V_drop = 10;
R1_ubnd = 500;R3_ubnd = 10^6;R4_ubnd = 10^6;
T_high = 100;

%INITIAL POINT CREATION
%GENERATE RANDOM NUMBERS USED TO DETERMINE INITIAL POINT
randnum = rand(150,5);
for j = 1:length(randnum(1,:))
   for i = 1:length(randnum(:,1))
      expo = randperm(5)+1;
      if j == 1
         x0_vec(i,j) = r_ref*D_min+randnum(i,j)*(R1_ubnd-r_ref*D_min);
      end
      if j == 2
         x0_vec(i,j) = 1+randnum(i,j)*(10^(expo(1))-1);
      end
      if j == 3
         x0_vec(i,j) = 1+randnum(i,j)*(10^(expo(2))-1);
      end
      if j == 4
         x0_vec(i,j) = 1+randnum(i,j)*(10^(expo(3))-1);
      end
      if j == 5
         x0_vec(i,j) = 1+randnum(i,j)*(20000-1);
      end
   end
```

```
end
clear i j

%INITIAL AND RUN MATLAB OPTIMIZATION
for i = 1:length(x0_vec(:,1))

   %PICK INITIAL POINT
   x0 = x0_vec(i,:);

   %SOLVE FOR OPTIMUM
   Lbnd = [r_ref*D_min 10^-6 10^-6 10^-6 10^-6];
   Ubnd = [R1_ubnd R3_ubnd R4_ubnd inf 20000];
   options = optimset('MaxFunEvals',3000,'MaxIter',3000,'TolCon',10^-10,'Tolfun',10^-10);
   [x,Tobj]=fmincon('Tresopt',x0,[],[],[],[],Lbnd,Ubnd,'TresNonLin',options,alpha,r_ref,T_ref,C_min,D_min,T_high,T_low,T_opt,V_drop);
   clc
   %OUTPUT OPTIMIZED CONSTRAINT VALUES
   [C,Ceq] = TresNonLin(x,alpha,r_ref,T_ref,C_min,D_min,T_high,T_low,T_opt,V_drop);
   disp('ITERATION NUMBER');disp(num2str(i));
   %SAVE RESULTS IN MATRIX ONLY IF CONSTRAINTS ARE SATISFIED
   if ((C(1) <= 0) & (C(2) <= 0) & (C(3) <= 0) & (C(4) <= 0))
      if ((abs(Ceq(1)) < 10^-6)) %& (abs(Ceq(2)) < 10^-6))
         Designvar(i,:) = x;Tobjective(i,:) = Tobj;nonlincont(i,:) = C;lincont(i,:) = Ceq;
      end
   end
end

%FILTER OUT ZERO SOLUTIONS
clear i j
j = 1;
for i = 1:length(Tobjective)
   if Tobjective(i) > 0
      optimums(j) = Tobjective(i);
      varopt(j,:) = Designvar(i,:);
      nonlincontopt(j,:) = nonlincont(i,:);
      optlincont(j,:) = lincont(i,:);
      init(j,:) = x0_vec(i,:);
      j = j+1;
```

```
   end
end

%HISTOGRAM OF OPTIMUM SOLUTIONS
figure;hist(optimums,30);xlabel('Optimized T_{unc} [C]');
ylabel('Frequency (250 total samples)');%title('Initial Point Sensitivity');grid on;
%leg = strcat('V_{drop}[volts] = ',num2str(V_drop));
leg = strcat('T_{high} [^{o}C] = ',num2str(T_high));
%legend(leg,'\alpha = 0.003 \Omega / \Omega^{o}C','R_{ref} = 298 \Omega','T_{ref} = 24.7 ^{o}C','C_{min} = 20','D_{min} = 0.3','T_{low} = 10
^{o}C','T_{opt} = 70 ^{o}C');grid on

%LOOK FOR MOST NON-LINEAR SOLUTION
[worst,wor] = min(varopt(:,4));

%DETERMINE THE MINIMUM SOLUTION
disp('-----------------------------------------------------');
disp('GLOBAL OPTIMUM OBJECTIVE FUNCTION VALUE (Tunc) ;  @ MOST NONLINEAR');
[ind1,opt] = min(optimums);disp(ind1);disp(optimums(wor));
%PARETO POINT
%DETERMINE SECOND OBJECTIVE VALUE
disp('SECOND OBJECTIVE VALUE (VDROP)');
optDV = varopt(opt,:);
vdrop = 24/(1+optDV(3)/optDV(2)+optDV(4)*optDV(5)/(optDV(4)*optDV(2)+optDV(5)*optDV(2)));
disp(vdrop);
disp('-----------------------------------------------------');
disp('OPTIMUM DESIGN VARIABLES ; MOST NON-LINEAR; INITIAL DESIGN POINT');
disp([optDV]);disp(varopt(wor,:));IP = init(opt,:);disp(IP)
disp('-----------------------------------------------------');
disp('INEQUALITY CONSTRAINT VALUES @ OPTIMUM (TLOW, CMIN, VDROP); @ MOST NON-LINEAR');
optNLC = nonlincontopt(opt,:);disp(optNLC);disp(nonlincontopt(wor,:));
disp('-----------------------------------------------------');
disp('EQUALITY CONSTRAINT VALUES @ OPTIMUM ; MOST NON-LINEAR');
optLC = optlincont(opt,:);disp(optLC);disp(optlincont(wor,:));
disp('-----------------------------------------------------');

%PLOT GLOBAL OPTIMUM SOLUTION
clear x
```

```
figure;R_dp = [0:39:20000];
x = optDV;
Tsens = 39*x(1)*x(4)/(alpha*r_ref*x(2))*(1./(x(4)+R_dp)-R_dp./((x(4)+R_dp).^2));
T_range = +x(1)*x(3)/(alpha*x(2)*r_ref)+R_dp*x(1)*x(4)./(alpha*x(4)*x(2)*r_ref+R_dp*alpha*x(2)*r_ref)-1/alpha+T_ref;
plot(T_range,Tsens,'r-');xlabel('Temperature Range [C]');ylabel('Temperature unc. [C]');axis([min(T_range) max(T_range) 0 0.5]);
%COMPARE TO CURRENT DESIGN SOLUTION
hold on
x = [227 26100 37500 40000 0];
Tsens2 = 39*x(1)*x(4)/(alpha*r_ref*x(2))*(1./(x(4)+R_dp)-R_dp./((x(4)+R_dp).^2));
T_range2 = +x(1)*x(3)/(alpha*x(2)*r_ref)+R_dp*x(1)*x(4)./(alpha*x(4)*x(2)*r_ref+R_dp*alpha*x(2)*r_ref)-1/alpha+T_ref;
plot(T_range2,Tsens2,'b-');
%MOST NON-LINEAR SOLUTION
hold on
x = varopt(wor,:);
Tsens3 = 39*x(1)*x(4)/(alpha*r_ref*x(2))*(1./(x(4)+R_dp)-R_dp./((x(4)+R_dp).^2));
T_range3 = +x(1)*x(3)/(alpha*x(2)*r_ref)+R_dp*x(1)*x(4)./(alpha*x(4)*x(2)*r_ref+R_dp*alpha*x(2)*r_ref)-1/alpha+T_ref;
plot(T_range3,Tsens3,'k-');
legend('OPTIMIZED DESIGN','CURRENT DESIGN','MOST NONLINEAR DESIGN');grid on
axis([min(T_range3) max(T_range3) 0 0.8]);

disp('R1 OPT; R1 INITIAL')
disp([optDV(1),IP(1)])
disp('-----------------------------------------------------');
disp('R3 OPT; R3 INITIAL')
disp([optDV(2),IP(2)])
disp('-----------------------------------------------------');
disp('R4 OPT; R4 INITIAL')
disp([optDV(3),IP(3)])
disp('-----------------------------------------------------');
disp('R5 OPT; R5 INITIAL')
disp(optDV(4));disp(IP(4));
disp('-----------------------------------------------------');
disp('Rdp OPT; Rdp INITIAL')
disp([optDV(5),IP(5)])
```

D.2.2 Program name: Exterior Penalty Algorithm

```
%UNCONSTRAINED OBJECTIVE FUNCTION
function Tobj = EXTPENFUNC(x,alpha,r_ref,T_ref,C_min,D_min,T_high,T_low,T_opt,V_drop,rp,R1Ubnd,R3Ubnd,R4Ubnd,R5Ubnd)
R1 = x(1);
R3 = x(2);
R4 = x(3);
R5 = x(4);
Rdp = x(5);

Tobj = 39*R1*R5^2/(alpha*r_ref*R3*(R5+Rdp)^2)....
   +rp*(-R1*R4/(alpha*R3*r_ref)-Rdp*R1*R5/(alpha*R5*R3*r_ref+Rdp*alpha*R3*r_ref)+1/alpha-T_ref+T_opt)^2....
   +rp*(max([0,(-R1*R4/(alpha*R3*r_ref)-20000*R1*R5/(alpha*R5*R3*r_ref+20000*alpha*R3*r_ref)+1/alpha-T_ref+T_high)]))^2....
   +rp*(max([0,((R1*R4/(R3*r_ref)-1)/alpha+T_ref-T_low)]))^2....
   +rp*(max([0,((C_min-(R3+R4)/(R1+r_ref)))]))^2....
   +rp*(max([0,(24/(1+R4/R3+R5*Rdp/(R5*R3+Rdp*R3))-V_drop)]))^2....
   +rp*(max([0,(r_ref*D_min-R1)]))^2....
   +rp*(max([0,(R1-R1Ubnd)]))^2....
   +rp*(max([0,(R4-R4Ubnd)]))^2....
   +rp*(max([0,(10^(-6)-R4)]))^2....
   +rp*(max([0,(Rdp-20000)]))^2....
   +rp*(max([0,(10^(-6)-Rdp)]))^2....
   +rp*(max([0,(R5-R5Ubnd)]))^2....
   +rp*(max([0,(10^(-6)-R5)]))^2....
   +rp*(max([0,(10^(-6)-R3)]))^2....
   +rp*(max([0,(R3-R3Ubnd)]))^2;

%EXTERIOR PENALTY APPROACH
clear all;close all;clc
%FIND SYMBOLIC GRADIENT OF OBJECTIVE
syms R1 R3 R5 Rdp alpha r_ref
Tobj = 39*R1*R5/(alpha*r_ref*R3)*(1/(R5+Rdp)-Rdp/((R5+Rdp)^2));
grad = [simplify((diff(Tobj,R1))),simplify((diff(Tobj,R3))),....
      simplify((diff(Tobj,R5))),simplify((diff(Tobj,Rdp)))]
pretty(grad)
hess = [simplify(diff((diff(Tobj,R1)),R1)),simplify(diff((diff(Tobj,R1)),R3)),...
```

```
        simplify(diff((diff(Tobj,R1)),R5)),simplify(diff((diff(Tobj,R1)),Rdp));...
        simplify(diff((diff(Tobj,R3)),R1)),simplify(diff((diff(Tobj,R3)),R3)),...
        simplify(diff((diff(Tobj,R3)),R5)),simplify(diff((diff(Tobj,R3)),Rdp));...
        simplify(diff((diff(Tobj,R5)),R1)),simplify(diff((diff(Tobj,R5)),R3)),...
        simplify(diff((diff(Tobj,R5)),R5)),simplify(diff((diff(Tobj,R5)),Rdp));...]
        simplify(diff((diff(Tobj,Rdp)),R1)),simplify(diff((diff(Tobj,Rdp)),R3)),...
        simplify(diff((diff(Tobj,Rdp)),R5)),simplify(diff((diff(Tobj,Rdp)),Rdp))];

%DESIGN PARAMETER DEFINITION
alpha = 0.003;r_ref = 298;T_ref = 24.7;
C_min = 20;D_min = .3;T_low = 10;
T_opt = 70;V_drop = 10;
R1Ubnd = 500;R3Ubnd = 10^6;R4Ubnd = 10^6;R5Ubnd = 10^12;
T_high = 140;
factor = [.1 1 10 100 1000 10^4 10^5 10^6 10^7];
options = optimset('MaxFunEvals',20000,'MaxIter',15000);

%INITIAL POINT CREATION
%GENERATE RANDOM NUMBERS USED TO DETERMINE INITIAL POINT
randnum = rand(100,5);
for j = 1:length(randnum(1,:))
   for i = 1:length(randnum(:,1))
      expo = randperm(5)+1;
      if j == 1
         x0_vec(i,j) = r_ref*D_min+randnum(i,j)*(R1Ubnd-r_ref*D_min);
      end
      if j == 2
         x0_vec(i,j) = 1+randnum(i,j)*(10^(expo(1))-1);
      end
      if j == 3
         x0_vec(i,j) = 1+randnum(i,j)*(10^(expo(2))-1);
      end
      if j == 4
         x0_vec(i,j) = 1+randnum(i,j)*(10^(expo(3))-1);
      end
      if j == 5
         x0_vec(i,j) = 1+randnum(i,j)*(20000-1);
```

```
        end
    end
end
clear i j

for i = 1:length(factor)
    for j = 1:length(x0_vec(:,1))
        %PICK INITIAL POINT
        iter = i;
        x0 = x0_vec(j,:);
        rp = factor(i)
        [x,Tobj] = fminunc('EXTPENFUNC',x0,options,alpha,r_ref,T_ref,C_min,D_min,T_high,T_low,T_opt,V_drop,rp,R1Ubnd,R3Ubnd,R4Ubnd,R5Ubnd)

        %CHECK TO SEE IF CONSTRAINTS ARE SATISFIED
        [C,Ceq] = TresNonLin(x,alpha,r_ref,T_ref,C_min,D_min,T_high,T_low,T_opt,V_drop);
        disp('ITERATION NUMBER');disp([num2str(i),num2str(j)]);
        %SAVE RESULTS IN MATRIX ONLY IF CONSTRAINTS ARE SATISFIED
        if ((C(1) <= 0) & (C(2) <= 0) & (C(3) <= 0) & (C(4) <= 0))
            if ((abs(Ceq(1)) < 10^-6))
                Designvar(i,j,:) = x;Tobjective(i,j,:) = Tobj;nonlincont(i,j,:) = C;lincont(i,j,:) = Ceq;
            end
        end
    end
end

%FILTER OUT ZERO SOLUTIONS
clear i j
k = 1;m=1;
mess = size(Tobjective);
for j = 1:iter
    for i = 1:mess(2)
        if Tobjective(j,i) > 0
            optimums(k) = Tobjective(j,i);
            che(m) = Tobjective(j,i);
            varopt(k,:) = Designvar(j,i,:);
            nonlincontopt(k,:) = nonlincont(j,i,:);
            optlincont(k,:) = lincont(j,i,:);
```

```
            init(k,:) = x0_vec(i,:);
            k = k+1;m = m+1;
        end
    end
    if exist('che') == 1
        optimumsrp(j) = min(che);
        clear che m
        m=1;
    end
end
optimumsrp
figure;semilogx(factor,optimumsrp,'ko');xlabel('Penalty Parameter');ylabel('T_{unc} [^{o}C]');
grid on;
%HISTOGRAM OF OPTIMUM SOLUTIONS
figure;hist(optimums,30);xlabel('Optimized T_{unc} [C]');
ylabel('Frequency (250 total samples)');%title('Initial Point Sensitivity');grid on;
%leg = strcat('V_{drop}[volts] = ',num2str(V_drop));
leg = strcat('T_{high} [^{o}C] = ',num2str(T_high));
%legend(leg,'\alpha = 0.003 \Omega / \Omega^{o}C','R_{ref} = 298 \Omega','T_{ref} = 24.7 ^{o}C','C_{min} = 20','D_{min} = 0.3','T_{low} = 10
^{o}C','T_{opt} = 70 ^{o}C');grid on

%LOOK FOR MOST NON-LINEAR SOLUTION
[worst,wor] = min(varopt(:,4));

%DETERMINE THE MINIMUM SOLUTION
disp('-----------------------------------------------------');
disp('GLOBAL OPTIMUM OBJECTIVE FUNCTION VALUE (Tunc) ;  @ MOST NONLINEAR');
[ind1,opt] = min(optimums);disp(ind1);disp(optimums(wor));
%PARETO POINT
%DETERMINE SECOND OBJECTIVE VALUE
disp('SECOND OBJECTIVE VALUE (VDROP)');
optDV = varopt(opt,:);
vdrop = 24/(1+optDV(3)/optDV(2)+optDV(4)*optDV(5)/(optDV(4)*optDV(2)+optDV(5)*optDV(2)));
disp(vdrop);
disp('-----------------------------------------------------');
disp('OPTIMUM DESIGN VARIABLES ; MOST NON-LINEAR; INITIAL DESIGN POINT');
disp([optDV]);disp(varopt(wor,:));IP = init(opt,:);disp(IP)
```

```
disp('-----------------------------------------------------');
disp('INEQUALITY CONSTRAINT VALUES @ OPTIMUM (TLOW, CMIN, VDROP); @ MOST NON-LINEAR');
optNLC = nonlincontopt(opt,:);disp(optNLC);disp(nonlincontopt(wor,:));
disp('-----------------------------------------------------');
disp('EQUALITY CONSTRAINT VALUES @ OPTIMUM ; MOST NON-LINEAR');
optLC = optlincont(opt,:);disp(optLC);disp(optlincont(wor,:));
disp('-----------------------------------------------------');

%PLOT GLOBAL OPTIMUM SOLUTION
clear x
figure;R_dp = [0:39:20000];
x = optDV;
Tsens = 39*x(1)*x(4)/(alpha*r_ref*x(2))*(1./(x(4)+R_dp)-R_dp./((x(4)+R_dp).^2));
T_range = +x(1)*x(3)/(alpha*x(2)*r_ref)+R_dp*x(1)*x(4)./(alpha*x(4)*x(2)*r_ref+R_dp*alpha*x(2)*r_ref)-1/alpha+T_ref;
plot(T_range,Tsens,'r-');xlabel('Temperature Range [C]');ylabel('Temperature unc. [C]');axis([min(T_range) max(T_range) 0 0.5]);
%COMPARE TO CURRENT DESIGN SOLUTION
hold on
x = [227 26100 37500 40000 0];
Tsens2 = 39*x(1)*x(4)/(alpha*r_ref*x(2))*(1./(x(4)+R_dp)-R_dp./((x(4)+R_dp).^2));
T_range2 = +x(1)*x(3)/(alpha*x(2)*r_ref)+R_dp*x(1)*x(4)./(alpha*x(4)*x(2)*r_ref+R_dp*alpha*x(2)*r_ref)-1/alpha+T_ref;
plot(T_range2,Tsens2,'b-');
%MOST NON-LINEAR SOLUTION
hold on
x = varopt(wor,:);
Tsens3 = 39*x(1)*x(4)/(alpha*r_ref*x(2))*(1./(x(4)+R_dp)-R_dp./((x(4)+R_dp).^2));
T_range3 = +x(1)*x(3)/(alpha*x(2)*r_ref)+R_dp*x(1)*x(4)./(alpha*x(4)*x(2)*r_ref+R_dp*alpha*x(2)*r_ref)-1/alpha+T_ref;
plot(T_range3,Tsens3,'k-');
legend('OPTIMIZED DESIGN','CURRENT DESIGN','MOST NONLINEAR DESIGN');grid on
axis([min(T_range3) max(T_range3) 0 0.8]);

disp('R1 OPT; R1 INITIAL')
disp([optDV(1),IP(1)])
disp('-----------------------------------------------------');
disp('R3 OPT; R3 INITIAL')
disp([optDV(2),IP(2)])
disp('-----------------------------------------------------');
disp('R4 OPT; R4 INITIAL')
```

```
disp([optDV(3),IP(3)])
disp('-------------------------------------------------');
disp('R5 OPT; R5 INITIAL')
disp(optDV(4));disp(IP(4));
disp('-------------------------------------------------');
disp('Rdp OPT; Rdp INITIAL')
disp([optDV(5),IP(5)])
```